Tip Effects on the Vortex Wake of an Axisymmetric Body at Angle of Attack

Thesis by

David Henry Bridges

In Partial Fulfillment

of the Requirements for the Degree of

Doctor of Philosophy

California Institute of Technology

Pasadena, California

1993

(Submitted December 4, 1992)

to Diana

and to my daughter, Laura Elizabeth

born September 21, 1992

amid the stress and strain and turbulence of fluid mechanics

you make me smile

Thus says the God who made the earth, the God who formed it to establish it – Yahweh is his name: Call to me and I will answer you and tell you great and hidden things that you have not known.

Jeremiah 33:2–3, NRSV

Of making many books there is no end, and much study is a weariness of the flesh.

Ecclesiastes 12:12b, NRSV

Acknowledgments

First, I would like to thank my advisor, Dr. Hans Hornung, for his enthusiastic support during the course of my work at GALCIT. His door was always open, and his help was always willing. I hope that in the years to come, I will maintain the same level of excitement in experimental fluid dynamics research that he feels.

I would also like to thank Dr. Hornung's secretary, Karen Cheetham. Karen's knowledge, wisdom, and support over the past five years have certainly made my life much easier than it otherwise might have been. I would like to express my appreciation to Herb Gaebler and Pavel Svitek, technicians in the Hydrodynamics Lab. Their knowledge and physical labor were enormously helpful during the reconstruction of the water channel in my lab and in the experiments I conducted in the Hydrodynamics Lab. Much valuable assistance in the construction of equipment were provided by Lou Johnson (now retired) and Michael Gerfen of Central Engineering. Mike was especially helpful in the construction of the elliptic cross section tips and the FSWT surface plate. Phil Wood's help in the Aero Shop and Harry Hamaguchi's work in the Hydrodynamics Photo Lab were also much appreciated. Aero librarians Jean Anderson and Pat Gladson helped to make my background research an achievable task. I would like to thank Dr. Kim Aaron for his help in obtaining and using his cone model. I would like to thank the other members of my committee, Professors D. Coles, A. Roshko, F. Culick, and C. Peck, for their contribution to this thesis through the examination and revision process.

I would like also to express my thanks to some of my fellow students for their contributions to my doctoral education: Phil Tokumaru, Derek Lisoski, John Budzinski, and especially Jeff Seto, my friend and confidant. They and others have provided a sense of community during my time at GALCIT.

I would like to express my thanks to the members of First Southern Baptist Church of Pasadena, and to our pastor and my good friend, Dr. Dewey F. Squyres, for their support and encouragement over the last five years. They have helped to make Pasadena a home away from home.

Finally, and most importantly, I would like to express, in words that can only attempt to reach the true depths of my feeling, my thankfulness and gratitude for my loving and forbearing wife Diana. Her support and encouragement have enabled my development as a fluid dynamicist, but more importantly, as a person, a believer, a husband, and a father. Diana, my thanks and my love.

The fine print

The first two years of my study at Caltech were supported by Office of Naval Research and ARCS Foundation graduate fellowships. Funds for my research were provided in part by Office of Naval Research Grant No. N00014-90-J-1305. Funds to purchase instrumentation for the reconstructed water channel were provided by NASA through JPL, Research Order No. 49-231-1001-0-3540, courtesy Dr. T. Kubota and Dr. Virendra Sarohia. The basic cone model was provided courtesy Dr. Fred Culick and Dr. Kim Aaron.

Abstract

Experiments on the effects of conditions at the tip of an axisymmetric body on the vortex wake of the body at large angle of attack in incompressible flow have been performed. The separation patterns that occur at the nose of a cone with a hemispherical tip have been documented for ranges of Reynolds number based on tip radius and of relative angle of attack. Tips with cross sections that vary smoothly from elliptic to circular have been designed and tested on a cone. The effectiveness of the tips in varying the cone side force coefficient as the tip is rotated has been demonstrated. The relation between tip roll angle and side force coefficient has been shown to be essentially independent of Reynolds number, for the range of Reynolds number tested, as well as cone base conditions and roll direction. The relation between tip roll angle and side force coefficient has been shown to be a strong function of angle of attack. The reasons for nonsmooth variation of side force coefficient with tip roll angle at higher angles of attack have been determined by examinations of the vortex wake geometry. Peaks in the magnitude of the side force coefficient after zero crossings have been shown to be caused by a rapid shift in the wake vortices away from a symmetric configuration as the tip rotates away from a symmetry condition. Reductions in magnitude of the side force coefficient between magnitude peaks have been demonstrated to be a result of the near vortex crossing over the cone centerline. This vortex crossover has been shown to occur near and after the breakaway from the cone of the far vortex. The ability of one of the elliptic cross section tips to produce smooth variations of side force coefficient with roll angle ahead of vortex breakaway has been demonstrated, suggesting that the tip might be an effective yaw control device for aircraft at high angle of attack.

Table of Contents

List of figures

List of symbols

$[\mathbf{A}]$	Inverse of force balance calibration matrix
a	Circular cylinder radius
$[\mathbf{B}]$	Force balance calibration matrix
b_{ij}	Calibration coefficients ($i, j \in \{XX, N1, N2, Y1, Y2, RR\}$)
C_Y	Side force coefficient
$\overline{C_Y}$	Time-averaged side force coefficient
C_x	Sectional normal force coefficient
C_y	Sectional side force coefficient
c_j	Coefficients in polynomials for elliptic cross section tips ($j = 1, 6$)
D	Cone base or cylindrical afterbody diameter
d	Vortex separation distance; depth coordinate of cone with respect to surface plate
$\mathbf{F}$	Total force on body
$\{\mathbf{F}\}$, $\{\mathbf{F}_{\text{app}}\}$	Vector of loads applied to force balance
F	Nose or elliptic cross section tip fineness ratio
F_j	Force balance applied loads ($j \in \{XX, N1, N2, Y1, Y2, RR\}$)
f_t	Elliptic cross section tip flatness factor
L	Overall model length
m	Cone slope $= \tan\left(\frac{\pi}{2} - \theta_c\right)$
$\mathbf{n}$	Surface normal vector
$N1$	Forward normal force element on force balance
$N2$	Rearward normal force element on force balance
n	Exponent in nondimensional vortex strength model
p	Pressure
R	Square of elliptic cross section tip radius

R_c	Local cone radius
R_t	Tip radius
R_j	Radius of curvature of polynomial at origin ($j = 1, 2$)
Re_D	Reynolds number based on cone base or cylindrical afterbody diameter
Re_t	Reynolds number based on tip radius
RR	Rolling moment element on force balance
r	Elliptic cross section tip radius; radial distance of vortex from centerline of cone
r^2	Linear regression correlation
r_{cj}	Radial coordinate of polynomial-cone generator tangency point ($j = 1, 2$)
r_j	Radius at tip-cone joint
S	Water channel speed setting; surface area
s	Streamwise position coordinate of cone with respect to surface plate
U	Tunnel speed; velocity in cross-flow plane
U_∞	Free-stream velocity
u	x component of velocity in potential flow calculations
V_j	Force balance output voltages ($j \in \{XX, N1, N2, Y1, Y2, RR\}$)
V_p	Output voltage of pressure transducer
V_{p0}	Output voltage of pressure transducer at zero speed
$\{\mathbf{V}\}$, $\{\mathbf{V}_{\text{out}}\}$	Force balance output voltage vector
v	y component of velocity in potential flow calculations
W	Complex velocity potential
X	Sectional normal force
XX	Chord force element on force balance
x, y	Vortex position coordinates

Y	Sectional side force
$Y1$	Forward side force element on force balance
$Y2$	Rearward side force element on force balance
z	Cone axial coordinate; complex number $x + iy$
z^*	Complex conjugate of complex number z
$z_{\text{laser sheet}}$	Axial coordinate of laser sheet
z_{cj}	Axial coordinate of polynomial-cone generator tangency point
α	Angle of attack
α_{AV}	Angle of attack for onset of asymmetric vortex wake
α_{SV}	Angle of attack for onset of symmetric vortex wake
α_{UV}	Angle of attack for onset of unsteady vortex shedding
β	Wake asymmetry angle; sideslip angle
Γ_j	Dimensional vortex filament strength ($j = 1, 2$)
γ_j	Nondimensional vortex strength $\gamma_j = \Gamma_j / 2\pi a U_\infty \sin\alpha,\ j = 1, 2$
θ_A	Nose apex angle
θ_c	Cone semi-angle
θ_m	Angle of mirror on laser sheet traverse
θ_t	Laser sheet traverse angle
λ	Laser wavelength
ν	Kinematic viscosity
ρ	Density
ϕ	Roll angle
ϕ_0	Zero roll angle

CHAPTER 1

Introduction

1.1 Statement of the problem

One of the many unsolved problems of fluid mechanics is that of the side force on an axisymmetric body at high angle of attack. If a pointed, axisymmetric body is placed in a flow such that there is an angle between the body axis and the free-stream velocity vector of the oncoming flow, the plane defined by the body axis and the free-stream velocity vector is a plane of symmetry with respect to the body and the oncoming flow. This plane is referred to as the incidence plane of the body. The angle between the body axis and the free-stream velocity vector is defined as the angle of attack α of the body (see Fig. 1.1). If α is large enough, the body will experience a force in a direction normal to the incidence plane. In other words, a *symmetric* body-and-flow condition will produce an *asymmetric* body force. This force is referred to as the out-of-plane force or side force, and can be as large as or larger than the in-plane lift and drag forces on the body.

This large side force is caused by the vortex wake which forms behind the body. At zero and small angles of attack, the flow remains attached to the body. When the angle of attack is increased to a value equal to or larger than a value usually denoted by α_{SV}, the flow separates from the body and rolls up into two vortices which remain attached to the body, one on either side (see Fig. 1.2). For a range of angle of attack larger than α_{SV}, these two vortices maintain an essentially steady, symmetric configuration behind the body, and the body side force remains zero.

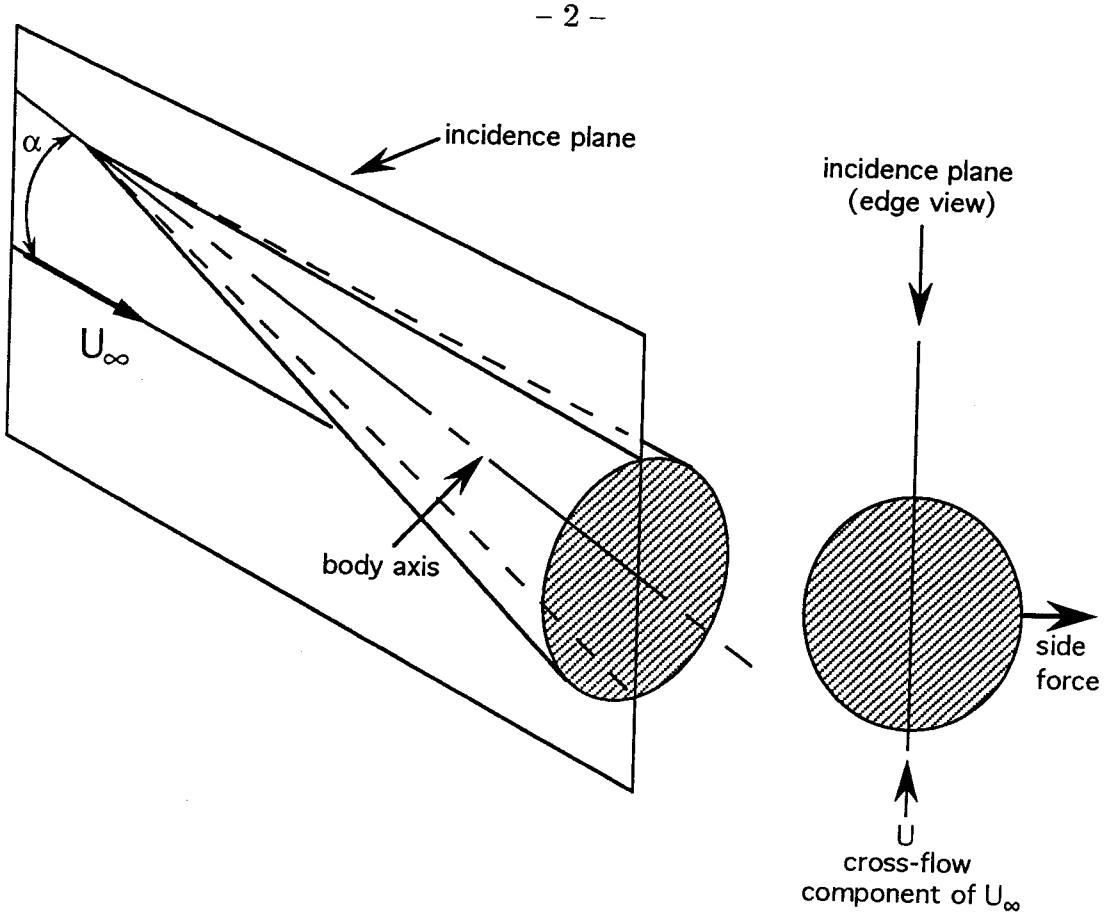

FIG. 1.1 Axisymmetric body at angle of attack: definitions

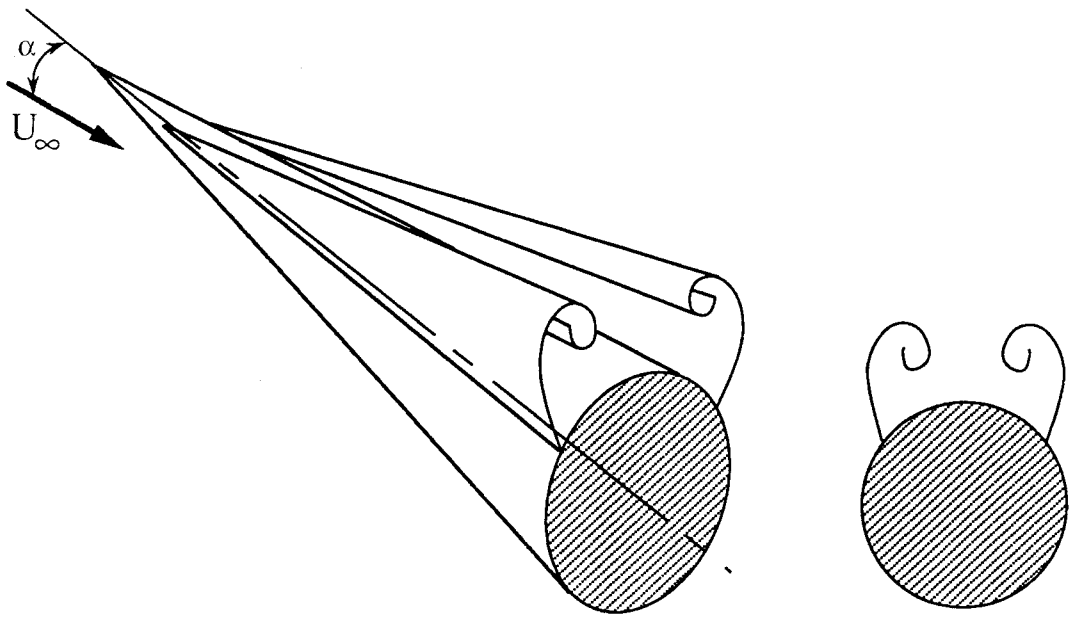

FIG. 1.2 Symmetric vortex wake: $\alpha_{SV} \leq \alpha \leq \alpha_{AV}$

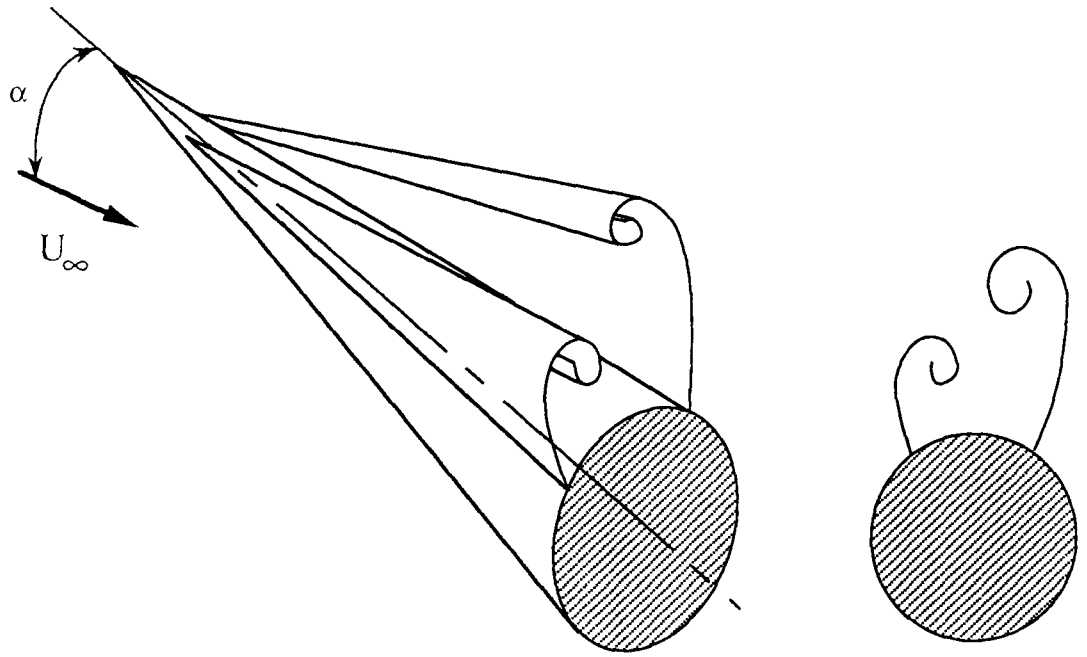

FIG. 1.3 Asymmetric vortex wake: $\alpha_{AV} \leq \alpha \leq \alpha_{UV}$

When the angle of attack is increased further, to a value equal to or greater than a value usually denoted by α_{AV}, the steady, symmetric vortex wake switches to a steady, asymmetric vortex wake (see Fig. 1.3). The asymmetric pressure distribution induced on the body by this asymmetric vortex configuration is the cause for the large body side forces. If the angle of attack is increased still further, to a value usually denoted by α_{UV}, the steady, asymmetric wake changes to an unsteady flow in which vortices are shed in a manner very similar to that in which vortices are shed from a two-dimensional circular cylinder. It is the switch from a steady, symmetric vortex wake to a steady, asymmetric vortex wake behind the symmetric body that is the main part of the problem to be solved in the flows just described.

The side force on an axisymmetric body at high angle of attack is not merely an academic problem. The flight envelopes of modern fighter aircraft and missiles include high angle of attack regimes. The flow past the nose of a modern fighter aircraft at high angle of attack bears a great resemblance to the flow past a pointed axisymmetric body, such as a missile, at high angle of attack. If the wake of the

missile or aircraft nose at high angle of attack suddenly assumes an asymmetric configuration, a large side force can suddenly be generated, leading to a large yawing moment and subsequent loss of control of the vehicle. Further, when a fighter aircraft is at high angle of attack, the rudder, the normal yaw control surface of the aircraft, is submerged in the wake of the aircraft's wing, and the effectiveness of the rudder, and hence the yaw control of the aircraft, is diminished. If some means could be found to control the magnitude and direction of the side force on the nose of the aircraft, then this side force could be used as a steering mechanism for the aircraft at those angles of attack where the rudder is ineffective. Thus a solution to the side force problem would have immediate applications in the military aircraft industry.

1.2 Review of earlier work

The first researchers to make note of the asymmetric vortex wake behind an axisymmetric body at high angle of attack were Allen and Perkins (1951a, 1951b). The first to measure the side force and yawing moment on an axisymmetric body at high angle of attack was Letko (1953). These studies were only the beginning of an intensive research effort that has produced a considerable number of papers over the last forty years. In recent years, a number of summary papers have appeared. One of the best introductions to the side force problem is the survey paper by Hunt (1982), in which can be found substantiation for all of the statements made in the opening paragraphs. Two authors who have produced a number of recent summary papers which present in some cases alternative viewpoints to those expressed by Hunt are Ericsson and Reding (1980, 1981a, 1981b). Two survey works which include emphases on modelling and design approaches are those of Wardlaw (1979) and Ericsson and Reding (1986). An introduction to the application of the results found in these papers to modern aircraft design can be found in the paper by Skow and Erickson (1982).

Some details of the flows described in the opening section are provided by Hunt. The angle at which the symmetric vortex wake first appears, α_{SV}, is on the order

of 10°. The angle at which the asymmetric vortex wake first appears, α_{AV}, is on the order of 30°. The angle at which unsteady vortex shedding first appears, α_{UV}, is on the order of 60°. These are rough estimates, as these angles are functions of many variables. As might be gathered from this discussion, the angle of attack is a very important parameter in these flows, if not the most important parameter. The experimental evidence seems to indicate that the correct normalizing factor for the angle of attack is the nose apex angle θ_A (Ericsson and Reding 1980; Hunt 1982). The nose apex angle for a cone is simply the cone semi-angle θ_c, while the apex angle for an ogive is given by

$$\theta_A = \tan^{-1}\left(\frac{F}{F^2 - 0.25}\right), \tag{1.2.1}$$

where F is the ogive fineness ratio, or the ratio of the ogive length to ogive base diameter (Ericsson and Reding 1986). Rainbird *et al.* (1963) conducted an extensive study of the boundary layers on and symmetric vortex wakes behind two cones with different semi-angles. The results for separation locations, vortex positions, and other boundary layer and wake properties were correlated by the relative angle of attack α/θ_c. Their results were also in general agreement with the results of an application of slender body theory, such as that described by Liepmann and Roshko (1957), from which the governing parameter for the flow was found to be α/θ_c. Keener and Chapman (1974) observed from experimental data for axisymmetric noses alone that the angle of attack at which the vortex wake became asymmetric, α_{AV}, was more or less a constant multiple of the apex angle θ_A, with $\alpha_{AV}/\theta_A \approx 2.1$, independent of whether the nose was a cone or ogive. Since for a given fineness ratio an ogive has a larger apex angle than a cone, this result implies that symmetric wakes may be obtained at higher angles of attack for an ogive than for a cone. This was what Keener and Chapman observed. Ericsson and Reding (1979) observed from experimental data for an axisymmetric body with cone and ogive noses with identical fineness ratios that the magnitude of the side force coefficient for the body had the same variation with relative angle of attack α/θ_A for both cone and ogive noses, although the apex angle of the ogive was twice that of the cone. An analysis

conducted by Keener and Chapman (1977) could explain why α_{AV} might increase with an increase in θ_A. There has been some debate over whether the asymmetric wake behind an axisymmetric body at high angle of attack is caused by viscous or inviscid effects. Keener and Chapman (1977) compared the onset of asymmetric wakes behind slender bodies and delta wings with large sweepback angles, where the separation point is fixed. The similarities between the two phenomena led Keener and Chapman to conclude that the asymmetric wake is the result of an inviscid instability that occurs when the two wake vortices are "crowded together" near the tip of the body. One vortex moves away from the body and the other vortex moves underneath the first. A larger nose apex angle would increase the distance between the vortices and thus reduce the vortex "crowding," so that a higher angle of attack would be required for onset of wake asymmetry.

Hunt also discusses the effects of two other parameters that are important in flows past bodies at high angle of attack, the Reynolds number and the Mach number. One general trend described by Hunt is that the maximum time-averaged side force on a body seems to occur when the boundary layers on the body ahead of separation are either fully laminar or fully turbulent, the side force having a minimum when the Reynolds number based on body diameter, Re_D, is in the transitional range. One work in particular which demonstrates this trend explicitly is that of Lamont (1980). Another trend described by Hunt, and shown in particular by Pick (1975), is that the side force seems to decrease as the Mach number M increases. Hunt attributes the decrease in side force to the presence of supersonic crossflow in the vortex wake which partially isolates the vortex wake from the body and thus diminishes the effects of the vortex wake configuration on the pressure distribution on the body. The reader is referred to the summary papers listed above for other general information regarding the side force problem.

Many efforts to model the flow past an axisymmetric body at high angle of attack have been attempted. These generally tend to fall into three categories: using an analogy between this flow and the flow past a circular cylinder impulsively

started from rest, modelling with discrete vortex elements such as filaments and sheets, and more direct computations using vortex particle, Euler, and Navier-Stokes methods.

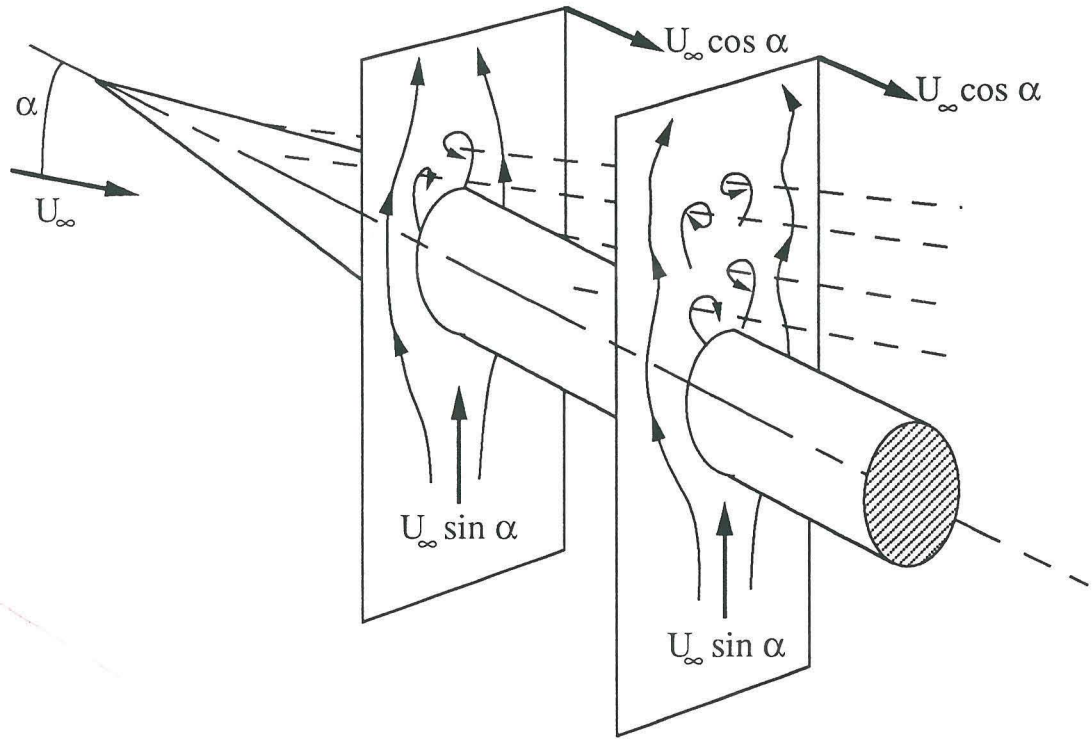

FIG. 1.4 Illustration of impulsive flow analogy

The impulsive flow analogy was first introduced by Allen and Perkins (1951a). If the axisymmetric body at high angle of attack has a pointed tip and then a cylindrical afterbody that is long enough, a series of steady vortices may develop which originate on the body and then break away from the body at some point and align themselves with the free-stream direction, while the portion of each vortex upstream of each breakaway point remains attached to the body. The breakaway points will alternate from side to side along the body. See Fig. 1.4. Consider a plane normal to the axis of the body being convected down the body with a speed equal to $U_\infty \cos\alpha$, the component of the free-stream velocity parallel to the body axis In this plane, there will be a cross-flow velocity given by $U_\infty \sin\alpha$. As this

plane convects down the body, it will encounter the vortices being formed on and breaking away from the body. The flow in this plane will bear a great resemblance to the flow past a circular cylinder impulsively started from rest. Studies and applications of this model may be found in Sarpkaya (1966), Thomson and Morrison (1971), and Lamont and Hunt (1976), among others. These studies attempted to use information that is known about the wake of the impulsively-started circular cylinder, such as the stable Kárman vortex street configuration and the variation with time of the lift and drag of the circular cylinder, to predict the steady flow past the axisymmetric body at high angle of attack. More recently, Hall (1987) has examined the impulsive flow analogy and has shown its usefulness in correlating various flow quantities. The impulsive flow analogy is not a complete solution to the high angle of attack problem, however, because of effects caused by the shape of the nose, which is neglected in the impulsive flow analogy (Ericsson and Reding 1980).

Modelling the vortex wake of a delta wing at high angle of attack with discrete vortex filaments was first suggested by Brown and Michael (1955). This is a potential flow analysis which assumes that the vorticity contained in the separated vortex sheets is collapsed into two discrete vortex filaments that extend from the apex of the delta wing. This model has also been used to compute the flow past axisymmetric bodies at high angle of attack and is most often used when the body is a right circular cone or a conical body with elliptic cross sections (Bryson 1959; Fiddes 1980). One of the key features of this model is the "no-force" condition. In order for the velocity potential to be single-valued, a cut extending from the vortex has to be introduced into the flow field. This cut usually connects the vortex to some point on the body, most often a point related to the separation point in some manner. Because of the jump in the velocity potential across this cut, there is a pressure difference across the cut, and hence a hydrodynamic force acting on the cut. Also, since the vortex filament is inclined to the flow direction so that there is a component of flow velocity normal to the filament, there exists a hydrodynamic

force on the filament. The "no-force" condition states that only the body and not the fluid can sustain forces (Brown and Michael 1955). Therefore, the vector sum of the forces on the cut and on the vortex filament are set equal to zero, and this condition is used as part of the calculation of the vortex strength and position. One development of these ideas and the related mathematical derivations is given by Smith (1968), who also extended the notion of the cut to obtain the shape and strength of the rolled-up vortex sheet that connects the vortex to the body for a delta wing. The first to apply the vortex filament model to the flow past a cone at high angle of attack was Bryson (1959), who limited the flows considered to symmetric vortex wakes by enforcing a symmetry condition. Dyer *et al.* (1982) showed that the vortex filament model could yield asymmetric vortex wakes behind circular cones even when the separation points on the body were symmetric. Pidd and Smith (1990) is representative of the current state of these models, and Chin and Lan (1988) provide a comparison of some of the different implementations of these models.

The advent of fast supercomputers, the development of codes and grid generation algorithms to take advantage of these computers, and the difficulties and expense involved in trying to conduct experiments at the correct Reynolds numbers have caused a shift in research emphasis from experimental to computational studies in the past few years. The recent book by Rom (1992) gives an extensive overview of current computational techniques for high angle of attack aerodynamics. The work of Hartwich *et al.* (1990) at NASA Langley Research Center and Degani and Schiff (1989a) at NASA Ames Research Center are representative of current computational efforts applying Navier-Stokes methods to the problem of an axisymmetric body at high angle of attack. When considering the results presented by these works, one should keep in mind the difficulties in computing large Reynolds number (10^6), massively-separated, three-dimensional, turbulent flows.

One of the difficulties encountered in analyzing the separated flow behind an axisymmetric body at high angle of attack is that the flow is a *three-dimensional*

separated flow. As pointed out by Hornung and Perry (1984), there is a debate over the very definition of separation in three dimensions. Maskell (1955) was one of the first to attempt a thorough analysis and description of three-dimensional, separated flows. One important concept introduced by Maskell was that of the limiting streamline. Because of the no-slip condition, fluid particles in contact with a body surface can have no velocity relative to the body, and hence streamlines cannot be defined on the body itself, if the standard definition of a streamline is used. However, a streamline passing a small distance above the surface can be defined using the standard definition of a streamline. When this small distance is allowed to approach zero in the limit, the limiting streamline is defined. The limiting streamlines are related to the skin friction distributions on the surface of the body. Legendre (1956) stated that isolated points on the body where the surface skin friction vector went to zero were singular points of the surface flow patterns, and that these points were of the node, focus, and saddle point types. Lighthill (1963) stated that the range of possible overall patterns of skin friction and vortex lines on a smooth surface was subject to a simple topological law, that on a simply-connected body, the number of nodes must exceed the number of saddle points by 2. Peake and Tobak (1980; see also Tobak and Peake 1982) used the results of Legendre and Lighthill to obtain simple topological rules governing the set of nodes and saddle points contained in the flow. Ahn and Simpson (1992) provided this outline of the development of topological ideas applied to three-dimensional separated flows. Peake and Tobak (1980) contains a more thorough description of the development of these ideas and an extensive collection of flow visualization photographs with accompanying topological descriptions to demonstrate the application of these ideas. Perry and Fairlie (1974) extended the work of Oswatitsch (1958) in relating the singular points discussed above to the critical points of phase-plane and phase-space theory of ordinary differential equations and in systematically classifying these critical points using local solutions of the Navier-Stokes and continuity equations. The type of critical point (focus, node, saddle) is determined by the signs and values of the invariants of the systems of ordinary differential equations obtained from

the local analyses of the Navier-Stokes and continuity equations. These invariants are combinations of pressure and shear stress gradients. Perry and Chong (1987) contains a description of this type of analysis. A more complete discussion of flow invariants and the resulting critical points can be found in Chong *et al.* (1990). Perry and Chong (1986) used such local solutions to the continuity and Navier-Stokes equations to synthesize three-dimensional separation patterns. By varying the number of critical points in the flow field and the flow field boundary conditions, they could reproduce a variety of separation patterns that were similar to those on the nose of an axisymmetric body, as described by Peake and Tobak (1982).

1.3 Importance of conditions at the body tip

According to Hunt, one of the most important factors in the axisymmetric body side force problem is the influence of the nose of the body on the side forces on the entire body. The data of Lamont and Hunt (1976) and Kruse *et al.* (1979) show that the side force on the entire body is greatest when the flow asymmetry, indicated in these two works by the sectional side force (side force per unit length), begins on the nose of the body. Coe *et al.* (1972) investigated bodies with conical, tangent ogive, and paraboloid noses and found a different side force-angle of attack characteristic for each nose shape. Keener and Chapman (1974), Jorgensen and Nelson (1974, 1975), Kruse *et al.* (1979), Keener *et al.* (1977), and more recently, Koren *et al.* (1992), also report changes in the side force-angle of attack characteristics with changes in nose shape. Further, Keener and Chapman (1974) and Keener, Chapman, Cohen, and Taleghani (1976) show that the side force on a tangent ogive forebody is essentially unaffected by the addition of a cylindrical afterbody. Keener, Chapman, and Kruse (1976) describe the effect of afterbody length on the forces on the body as a whole as a delay in the onset of side forces as angle of attack is increased and a slight reduction of the maximum side force as afterbody length is increased. Hall (1987) has shown that the sectional side force coefficient nearest to the apex of the body nose can determine the side force distribution on the entire body. The test conditions in these papers cover wide ranges of Reynolds and Mach

numbers, and so the results stated are relevant for a wide variety of flow conditions. The importance of the tip apex angle θ_A discussed in Sec. 1.2 is also an indication of the importance of the conditions at the tip of the body (see Ericsson and Reding 1979). Ericsson and Reding (1980) contains a review of the importance of nose-induced asymmetric vortices as opposed to those occurring on the afterbody.

1.3.1 Tip blunting

Hunt also points out works that show that not only is the shape of the nose of the body important to the side force behavior, but also that conditions at the tip of the nose are significant contributors to side force behavior characteristics. One such tip effect is that of tip rounding or tip blunting. Letko (1953) documented a substantial reduction in yawing moment coefficient for an axisymmetric body at high angle of attack as a result of cutting off portions of the sharp tip of the body. Gowen and Perkins (1958), and more recently, Jorgensen and Nelson (1974, 1975), Keener and Chapman (1974), Pick (1975), Keener *et al.* (1977), Kruse *et al.* (1979), and Chu *et al.* (1988), among others, have shown that increasing the radius of the nose of an axisymmetric body at high angle of attack generally leads to a decrease in the side force on the body.

As was pointed out earlier, experiments have shown that the side force reaches maximum values when it begins on the nose of the axisymmetric body. According to Ericsson and Reding (1980), nose-induced separations on blunt axisymmetric bodies at high angle of attack prevent the formation of open separations and wake vortices on the nose of the body. These open separations are associated with high wake asymmetry. The wake vortices are generated by the afterbody instead, resulting in lower side forces. Hunt (1982) makes a similar argument. Separation patterns at the noses of axisymmetric bodies at angle of attack such as those discussed by Ericsson and Reding have been documented in the transonic range by Hsieh and Wang (1976), Hsieh (1977), and Bippes and Turk (1984). These same separation patterns can also occur for zero Mach number, as is illustrated by Werlé (1962) and Bippes and Turk

(1984). Some examples of such separation patterns are shown in Fig. 1.5, which was taken from Peake and Tobak (1982a). The separation pattern in the figure labeled "Legendre-type separation"* was included to represent a class of separation patterns in which the vortex appears to emerge from the surface of the body in a direction normal to the body surface, as opposed to vortices that originate in directions close to parallel to the body surface, as in the local separation, or vortices that do not intersect the body surface at all, as in the "U"-shaped separation. The separation patterns documented by Hsieh and Wang (1976), Hsieh (1977), and Bippes and Turk (1984) were predominantly Legendre-type separations. The local separation in this figure corresponds to the open separation discussed by Ericsson and Reding. It should be noted that all of the separation patterns shown in this figure are at the origins of the wake vortices, as opposed to the nose separation patterns discussed by Ericsson and Reding, which were distinct from the wake vortices. However, the separation patterns in this figure do give an indication of the nature of the nose separation patterns discussed by Ericsson and Reding.

The analysis by Keener and Chapman (1977) with regard to the effects of vortex "crowding" that was discussed in Sec. 1.2 might also be applicable at this point. If for some reason the vortices should originate at points on the body where distance between the vortices is large enough to prevent "crowding," then, by this analysis, the vortex wake asymmetry should be eliminated, or at least reduced. This seems to be the case in the analysis by Ericsson and Reding. The appearance of the nose-induced separations forced the vortices to originate further back, on the afterbody, where the distance between vortices was greater. As was pointed out in reference to Fig. 1.5, it is possible for the wake vortices to originate in the nose separation patterns themselves. Such vortex origins could result in reduced wake asymmetry if either the distance between the vortices caused by the global separation was large enough to prevent "crowding," or the freedom of movement that exists between vortices originating in local separations was reduced by the

* Names for separation patterns in figure provided by author.

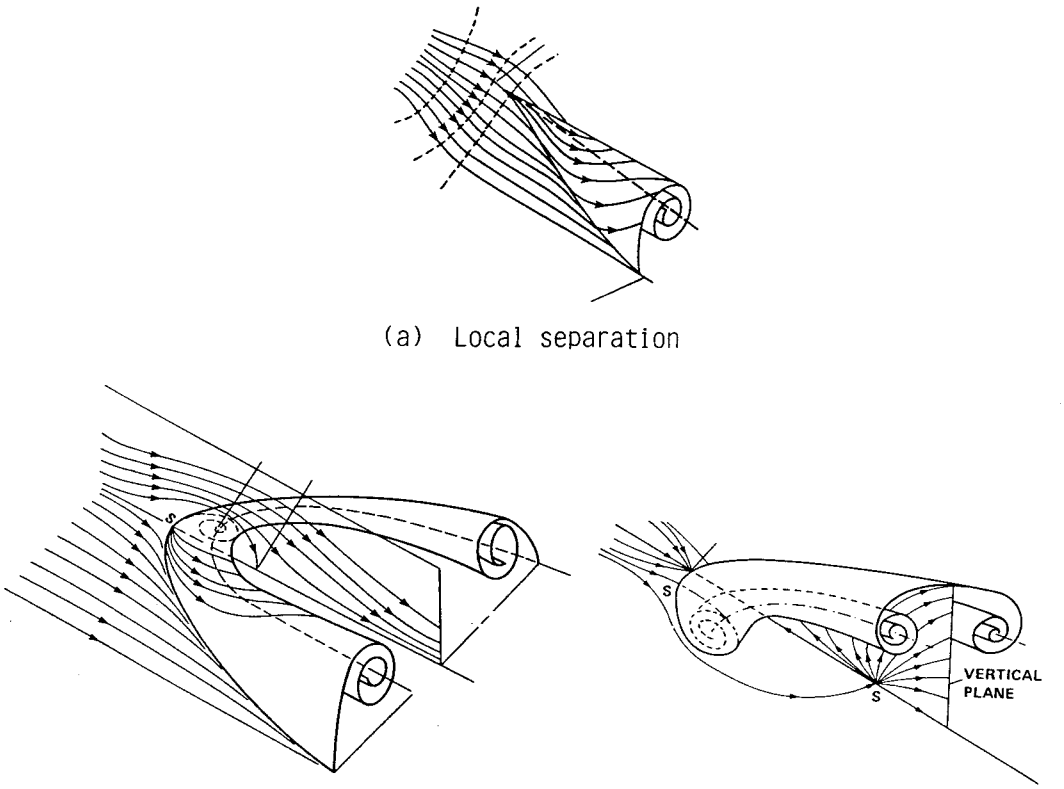

FIG. 1.5 Separation patterns on axisymmetric bodies (from Peake and Tobak 1982a)

connection of the wake vortices in the global separations. In any case, there does appear to be a connection between the appearance of the global separations on blunt bodies such as those shown in Fig. 1.5 and the reduction of wake asymmetry caused by tip blunting.

The separation patterns shown in Fig. 1.5 are all located at the origins of the wake vortices. Another type of separation at the nose of an axisymmetric body at angle of attack has been observed. Small, localized regions of separated flow can occur near the tip of a blunted body. These regions are usually referred to as "separation bubbles." Werlé (1962) contains photographs of the flow past a cylinder with a blunt axisymmetric nose at zero angle of attack. These photographs show the existence of a separation bubble which extends completely around the circum-

ference of the body slightly downstream of the transition from nose to cylinder. This separation bubble is analogous to the separation bubbles which form on two-dimensional airfoils at low Reynolds number. At small angles of attack, the bubble which forms on the axisymmetric body is a small, localized region of separated flow on the lee side of the body which does not extend around the circumference of the body. Such bubbles were observed by Hall *et al.* (1957) and are discussed in Ericsson and Reding (1980). In Ericsson and Reding, these bubbles are referred to as "nose-induced separations." In these flows, the separation bubble near the tip was a flow feature distinct from the wake vortices which formed further aft on the body and which originated in local separations.

The flow separation patterns shown in Fig. 1.5 were analyzed in the context of the topological descriptions of the flow field discussed above. Peake and Tobak (1980, 1982a, 1982b) have shown a large variation with angle of attack and Mach and Reynolds numbers of the skin friction and flow patterns on and around axisymmetric bodies. In particular, they have documented the existence of a large variety of flow structures on and near the noses of blunt bodies at angle of attack as the Mach and Reynolds numbers are varied.

The variation of side force with Reynolds number was described briefly in Sec. 1.2. Detailed analyses of Reynolds number effects may be found in Lamont (1980), Hunt (1982), Polhamus (1984), Champigny (1984), and Ericsson and Reding (1986). One important point that should be kept in mind when considering the effects of Reynolds number on the flow past a pointed, axisymmetric body at high angle of attack is the proper definition of Reynolds number for such a body. The Reynolds number discussed in the literature is usually based on the afterbody diameter or the nose base diameter, if there is no afterbody. If the body in question is a sharp-tipped right circular cone with no afterbody, the only physical length scales available with which to define a Reynolds number are the cone length and base diameter. If interest is centered on the flow near the tip of the cone, where base effects are unimportant, then neither of these length scales is suitable for defining

the Reynolds number. Changes in the flow field near the tip of the body might be expected if the flow velocity were increased, but not if the cone were made longer. Both of these changes would increase the Reynolds number based on base diameter (for a fixed cone semi-angle), but only the first should actually affect the flow near the tip. In this case, a more relevant Reynolds number would seem to be that based on the local diameter. This Reynolds number would vary along the cone but would probably be an accurate indicator of local conditions at any particular location on the cone. This proposition is supported by the photographs of Keener (1986), which show the surface skin friction patterns on a tangent ogive at various angles of attack, using the oil flow technique. For a Reynolds number based on nose base/afterbody diameter on the order of 10^6, where the flow on the cylindrical afterbody is fully turbulent, the photographs show evidence of laminar, transitional, and turbulent separation on the ogive nose of the body, in that order as distance from the nose tip and hence local Reynolds number increases. The necessity of using the local diameter in defining the Reynolds number for a conical flow field was also pointed out by Hall (1987) in his discussion of the impulsive flow analogy.

If, however, the circular cone described in the previous paragraph is blunted in some manner such that the tip has a finite radius of curvature, then a length scale is introduced that can be used to define a Reynolds number that should govern the flow at the tip of the cone. Recall the discussion above of the effects of nose blunting and the appearance of various structures near the noses of blunted bodies as the angle of attack and Reynolds number were varied. Even if the asymmetric wake is an inviscid phenomenon, the appearance of flow separation structures should be dependent at least in part on viscous effects. It is plausible then to suggest that the appearance and behavior of such structures might be governed by a Reynolds number based on the tip radius, referred to as the tip Reynolds number and denoted by Re_t.

1.3.2 Tip asymmetry

Another tip effect described by Hunt is that of tip asymmetry. This effect is usually discussed in the context of variations of side force with roll angle. Not only does an axisymmetric body placed at high angle of attack experience an asymmetric wake and a large side force, but the wake asymmetry and the side force can vary significantly as the model is rolled about its axis. These variations with roll angle were documented by Coe *et al.* (1972), Keener and Chapman (1974), Hunt and Dexter (1978), Ericsson and Reding (1979), Lamont (1980), and Dexter and Hunt (1981), among others. In particular, Dexter and Hunt (1981) established the dependence of the body side force on the roll orientation of the nose of the body. Rotating only the tangent ogive nose of an axisymmetric body at high angle of attack produced a variation in local side force coefficient with nose roll angle that was almost identical to the variation obtained by rotating the entire body, for two different noses. In all of these experiments, the variations with roll angle were attributed to small geometric imperfections near the body tip, the conclusion also drawn by Ericsson and Reding (1979). More recent works that also show wake asymmetry variations attributed to geometric imperfections or disturbances at the body tip are Chu *et al.* (1988), Zilliac *et al.* (1991), and Modi and Stewart (1992). The level of flow sensitivity to tip disturbances was shown by Zilliac *et al.*, who discovered that the accumulation on the body tip of dust particles with diameters on the order of 3 μm (0.014% of the body diameter) produced large changes in the side force-roll angle characteristic which were eliminated when the dust particles were removed with lens tissue.

Once the importance of body tip conditions had been established, researchers began to deliberately introduce small perturbations to the body tip. Moskovitz (1989) and Moskovitz *et al.* (1989) studied the effects of tip roughness, bluntness, and geometric disturbances in the form of beads attached to the nose of the body near the tip, and found that all had large effects on the body side force. In particular, they found that the closer to the tip the beads were attached, the larger the effect

the beads had on the side force-roll angle characteristic. A similar increase in disturbance effectiveness with decrease in distance from the body tip was observed computationally by Degani and Schiff (1989b) for a disturbance consisting of a small jet, and by Degani (1991) for a small "bump" on the body surface. One result of these two numerical investigations was that the vortex wake asymmetry only existed when the disturbance was present. Whenever the disturbance was removed, the flow would always return to a symmetric state. Since it should be possible to produce a perfectly symmetric body computationally, this result supports the theory that small geometric disturbances were responsible for the wake asymmetry reported in the investigations discussed above. One should not conclude from this discussion, however, that the issue of the effects of microasymmetry at the body tip is completely resolved. Ericsson (1990) refers to nose microasymmetry as a "fickle effect" that will be dominated by moving wall effects which will occur whenever an aircraft or missile executes a maneuver that places it into a high-angle-of-attack regime.

As was stated in Sec. 1.1, one of the reasons for the investigation of the side force problem is the possibility of using the side force on the nose of an aircraft or missile for control. Various methods for manipulating the vortex wake for control purposes have been attempted. One active wake control method that has been investigated extensively is that of blowing from a small jet placed near the tip of the body. The works of Malcolm and Ng (1991), Guyton *et al.* (1991), and Guyton and Maerki (1992) are representative of these studies. Another active method of control that has been studied by Fidler (1980) and Modi and Stewart (1992), among others, is that of spinning the tip of the body. The most extensively investigated passive method of vortex wake control has been that of strakes near the body tip. The work of Malcolm and Ng (1991) is representative of these studies. The success of these attempts has been mixed. The method employed is usually able to predictably set the sign of the side force but is less successful at providing a smooth variation of side force with control parameter, whether the parameter is jet blowing rate, strake

deflection, or nose tip rotation rate. Recent work by Bernhardt and Williams (1992) has shown that for a limited Reynolds number range, a continuous variation of side force coefficient with jet suction ratio may be obtained.

The realization that the vortex wake configuration and thus the body side force were extremely sensitive to conditions at the body tip has caused attention to be focused on the possibility of developing a tip shape that could be used as a control mechanism. The ability of a small perturbation in tip shape to create a large yawing moment on an actual aircraft configuration was demonstrated by Chambers *et al.* (1970), in tests on a one-tenth scale model of the F-111 fighter-bomber. These researchers discovered that a flat spot on one side of the nose tip would repeatably produce a large out-of-trim yawing moment in the opposite direction. The influence of a change in nose shape on the stability of another sharp-nosed aircraft, in this case a full-scale, flying, production version of the Northrop F-5F, was documented by Edwards (1978). A change from the production sharp nose with slightly elliptic cross sections to a blunted nose with more elliptic cross sections produced a large increase in lateral-directional stability caused by the alleviation of side forces on the nose of the aircraft. These two works seem to indicate that modifications to the basic tip shape, without the additions of strakes or jets, might be effective in controlling vortex wake asymmetry and nose side force on an aircraft.

The reason that a variation in basic tip shape might be more effective than strakes or jets in modifying the vortex wake asymmetry is related to the "viscous versus inviscid" debate mentioned in Sec. 1.2. Strakes work by fixing the circumferential location of separation on the body. Jets work by either promoting boundary layer separation through the creation of an adverse pressure gradient or by preventing boundary layer separation through entrainment. All of these mechanisms are viscous in nature. If, however, it is true that the inviscid part of the problem is the most significant, then a variation of basic tip shape might be more effective in controlling wake asymmetry, since it would work by varying the pressure distribution on the body. Using this inviscid mechanism to control the vortex wake asymmetry

would have the added advantage of minimizing Reynolds number effects, so that a given tip shape might be effective in both laminar and turbulent regimes.

The mechanism by which an asymmetry in tip shape might produce a variation in wake asymmetry through a variation of the pressure distribution is described by Hunt (1982, p. 6):

> "Perhaps more plausible is that the critical imperfections on an axisymmetric body take the form of eccentricities in the cross-sectional shape. The pressures and, hence, velocities at separation will then differ on the two sides of the body, with the result that the rate of feeding of vorticity into the primary vortices will differ and hence asymmetry will be promoted. The influence of roll angle will then arise because, as the body is rotated, the eccentricity will rotate and the magnitude and sense of the perturbation will change. For a cone, an eccentricity very near the nose might well determine the entire flow along the body since, in conical flow, similarity is preserved at all stations along the body."

Thus it would appear that, if this analysis is correct, a mechanism might exist that would cause a smooth variation in vortex wake asymmetry and side force as the body tip is rotated, for the proper choice of asymmetric body tip. Such an analysis was reinforced by the work of Moskovitz (1989) and Moskovitz *et al.* (1991). After studying various published data, Moskovitz concluded that the flow field asymmetry variation with body roll angle could be divided into two parts: a regular variation caused by the body being out of round, and irregular variations caused by surface imperfections. Further, he reasoned that a body with elliptic cross sections would produce a side force that would vary smoothly with body roll angle and would undergo four changes in sign over one complete revolution; *i.e.*, the side force variation with body roll angle would be a smooth two-cycle sinusoid. To validate his hypotheses, Moskovitz constructed tips with cross sections that were elliptic near the pointed end of the tip and that gradually became circular near the base of the tip, where the tip attached to the nose of the axisymmetric body. These tips were tested on axisymmetric bodies with conical and ogive noses. At an angle of attack of 30°, Moskovitz obtained smooth two-cycle sinusoids for the sectional side force coefficient-roll angle characteristics for both conical and ogive

noses, as expected. For angles of attack of 40^o and 50^o, the variation of sectional side force coefficient with roll angle for the body with the ogive nose was also a mostly smooth, two-cycle sinusoid. These results would seem to validate the hypotheses of Moskovitz and the analysis by Hunt. However, the results for the elliptic tip on the body with a conical nose at angles of attack of 40^o and 50^o were not as supportive.

At angles of attack of 40^o and 50^o, for the body with a conical nose and elliptic cross section tip, Moskovitz obtained side force coefficients that varied with roll angle as a two-cycle square wave. These results were similar to those of Zilliac *et al.* (1991) for two different modifications to the tip of an axisymmetric body with an ogive nose. The first modification was the addition of a small, cylindrical, transverse rod, mounted directly on the tip of the body. The second was the machining of two flats, one on either side of the axisymmetric ogive tip, to produce what is usually referred to in the literature as a "chisel" tip. Both of these tip geometries produced smooth, two-cycle, sinusoidal variations of body side force coefficient with roll angle for angles of attack of 30^o or less, and two-cycle square wave variations of side force coefficient with roll angle for angles of attack greater than 30^o. It would appear from these results that the nose shapes constructed and tested by Moskovitz were not a complete solution to the side force control problem.

1.4 Research goals and thesis overview

Since the vortex wake behind an axisymmetric body at angle of attack has been shown in the literature to be strongly dependent upon conditions at the tip of the body, the goal of the present study was to explore the effects of tip geometry on vortex wake asymmetry. Two sets of effects in particular were to be studied, those of tip Reynolds number and of tip asymmetry.

As was pointed out in Sec. 1.3.1, there is a possibility that the reduction of vortex wake asymmetry caused by tip blunting might be related to the appearance of various flow separation patterns at the tip of the body. Further, it was argued that these patterns might be governed by the Reynolds number based on the tip

radius, the tip Reynolds number Re_t. While the existence of various flow patterns and structures at the tips of axisymmetric bodies at angle of attack have been documented, no systematic study to determine the ranges of angle of attack and Reynolds number over which different structures might appear has been conducted. Thus the first purpose of the present study was to systematically vary the tip Reynolds number Re_t and the relative angle of attack α/θ_A of an axisymmetric body and record the appearance of the various flow separation patterns. Hemispherical tips were attached to a right circular cone and dye was injected from within the cone. Side views of the resulting flow patterns were videotaped and classified according to type of separation pattern for ranges of angle of attack and tip Reynolds number. Chapter 2 describes these experiments and their results.

The elliptic cross section tips designed and constructed by Moskovitz and discussed in Sec. 1.3.2 seemed to provide the desired results for some angles of attack and for some bodies, but not all. The similarity of his results to those obtained by Zilliac *et al.* for the cruder transverse rod and chisel tip geometries, particularly the square wave variations of side force with roll angle, seemed to suggest that the effects of slight tip asymmetry in the form of elliptic cross sections had not been totally isolated by the tips constructed by Moskovitz. This supposition was reinforced by an examination of photographs of the tips in the thesis by Moskovitz, which illustrated the rather crude nature of the tips. Thus the second purpose of the present study was to design and construct cone tips with *slight* tip asymmetry, in the form of elliptic cross sections that gradually merged into circular cross sections, and then to test the effectiveness of these tips in producing smooth variations of wake asymmetry and body side force with roll angle. The major and minor axes of the elliptic cross sections were obtained by inverting two sixth-degree polynomials that gave axial body distance as a function of body radius. These polynomials were used so that the radius, slope, and curvature of the polynomials could be matched to the radius, slope, and curvature of the cone at the points where the polynomials became tangent to generators of the cone. Chapter 3 describes the design and

construction of two such tips.

One of the two elliptic cross section cone tips was used in a preliminary flow visualization experiment. Cross sections of the vortex wake behind a right circular cone with the elliptic tip were obtained by injecting fluorescein dye from within the cone and illuminating the vortex wake with a laser sheet normal to the axis of the cone. The variation of the angle that a line connecting the two vortex cores made with the horizontal as the cone roll angle was varied was used as an indicator of the effectiveness of the tip in controlling the vortex wake configuration. Chapter 4 describes these experiments and their results.

Because of the results obtained from these preliminary experiments, a set of force measurement experiments was planned and conducted, in order to determine the variation of the body side force with roll angle. The variation of the side force coefficient with roll angle for a right circular cone with two different elliptic cross section tips was measured for ranges of angles of attack and tip Reynolds numbers. These experiments are described in Chapter 5.

The force measurement experiments produced some rather unexpected results, and so more flow visualization experiments were conducted, in order to understand the side force behavior. The same experimental setup as described above was used to document the structure of the vortex wake. Variations of the vortex locations with roll angle and the vortex trajectories along the body were documented, and a simple potential flow analysis was used to estimate the effect of the vortex wake configuration on the body side force. These flow visualization experiments and accompanying results are described in Chapter 6. Chapter 7 contains the conclusions of this study.

CHAPTER 2

Tip Reynolds number effects

2.1 Introduction

As was discussed in Sec. 1.4, the purpose of the experiments to be described in this chapter was to determine the types of flow separation patterns and structures that would occur as the tip Reynolds number and relative angle of attack of an axisymmetric body were varied. In particular, since it has been shown that the reduction of wake asymmetry caused by tip blunting may be related to the appearance of global separations at the tip of the body, such as those shown in Fig. 1.5, the values of Re_t and α/θ_c at which these separation patterns might be expected to be found were to be determined.

2.2 Experimental apparatus and procedure

2.2.1 Facility

The facility used in the Re_t–α/θ_c experiments was a low-speed, free-surface water channel. A schematic diagram of this facility is shown in Fig. 2.1. A description of the water channel as originally constructed and operated at the NASA Jet Propulsion Laboratory (JPL) can be found in Gharib (1985). The flow from the return pipe emptied into a 22^o half-angle diffuser. Three perforated plates were installed in the diffuser to provide pressure drops that matched the pressure rise in the diffuser, in order to prevent severe separation from the diffuser walls. The flow then passed into a straight-wall settling chamber which contained more flow manipulators, including perforated plates, a honeycomb, and 4 turbulence reduction

screens. The quieted flow passed through a 4:1, fifth-order polynomial contraction and into the test section. The test section was 1.52 m long and 46 cm wide. The bottom and side walls of the test section were glass, allowing optical access from the bottom and both sides. After the test section, the flow passed through another honeycomb before passing through the bottom of the water channel and into the pump at the head of the return line.

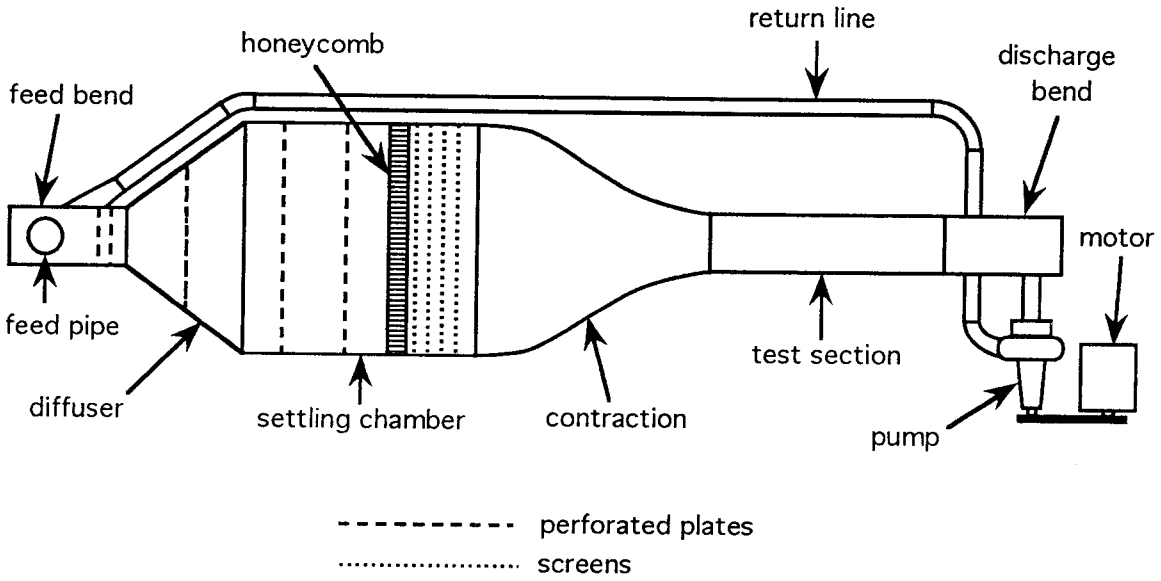

FIG. 2.1 Water channel schematic

The channel was disassembled and reassembled in the basement of the Guggenheim Aeronautical Laboratory building in a slightly different configuration, the one shown in Fig. 2.1. The principal differences between the two configurations were the location of the return line and the method of flow speed control. In the new configuration, the return line was located on the floor of the room in which the channel was located, resulting in a pump location approximately 1.5 m below the level of the free surface of the water, as opposed to a 5 m free surface-pump level difference in the old configuration.

To vary the flow speed, an Eaton Dynamatic AF-500507-0480 adjustable frequency AC drive was acquired to vary the speed of the 50 hp AC motor driving

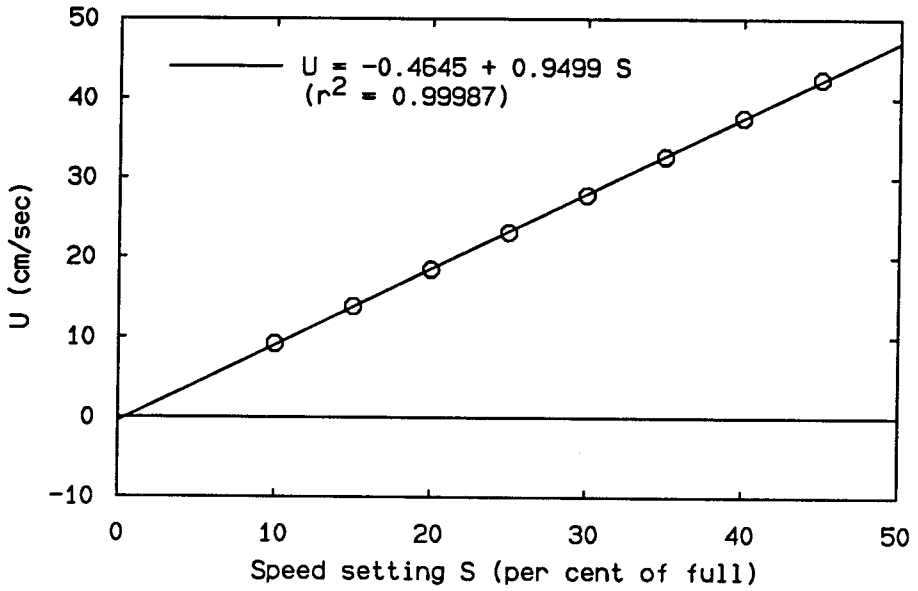

FIG. 2.2 Water channel speed calibration

the 50 hp centrifugal pump, replacing the bypass and throttle valve arrangement of the old configuration. The AC drive speed setting was calibrated using a laser Doppler velocimeter (LDV) system. The channel was filled to a certain level (51 cm) which was marked as a reference level. The AC drive speed setting was varied, and the mean u-component of the velocity at the center of test section was measured. The calibration data are shown in Fig. 2.2, along with the calibration curve resulting from a linear regression fit to the data and the associated value of the linear regression correlation. The test section mean velocity, U, is given as a function of the AC drive speed setting, in per cent of the drive full speed. The data showed a slight nonlinearity, as indicated by the nonzero intercept. However, at a speed of 10 cm/sec, the difference between the measured speed and the speed calculated from the calibration curve was less than 0.125 cm/sec, an error of 1.25%. The errors for $U > 10$ cm/sec were less than 1%. Because of these small errors, this calibration curve was considered adequate for the experiments that were conducted in this facility.

As originally constructed, the water channel had a very low free-stream tur-

bulence level. Gharib (1985) reports that over a range of frequencies up to 25 Hz or more, the free-stream turbulence level was on the order of 0.05% or less, with most of the energy of the free-stream velocity fluctuations that were present concentrated at frequencies below 0.5 Hz, for a free-stream speed of 25 cm/sec. Hot film anemometer studies were conducted in the reconstructed channel to see if the channel in its new configuration still had these low values of free-stream turbulence. The channel speed was set at 20 cm/sec. The output of a TSI 1210-20 Pt hot film sensor positioned in the center of the test section was passed through a TSI 1054B constant-temperature linearized anemometer with a TSI 1117 linearizer card. The output from the card was then filtered with a bandpass filter with cutoff frequencies set at 1 and 200 Hz. The frequencies below 1 Hz were removed to eliminate the effect of U-tube oscillations which are characteristic of such facilities and which were not expected to contribute significantly to the flow patterns to be studied. The frequencies above 200 Hz were removed to eliminate the instrument noise revealed by a check of the anemometer signal with a Hewlett-Packard 3582A spectrum analyzer. An average value of the RMS level of the output of the bandpass filter was obtained from a Hewlett-Packard 3468B digital multimeter. Since the output of the hot film anemometer had been linearized, the turbulence factor for the flow could be obtained by dividing the RMS voltage level by the mean voltage level. The mean voltage level was obtained using the same multimeter to measure the mean of the hot film signal filtered with a low-pass filter whose cutoff frequency had been set at 200 Hz. The turbulence level thus obtained was on the order of 0.1% or less. An analysis of the hot film anemometer signal using the spectrum analyzer yielded no significant broadband noise characteristic of free-stream turbulence. These results seemed to indicate that the facility had retained its low free-stream turbulence characteristics.

Gharib (1985) also reports that the water channel had good flow uniformity in the test section. A 30 cm X 30 cm square area in the center of the test section was surveyed by Gharib, and the resulting non-uniformity was less than 1% of the

centerline mean velocity. No such surveys were conducted in the reconstructed channel, but a hydrogen bubble wire test of the flow in the test section revealed no major flow non-uniformities.

2.2.2 Model and sting

The basic axisymmetric body that was used in all of the experiments of this study was a right circular cone, the simplest pointed, axisymmetric body, and what might be considered to be a "first-order approximation" to the pointed noses of aircraft and missiles. The cone had a 5° semi-angle θ_c and a 9.9 cm base diameter, yielding a 56.6 cm overall length with a sharp conical tip in place (Fig. 2.3).

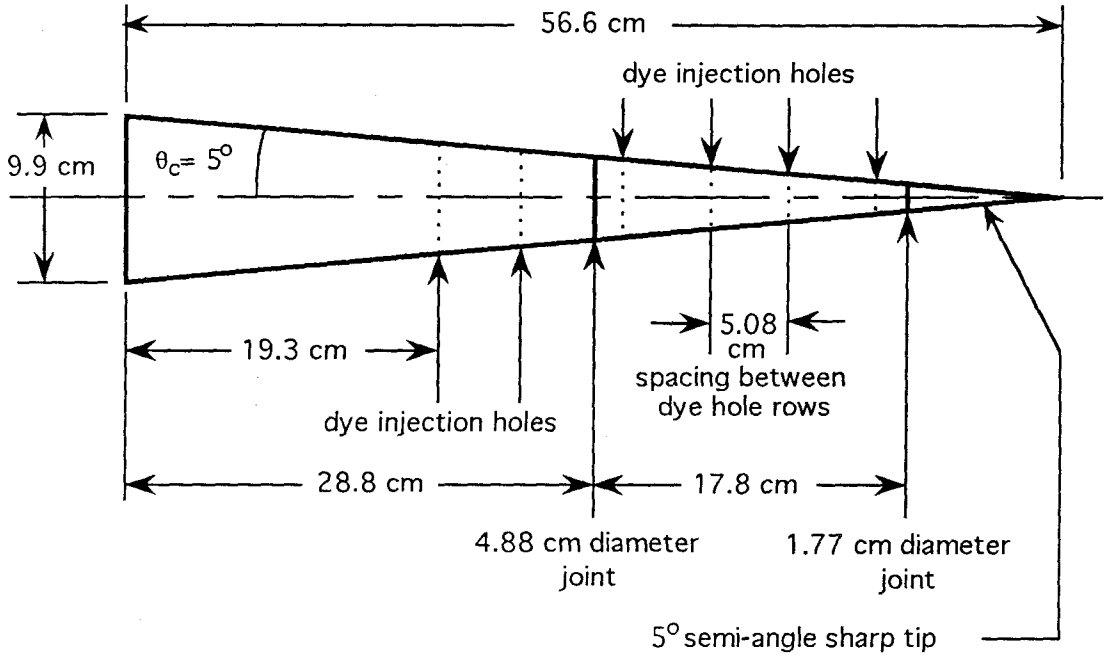

FIG. 2.3 Cone model

The cone was constructed from aluminum and was anodized black. The cone had threaded joints at the 1.77 cm and 4.89 cm diameter locations. The cone also had 6 rows of 24 equally circumferentially spaced, 0.0508 cm diameter holes drilled at 19.3 cm, 24.3 cm, 29.4 cm, 34.5 cm, 39.6 cm, and 44.6 cm from the base of the cone, for the purpose of injecting dye from within the cone.

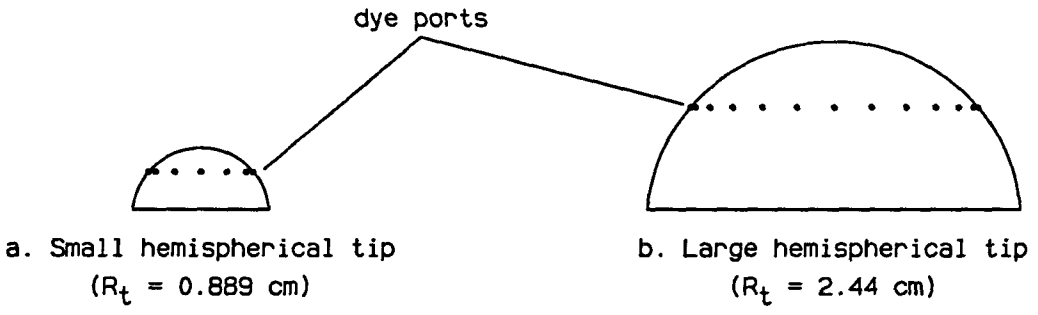

FIG. 2.4 Axisymmetric cone tips

Two tips for the cone were used in the tip Reynolds number experiments. These are shown in Fig. 2.4. Both tips were hemispheres truncated at the 85° latitude so that their slopes would match the slope of the 5° cone at the diameter where each tip was attached to the cone. The smaller tip was constructed to attach to the cone at the 1.77 cm diameter joint, yielding a tip radius R_t of 0.889 cm. With this tip in place, the model had an overall length-to-tip radius ratio L/R_t of 53.3. The larger tip was constructed to attach to the cone at the 4.89 cm diameter joint, yielding a tip radius R_t of 2.44 cm. With this tip in place, the model had an overall length-to-tip radius ratio L/R_t of 12.7. Both tips were hollow, and each tip had a row of equally circumferentially spaced, 0.0508 cm diameter holes drilled at the 50^0 latitude so that dye could be injected from within the tip. The small tip had 12 dye injection holes and the large tip had 24.

The cone was sting-mounted. The sting is shown in Fig. 2.5. The sting rotated about the pivot screw to adjust the angle of attack. The rotating portion had holes drilled so that by passing the set screw through one of the holes, the sting was locked at a particular angle of attack. The holes were drilled such that the sting could be set at angles of attack α from 0° to 100° in 10° increments. Adjustment screws in the sting base mount allowed for 10° adjustments so that the entire angle of attack range from 0° to 100° could be traversed. Once set, the angle of attack was measured with a digital inclinometer to within 0.1°. The DC motor and linkage shown in the figure allowed the cone to be rotated about its axis continually or set

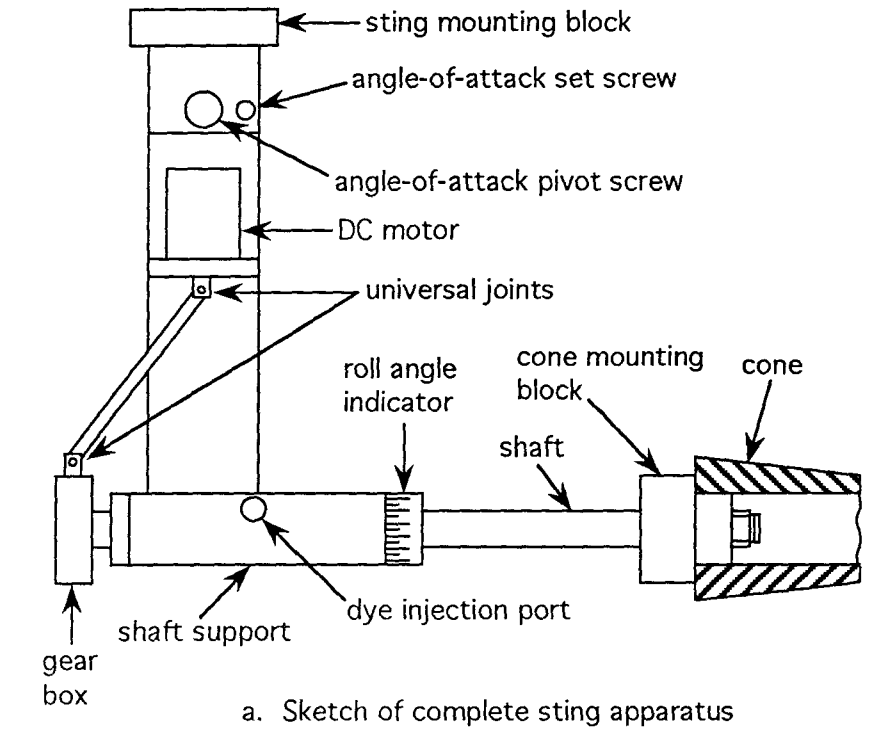

a. Sketch of complete sting apparatus

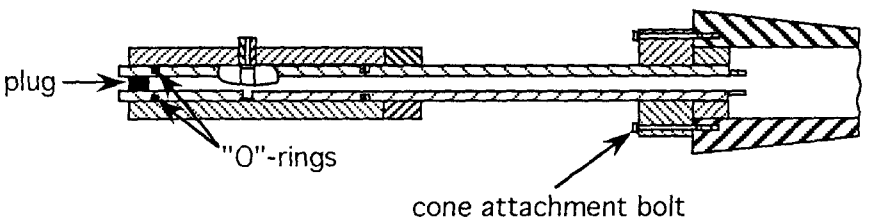

b. Cutaway sketch of shaft showing dye injection path

FIG. 2.5 Schematic of sting mount for cone

to a particular roll angle. The roll angle indicator shown in the figure was marked in 5° increments. The roll angle of the cone could be set to one of the marks on the indicator to an accuracy of $\pm 1^{o}$. The cutaway diagram in Fig. 2.5b shows how the cone shaft was supported. The figure also shows how the capability to inject dye from within the model was provided by the sting.*

* The sting actually had two dye injection paths and 3 "O"-rings. Since only one dye path was used, the other path and 1 "O"-ring have been omitted from the cutaway drawing for purposes of clarity.

2.2.3 Procedure

For these experiments, the angle of attack of the cone with one of the two hemispherical tips attached and the free-stream speed of the water channel were set. Opaque dye was injected from within the model, which was backlit with fluorescent lights. The resulting flow was videotaped through the glass side wall of the channel test section, so that side views of the flow patterns were recorded.

The cone was always assembled under water to prevent bubbles from being trapped within the cone. The height of the cone was adjusted so that the distance between the cone tip and the floor of the test section was at least as much as the distance between the cone base and the side walls of the test section. This practice sometimes resulted in the cone not being completely submerged at large angle of attack. The water channel blockage by the cone with the sharp conical tip, at an angle of attack of 60^o, was calculated to be approximately 6%. Since all of the tips used in this water channel produced less blockage than the sharp tip, and since 60^o was the maximum angle of attack studied in this water channel, the value of 6% for the blockage was actually a maximum for all of the models and conditions of the experiments conducted in this facility. The angle of attack of the cone was varied from 0^o to 60^o in 5^o increments. The range of angle of attack studied yielded values of the relative angle of attack α/θ_c in the range $0 \leq \alpha/\theta_c \leq 12$. As was stated previously, once the angle of attack was set, it was measured with a digital inclinometer to within 0.1^o. The uncertainty in the angle of attack was thus 2% of the cone semi-angle θ_c.

The tip Reynolds number was varied by changing the channel speed and by using the two hemispherical tips with different R_t. The tip Reynolds number was defined as $Re_t = U_\infty R_t/\nu$, where U_∞ was the free-stream speed, R_t was the tip radius, and ν was the kinematic viscosity. The flow speed was set using the procedure described in Sec. 2.2.1. Once the channel speed was set, the flow was allowed to stabilize for at least 20 minutes before images of the flow were recorded. The temperature of the water was monitored using an Omega HH71 type "J"digital

thermometer with a type "J" grounded thermocouple probe. The water channel was located in an air-conditioned room, and the air conditioner was always set to the same level and constantly running. Because of the more or less constant room temperature during the experiments, the water temperature never varied more than 0.5°C from 20.0°C, so a value for the kinematic viscosity ν of 0.01 cm^2/sec (Fox and MacDonald 1978) was used in the definition of Re_t for all of the values of Re_t to be discussed in this chapter. Combining an estimated 2.4% uncertainty in ν with the 1% uncertainty in the free-stream speed discussed in Sec. 2.2.1 and the 0.1% or less uncertainty in R_t for the two tips yielded a value of approximately 3% for the estimated uncertainty in Re_t. At each angle of attack, the free-stream speed was varied from 10 to 50 cm/sec in 5 cm/sec increments for the 2.44 cm radius tip, yielding a Re_t range $2,440 \leq Re_t \leq 12,200$. The specific values of Re_t studied with this tip were 2,440; 3,660; 4,880; 6,100; 7,320; 8,540; 9,760; 10,980; and 12,200. For the 0.889 cm radius tip, the free-stream speed was varied from 10 to 30 cm/sec in 5 cm/sec increments, yielding a Re_t range $889 \leq Re_t \leq 2,667$. The specific values of Re_t studied with this tip were 889; 1,334; 1,778; 2,223; and 2,667. Thus a Re_t range $889 \leq Re_t \leq 12,200$ was covered in the experiments.

The opaque dye used was a food coloring that had been mixed with isopropyl alcohol in order to match its density to that of the water. The specific gravity of the dye-alcohol mixture was measured in a tall, graduated cylinder using a hydrometer and could be measured to an accuracy of 0.05%. The dye was contained in a reservoir mounted approximately 1 m above the free surface of the water channel. The reservoir was connected to the dye injection port on the sting. The rate of dye injection was controlled with a needle valve. Once the channel speed had stabilized, the valve would be opened until the dye began to seep out of the model. The rate of dye injection would be adjusted to produce a minimum disturbance to the flow, based on a visual inspection. As was stated before, the model was backlit with fluorescent lights. Once the dye had sufficiently permeated the flow patterns, a side view of the flow would be videotaped for 1 to 2 minutes.

These investigations were conducted in water for a number of reasons. One was the ability to achieve larger Reynolds numbers at lower speeds than in air. The use of large tips further increased the available Reynolds number, as well as increasing the scale of the problem, so that the details of the separation patterns could be observed. Flow visualization in water is easier than in air, and the low speeds and relatively large model sizes aided the observation of the flow patterns significantly. Finally, as discussed in Sec. 1.2, these patterns are governed by both Reynolds and Mach numbers. Since the parameter of primary interest in this problem was the tip Reynolds number, the use of water set the Mach number to zero so that tip Reynolds number effects were isolated from the effects of compressibility.

2.3 Results

2.3.1 Classification of flows

The results of the Re_t–α/θ_c experiments are shown in Fig. 2.6. This figure shows the different separation patterns that were observed at points in Re_t–α/θ_c parameter space.

The relative angle of attack range of $0 \leq \alpha/\theta_c \leq 12$ corresponded to an angle of attack range $0^o \leq \alpha \leq 60^o$. The experiments indicated that for the cone with the hemispherical tips, this range covered the attached flow range $0 \leq \alpha \leq \alpha_{SV}$, the symmetric wake range $\alpha_{SV} \leq \alpha \leq \alpha_{AV}$, and entered the asymmetric wake range $\alpha_{AV} \leq \alpha \leq \alpha_{UV}$, as discussed in Sec. 1.1. Symmetric wakes were observed up to an angle of attack of 50^o ($\alpha/\theta_c = 10$), and asymmetric wakes were observed at angles of attack of 55^o and 60^o ($\alpha/\theta_c = 11$ and 12, respectively). Here, the terms "symmetric" and "asymmetric" are used to refer to the portions of the vortices that remained attached to the cone. In some cases, the portions of the vortices which remained attached to the cone were symmetric (at least from a visual inspection), but the points at which the vortices broke away from the cone were asymmetric. No unsteady, Kárman-like vortex shedding was observed.

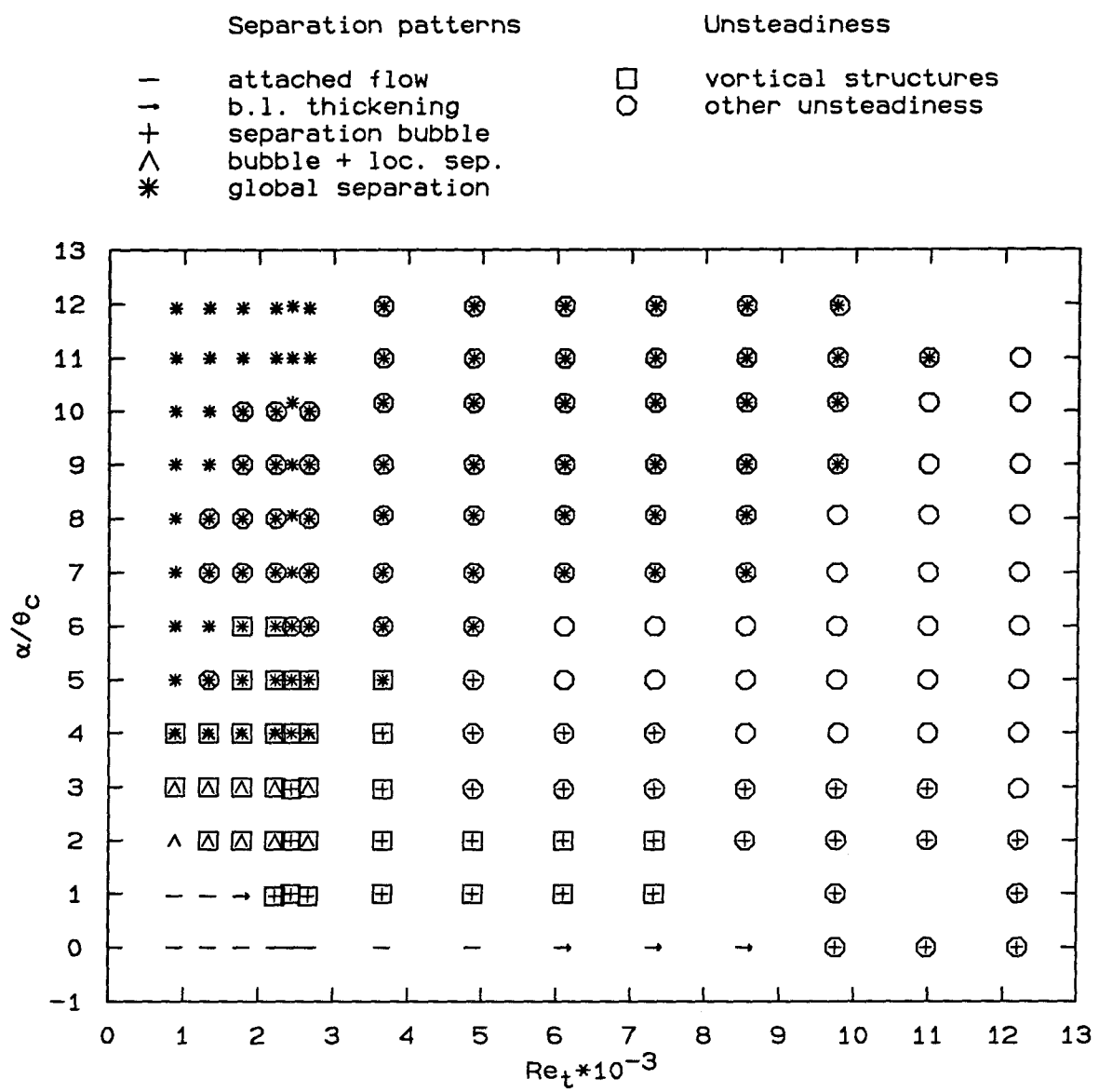

FIG. 2.6 Separated flow patterns in Re_t-α/θ_c parameter space

Four different basic separation patterns that were dependent upon Re_t and α/θ_c were observed. These are shown by solid symbols (arrows, crosses, wedges, and asterisks) in Fig. 2.6. These patterns will be discussed in detail below. A number of types of unsteadiness were observed, with one type, the shedding of vortical structures, being of particular interest. The types of unsteadiness are shown by the open symbols (circles and squares) and will be discussed in detail below. If, in Fig. 2.6, a solid symbol indicating the type of basic separation pattern observed

is not accompanied by an open symbol indicating the type of unsteadiness, that pattern was steady. Similarly, if an open symbol indicating the type of unsteadiness is not accompanied by a solid symbol indicating the type of separation pattern, that pattern could not be determined from the videotape. This tended to happen at the larger values of Re_t and α/θ_c, where rapid diffusion of the dye occurred. There are four points in Fig. 2.6 at which no symbol appears. These points were unintentionally omitted from the experimental grid.

2.3.2 Basic flow separation patterns

The basic flow separation patterns from Fig. 2.6 are shown in Fig. 2.7 for clarity. These patterns were identifiable flow patterns that seemed to be dependent primarily upon Re_t and α/θ_c. Any unsteadiness that occurred seemed to be superimposed upon these basic patterns.

For some Re_t and α/θ_c, the flow remained attached to the cone. The flow conditions at which this occurred are indicated by dashes (–) in Fig. 2.6 and Fig. 2.7. These occurred for a large Re_t range at $\alpha/\theta_c = 0$, and for a smaller range of Re_t at $\alpha/\theta_c = 1$, as might have been expected.

The first basic separation pattern observed was a thickening of the boundary layer immediately behind the joint between the hemispherical tip and the cone. These patterns are indicated by arrows (→). The thickening of the boundary layer seemed to be a precursor to the separation bubble, the second separated flow pattern observed, indicated by a cross (+). Separation bubbles were labeled as such when it was possible to distinguish clearly a separation streamline and reversed flow. In Fig. 2.6 and Fig. 2.7, the separation bubbles are to be understood in the two ways discussed in Sec. 1.3. For $\alpha/\theta_c = 0$, the separation bubble extended completely around the circumference of the cone. The bubble usually developed immediately behind the joint between the hemispherical tip and the cone itself. For $\alpha/\theta_c > 0$, the separation bubble was a region of separated and reattached flow on the lee side of the cone that did not extend completely around the circumference of the cone.

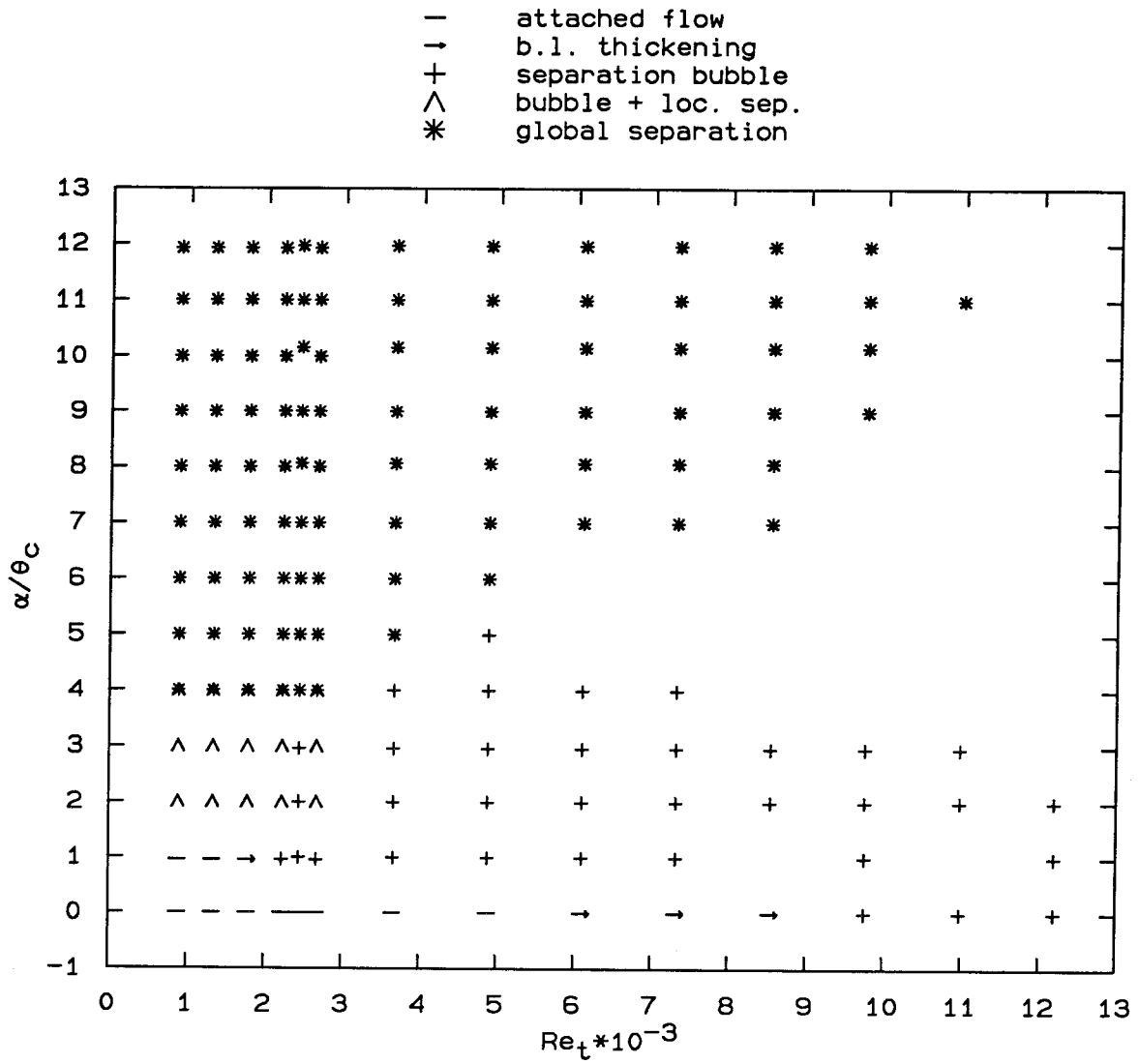

FIG. 2.7 Basic flow separation patterns

From Fig. 2.7, it can be seen that, for $\alpha/\theta_c = 0$, the boundary layer began to thicken to a point where the thickening could be detected by visual inspection at Re_t somewhere between 5,000 and 6,000, and the subsequent recognizable separation bubble appeared at Re_t somewhere between 8,540 and 9,760. Note that this progression from attached flow to boundary layer thickening to separation bubble occurred over a Re_t range $1,778 \leq Re_t \leq 2,223$ for $\alpha/\theta_c = 1$.

The third basic flow separation pattern was a combination of an $\alpha/\theta_c > 0$ separation bubble near the tip plus wake vortices that appeared to originate from

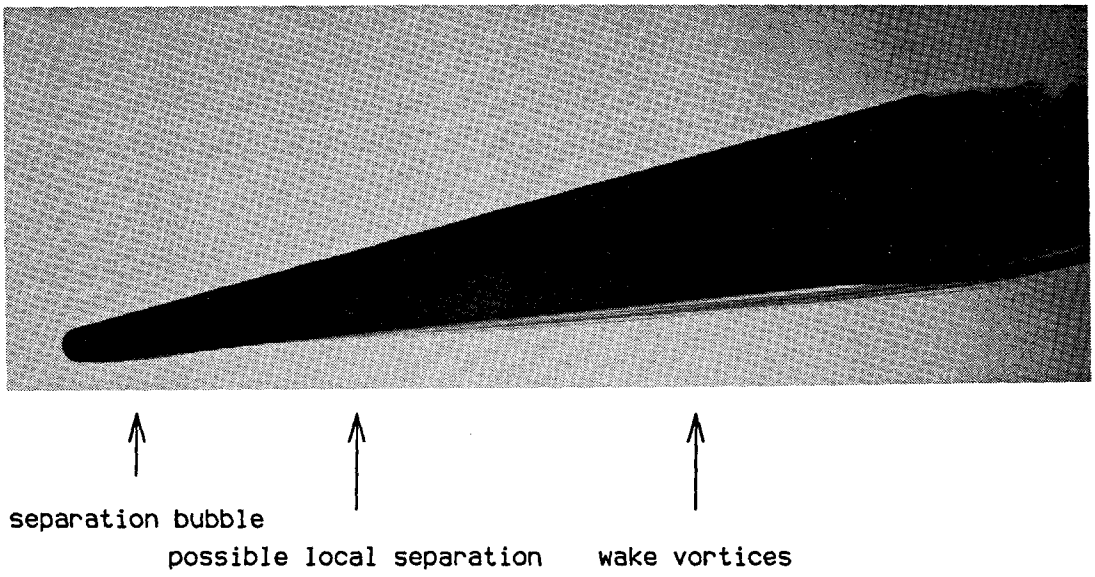

FIG. 2.8 Example of separation bubble plus local separation: $Re_t = 889$, $\alpha/\theta_c = 2$

local separations further down the body (see Fig. 1.5). This pattern was labeled "separation bubble plus local separation" (for future reference) and is indicated by the wedge symbol ($\wedge$) in Fig. 2.6 and Fig. 2.7. This pattern is illustrated in Fig. 2.8, which is an image of the flow at $Re_t = 889, \alpha/\theta_c = 2$. In this picture, the separation bubble is discernable near the tip and the wake vortices are discernable near the base. The possible local separation is indicated. It is not totally certain that the wake vortices in these flows were originating from local separations, because a black cone model was used. This prevented the determination of separation features on the cone surface itself. A laser sheet traverse of the vortex wake with fluorescein dye for $Re_t = 889$, $\alpha/\theta_c = 2$ was also inconclusive regarding the local separation issue. However, it was reasonably clear that the wake vortices were not originating in the separation bubble at the tip (which would have made the pattern a global separation, to be discussed next), and so the conclusion was drawn that the origins of the wake vortices had to have been in local separations.

One other aspect of the local separation should be noted. In Fig. 2.7, as Re_t increases from 2,223 to 2,440 to 2,667 for $\alpha/\theta_c = 2$ and $\alpha/\theta_c = 3$, the pattern appears to switch from separation bubble plus local separation to separation bubble only to separation bubble plus local separation. This is probably a length ratio

or base effect. The Re_t values of 2,223 and 2,667 were obtained using the small hemispherical tip. In this configuration, the ratio of overall model length to tip radius (L/R_t) was approximately 53, and the vortices seemed to originate roughly 17 tip radii downstream of the joint between the tip and the cone. The case $Re_t = 2,440$ was obtained using the large hemispherical tip. In this configuration, the model had a length ratio L/R_t of approximately 13. If the length from tip to vortex origin scaled with R_t, then there would not have been enough room left on the cone in the second configuration for the vortices to form, and so only the separation bubble would appear.

The fourth basic flow separation pattern was the "U"-shaped global separation, indicated with asterisks ($*$) in Fig. 2.6 and Fig. 2.7, and labeled simply "global separation" in these figures. In these experiments, this was the only global separation of the two in Fig. 1.5 encountered, so it will be referred to as simply "the global separation" for purposes of discussion for the remainder of this chapter. This pattern is illustrated in Fig. 2.9, which is an image of the flow at $Re_t = 889$, $\alpha/\theta_c = 8$. In the majority of the cases in which the wake vortices originated from a global separation, the vortex wakes appeared from a visual inspection to be symmetric. It is possible that if a longer cone model had been used, the wake vortices might have become asymmetric further downstream. In some cases, there was asymmetry in the form of asymmetric vortex breakaway locations (as discussed in Sec. 2.3.1), but in the regions where the vortices remained "attached" to the cone, they were symmetric. For $\alpha/\theta_c = 12$ and $\alpha/\theta_c = 13$, however, even the attached vortices were (visually) asymmetric.

For $\alpha/\theta_c = 4$ and $889 \leq Re_t \leq 2,667$ (but not for $Re_t = 2,440$, obtained with the large hemispherical tip), it was unclear from the videotape images whether the pattern was the separation bubble plus local separation or the global separation. These points were thus labeled with both the wedge ($\wedge$) and asterisk ($*$) symbols. An examination of the videotape record revealed that this pattern was possibly the merging of the local separations with the separation bubble. As the angle of attack

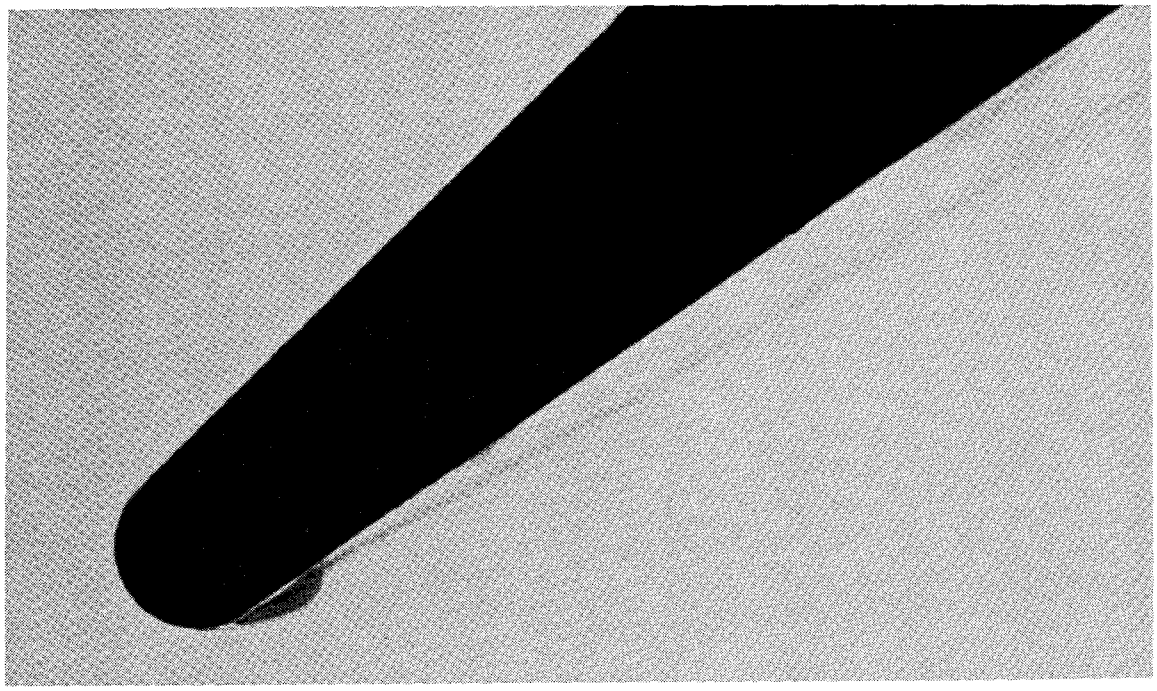

FIG. 2.9 Example of global separation: $Re_t = 889$, $\alpha/\theta_c = 8$

increased, the cross-flow Reynolds number along the cone increased, increasing the local cross-flow Reynolds number at each point on the cone. The local cross-flow Reynolds number is the Reynolds number based on the local cone diameter and the component of the free-stream velocity normal to the cone axis. If, as seems reasonable, a threshold cross-flow Reynolds number was required for local separations to form, then, as the angle of attack was increased, this threshold value would exist at points closer and closer to the cone tip, so that the local separations would move toward the cone tip and the separation bubble at the tip. Eventually, the local separations and the separation bubble at the tip would have to merge, creating the global separation. Because the primary purpose of these experiments was to catalog flow patterns, the videotape equipment was not set up in such a manner that the resulting video images could be analyzed quantitatively, and so the conjecture of the existence of a threshold cross-flow Reynolds number and the movement of the local separations could not be proved quantitatively. However, the explanation offered here for the appearance of these apparently merging flow patterns is plausible.

In Fig. 2.6, there is a rather large region in which the only symbol is the one for the type of unsteadiness. This means that the separation pattern at that particular Re_t and α/θ_c could not be determined from the videotape. This occurred for $Re_t \geq 6,100$. The primary reason for the inability to determine the pattern was the rapid diffusion of the dye in an apparently turbulent wake. It is probable that some other means of measuring the flow, such as velocity measurements or analysis of surface skin friction patterns, would reveal these patterns to be global separations or separation bubbles or some other type of separation, at least in a mean-flow sense. It is also possible that if higher values of Re_t had been obtained with the longer model, more of the separation bubbles would in fact have included local separations or would have been global separations. One conclusion can be drawn from the figure concerning global separations. It is apparent from the figure that as α/θ_c increased, a recognizable global separation pattern persisted to higher values of Re_t.

As can be noted from Fig. 2.7, separation bubbles, either alone or in combination with local separations, occurred at low values of both Re_t and α/θ_c. This might have been expected. Flow separations on circular cylinders and spheres typically occur at relatively low Reynolds numbers (see the photographs in Van Dyke 1982, for example), because of large adverse pressure gradients. In some sense the hemispherical tip on the cone at non-zero angle of attack resembled a sphere. When the cone was at an angle of attack greater than 5^o ($\alpha/\theta_c > 1$), the adverse pressure gradient on the lee side of the tip caused the flow on the lee side of the cone downstream of the tip to separate and form a bubble. The adverse cross-flow pressure gradients that caused the local separations to form were less severe, because of the axial flow component. This resulted in a larger cross-flow Reynolds number being required for the local separations to form, if the earlier analysis regarding the threshold Reynolds number is correct. The relative values of the Reynolds numbers required for the formation of separation bubbles and local separations indicates that perhaps the separation bubbles at the nose, referred to as "nose-induced separations" by Ericsson and Reding (1980), did not delay the formation of local separations further aft

on the body, as suggested by Ericsson and Reding and discussed in Sec. 1.3. Rather, the separation bubbles simply formed before the local separations. Then, as discussed above, the local separations moved forward on the model as the cross-flow Reynolds number was increased until they merged with the separation bubble at the tip to form a global separation.

2.3.3 Unsteady flows

The regions in Re_t–α/θ_c space in which flow unsteadiness occurred are shown in Fig. 2.6 and in Fig. 2.10, for purposes of clarity. It is obvious that a number of flow conditions resulted in unsteady flows. A number of different types of unsteady flows were observed, including the shedding of vortical structures. The flow conditions resulting in the shedding of vortical structures are labeled with squares in Fig. 2.6 and Fig. 2.10. All flow conditions resulting in other types of unsteady flows are labeled with circles. As stated in Sec. 2.3.1, no Kárman-like vortex shedding was observed. Since the primary emphasis of these experiments was on the appearance of steady separated flow patterns, the types of flow unsteadiness will be discussed only briefly, with slightly more attention being paid to the shedding of vortical structures.

One reason for the flow unsteadiness to be separated from the basic flow separation patterns was that the flow unsteadiness seemed to be governed by water channel speed, and not by Re_t. A possible explanation for this phenomenon will be given shortly. Another reason for the separation of flow unsteadiness was that, in many cases, the particular type of unsteadiness seemed to be superimposed on the basic separation pattern without causing any real disturbance to the pattern. It was still possible to easily identify the basic pattern, even though the flow unsteadiness was present. In other cases, however, the flow unsteadiness seemed to disrupt the basic separation pattern. This appeared to be the case for the unidentifiable separation patterns.

The primary flow unsteadiness encountered was Kelvin–Helmholtz instability.

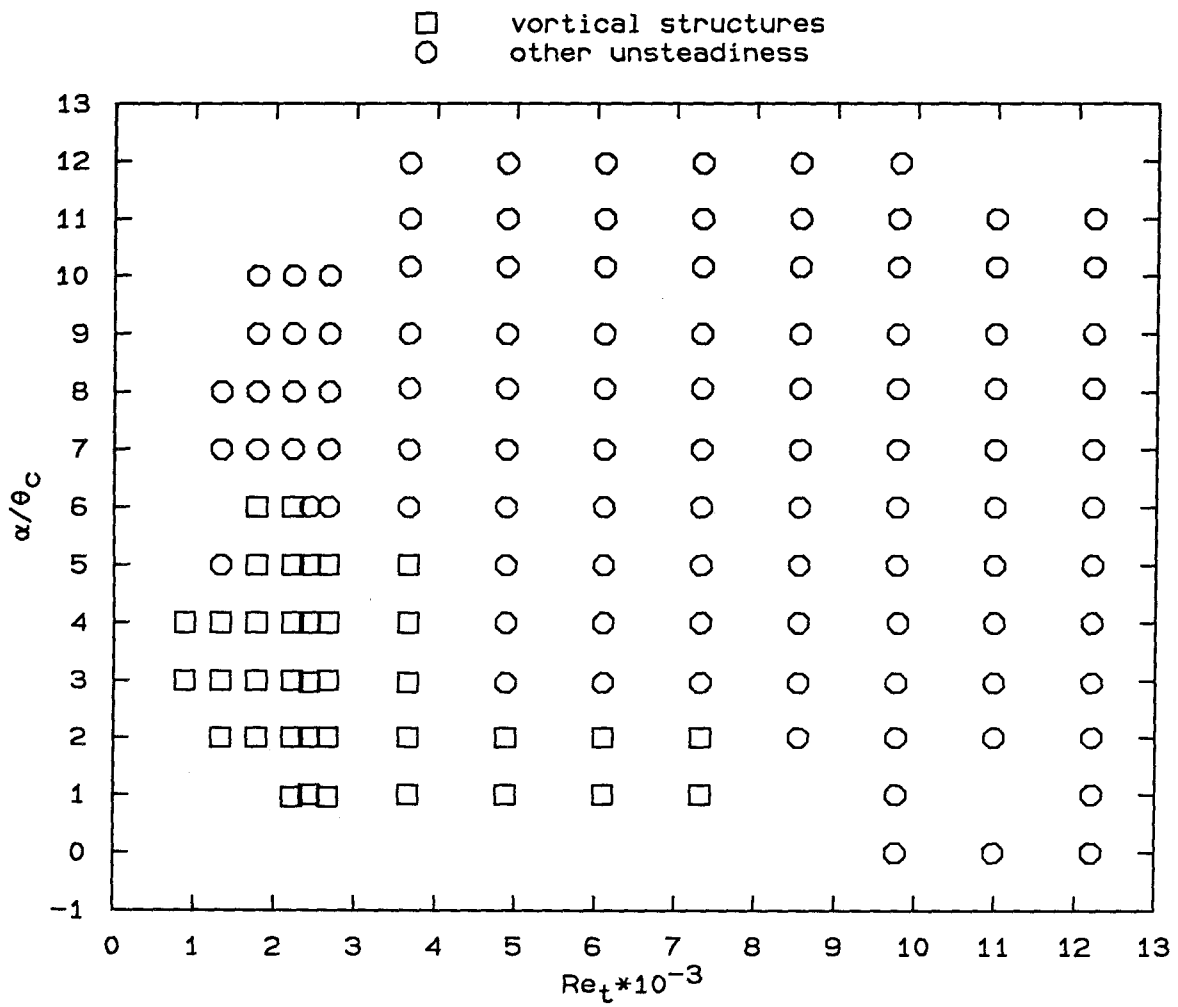

FIG. 2.10 Unsteady flows

For smaller values of α/θ_c and values of Re_t large enough to cause the boundary layer at the tip to separate, long separation bubbles would form that bore many similarities to free shear layers, one resemblance in particular being the Kelvin–Helmholtz instability. This instability occurred in situations where disturbances introduced into the bubble by the dye injection process would propagate along the bubble edge, either growing or decaying, depending upon the flow conditions. Disturbances that grew would eventually cause the shear-layer-like edge of the bubble to roll up into vortices or otherwise disrupt the separation bubble. For the smaller hemispherical tip, the rollup process became roughly periodic for some values of α/θ_c at $Re_t = 1,334$, and then for all values of α/θ_c except 11 and 12 for

$Re_t = 1,778$. These two values of Re_t corresponded to water channel speeds of 15 and 20 cm/sec, respectively. For the larger hemispherical tip, the rollup became periodic for all values of α/θ_c at $Re_t = 3,660$, corresponding to a water channel speed of 15 cm/sec. Both tips yielded primarily steady flows at a water channel speed of 10 cm/sec.

The reason that such behavior caused concern can be understood from a detailed examination of Fig. 2.6. At $Re_t = 2,440$, a steady global separation was observed for $7 \leq \alpha/\theta_c \leq 10$. These flows were obtained with the large hemispherical tip at a free-stream speed of 10 cm/sec. Note from the figure that these steady global separations seemed to occur between unsteady global separations that were observed at $Re_t = 2,223$ and 2,667 for the same range of α/θ_c. These flows were obtained with the small hemispherical tip at free-stream speeds of 25 and 30 cm/sec, respectively. Thus it would appear that the occurrence of unsteadiness was governed by some factor other than Re_t. The studies by Ho and Huerre (1984) and Lowson (1989), among others, have indicated that shear layers are very susceptible to periodic disturbances. It is plausible that the following scenario occurred. At a water channel speed of 15 cm/sec, a very small but periodic vibration occurred somewhere in the water channel machinery that was transmitted through the sting mechanism to the cone, causing periodic disturbances in the dye jets (themselves susceptible to Kelvin–Helmholtz instability). These periodic disturbances were fed into the separated boundary layer which bore resemblances to the free shear layer, causing the separated boundary layer to roll up into vortices, a behavior characteristic of free shear layers. Either the lack of separated boundary layer susceptibility to disturbances at a free-stream speed of 10 cm/sec, or the lack of channel vibration at 10 cm/sec, could explain the existence of steady flows at $Re_t = 2,440$ for $7 \leq \alpha/\theta_c \leq 10$ while the flows for the same α/θ_c at $Re_t = 2,223$ and 2,667 were unsteady. Since the steady basic separation patterns were of primary interest, and since shear layer stability studies lay outside the realm of these experiments, no attempt was made to investigate these phenomena in more detail.

One type of unsteady flow did receive slightly more attention. Perry and Lim (1978) and Perry *et al.* (1980) describe the existence and behavior of coherent structures in coflowing jets and wakes. These structures usually took the form of what they called "vortex loops." The existence of such structures was noted in the present experiments. The regions in Re_t–α/θ_c space where these structures were found are shown in Fig. 2.6 and Fig. 2.10. An image of such a flow at $Re_t = 1,180$ and $\alpha/\theta_c = 4$ is found in Fig. 2.11, where it is compared to the flow past a rivet head, with a Reynolds number based on the height of the rivet head of 150 (photograph from Perry *et al.* 1980).

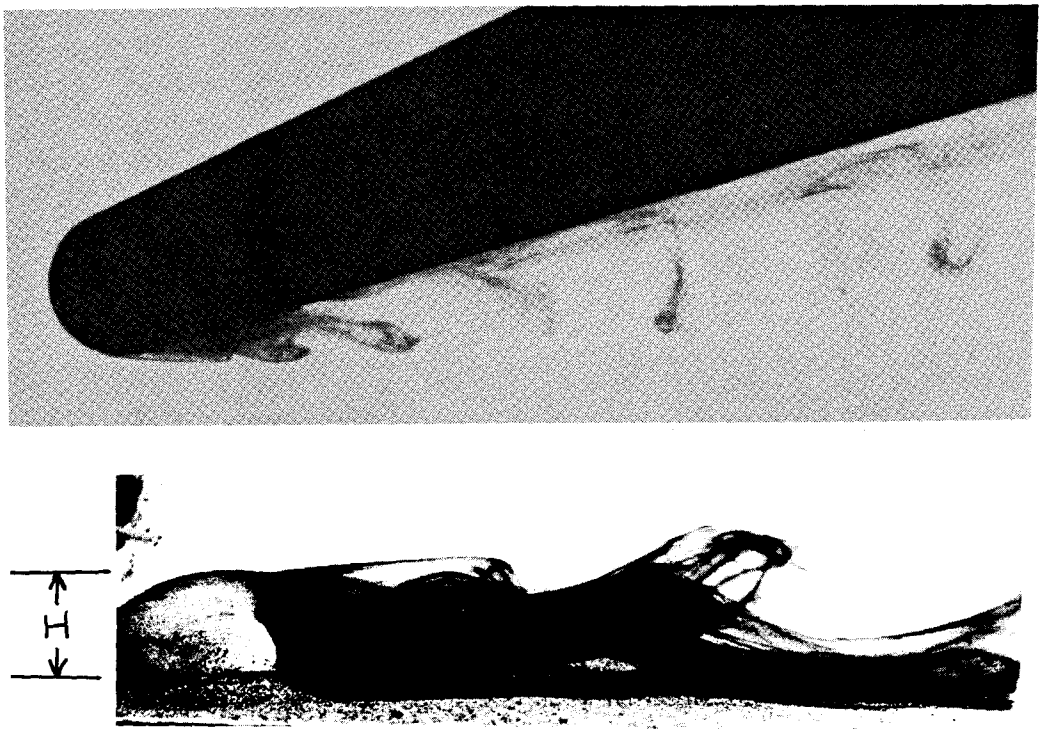

FIG. 2.11 Comparison of vortical structures shed from blunted cone ($Re_t = 1,180$, $\alpha/\theta_c = 4$) and rivet head ($Re_H = 150$; photograph from Perry *et al.* 1980)

The behavior of the structures in the present experiments matched very closely the behavior of the vortex loops described by Perry and Lim (1978) and Perry *et al.* (1980). In these references, the frequency of the appearance of the vortex

loops was found to lock in to a forcing frequency. In the present experiments, at a water channel speed of 10 cm/sec (*i.e.*, a non-periodic-disturbance case, as described above), the structures appeared randomly. However, for a water channel speed of 15 cm/sec or greater (*i.e.*, a case where a periodic disturbance was apparently present), the structures appeared to lock in to some frequency, probably that of the periodic disturbance. In Perry and Lim (1978), the vortex loops were observed to point up (against gravity) in positively buoyant wakes and down (with gravity) in negatively buoyant wakes. In some of the flows in the present experiments, the loops of the vortical structures pointed up, while in others, the loops pointed down. As was discussed previously, the specific gravity of the dye was matched to that of water by mixing with alcohol, to an accuracy of 0.05% or better. Within that accuracy range, however, the dye could be slightly lighter or slightly heavier than water. The connection between dye buoyancy and vortex loop orientation was not confirmed directly in these experiments, since no systematic record was kept of buoyancy errors or vortex loop orientations. However, the buoyancy effect as described by Perry and Lim is a plausible explanation for the variations in the vortex loop orientation observed in these experiments.

2.3.4 The missing flow pattern

As was mentioned in Sec. 2.3.2, only the "U"-shaped global separation pattern shown in Fig. 1.5 was observed in these experiments. This was somewhat puzzling, since these experiments were conducted over ranges of Re_t and angle of attack within which Legendre and others recorded the existence of the Legendre-type global separation. The appearance of the Legendre-type separation has been observed in particular near the nose of a hemisphere-cylinder (Hsieh and Wang 1976; Hsieh 1977; Bippes and Turk 1984). The hemisphere-cylinder would seem to be a geometry very close to that of a small-semi-angle cone with a hemispherical tip, so the appearance of the Legendre-type separation would have been expected. It is believed, however, that this pattern is very sensitive to fineness ratio effects. Bippes and Turk (1984) contains photographs of the flow past an ellipsoid and a hemisphere-cylinder, both at

$\alpha = 28^o$ and $Re_D = 5,000$ (which would correspond to $\alpha/\theta_c = 5.6$ and $Re_t = 2,500$ for the model in the current experiments). The Legendre-type global separation appears on the hemisphere-cylinder but not on the ellipsoid. Werlé (1982) contains photographs of the flow past a hemisphere-cylinder and a rounded-nose ogive at $\alpha = 20^o$ and $Re_D = 6,000$ ($Re_t = 3000$). The Legendre-type separation is present on the hemisphere-cylinder, but its appearance on the rounded nose ogive seems to depend on the manner in which dye is injected into the flow from the model. There is also a photograph of the flow past a cone with a hemispherical tip at $\alpha = 40^o$ and $Re_D = 8,000$ (the cone semi-angle and tip radius are not given). This photograph is inconclusive as to whether the flow is a "U"-shaped global separation or a Legendre-type global separation. The videotape record of the current experiments indicated that at $\alpha = 40^o$ ($\alpha/\theta_c = 8$), the cone with a hemispherical tip experienced a definite "U"-shaped global separation for all Re_t, which probably would have included the value of Re_t in Werlé's photograph. It is possible that some of the merging flows discussed in Sec. 2.3.2 were Legendre-type separations. However, the discussion above would seem to indicate that the appearance of the Legendre-type global separation is a strong function of body fineness ratio and afterbody shape, and that there is apparently sufficient difference between the hemisphere-cylinder and the hemisphere-cone to preclude the appearance of the Legendre-type separation on the cone.

CHAPTER 3

Elliptic cross section tip design and construction

3.1 Why an ellipse?

As was pointed out in Sec. 1.3.2, Hunt (1982) described how eccentricities in cross-sectional body shape, particularly at the tip, might produce a variation in vortex wake asymmetry with body roll angle. Moskovitz (1989) and Zilliac *et al.* (1991) both reasoned and verified experimentally that imposing planes of symmetry upon the body tip would regularize the behavior of the vortex wake with body roll angle. The elliptic cross section tips of Moskovitz and the transverse cylindrical rod and chisel tips of Zilliac *et al.* both produced side force variations with roll angle that went through zero side force more or less at the roll angle where one of the planes of symmetry of the tip coincided with the incidence plane (see Sec. 1.1). The resulting side force variations with four zero crossings in one complete revolution thus had the same periodicity as two-cycle sinusoids.

Prior to the work of Moskovitz, little research into the use of elliptic cross section bodies as a control device was performed. More work was done in studying the effectiveness of elliptic cross section bodies in improving the lateral-directional stability of missile configurations. Graves (1977), Gregoriou (1982), and Allen and Pittman (1984) report an improvement in lateral-directional stability of missile configurations at angle of attack with elliptic instead of circular cross sections (see also references in Graves 1977). A discussion of various studies of the effects on fuselage/ missile lateral-directional stability characteristics of body cross- sectional shape, including elliptical, is given by Polhamus (1984). As was mentioned in Sec. 1.3.2, the lateral-directional stability of a production model F5-F was improved by using an elliptic cross section nose on the aircraft (Edwards 1978).

None of these works, however, discuss the effects of rotating the elliptic cross section body or tip about its longitudinal axis. In all of the discussions that follow, the roll angle ϕ of the elliptic cross section bodies or tips will be defined to be the angle between the plane formed by the major axes of the elliptic cross sections and the normal to the incidence plane. Zero ϕ will correspond to the major axes being perpendicular to the incidence plane. Exceptions to these definitions will be noted. Jorgensen (1977) compared the side force on a 2:1 elliptic cross section missile configuration at roll angles of 0^o and 90^o, both of which presented a symmetric body shape to the oncoming flow. Jorgensen found essentially zero side forces at $\phi = 0^o$ and large side forces at $\phi = 90^o$, for an angle of attack of 50^o.

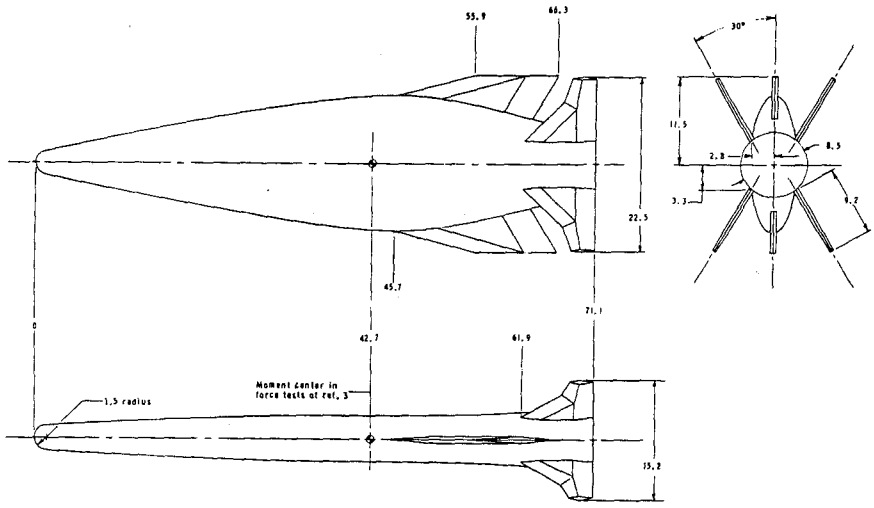

FIG. 3.1 Elliptic cross section missile configuration (Allen *et al.* 1983)

Allen *et al.* (1983) examined in more detail the effect of rotating an 3:1 elliptic cross section body about its longitudinal axis. The body used in these experiments is shown in Fig. 3.1. The body was rotated from $\phi = 0^o$ to $\phi = 90^o$ in 22.5^o increments. Pressure distributions on a body-alone configuration (no wings) at a station x/L = 0.6, for a nominal body angle of attack of 20^o, are shown in Fig. 3.2. The data show a gradual transition between distributions that are symmetrical about the most windward point on the body section, indicating that the side force on the body had the same periodicity as a two-cycle sinusoid and probably varied

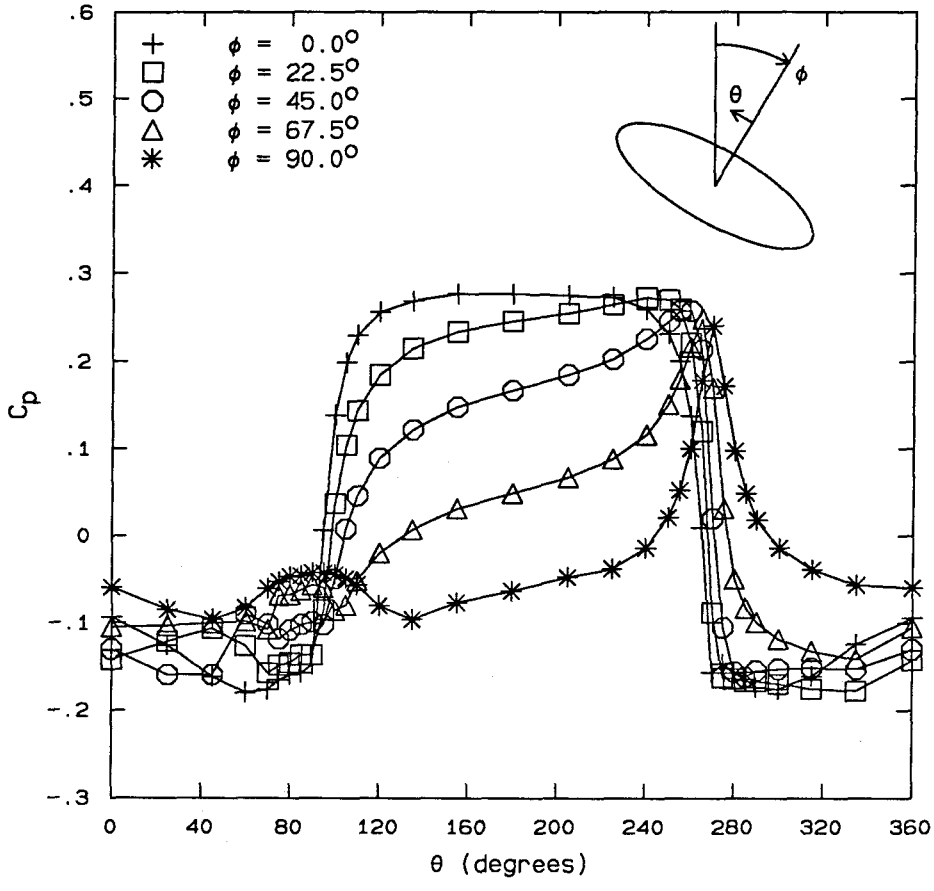

FIG. 3.2 Elliptic cross section missile pressure distributions: $\alpha = 20^o$ (nominally), x/L = 0.6, M = 2.5, blunt nose configuration (Allen *et al.* 1983)

smoothly with roll angle. Similar results were reported for an angle of attack of 25^o, the highest angle studied (see also Allen and Pittman 1984 for a discussion of these results).

A computational work which supports the idea of using an elliptic cross section tip to control vortex wake asymmetry is that of Hartwich *et al.* (1990). Hartwich *et al.* computed the flow past an axisymmetric body with a tangent ogive nose that had elliptic cross sections at the tip. The pressure distributions for a tip roll angle of 45^o (*i.e.*, the roll angle at which the tip presented the maximum asymmetry to the oncoming flow) and a large angle of attack matched very closely experimental pressure distributions at conditions of maximum flow asymmetry, obtained on a

similar body with a nominally axisymmetric tip. Thus this work showed computationally that an elliptic cross section tip could produce the same maximum side force on a body as that obtained from experiment.

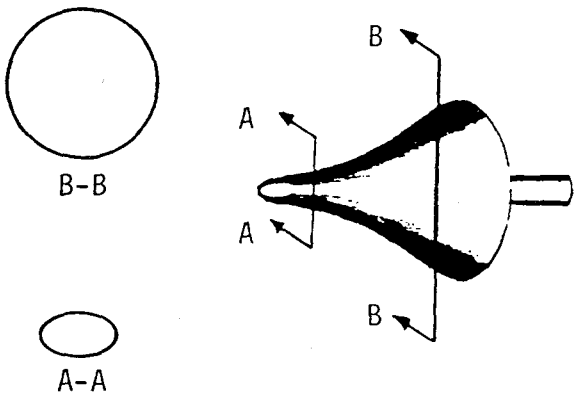

FIG. 3.3 Sketch of elliptic cross section tip used by Moskovitz (figure from thesis by Moskovitz, 1989)

These works taken together indicate that the hypothesis of Moskovitz was reasonable: an elliptic cross section tip should produce a controllable side force on an axisymmetric body. They do not explain, however, why the tips used by Moskovitz failed to produce a smooth variation in side force with roll angle for the bodies with conical noses at angles of attack higher than 30°. Perhaps the reason for this failure lies in the construction method used by Moskovitz. As Moskovitz points out in his thesis (1989), the tips were filed into elliptic cross sections by hand. The drawings and photographs of the tips in the thesis show the somewhat crude nature of the resulting tips. An example is shown in Fig. 3.3. In particular, this figure illustrates that the profiles of the resulting tips were not smooth, with changes in curvature between the elliptic tip and the circular tip base. Because of the promise of vortex wake control demonstrated by the elliptic cross section tip in the experiments by Moskovitz and others, it was decided to design and construct a

new elliptic cross section tip that avoided some of the defects in the tips used by Moskovitz, and to test the resulting tips on a right circular cone model. The design and construction of the tips is discussed next.

3.2 Design

The goal of the design process was to produce a tip with elliptic cross sections at the end of the tip and a smooth transition to circular cross sections at the base of the tip, where the tip would be attached to the cone. Since the tip was to be attached to a cone, matching the slope and curvature of the tip to the cone slope and zero curvature of the cone at some point on a cone generator would ensure a smooth transition from the tip to the cone. The goal was accomplished using two sixth-degree polynomials in tip radius r for the axial distance z from the end of the tip (see Fig. 3.4).

The polynomials were of the form

$$z = c_6 r^6 + c_5 r^5 + c_4 r^4 + c_3 r^3 + c_2 r^2 + c_1 r + c_0. \tag{3.2.1}$$

The use of sixth-degree polynomials allowed the radius, slope, and curvature of the tip to match that of the cone at the point where the polynomial became tangent to the cone generator (the points $(r_{ci},\ z_{ci})$, $i = 1, 2$ in Fig. 3.4). The radius of curvature of the polynomial at the origin could be varied by varying z_{ci}. Smaller values of z_{ci} yielded larger radii of curvature at the origin. By choosing two different values of z_{ci}, two polynomials with different radii of curvature at the origin, and hence different "widths" near the origin, could be constructed. These two polynomials then provided the major and minor axes of the elliptic cross sections. For purposes of discussion, the subscript "1" will be associated with the polynomial providing the major axes, and the subscript "2" will be associated with the polynomial providing the minor axes, so that $z_{c1} < z_{c2}$. Since the polynomials both smoothly joined the cone at the points of tangency, the elliptic cross sections would smoothly transition to circular cross sections.

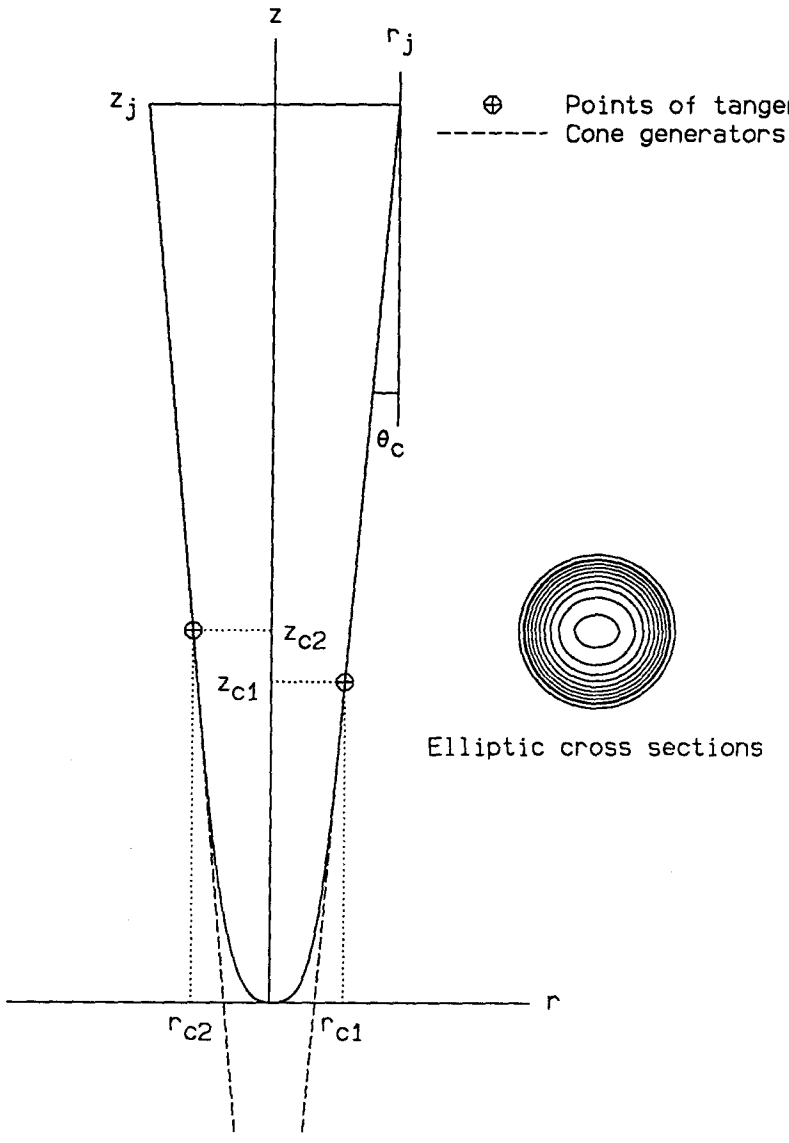

FIG. 3.4 Elliptic cross section tip definitions

Each polynomial was constructed to be symmetric about the z axis. This meant that the coefficients with odd subscripts in Eq. 3.2.1 were all zero. The value of c_0 was the shift in z of the origin of the polynomial from the origin of the z axis. In practice, the base of the tip was chosen as the origin for the z axis, so that $c_0 = -z_j < 0$. To simplify matters, c_0 will be taken to be zero in this chapter. The other coefficients for each polynomial were determined from the following conditions (the i subscript denoting the two different polynomials will be

dropped for convenience):

$$z(r_c) = z_c \tag{3.2.2a}$$

$$z'(r_c) = \tan(\frac{\pi}{2} - \theta_c) = m \tag{3.2.2b}$$

$$z''(r_c) = 0. \tag{3.2.2c}$$

These conditions yielded the following set of linear algebraic equations for the coefficients c_6, c_4, and c_2:

$$\begin{bmatrix} r_c^6 & r_c^4 & r_c^2 \\ 6r_c^5 & 4r_c^3 & 2r_c \\ 30r_c^4 & 12r_c^2 & 2 \end{bmatrix} \begin{Bmatrix} c_6 \\ c_4 \\ c_2 \end{Bmatrix} = \begin{Bmatrix} z_c \\ m \\ 0 \end{Bmatrix}. \tag{3.2.3}$$

The equation for the radius of the cone as a function of z for $z > z_c$ is

$$r = (z - z_j)/m + r_j \tag{3.2.4}$$

where z_j is the (specified) axial location of the tip-cone joint and r_j is the cone radius at that location. Once z_c was specified, r_c was calculated from Eq. 3.2.4 and then Eq. 3.2.3 was solved numerically using double precision arithmetic. Since θ_c was 5^o, m was equal to $\tan 85^o = 11.43$. Two choices of z_c produced two solutions to Eq. 3.2.3 and thus two polynomials with the desired radius, slope, and curvature matches to the cone and different widths near the origin, so that the major and minor axes of the elliptic cross sections were obtained.

In order to produce the tip, however, the major and minor axes of the elliptic cross sections had to be given as a function of the axial coordinate z, which meant that Eq. 3.2.1, with the non-zero coefficients given by Eq. 3.2.3, had to be inverted. Initially, this was done numerically. Then, it was realized that since the coefficients of the odd powers of r in Eq. 3.2.1 were zero, Eq. 3.2.1 could be expressed as a cubic in $R = r^2$:

$$R^3 + \frac{c_4}{c_6}R^2 + \frac{c_2}{c_6}R - \frac{z}{c_6} = 0. \tag{3.2.5}$$

An analytic solution to a cubic polynomial is given by Abramowitz and Stegun (1964). Two functions $A_1(z)$ and $A_2(z)$, given by

$$\begin{aligned} A_1(z) &= a_0 + a_1 z, \\ A_2(z) &= a_2 + a_3 z + a_4 z^2, \end{aligned} \tag{3.2.6}$$

with

$$\begin{aligned} a_0 &= \frac{1}{6}\left(\frac{c_2}{c_6}\right)\left(\frac{c_4}{c_6}\right) - \frac{1}{27}\left(\frac{c_4}{c_6}\right)^3, \\ a_1 &= \frac{1}{2c_6}, \\ a_2 &= \left[\frac{c_2}{3c_6} - \frac{1}{9}\left(\frac{c_4}{c_6}\right)^2\right]^3 + a_0^2, \\ a_3 &= 2a_0 a_1, \\ a_4 &= a_1^2, \\ a_5 &= -\frac{1}{3}\left(\frac{c_4}{c_6}\right), \end{aligned} \tag{3.2.7}$$

are useful in evaluating the solution given by Abramowitz and Stegun. If $A_2(z) > 0$ for $0 \leq z \leq z_c$, then the solution to Eq. 3.2.5 is given by

$$R = \left[A_1(z) + A_2(z)^{\frac{1}{2}}\right]^{\frac{1}{3}} + \left[A_1(z) - A_2(z)^{\frac{1}{2}}\right]^{\frac{1}{3}} + a_5. \tag{3.2.8}$$

If $A_2(z) < 0$ for $0 \leq z \leq z_c$, then the solution to Eq. 3.2.5 is given by

$$\begin{aligned} R = &-\frac{1}{2}\left\{\left[A_1(z) + A_2(z)^{\frac{1}{2}}\right]^{\frac{1}{3}} + \left[A_1(z) - A_2(z)^{\frac{1}{2}}\right]^{\frac{1}{3}}\right\} \\ &+ a_5 \\ &- \frac{i\sqrt{3}}{2}\left\{\left[A_1(z) + A_2(z)^{\frac{1}{2}}\right]^{\frac{1}{3}} - \left[A_1(z) - A_2(z)^{\frac{1}{2}}\right]^{\frac{1}{3}}\right\} \end{aligned} \tag{3.2.9}$$

In the simplification process, the roots and signs were chosen so that Eq. 3.2.8 and Eq. 3.2.9 would yield the proper real solutions. Further analysis revealed that the solutions given by Eq. 3.2.9 could be expressed completely in terms of real functions. Since $A_2(z)$ is negative for $0 \leq z \leq z_c$, the combination $A_1(z) + A_2(z)^{\frac{1}{2}}$ can be expressed as $a + ib$, where $a = A_1(z)$ and $b = \sqrt{-A_2(z)}$. Then,

$$\begin{aligned} (a+ib)^{\frac{1}{3}} + (a-ib)^{\frac{1}{3}} &= \left(\eta e^{i\zeta}\right)^{\frac{1}{3}} + \left(\eta e^{-i\zeta}\right)^{\frac{1}{3}} \\ &= \eta^{\frac{1}{3}}\left(e^{i\frac{\zeta}{3}} + e^{-i\frac{\zeta}{3}}\right) \\ &= 2\eta^{\frac{1}{3}}\cos\left(\frac{\zeta}{3}\right), \end{aligned}$$

and

$$\begin{aligned}(a+ib)^{\frac{1}{3}} - (a-ib)^{\frac{1}{3}} &= \left(\eta e^{i\zeta}\right)^{\frac{1}{3}} - \left(\eta e^{-i\zeta}\right)^{\frac{1}{3}} \\ &= \eta^{\frac{1}{3}}\left(e^{i\frac{\zeta}{3}} - e^{-i\frac{\zeta}{3}}\right) \\ &= 2i\eta^{\frac{1}{3}}\sin\left(\frac{\zeta}{3}\right),\end{aligned}$$

where $\eta = \sqrt{a^2+b^2}$ and $\zeta = \tan^{-1}(b/a)$ are the polar components of the complex number $a+ib$. Using these results, Eq. 3.2.9 becomes

$$R = \eta^{\frac{1}{3}}\left(\sqrt{3}\sin\frac{\zeta}{3} - \cos\frac{\zeta}{3}\right) + a_5. \tag{3.2.10}$$

Then, r as a function of z is given by either

$$r = \left(\left[A_1(z) + A_2(z)^{\frac{1}{2}}\right]^{\frac{1}{3}} + \left[A_1(z) - A_2(z)^{\frac{1}{2}}\right]^{\frac{1}{3}} + a_5\right)^{\frac{1}{2}}, \tag{3.2.11}$$

if $A_2(z) > 0$ for $0 \le z \le z_c$, or

$$r = \left[\eta^{\frac{1}{3}}\left(\sqrt{3}\sin\frac{\zeta}{3} - \cos\frac{\zeta}{3}\right) + a_5\right]^{\frac{1}{2}}, \tag{3.2.12}$$

if $A_2(z) < 0$ for $0 \le z \le z_c$, where

$$\eta = \sqrt{A_1(z)^2 - A_2(z)},$$
$$\zeta = \tan^{-1}\frac{\sqrt{-A_2(z)}}{A_1(z)},$$

and $A_1(z)$ and $A_2(z)$ are given by Eq. 3.2.6, Eq. 3.2.7, and the solutions to Eq. 3.2.3.

These results were used in the following manner. The values z_{c1} and z_{c2}, with $z_{c1} < z_{c2}$, were used along with z_j and r_j to calculate r_{c1} and r_{c2} from Eq. 3.2.4. Equation 3.2.3 was then solved twice for two different sets of coefficients c_6, c_4, and c_2. These coefficients were used in Eqs. 3.2.6, 3.2.7, and either 3.2.11 or 3.2.12 to compute $r_1(z)$, the major axes of the elliptic cross sections, and $r_2(z)$, the minor axes of the elliptic cross sections. Since $z_{c1} < z_{c2}$, there was a region $z_{c1} \le z \le z_{c2}$ in which $r_1(z)$ given by Eq. 3.2.11 or Eq. 3.2.12 was no longer valid. In this region, $r_1(z)$ was obtained from

$$r_1 = r_{c1} + (z - z_{c1})/m. \tag{3.2.13}$$

Certain quantities were defined to characterize the tip. The length scale chosen for the tip was the geometric mean of the radii of curvature of the two polynomials at the origin. The formula for the radius of curvature

$$R = \frac{\left[1 + \left(\frac{dz}{dr}\right)^2\right]^{\frac{3}{2}}}{\frac{d^2z}{dr^2}}, \tag{3.2.14}$$

evaluated at the origin, reduced to

$$R = \frac{1}{2c_2} \tag{3.2.15}$$

for the sixth-degree polynomials. Radii of curvature R_1 and R_2 were calculated at the origin for $z_1(r)$ and $z_2(r)$, respectively. The length scale, denoted by R_t since it was analogous to the tip radius discussed in Ch. 2, was then computed from

$$R_t = \sqrt{R_1 R_2}. \tag{3.2.16}$$

The ratio of the two radii of curvature at the origin, R_1/R_2, was defined as a measure of the "flatness" of the tip and denoted by f_t, the tip flatness factor. The fineness ratio of the tip, F, was defined as the ratio of the distance to the second point of tangency divided by the tip diameter at that point, or

$$F = \frac{z_{c2}}{2r_{c2}}. \tag{3.2.17}$$

3.3 Construction

Two elliptic cross section tips were constructed.* The major and minor axes of the elliptic cross sections were computed at 0.001 in intervals in z for the length of each tip and were then fed into a computer-controlled milling machine, which ground out the tips. Both were constructed from aluminum and were anodized black. During the machining process, a reference mark was placed on the base of each tip to indicate the location of the major axes of the tip.

---

* The English system of units will be used in this section since the tip designs had to be specified in inches for the equipment used to construct the tips. All quantities in equations will be in terms of inches. Metric equivalents will be specified where appropriate.

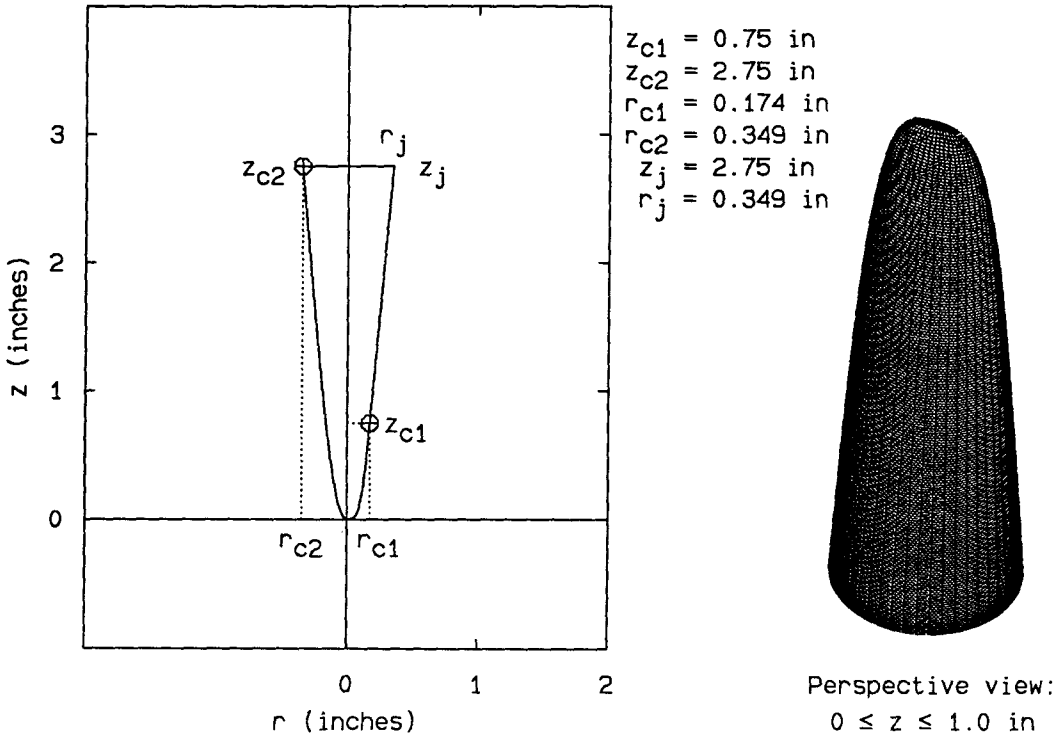

FIG. 3.5 Small elliptic cross section tip

The first tip was the smaller of the two and will thus be referred to as the "small elliptic cross section tip." This tip is shown in Fig. 3.5, along with the tip dimensions. This tip was designed to be attached to the cone at the 0.698 in = 1.77 cm diameter location (see Fig. 2.3). Note that for this tip, $z_{c2} = z_j$; *i.e.*, the tip cross sections became circular at the base of the tip. The polynomial used to generate the major axes of the small tip was

$$z = -17757.1r_1^6 + 1342.14r_1^4 + 0.406036r_1^2, \quad 0 \le z \le 0.75, \tag{3.3.1}$$

with

$$a_0 = +1.6280 \times 10^{-5} \qquad a_3 = -9.1684 \times 10^{-10}$$
$$a_1 = -2.8158 \times 10^{-5} \qquad a_4 = +7.9286 \times 10^{-10}$$
$$a_2 = -2.8100 \times 10^{-14} \qquad a_5 = +2.5194 \times 10^{-2}.$$

For this set of a_i, $A_2(z)$ (Eq. 3.2.6) was negative for $0 \le z \le z_{c1}$, and so Eq. 3.2.12 was used to compute $r_1(z)$. The polynomial used to generate the minor axes of the

small tip was

$$z = 142.133r_2^6 - 85.5468r_2^4 + 30.8889r_2^2, \quad 0 \leq z \leq 2.75, \tag{3.3.2}$$

with

$$\begin{aligned} a_0 &= -1.3725 \times 10^{-2} & a_3 &= -9.6565 \times 10^{-5} \\ a_1 &= +3.5178 \times 10^{-3} & a_4 &= +1.2375 \times 10^{-5} \\ a_2 &= +2.2173 \times 10^{-4} & a_5 &= +2.0063 \times 10^{-1}. \end{aligned}$$

For this set of a_i, $A_2(z)$ was positive for $0 \leq z \leq z_{c2}$, and so Eq. 3.2.11 was used to compute $r_2(z)$. For $z_{c1} = 0.75\,\text{in} < z < z_j = 2.75\,\text{in}$, r_1 was obtained from

$$z = 11.43(r_1 - 0.349) + 0.75. \tag{3.3.3}$$

For this tip, the tip radius R_t was 0.141 in = 0.359 cm, the flatness factor f_t was 76.0, and the fineness ratio F was 3.9. The overall length of the model with this tip was 21.1 in = 53.6 cm.

The second tip was larger than the first and hence will be referred to as the "large elliptic cross section tip." This tip is shown in Fig. 3.6, along with the tip dimensions. This tip was designed to be attached to the cone at the 1.92 in = 4.88 cm diameter location. Note that for this tip, $z_{c2} = 2.9\,\text{in} < z_j = 7.0\,\text{in}$; *i.e.*, a large portion of this "tip" was actually part of the conical nose. The polynomials used to generate this tip were

$$z = -46.8590r_1^6 + 37.2152r_1^4 + 0.680086r_1^2, \quad 0 \leq z \leq 2.5, \tag{3.3.4}$$

with

$$\begin{aligned} a_0 &= +2.0474 \times 10^{-2} & a_3 &= -4.3693 \times 10^{-4} \\ a_1 &= -1.0670 \times 10^{-2} & a_4 &= +1.1386 \times 10^{-4} \\ a_2 &= -1.3430 \times 10^{-6} & a_5 &= +2.6473 \times 10^{-1}, \end{aligned}$$

and

$$z = -29.5260r_2^6 + 25.4539r_2^4 + 2.67760r_2^2, \quad 0 \leq z \leq 2.9, \tag{3.3.5}$$

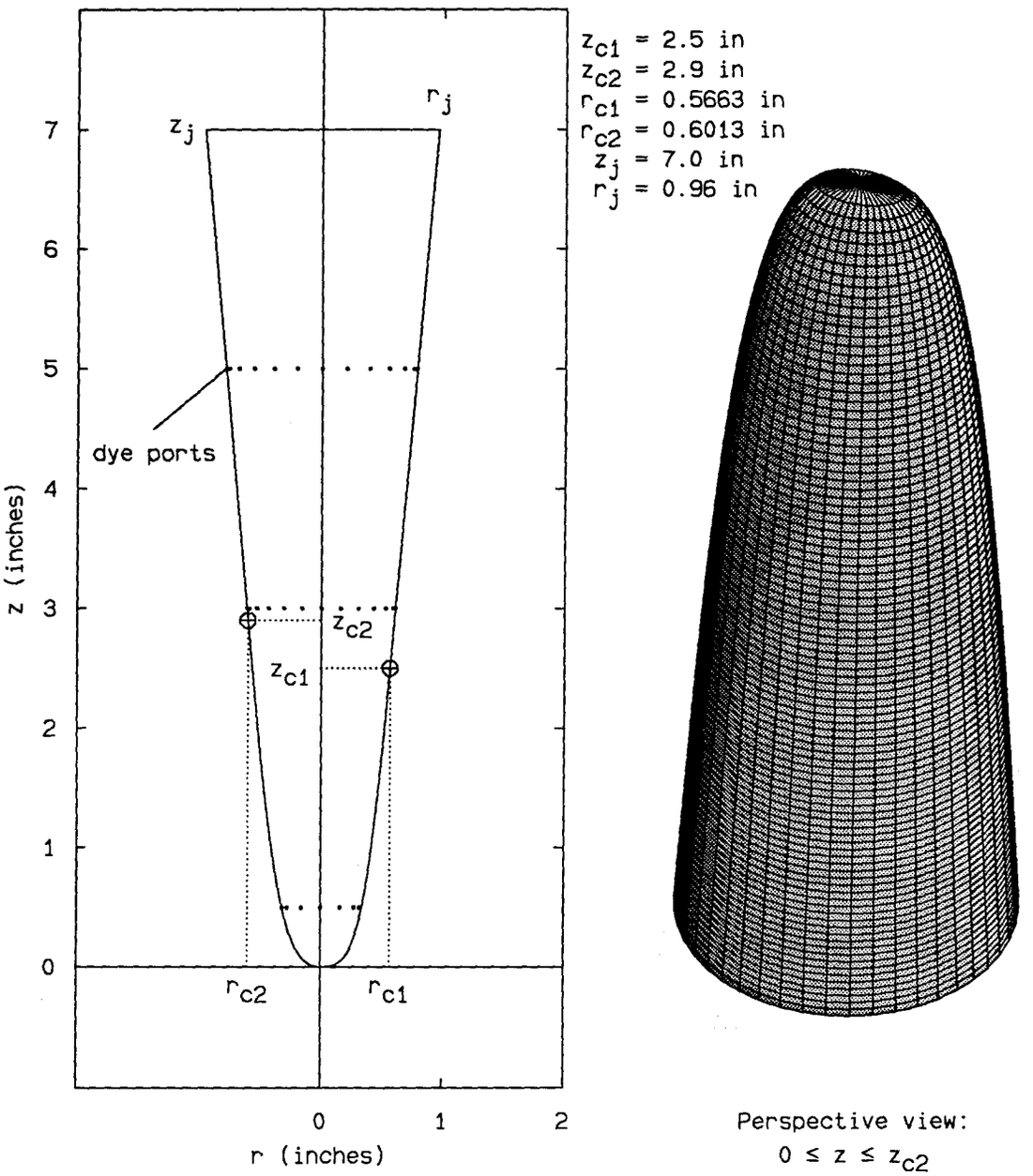

FIG. 3.6 Large elliptic cross section tip

with

$$a_0 = +3.6759 \times 10^{-2} \qquad a_3 = -1.2450 \times 10^{-3}$$

$$a_1 = -1.6934 \times 10^{-2} \qquad a_4 = +2.8677 \times 10^{-4}$$

$$a_2 = -8.4215 \times 10^{-5} \qquad a_5 = +2.8736 \times 10^{-1}.$$

For both of these sets of a_i, $A_2(z)$ was negative for $0 \le z \le z_c$, and so Eq. 3.2.12 was used to compute both r_1 and r_2. For $z_{c1} = 2.75\,\text{in} < z < z_j = 7.0\,\text{in}$, r_1 was

obtained from

$$z = 11.43(r_1 - 0.5663) + 2.5. \tag{3.3.6}$$

For $z_{c2} = 2.9\,\text{in} < z < z_j = 7.0\,\text{in}$, r_2 was obtained from

$$z = 11.43(r_2 - 0.6013) + 2.9. \tag{3.3.7}$$

For this tip, the tip radius R_t was 0.370 in = 0.942 cm, the flatness factor f_t was 3.9, and the fineness ratio F was 2.4. The overall model length with this tip was 18.0 in = 46.6 cm. The large elliptic cross section tip was constructed with dye ports to allow the injection of dye from within the tip. The rows of dye ports were located at 0.5 in, 3.0 in, and 5.0 in from the small end of the tip. The row at 0.5 in had 12 equally circumferentially spaced 0.02 in diameter holes, and the rows at 3.0 in and 5.0 in had 24 equally circumferentially spaced 0.02 in diameter holes.

CHAPTER 4

Initial experiments with elliptic cross section tips

4.1 Introduction

In order to study the effectiveness of the elliptic cross section tips discussed in Ch. 3 in controlling the asymmetry of the vortex wake of a right circular cone, flow visualization experiments were conducted. Cross sections of the vortex wake, produced by a laser sheet, were used to locate the vortex cores. The angle a line connecting the two cores made with the horizontal was used as a simple measure of the vortex wake asymmetry. The variation of this angle β with the body roll angle ϕ was studied. Preliminary experiments indicated that the small elliptic cross section tip would produce square-wave variations of β with ϕ, so attention was focused on the large elliptic cross section tip. The experiments and results with this tip are discussed in this chapter.

4.2 Model

The basic model used in the experiments was the right circular cone described in Sec. 2.2.2 and shown in Fig. 2.3. As stated before, only the large elliptic cross section tip was used in these experiments. As discussed in Sec. 3.3, this tip was designed to be attached to the cone at the 4.88 cm diameter location. The cone was mounted on the sting apparatus described in Sec. 2.2.2. As was described in Sec. 2.2.2, the DC motor and linkage allowed the roll angle of the cone to be set to one of the marks on the roll angle indicator to an estimated accuracy of $\pm 1^{\circ}$.

4.3 Apparatus and procedure

The flow visualization experiments were conducted in the low-speed, free-surface water channel described in Sec. 2.2.1 and shown in Fig. 2.1. The experimental apparatus for the flow visualization experiments is shown in Fig. 4.1. The cone was always assembled under water to prevent air bubbles from being trapped within the cone. The angle of attack of the cone could be set with an accuracy of $\pm 0.1^o$, as discussed before. Fluorescein dye powder was mixed with water and injected into the flow from within the model, using the same dye injection apparatus and procedure described in Sec. 2.2.3. The vortex wake was illuminated with a laser sheet which was created with an argon-ion laser ($\lambda = 514.5$ nm) and a cylindrical lens. The sheet-creating optics were mounted on an adjustable angle traverse, as shown in 4.1. The sheet was set up so that it intersected the cone in a plane perpendicular to both the cone axis and the incidence plane. In order for the sheet to intersect the vortex wake normal to the axis of the cone, the traverse had to be set at an angle θ_t which was larger than the angle of attack α, because of the difference in the indices of refraction of air and water. The traverse angle was calculated assuming a value of 1.33 for the index of refraction of water. The mirror angle θ_m was then set to $\theta_t/2$. The intersection of the laser sheet with the fluorescein-dye-seeded vortex wake created an image of the cross section of the vortex wake. This image passed through the bottom of the channel test section, reflected off the mirror mounted below the channel, and was recorded by the video camera, also mounted below the channel. The angular alignments of the traverse, mirror, and camera could all be set to an accuracy of $\pm 0.1^o$. The axial location of the laser sheet was set to the dye hole row at the 12.7 cm axial station of the large elliptic cross section tip (the first row from the base of the tip). By setting the laser sheet at this location, the fluorescein dye coming from the holes and illuminated by the laser sheet served as a locator for the cone itself.

Because of a limitation on the maximum traverse angle caused by space limitations beneath the channel test section, the maximum angle of attack that could

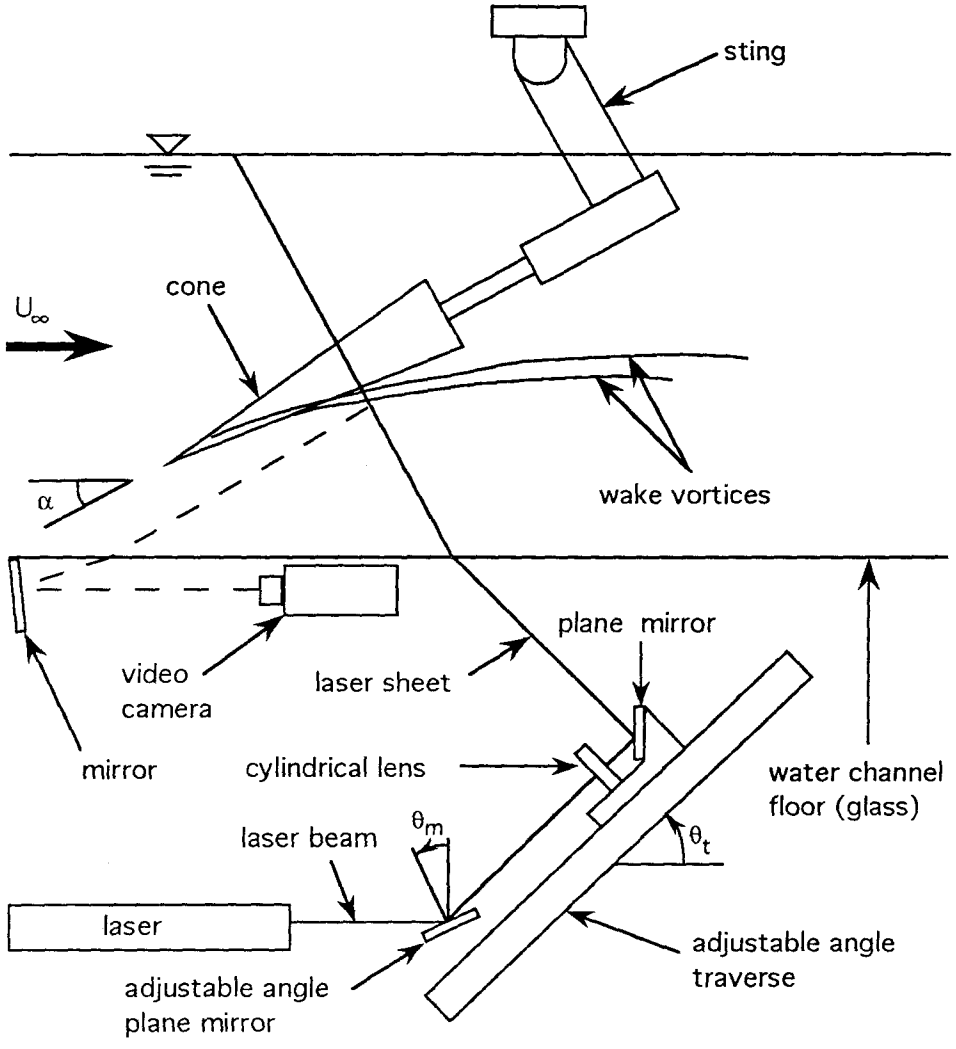

FIG. 4.1 Schematic of apparatus for vortex wake flow visualization experiments

be studied using the apparatus in the configuration shown in Fig. 4.1 was approximately 45°. Total internal reflection limited the minimum angle of attack that could be studied to approximately 41°. A preliminary study using a slightly different configuration was conducted at an angle of attack of 30° ($\alpha/\theta_c = 6$), but the maximum asymmetry angle β in this experiment was rather small. Because of the two limitations on angle of attack and the small asymmetry angles at 30° angle of attack, the decision was made to concentrate on an angle of attack of 45° ($\alpha/\theta_c = 9$), which was well into the angle-of-attack range within which Moskovitz (1989) discovered

square wave variations of sectional side force coefficient with roll angle for elliptic cross section tips on bodies with conical noses.

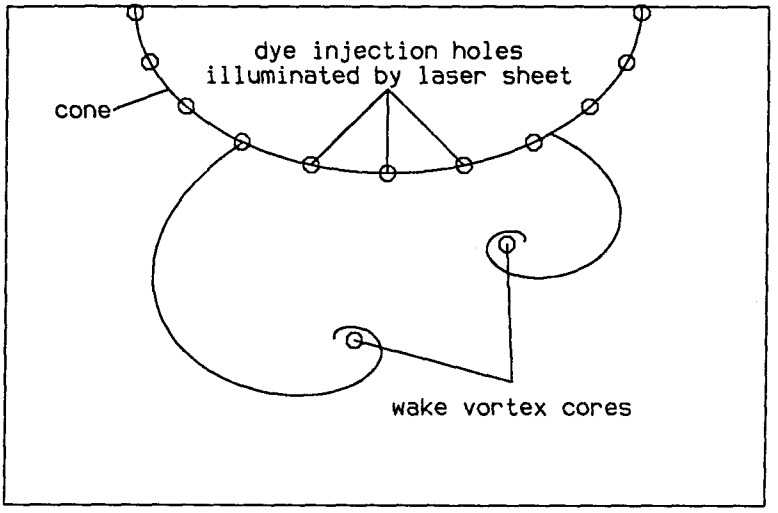

a. Typical video image with index of refraction distortion

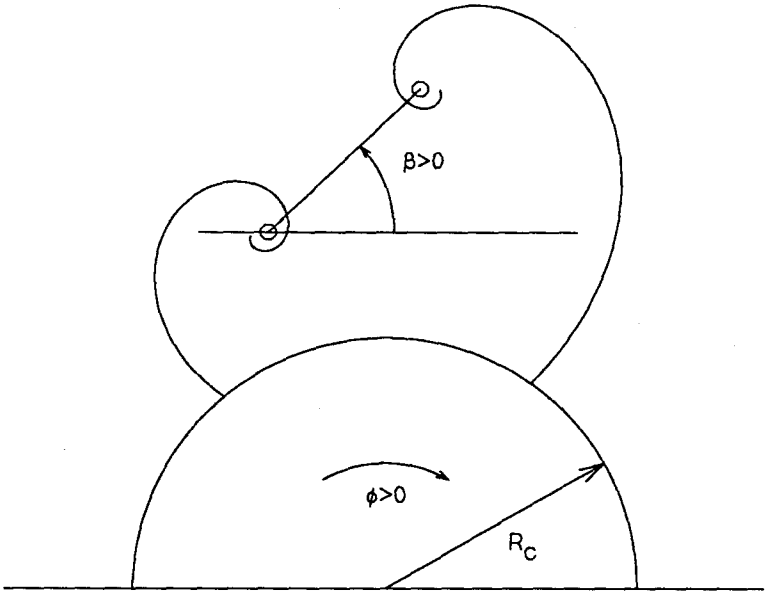

b. Corrected image (view from base of cone)

FIG. 4.2 Vortex wake cross section images

A typical vortex wake image is shown in Fig. 4.2a. This image was processed from the videotape using a framegrabber and digital image processing software.

Because of the distortion caused by the change in index of refraction as the image passed from the channel to the air, the cross section of the cone appeared as an ellipse. By digitizing points on the circumference of the cone illuminated by the dye from the dye ports, and then fitting the equation of an ellipse to these points, the center and the major and minor axes of the elliptical cone image could be calculated. After these values were obtained, the locations of the vortex cores were digitized. Because the fluorescein dye was entrained into the primary vortices very near the tip of the model, the dye remained concentrated in the vortex cores, so that the cores appeared as small, bright dots on the video image. By subtracting the x and y coordinates of the center of the cone image from the x and y coordinates of vortex cores, and then normalizing the core x with the major axis of the ellipse and the core y with the minor axis of the ellipse, the distortion could be removed and the correct values for the vortex core locations, nondimensionalized by the cone radius R_c at the axial location of the laser sheet, could be obtained. A typical corrected image is shown in Fig. 4.2b. The view in this image is from the base of the cone, the so-called "pilot's eye" view. The direction of positive roll angle ϕ is shown in this figure. The signs of the core x and y coordinates were adjusted to give the proper core locations in this view. The angle β shown in the figure was defined as the angle between a line in the laser sheet plane connecting the two vortex cores and a line in the laser sheet plane perpendicular to the incidence plane (a horizontal line in Fig. 4.2b). This angle was used as a measure of the wake asymmetry and was calculated such that $\beta > 0$ corresponded to the right vortex being higher than the left vortex in the pilot's eye view, as shown in the figure.

As stated before, the angle of attack studied was 45^o ($\alpha/\theta_c = 9$). The free-stream speeds studied were 10 and 20 cm/sec, yielding values of Re_t for the large elliptic cross section tip of 942 and 1,884. For each speed and angle of attack, the roll angle ϕ was varied from 0^o to 360^o in 10^o increments and set with $\pm 1^o$ accuracy, as mentioned above. Positive ϕ was taken to be clockwise rotation when viewed from the base of the cone (Fig. 4.2b). Zero ϕ corresponded to the major axes of

the elliptic cross sections being horizontal. Zero ϕ could be set to $\pm 0.2^o$ accuracy. The flow was allowed to stabilize for one minute after the roll angle was set, and then the dye was turned on and the vortex wake was digitized for one minute. Five images were digitized out of each minute of videotape. The average location of each vortex core and the RMS deviation from this average were calculated and used to compute the asymmetry angle β and the estimated error in β.

4.4 Results

The results of these experiments are shown in Fig. 4.3. This figure shows the variation in wake asymmetry angle β with the cone roll angle ϕ for $\alpha/\theta_c = 9$ and $Re_t = 942,\ 1,884$. The Reynolds numbers based on cone base diameter (Re_D) for these two cases were 9,900 and 19,800, respectively. The cross flow Reynolds numbers for these two cases, computed using the cone diameter at the axial location of the laser sheet, were approximately 2,830 and 5,660, respectively. These figures show that the wake asymmetry angle varied with roll angle approximately as a two-cycle sinusoid. Included in each figure is a fit to a two-cycle sine wave, with the fit parameters, for comparison purposes. A comparison of the two figures shows that doubling Re_t had little apparent effect on the flow asymmetry, other than a very slight increase in the maximum value of the asymmetry angle β and slightly noisier data.

One explanation for the noise level and some of the irregularity of the data curves is that the location of the laser sheet, chosen such that the laser sheet would intersect the vortex wake where the asymmetry was large enough for good data acquisition, was near the the point where the primary wake vortices began to separate from the model. This led to some unsteadiness in the flow image, to the point in some cases where a bimodal flow seemed to occur. A larger number of samples from each segment of videotape would probably reduce the irregularities and the measurement errors. However, the present measurements were judged sufficient to demonstrate the effectiveness of the elliptic cross section tip in controlling vortex wake asymmetry. The noise in the data, plus the uncertainties in setting the zero

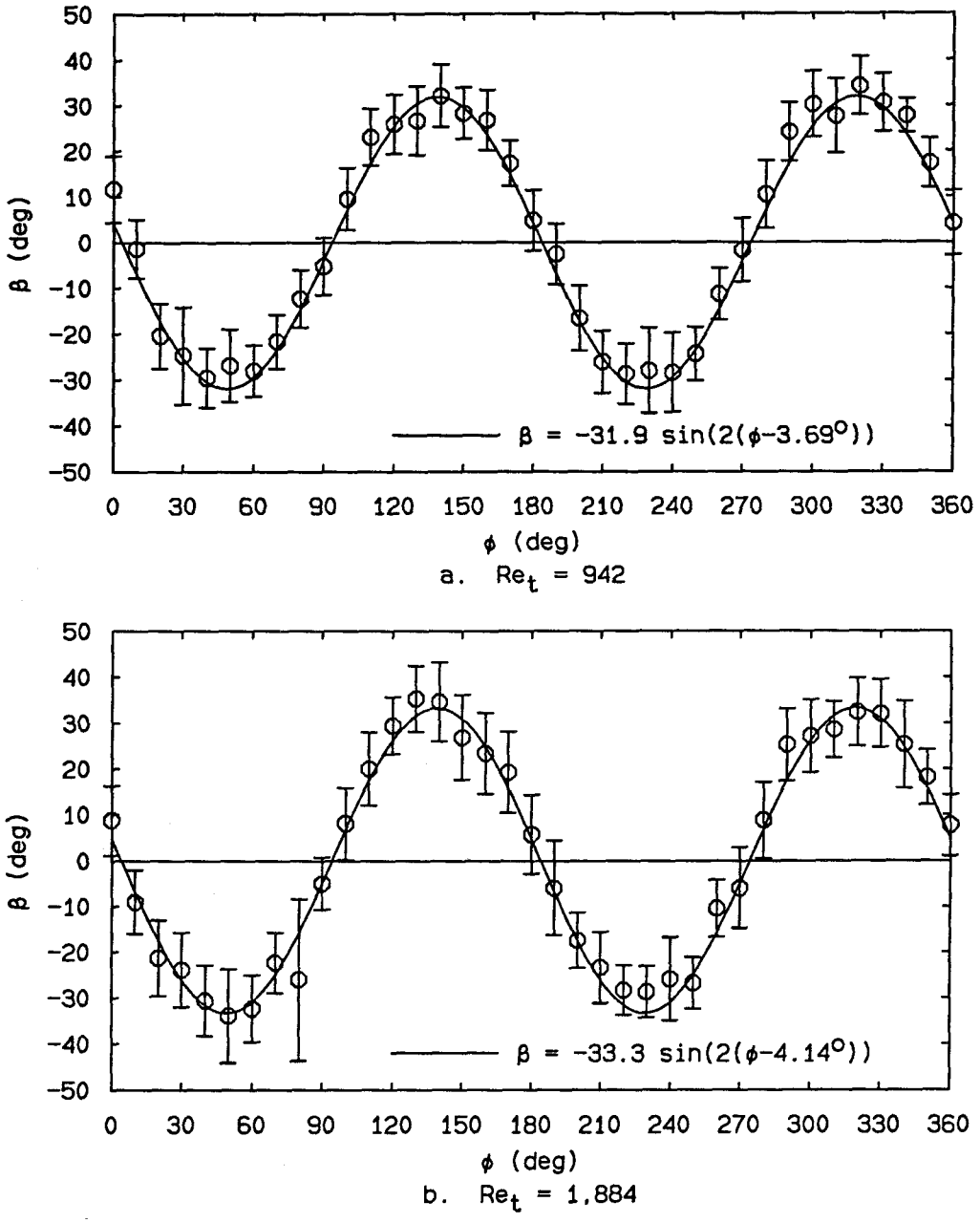

FIG. 4.3 Vortex wake asymmetry variations: $\alpha/\theta_c = 9$

value of ϕ and in the roll angle settings during the roll angle sweeps, are probably sufficient to explain the existence of the phase shifts in the curve fits to the data shown in Fig. 4.3.

During the data acquisition from the videotape, it was noticed that the two

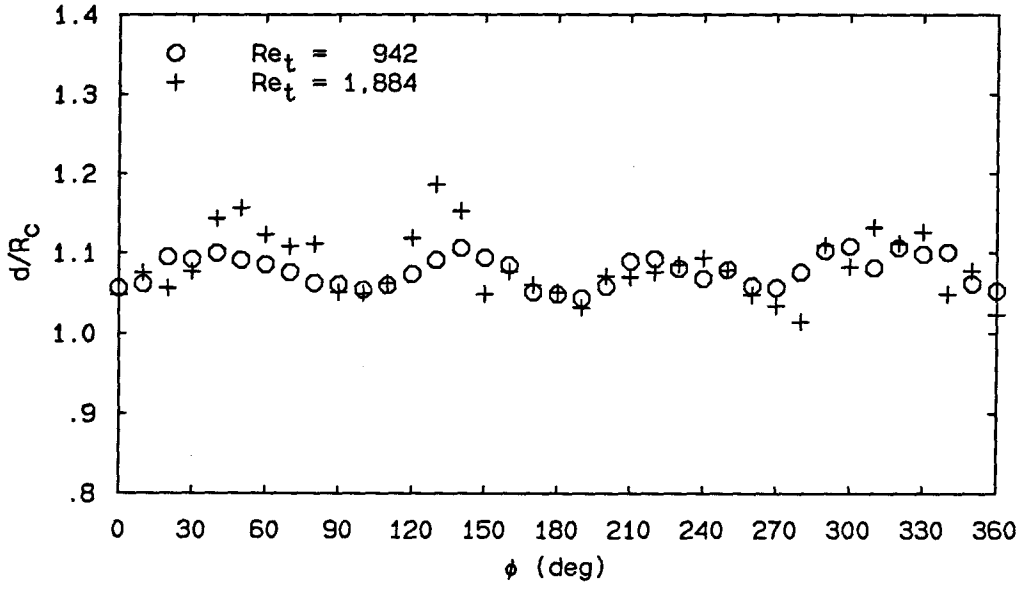

FIG. 4.4 Vortex separation distance variations: $\alpha/\theta_c = 9$

vortices always seemed to move in tandem. Once the data were reduced, the distance between the vortex cores in the laser sheet plane was computed. The variation of this distance with roll angle is shown in Fig. 4.4 for the two values of Re_t studied. In this figure, the vortex separation distance is normalized by the cone radius R_c at the axial location of the laser sheet. Note that the ordinate scale in Fig. 4.4 is in the range $0.8 \leq d/R_c \leq 1.4$. The vortex center separation is roughly constant, with at most a 20% deviation for the case $Re_t = 1,884$ (note that the data for $Re_t = 1,884$ is noisier than the data for $Re_t = 942$). The data for $Re_t = 942$ do show a small but essentially smooth variation with ϕ. The period of this variation is approximately half that of the period of the variation of β with ϕ. Each maximum in the vortex separation corresponds to a value of ϕ where the magnitude of β has a maximum, and each minimum in d/R_c corresponds to a value of ϕ where β has a minimum.

The discovery of the roughly-constant vortex separation distance piqued further interest in the vortex wake geometry itself. Figure 4.5 contains loci of vortex locations for the case $\alpha/\theta_c = 9$, $Re_t = 942$. The case $Re_t = 942$ only was examined since the data for this case were less noisy. Figure 4.5a contains all the recorded

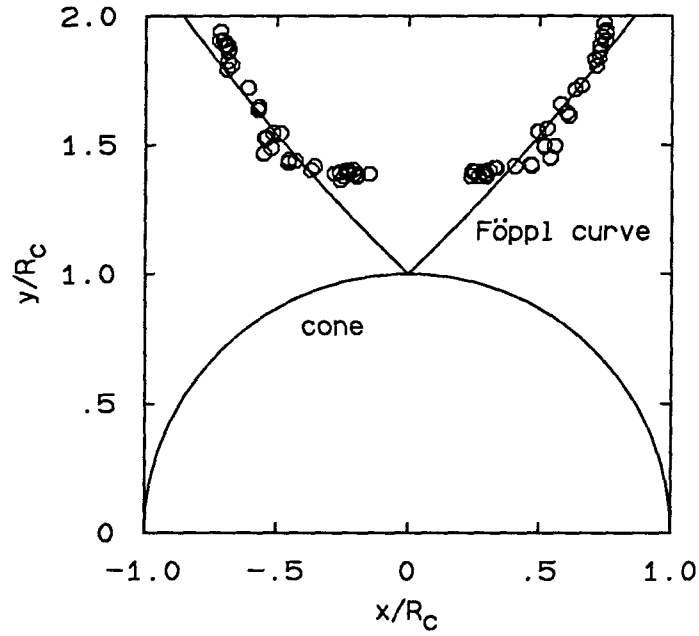

a. All recorded vortex locations
($0^o \leq \phi \leq 360^o$)

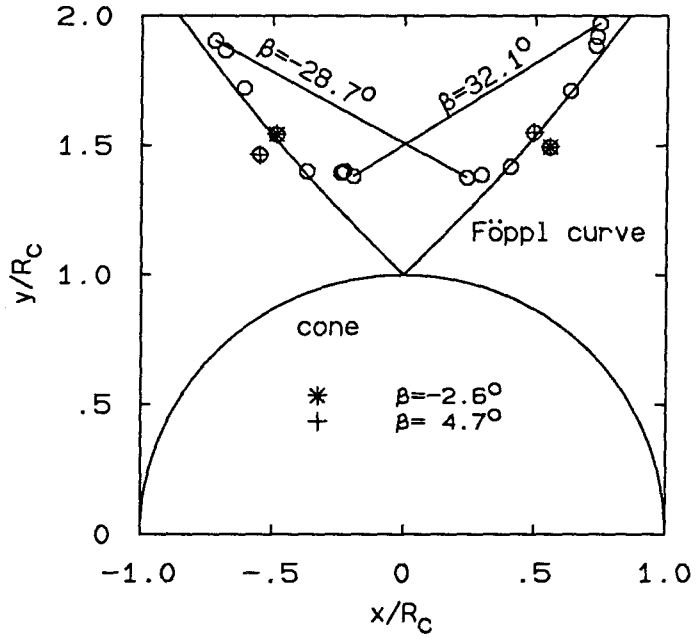

b. Single cycle between maxima in β
($140^o \leq \phi \leq 220^o$)

FIG. 4.5 Vortex core loci: $\alpha/\theta_c = 9$, $Re_t = 942$

vortex locations as ϕ was varied from 0^o to 360^o. The Föppl potential flow solution for the locations of two stationary vortices behind a circular cylinder in cross flow (Milne-Thomson 1968, p. 370) is included for purposes of comparison. Figure 4.5b

is included for purposes of clarity. This figure shows the locus of vortex core locations for $140^o \leq \phi \leq 220^o$. Over this range of ϕ, β varies from a maximum of 32.1^o to a minimum of -28.7^o. The vortex core locations labeled with an asterisk ($*$) and a cross ($+$) correspond to the measured flows that were closest to symmetric ($\beta = 0$). The relation between these vortex locations and the Föppl curve is of some interest. Consider the right vortex in the pair labeled "$\beta = -28.7^o$." As β increases, this vortex moves to the right along a seemingly smooth curve toward the vortex location on the right labeled with an asterisk ($*$), corresponding to $\beta = -2.6^o$. When β changes sign, however, there seems to be a discontinuity in the curve (or at least a large change of curvature of the curve) as the right vortex assumes the position labeled with a cross ($+$), corresponding to $\beta = 4.7^o$. This position happens to lie very close to the Föppl curve. As β continues to increase, the right vortex continues to move up and to the right, tracking the Föppl curve for a while but eventually leaving it as β approaches its maximum of 32.1^o. The left vortex in the pair follows an essentially reversed version of this path. The vortex core locus thus seems to be composed of two parts: a part that is transverse to the Föppl curve when the vortex is closer to the cone than the symmetric vortex location, and a part that almost coincides with, or at least appears to be tangent to, the Föppl curve when the vortex is farther away from the cone than the symmetric vortex location.

CHAPTER 5

Tip asymmetry effects on cone side forces

5.1 Introduction

As was shown in Ch. 4, the vortex wake asymmetry angle β varied with the cone roll angle ϕ approximately as a two-cycle sinusoid. This seemed to indicate that the elliptic cross section tip was effective in providing smooth control of the vortex wake asymmetry. Because of these promising results, experiments were conducted to determine the variation of the side force coefficient with body roll angle. These experiments are discussed in this chapter.

5.2 Experimental apparatus

5.2.1 Facility

The force measurement experiments were conducted in the Free Surface Water Tunnel (FSWT) of the Hydrodynamics Laboratory of the Graduate Aeronautical Laboratories, California Institute of Technology (GALCIT).* This facility is described in detail by Ward (1976). The test section of the FSWT was 20 in (50.8 cm) wide, 20 in (50.8 cm) high, and 6.5 ft (2 m) long. The speed range of the FSWT was 0–24 ft/sec (7.3 m/sec). The free-stream turbulence in the test section with flow conditioning screens in place was 0.38% at a free-stream speed of 15 ft/sec (4.57 m/sec) (see Ward 1976).

---

* Because of the use of the English system of units in much of the equipment and instrumentation in the Hydrodynamics Laboratory, the English system of units will be used in this chapter. Metric equivalents will be given where appropriate.

5.2.2 Model

The basic model used in these experiments was the right circular cone described in Sec. 2.2.2 and shown in Fig. 2.3. Four different tips were used with the cone: the two elliptic cross section tips described in Ch. 3, the sharp conical tip shown in Fig. 2.3, and the "chisel tip" shown in Fig. 5.1. This tip was constructed by machining two flats on the sides of a sharp conical tip and was designed to be attached to the cone at the 0.698 in (1.77 cm) diameter location.

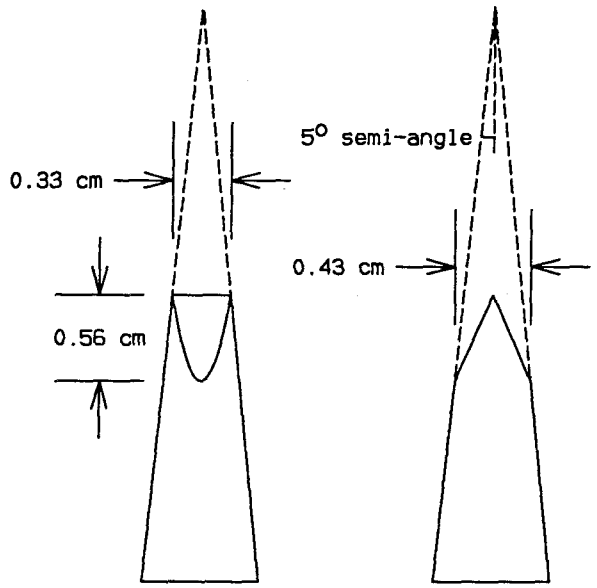

FIG. 5.1 Sketch of chisel tip

5.2.3 Sting

The cone was attached to the sting described in Sec. 2.2.2. Because of the number of roll angle sweeps planned, the mechanism used to vary the roll angle was modified so that the roll angle sweeps could be controlled by computer. The continuous-drive DC motor was replaced with a Linear Precision Industries P51-M342 stepper motor and stepper motor drive. The resolution of the stepper motor used was 200 steps per revolution. The stepper motor drive stepped the motor on the trailing edge of a square-wave signal that was at least 10 μsec wide. A

Dynamics Research Corporation C153 rotary optical encoder with a resolution of 50 lines per revolution and a quadrature output which multiplied the resolution by 4 was mounted on the free shaft of the stepper motor. The optical encoder was used to confirm that the step commands issued to the stepper motor during a roll angle sweep were actually executed. The stepper motor was mounted on the sting. A sketch of the sting and other apparatus is shown in Fig. 5.2.

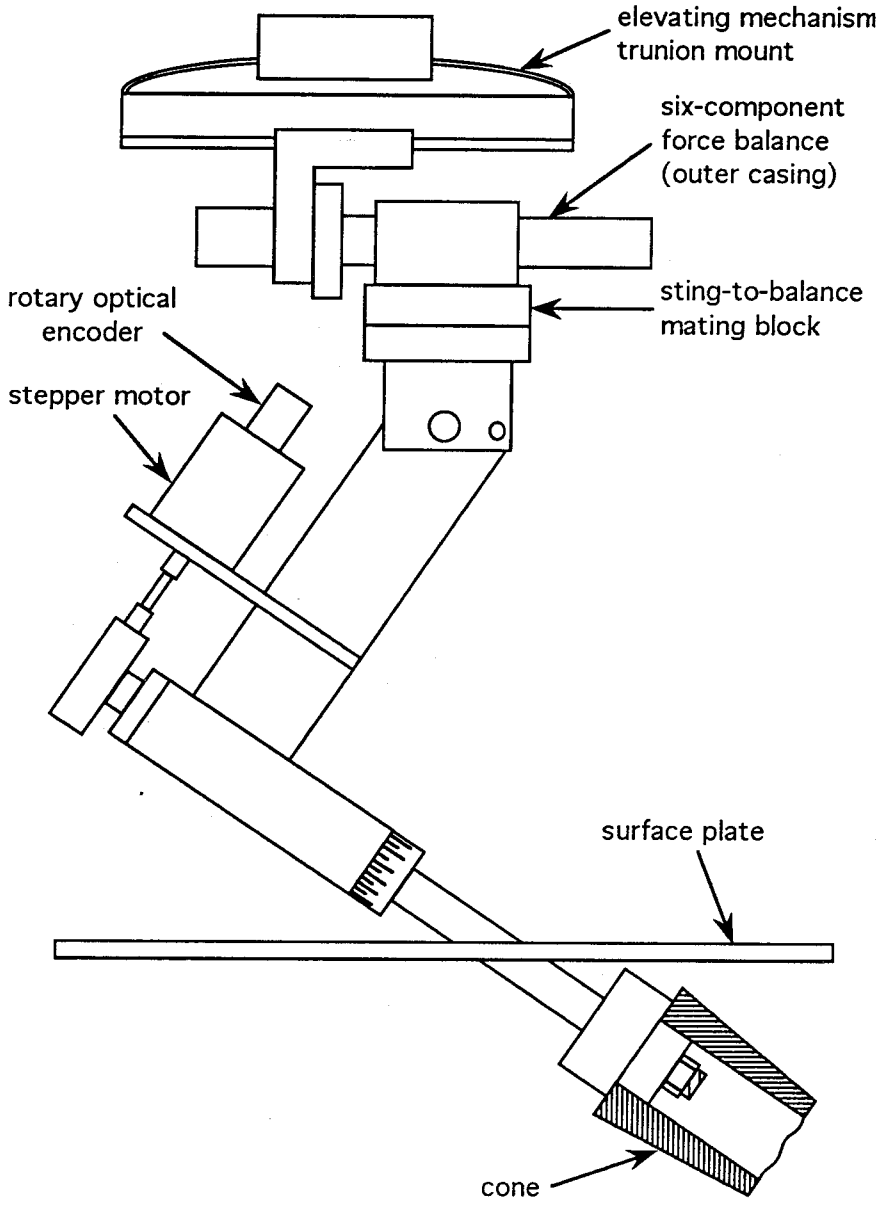

FIG. 5.2 Sketch of apparatus for force measurements

The sting was attached to the mounting plate of a six-component force balance (to be discussed in the next section). The force balance was in turn attached to an elevating mechanism used with the FSWT. The elevating mechanism had a trunnion pitch adjustment which could be adjusted through a continuous $\pm 10^o$ range in pitch. The elevating mechanism also had a $\pm 5^o$ yaw adjustment. The elevating mechanism was locked to the top of the test section of the FSWT during tests.

5.2.4 Free-surface plate

The experiments were originally planned to span a speed range from 0 to 2 m/sec. This range included speeds known to cause serious surface effects in the FSWT. To minimize or eliminate these effects, a surface plate was constructed. This plate is shown in Fig. 5.3. The plate was designed to cover the first half of the test section of the FSWT. The plate was constructed from Lucite and was suspended from support bars attached to the top of the test section. Grooves were machined into the sides of the plate which were then sealed against the glass walls of the test section using rubber hosing. The hoses were stretched in the grooves and the plate was lowered into position in the test section. Once the plate was positioned properly, the hoses were released. As they attempted to return to their original length, they filled the grooves in the sides of the plate and thus sealed the gap between the plate and the test section walls.** The leading edge of the plate was beveled to facilitate mating with the outlet ceiling of the FSWT contraction. The joint between the contraction outlet ceiling and the leading edge of the plate was smoothed using wax. The plate also had an adjustable-angle trailing edge flap which could be used to adjust the streamwise pressure distribution on the plate.

The plate had a 4.0 in (10.2 cm) wide slot through which the model was lowered into the test section. Inserts were then installed to close the slot. The fore and aft inserts were used for all tests. Two different pairs of inserts were used in the remaining slot opening to create two different sting access holes in the surface plate.

** This plate-sealing procedure was designed and implemented by the staff of the Hydrodynamics Laboratory.

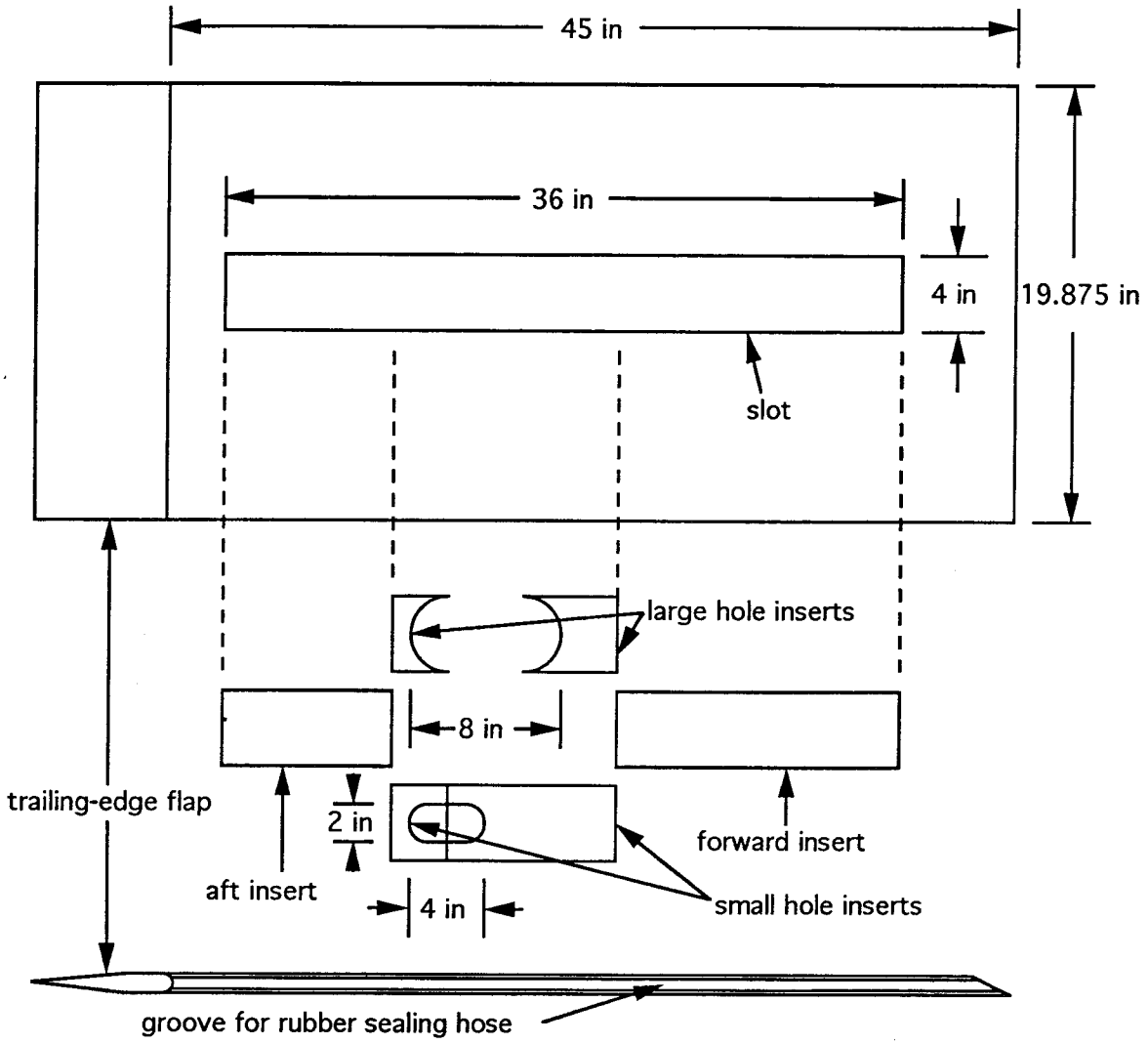

FIG. 5.3 FSWT surface plate

These are shown in the figure. The small access hole was used when the cone was completely submerged and only the sting shaft penetrated the surface plate. The large access hole was used when the cone was placed at a high angle of attack, so that the base of the cone protruded through the surface plate. The large access hole was also used when the cone was at low angle of attack and clearance limitations on the sting shaft support prevented the cone from being lowered into the channel far enough so that the base of the cone would clear the bottom of the surface plate.

5.3 Instrumentation

5.3.1 Force balance

The forces on the cone were measured using a Task Corporation 2.00 Mk II A internal six-component balance. The balance contained two normal force elements for determination of normal force (lift) and pitching moment, two side force elements for determination of side force and yawing moment, a chord-force (drag) element, and a rolling moment element. The range of each of the two normal-force elements was ± 40 lb_f. The range of each of the two side force elements was ± 14 lb_f. The range of the chord-force element was ± 25 lb_f. The range of the rolling moment element was ± 260 in-lb_f. The normal and side force elements were equipped with relaxation members at either end and were arranged to act in roll as a set of crossed ribbon flexures. Similar relaxation members provided compliance in the chord force direction. The rolling moment element contained relaxation members at either end which were designed to transmit pure rolling moment to the gauge section. The chord force element was located inside the rolling moment element and transmitted axial force from the outer case of the balance to the inner rod. All gauged sections except the rolling moment element were of the bending beam type containing 4 active 121Ω strain gauges. Rolling moment was resisted by a torque tube to which were bonded 4 active strain gauges.[†] The four active gauges of each element were wired in a bridge arrangement. The bridges were excited with a 4.0V DC excitation voltage. Each bridge also contained a nulling-resistor circuit which allowed each bridge to be balanced in the zero-force condition so that the bridge output was zero. The signal from each bridge was then fed into a Astro-Data 885 wideband differential DC amplifier with the amplifier gain set to 1000. The voltage from each amplifier was displayed on an averaging panel voltmeter with a resolution of ± 1 mV. The signal from each amplifier was also fed to a BNC connector panel. The calibration of the force balance will be discussed in a later section.

[†] Information from Task Corporation balance calibration manual, on file in Hydrodynamics Laboratory.

5.3.2 Speed measurements

The test section free-stream speed was determined by measuring the static pressure drop across the contraction using a Druck PDCR 130/WL 5 psid, wet-wet differential pressure transducer. The voltage output of the transducer was calibrated to the test section speed, which was measured with an LDV system. The output of the pressure transducer was read by a digital multimeter with a resolution of ±1 mV. The calibration data are shown in Fig. 5.4.‡ This figure includes a linear regression fit to the data and the associated linear regression correlation value. The equation of this line in metric units was given by

$$U = 0.0305 + 2.800(V_p - V_{p_0})^{\frac{1}{2}}, \tag{5.3.1}$$

where U was the test section speed in m/sec, V_p was the output voltage of the differential pressure transducer when the tunnel was at speed, and V_{p_0} was the output voltage of the pressure transducer at a tunnel speed of zero.

5.3.3 Computer control and data aquisition

The experiments were controlled by a Gateway 2000 80386-microprocessor based 20 MHz computer. A Scientific Solutions 12-bit analog-to-digital converter card was used in conjunction with the computer. The card had 8 analog input channels and 2 analog output channels. The analog outputs provided the step and direction signals to the stepper motor drive. The analog input channels were used to read the output voltages of the force balance-amplifier system. The card required that all of the ranges of the input channels be set together. The range setting was ±10 V. With this range setting and the 12-bit resolution of the analog-to-digital converter, the resolution of the converter was ±0.00488 V. This card was used for both the force balance calibration and the force measurement experiments.

---

‡ The calibration was performed by the Hydrodynamics Laboratory staff, who provided the calibration data.

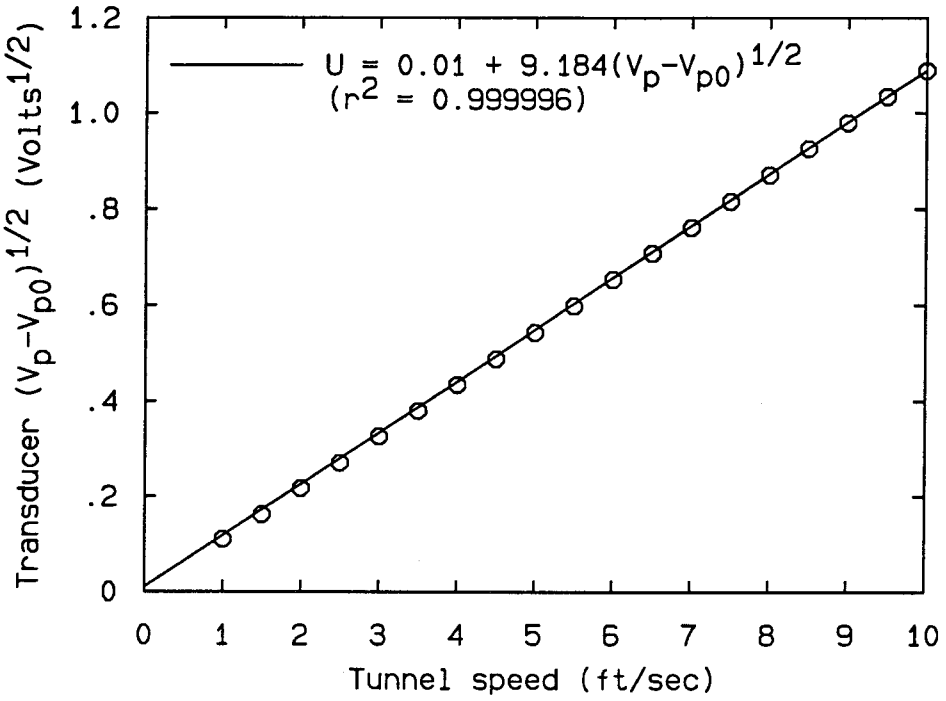

FIG. 5.4 FSWT test section speed calibration

The output of the rotary optical encoder was read by the computer with a Technology 80 quadrature encoder input card. This card decoded the quadrature output of the optical encoder and counted the resulting pulses with a 24-bit counter. This count was compared to the count of step commands issued to the stepper motor to ensure that the step commands had been executed.

5.4 Force balance calibration

5.4.1 Theory

As stated before, the force balance used in these experiments was a six-component internal balance. Typically, the interactions between elements (or "crosstalk") is larger for an internal balance than an external balance. If the outputs of the balance elements are linear in both direct reactions and interactions, then the first-order expression for the output

$$\{\mathbf{V}_{\text{out}}\} = [\mathbf{B}]\,\{\mathbf{F}_{\text{app}}\}\,, \tag{5.4.1}$$

is sufficient to describe the response of the balance to the applied loads. In this equation, $\{\mathbf{V}_{\mathbf{out}}\}$ is the column vector of balance output voltages, [**B**] is the matrix of first-order reaction and interaction coefficients, and $\{\mathbf{F}_{\mathbf{app}}\}$ is the column vector of applied loads.

As described in Sec. 5.3, the force balance had 2 normal-force elements, which will be denoted by $N1$ and $N2$; 2 side-force elements, denoted by $Y1$ and $Y2$; 1 chord-force element, denoted by XX; and 1 rolling moment element, denoted by RR. In this discussion, each applied load will be denoted by an "F" with the element name as a subscript; *e.g.*, the forward normal force load will be denoted by F_{N1}. Each output voltage will be denoted by a "V" with the element name as a subscript; *e.g.*, the output voltage of the forward normal force element will be denoted by V_{N1}. The elements of the response coefficient matrix [**B**] will be denoted by a "b" with two subscripts. The first subscript will be the name of the element producing the output voltage, and the second subscript will be the name of the element to which the load is being applied; *e.g.*, b_{Y1Y2} will be the response of the $Y1$ element to a load applied to the $Y2$ element. Using this notation, Eq. 5.4.1 becomes

$$\begin{Bmatrix} V_{XX} \\ V_{N1} \\ V_{N2} \\ V_{Y1} \\ V_{Y2} \\ V_{RR} \end{Bmatrix} = \begin{bmatrix} b_{XXXX} & b_{XXN1} & b_{XXN2} & b_{XXY1} & b_{XXY2} & b_{XXRR} \\ b_{N1XX} & b_{N1N1} & b_{N1N2} & b_{N1Y1} & b_{N1Y2} & b_{N1RR} \\ b_{N2XX} & b_{N2N1} & b_{N2N2} & b_{N2Y1} & b_{N2Y2} & b_{N2RR} \\ b_{Y1XX} & b_{Y1N1} & b_{Y1N2} & b_{Y1Y1} & b_{Y1Y2} & b_{Y1RR} \\ b_{Y2XX} & b_{Y2N1} & b_{Y2N2} & b_{Y2Y1} & b_{Y2Y2} & b_{Y2RR} \\ b_{RRXX} & b_{RRN1} & b_{RRN2} & b_{RRY1} & b_{RRY2} & b_{RRRR} \end{bmatrix} \begin{Bmatrix} F_{XX} \\ F_{N1} \\ F_{N2} \\ F_{Y1} \\ F_{Y2} \\ F_{RR} \end{Bmatrix}. \tag{5.4.2}$$

In order to determine the elements of [**B**], one of the six loads of $\{\mathbf{F}\}$ is applied while the others are kept zero. Several values of this load are applied, and the six output voltages $\{\mathbf{V}\}$ are read for each value of the load. The output voltages on each of the six channels should be a linear function of the value of the applied load. A linear regression curvefit to these data produces the elements in the column of [**B**] corresponding to the load being applied to the balance. All six columns of [**B**] are determined by repeating this procedure for each of the six loads $\{\mathbf{F}\}$. Once [**B**]

has been completely determined, the loads on the balance can be determined from the output voltages from

$$\{\mathbf{F}\} = [\mathbf{A}]\{\mathbf{V}\}, \tag{5.4.3}$$

where $[\mathbf{A}]$ is the inverse of $[\mathbf{B}]$. This equation assumes that the zero operating point is a zero load condition, and that the output voltages are the change in output voltage from the zero load condition. Alternatively, Eq. 5.4.3 could be expressed as

$$\{\Delta\mathbf{F}\} = [\mathbf{A}]\{\Delta\mathbf{V}\}, \tag{5.4.4}$$

where $\{\Delta\mathbf{F}\}$ and $\{\Delta\mathbf{V}\}$ are the changes from the zero load condition.

5.4.2 Calibration procedure

The force balance was mounted on a calibration stand. The force balance casing provided load application points at which essentially pure loads could be applied to the individual load elements. After the balance and computer electronics had been given time to warm up, the bridge resistors were adjusted to give the zero voltages and the averages and RMS values of the zero voltages were recorded. These were all essentially zero for all of the elements except the XX element, which had an internal offset. Its zero voltage was usually set to 2.000 V with the bridge balance resistor. Weights were hung from the load application points for one of the elements and the 6 output voltages were measured by the computer, which calculated the average and RMS values of the voltages. After a series of weights had been added and removed, the computer used a linear regression routine to calculate the values and uncertainties of the elements of $[\mathbf{B}]$ from the weights and the average and RMS values of the voltages. This calibration was repeated a number of times before, during, and after the experiments. The ranges of applied loads used were determined from estimates of the expected maximum loads during the experiment.

5.4.3 Calibration results

The results of the calibrations showed that most interactions between elements were negligible. This resulted in many of the off-diagonal elements of [**B**] being zero. The non-zero elements of [**B**] were

$$b_{XXXX} = -0.194 \pm 0.001$$

$$b_{N1N1} = +0.122 \pm 0.001 \qquad b_{N1N2} = 0.0036 \pm 0.0002$$

$$b_{N2N1} = 0.0034 \pm 0.0002 \qquad b_{N2N2} = 0.135 \pm 0.001$$

$$b_{Y1Y1} = -0.276 \pm 0.001 \qquad b_{Y1Y2} = -0.0149 \pm 0.0002$$

$$b_{Y2Y1} = -0.0150 \pm 0.0002 \qquad b_{Y2Y2} = -0.349 \pm 0.001$$

$$b_{RRRR} = 0.0221 \pm 0.001 \tag{5.4.5}$$

where the units of all of the coefficients are V/lb_f, except b_{RRRR}, which has units of V/in-lb_f. The associated linear regression correlation values r^2 were all 0.9999 or better, indicating a highly linear balance response to applied loads. These values were repeatable to within 1% of the initial values among all of the different calibrations conducted. The only significant interactions were between the two normal-force elements and the two side-force elements. The nature of the resulting [**B**] array made its inversion a simple matter of inverting two 2X2 matrices and taking the inverse of two scalar numbers. This was done in the data reduction program, which also used the uncertainties in the elements of [**B**] to compute the error bars on the forces.

5.4.4 Nonlinearities in side force interactions

During the experiments, it was discovered that a smaller range of side forces than had been expected would be of interest. A more thorough calibration of the balance side force elements in the range ±2.5 lb_f was conducted after the experiments. The results of this calibration for the interactions between the side force elements are shown in Fig. 5.5. This figure shows that the interactions between the two side force elements were nonlinear for applied loads of 1 lb_f or less.

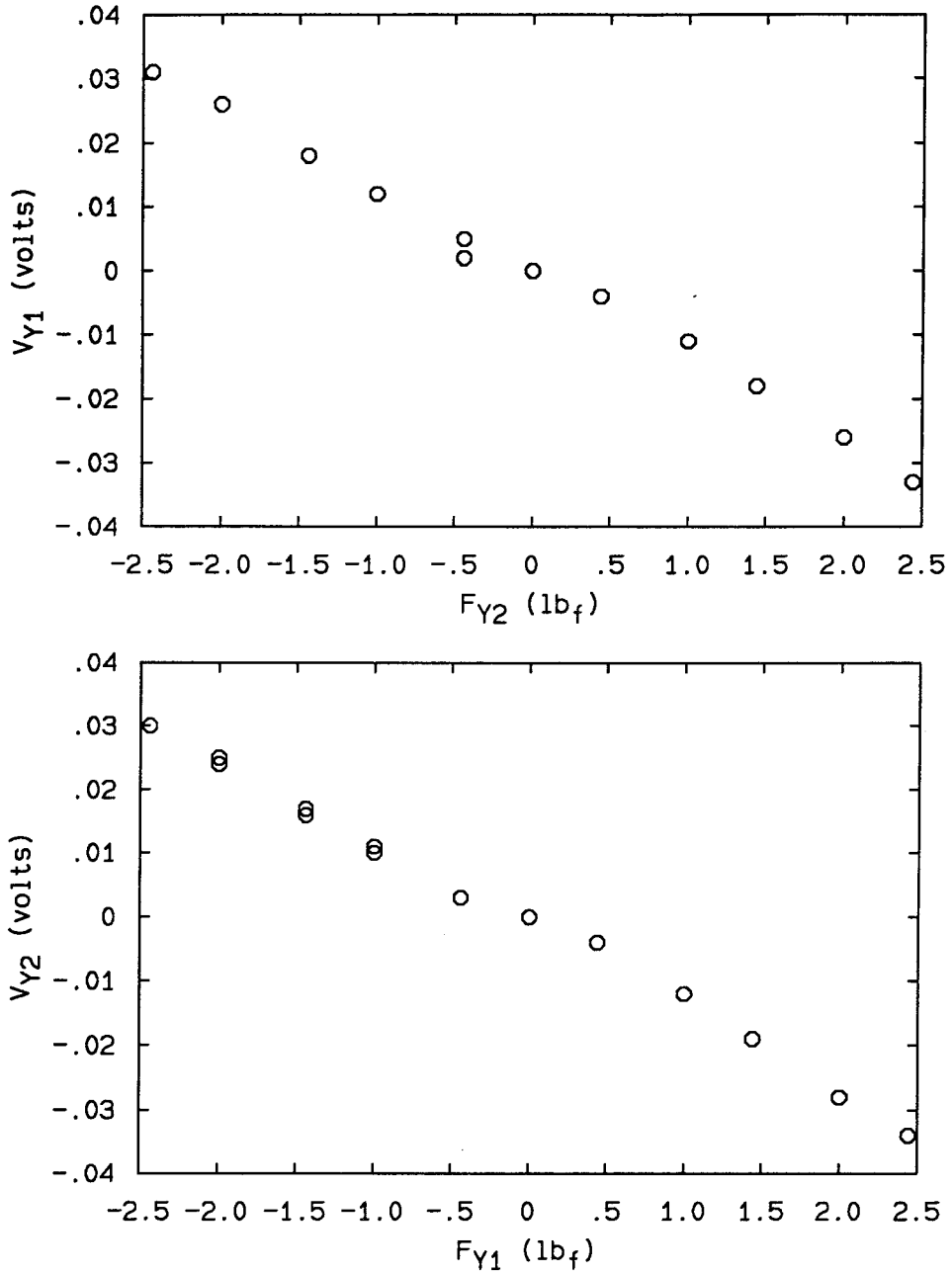

FIG. 5.5 Interactions between balance side force elements

During this calibration, the sting without the cone was attached to the force balance on the calibration stand and was set to an angle of attack of 40°. Pure side force loads were applied to the sting at the point of cone attachment. The balance output voltages were used with the calibration results to compute the side forces. These computed forces were then compared with the actual forces. It was discovered

that for an applied load of 1 lb_f, the difference between the computed and actual side force, using only the diagonal terms b_{Y1Y1} and b_{Y2Y2} to compute the side force, was less than half the same difference using the diagonal terms *and* the interaction coefficients to compute the side force (1.3% error as opposed to 2.7% error). For an applied load of 2 lb_f, the difference between the computed and actual side force, using only the diagonal terms to compute the side force, was approximately the same as the difference using the diagonal and interaction terms (2.1% and 1.9% errors, respectively). For increasingly larger loads, the use of both diagonal and interaction coefficients gave increasingly better results. However, since it was clear that most of the side forces would be in the range 2 lb_f or less, it was decided to use only the two diagonal terms b_{Y1Y1} and b_{Y2Y2} to compute the side force, with a resulting estimated error of approximately 2%.

5.5 Experimental procedure

The balance and sting were attached to the elevating mechanism and the cone was attached to the sting. In this configuration, the balance measured the forces on the entire tip-cone model plus whatever portion of the sting mechanism that happened to be submerged. The sting was set so that the cone was horizontal ($\alpha = 0^o$) and the cone was rotated about its axis using the stepper motor to set the zero roll angle ϕ_0. Each of the four different tips used in the side force measurement experiments required a different procedure for setting ϕ_0. As was discussed in Ch. 3, the two elliptic cross section tips had reference marks on their bases corresponding to the location of the major axes of the elliptic cross sections. A roll angle measurement block was constructed for the large elliptic cross section tip and was used in conjunction with the digital inclinometer. The cone was rotated until the reference mark on the large elliptic cross section tip was within one stepper motor step of vertical. The zero roll angle was then measured to an accuracy of $\pm 0.1^o$ using the block and inclinometer. The zero roll angle for the small elliptic cross section tip was set by rotating the cone until the reference mark was within ± 2 motor steps of being aligned with a reference point directly above the centerline of the cone, so

that the accuracy of ϕ_0 for the small elliptic cross section tip was $\pm 3.6^o$. Note that here, the zero roll angle for the two elliptic cross section tips was defined such that the plane formed by the major axes of the elliptic cross sections coincided with the incidence plane. This was a change from the definition of zero roll angle in Sec. 3.1, in which the major axis was perpendicular to the incidence plane at $\phi = \phi_0$. The zero roll angle of the chisel tip was set by rotating the cone until the flat of the tip was within ± 2 motor steps of vertical alignment with a reference point directly above the centerline of the cone, so the accuracy of ϕ_0 was $\pm 3.6^o$ for the chisel tip. In all cases, the cone was stepped to ϕ_0 in the direction that the subsequent roll angle sweep was to be conducted so that any slack in the gearing system would be taken up. The conical tip had no *á priori* preferred roll angle. During the tests with the conical tip, each subsequent test was begun where the previous test had ended, so that the arbitrarily chosen ϕ_0 was the same for all tests.

Once ϕ_0 was set, the cone was lowered into the test section and the angle of attack was set and measured to $\pm 0.1^o$ using the digital inclinometer. Air within the cone was allowed to escape from the base of the cone, and then the cone mounting bolts were tightened completely. The blockage for the cone with a sharp conical tip at $\alpha = 60^o$, the maximum angle of attack studied in the experiments, was estimated to be approximately 9.3%, a maximum for all of the tips and angles of attack studied in these experiments. The blockage for the cone with the large elliptic cross section tip at $\alpha = 30^o$, the minimum angle of attack studied in the experiments, was estimated to be approximately 5%, a minimum for all of the tips and angles of attack studied in these experiments.

The sideslip angle β was set to zero with an accuracy of $\pm 0.1^o$. In their tests, Zilliac *et al.* (1991) deliberately set β to $\pm 0.25^o$ to determine the effects of slight model misalignment on the side forces, and found these effects to be minimal. Once the angle of attack was set, the surface plate inserts (Fig. 5.3) were installed. Because of clearance limitations, the large access hole inserts were used at small angle of attack. For larger angle of attack, the small access hole inserts were used. At

very high angle of attack, the large access hole inserts were used, so that the cone could be raised to allow adequate spacing between the cone tip and the bottom of the FSWT test section.

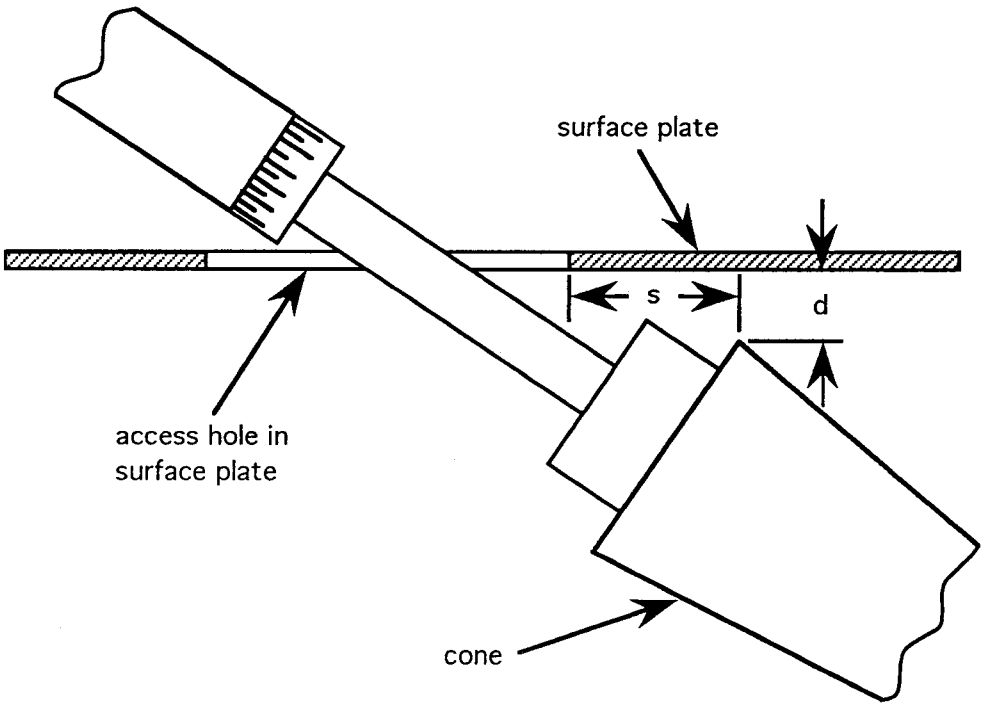

FIG. 5.6 Cone-surface plate position definitions

Since the cone was projecting into the water tunnel through an access hole in the surface plate, base effects were a source of concern during these tests. The position of the cone base relative to the access hole in the plate was determined and recorded for each test. Figure 5.6 shows the two quantities that were measured for each test. The distance from the foremost point of the access hole to the upper "corner" of the cone base is denoted by s in the figure. This quantity had the same definition for both large and small access holes (see Fig. 5.3). If the cone base corner was aft of the front of the access hole, s was negative. The spacing between the lower surface of the plate and the upper corner of the cone base is denoted by d in the figure. If the cone base corner was above the bottom of the surface plate, d was negative. The cone was always centered spanwise in the test section. Usually, if the large access hole was used, the cone base was centered streamwise in the access

hole. If the small access hole was used, the sting shaft was centered streamwise in the access hole.

Once the cone was put into position and the inserts installed, the tunnel water level was adjusted until it was at the center of the surface plate. The balance bridge voltages were then set to their zero levels, which were sampled 100 times by the computer. Averages and RMS values of the zero voltages were computed. The tunnel was turned on and the speed was set. Four nominal speeds, 30, 50, 70, and 90 cm/sec, were studied. The corresponding changes in pressure transducer voltages for these speeds were 0.0112, 0.0315, 0.0620, and 0.103 V, respectively. During the experiments, the output voltage from the pressure transducer was monitored visually using a digital multimeter with a resolution of 1 mV. It was estimated that for the speeds and voltages listed above, the corresponding fluctuations in voltage were 1, 2, 3, and 3 mV, respectively, yielding uncertainties in the tunnel speeds of 4, 3, 2, and 1%, respectively. While the test section speed was stabilizing, the tunnel water level was adjusted back to the center of the surface plate. Disturbances caused by the cone base resulted at some speeds in either the entrainment of air through the access hole into the test section or the discharge of water through the access hole out of the test section. To alleviate these difficulties, at these test conditions a small free surface reservoir was constructed on top of the surface plate, around the access hole. The tunnel water level was adjusted and water was added to the reservoir until the reservoir level was more or less constant.

Once the tunnel speed and water level had been stabilized, the roll angle sweep began. Each sweep contained 73 roll angles. These were chosen so that multiples of 45^o and 90^o would be included within a reasonable number of roll angles. The resulting roll angle step profile thus had extra points near roll angles that were multiples of 90^o, the points where the side forces were expected to pass through zero. The computer stepped the cone to a particular roll angle and the motion was confirmed by the rotary optical encoder. After the step, the computer delayed for 4 axial flow periods (the model length divided by the axial component of the

flow velocity, $U_\infty \cos\alpha$). After the delay, the computer sampled the balance output voltages 100 times, with the samples evenly spaced over 4 axial flow periods, and computed the average and RMS values of the voltages. Then, the cone was stepped to the next roll angle and the process was repeated until the roll angle sweep was completed.

Once a test was completed, the voltages were converted to forces using the results of the balance calibrations. These forces were then converted to coefficients using the free-stream dynamic pressure and the cone base area. The side force was defined to be positive to the right in the pilot's eye view of Fig. 4.2. Because the variation of side force with cone roll angle for a given test condition (speed and angle of attack) was of primary interest, and because the difference between the minimum blockage (5%) and the maximum blockage (9.3%) was small, so that the change in blockage between test conditions was small, no blockage corrections were applied to the data.

5.6 Test grid

The side forces were measured on the cone with the large elliptic tip at nominal angles of attack of 30°, 35°, 40°, 45°, 50°, and 60°, corresponding to nominal α/θ_c values of 6, 7, 8, 9, 10, and 12, respectively, and at nominal speeds of 30, 50, 70, and 90 cm/sec at each angle of attack, corresponding to nominal Re_t values of 2,800, 4,700, 6,600, and 8,500, respectively. At $\alpha = 60^o$ ($\alpha/\theta_c = 12$), the nominal speeds were 50 and 75 cm/sec, corresponding to nominal Re_t values of 4,700 and 7,100, respectively. The side forces were measured on the small elliptic tip at nominal angles of attack of 30°, 40°, 50°, and 60° ($\alpha/\theta_c = 6$, 8, 10, and 12, respectively), and at nominal speeds of 50 and 75 cm/sec (Re_t = 1,800 and 2,700, respectively) at each angle of attack. A number of experiments were performed to check the reliability of the results. Roll angle sweeps in both roll angle directions were performed using the cone with the large elliptic cross section tip at nominal angles of attack of 30°, 40°,

and 50^o and a nominal speed of 50 cm/sec to check for roll hysteresis effects. Two tests were performed at $\alpha = 50^o$, one for U_∞ increased from 0 to 50 cm/sec, the other for U_∞ decreased to 50 from 90 cm/sec, to check for speed hysteresis effects. Tests were performed for 3 different end conditions at nominal angles of attack of 30^o, 40^o, and 50^o and a nominal speed of 50 cm/sec to determine end effects. The side forces on the cone with a sharp conical tip were measured at a nominal speed of 50 cm/sec and nominal angles of attack of 30^o, 40^o, and 50^o, to determine the roll angle-side force characteristics of the baseline configuration. The side forces on the cone with the chisel tip were measured at a nominal speed of 50 cm/sec and nominal angles of attack of 30^o, 40^o, and 50^o, for purposes of comparison.

5.7 Results

5.7.1 Basic side force data

The basic results for the side force coefficient of the cone with the two elliptic cross section tips are shown in Figs. 5.8 through 5.17. Each figure shows the variation of the side force coefficient C_Y with the cone roll angle ϕ for all of the speeds tested at each particular angle of attack. As stated previously, the side force Y was the side force on the entire tip-cone model and submerged portion of the sting. The side force coefficient C_Y was defined as the side force Y nondimensionalized by the free-stream dynamic pressure $\frac{1}{2}\rho U_\infty^2$ and the cone base area $\pi D^2/4$. Both the tip Reynolds number Re_t (the Reynolds number based on the tip radius R_t), and Re_D, the Reynolds number based on cone base diameter D, are shown for each different ϕ–C_y characteristic. The particular tip used, the relative angle of attack α/θ_c, the zero roll angle ϕ_0, the cone base coordinates s/D and d/D from Fig. 5.6, and the particular surface plate access hole used are included in the captions to each figure. Figure 5.7 is included as an aid in visualizing the orientation of the elliptic cross sections with respect to the oncoming flow.

The error bars in each of these figures were computed from the RMS levels of the balance side force element output voltages and the estimated uncertainties

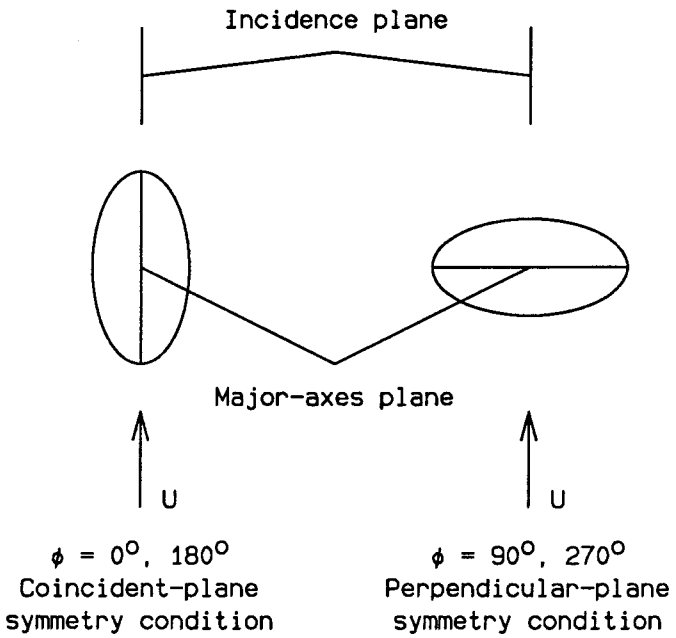

FIG. 5.7 Elliptic cross section orientations

in calibration constants, tunnel speed, water density, and cone base diameter. In some cases the error bars were quite large. The large error was attributed to two factors: unsteadiness in the side forces (to be discussed in detail in a later section), and low side forces caused by low dynamic pressures with resulting analog-to-digital resolution limitations. Large errors associated with small side forces are particularly evident in Figs. 5.8 through 5.12 at the lowest values of Re_t, obtained with a nominal tunnel speed of 30 cm/sec. At this tunnel speed, the dynamic pressure times the cone base area, $\frac{1}{2}\rho U_\infty^2$ times $\pi D^2/4$, was on the order of 0.1 lb_f. At this level of force, the ratio of the maximum side force element voltage output to the resolution of the analog-to-digital converter (0.00488 V) was typically around 8. As the speed increased, the size of the error decreased, as can be seen in the figures. At 90 cm/sec, the highest nominal tunnel speed, the maximum signal-to-resolution ratio was typically around 100. At 50 cm/sec, the maximum signal-to-resolution ratio was typically around 30.

Some general trends can be seen in the figures. The side force does go through

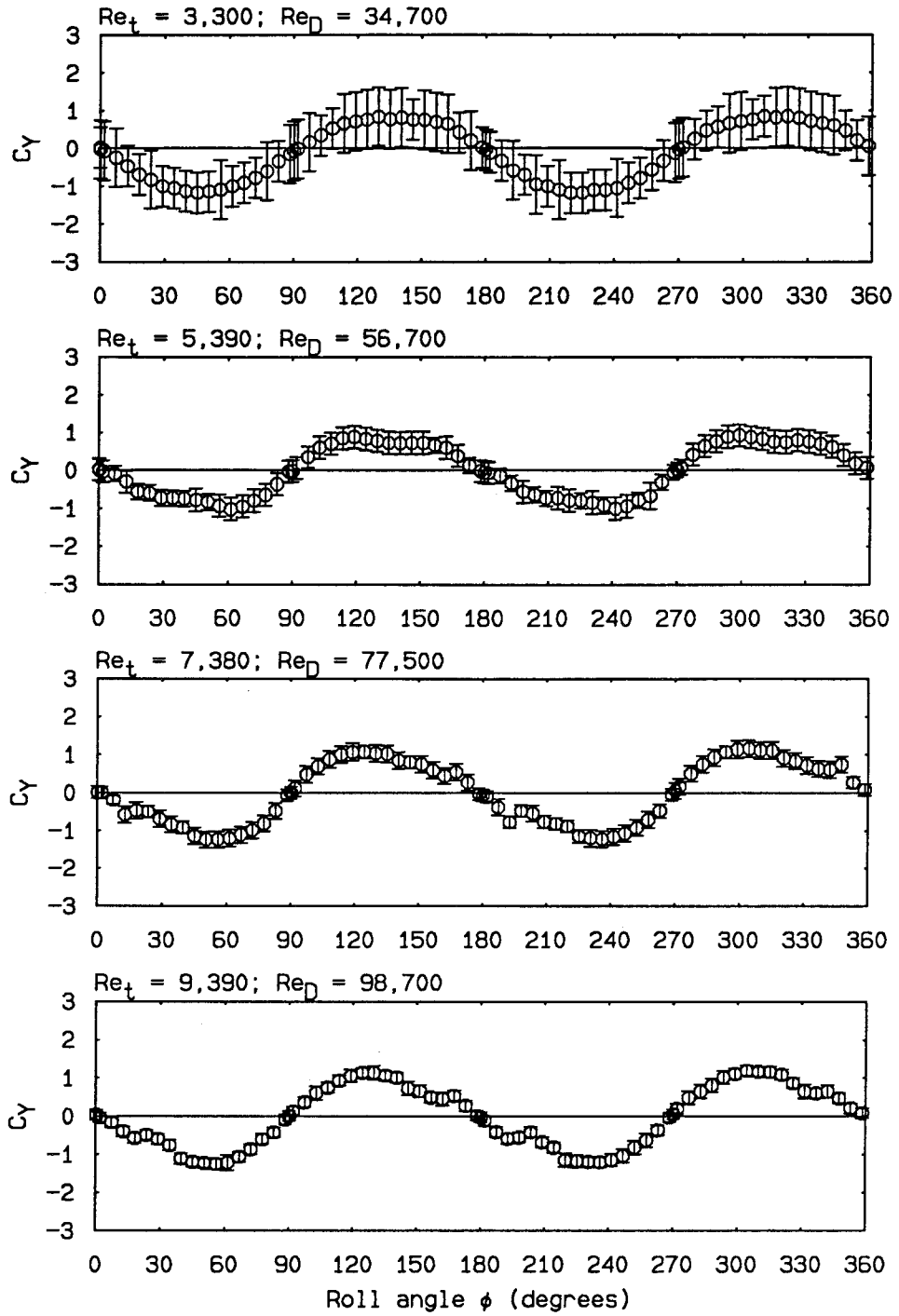

FIG. 5.8 Roll angle-side force characteristics: large elliptic cross section tip, $\alpha/\theta_c = 6.0$, $\phi_0 = 0.2^o$, $s/D = 0.0$, $d/D = 0.070$ (large access hole)

zero at multiples of 90^o, where the tip is symmetric with respect to the oncoming flow, as expected. There are other zero crossings at higher angles of attack. These will be discussed in more detail in a later section that will deal with the variations

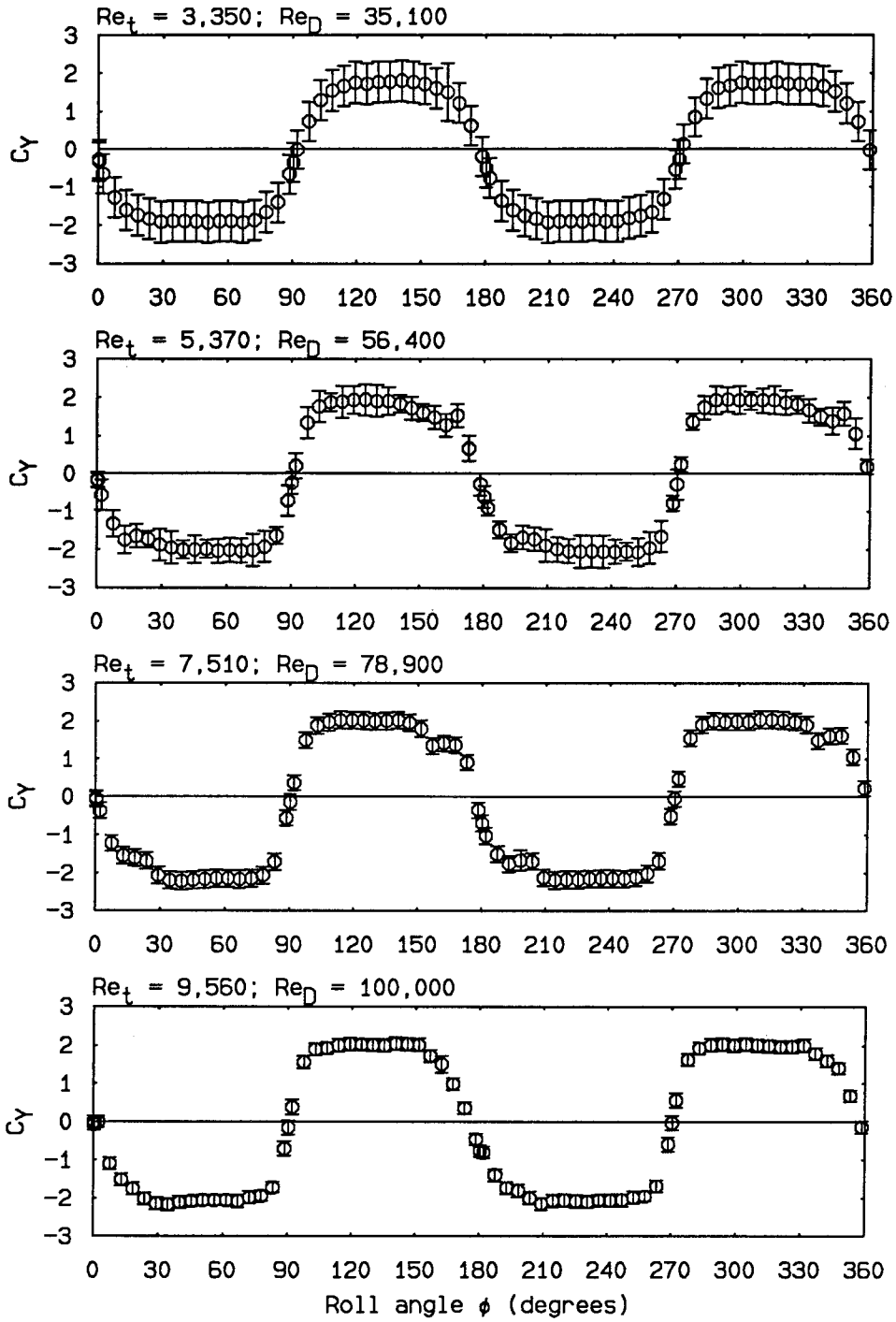

FIG. 5.9 Roll angle-side force characteristics: large elliptic cross section tip, $\alpha/\theta_c = 7.0$, $\phi_0 = 0.3^o$, $s/D = 0.66$, $d/D = 0.15$ (small access hole)

with angle of attack of the relation between roll angle and side force coefficient.

Some of the curves seem to exhibit a behavior that is periodic with period 180^o.

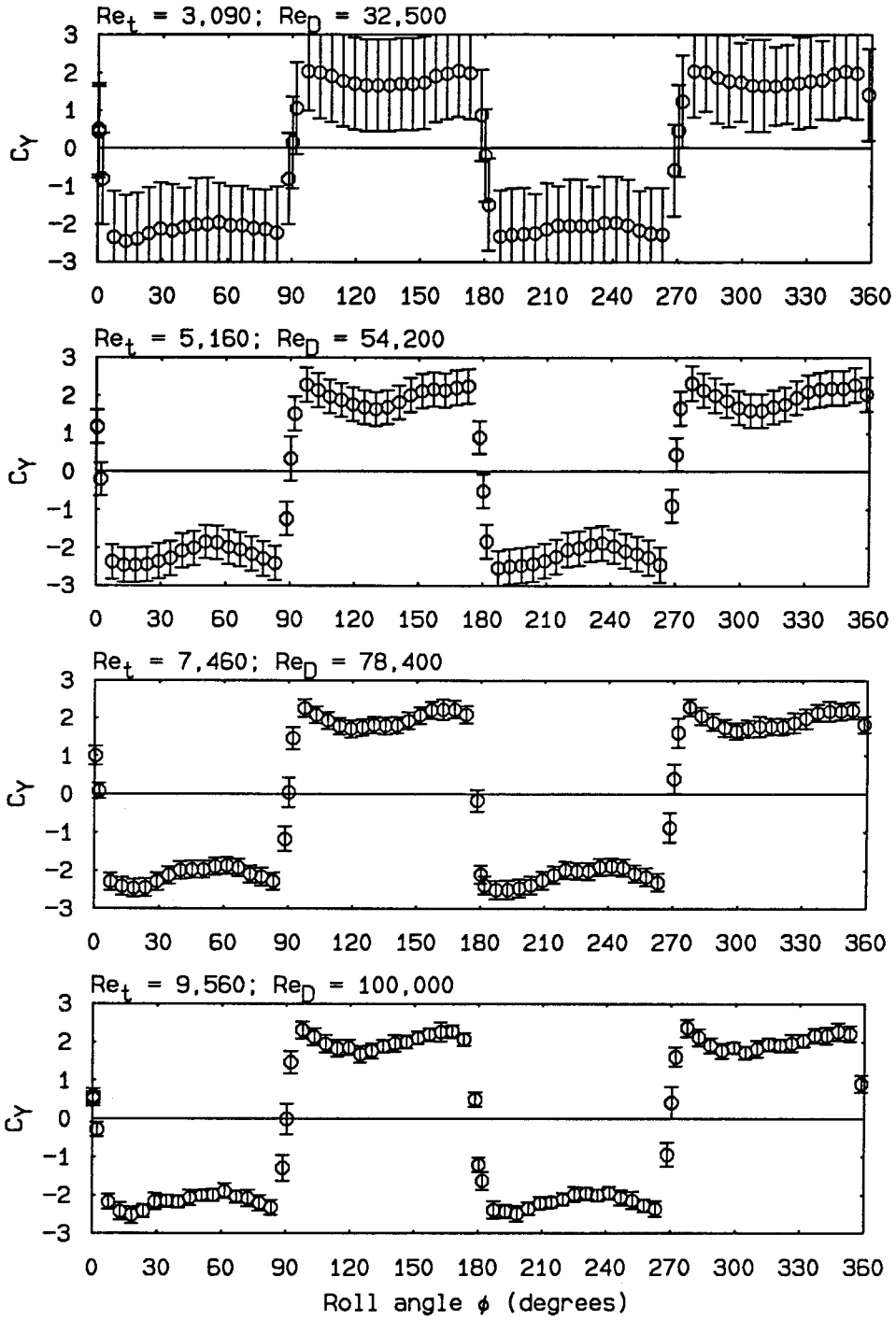

FIG. 5.10 Roll angle-side force characteristics: large elliptic cross section tip, $\alpha/\theta_c = 7.8$, $\phi_0 = 0.3°$, $s/D = 0.58$, $d/D = 0.18$ (small access hole)

For example, in Fig. 5.9, at $Re_t = 7{,}510$, the changes in C_Y as ϕ increases through $90°$ and $270°$ seem to be very similar to each other, and to be more rapid than the changes in C_Y as ϕ increases through $180°$ and $360°$, which also seem to be very sim-

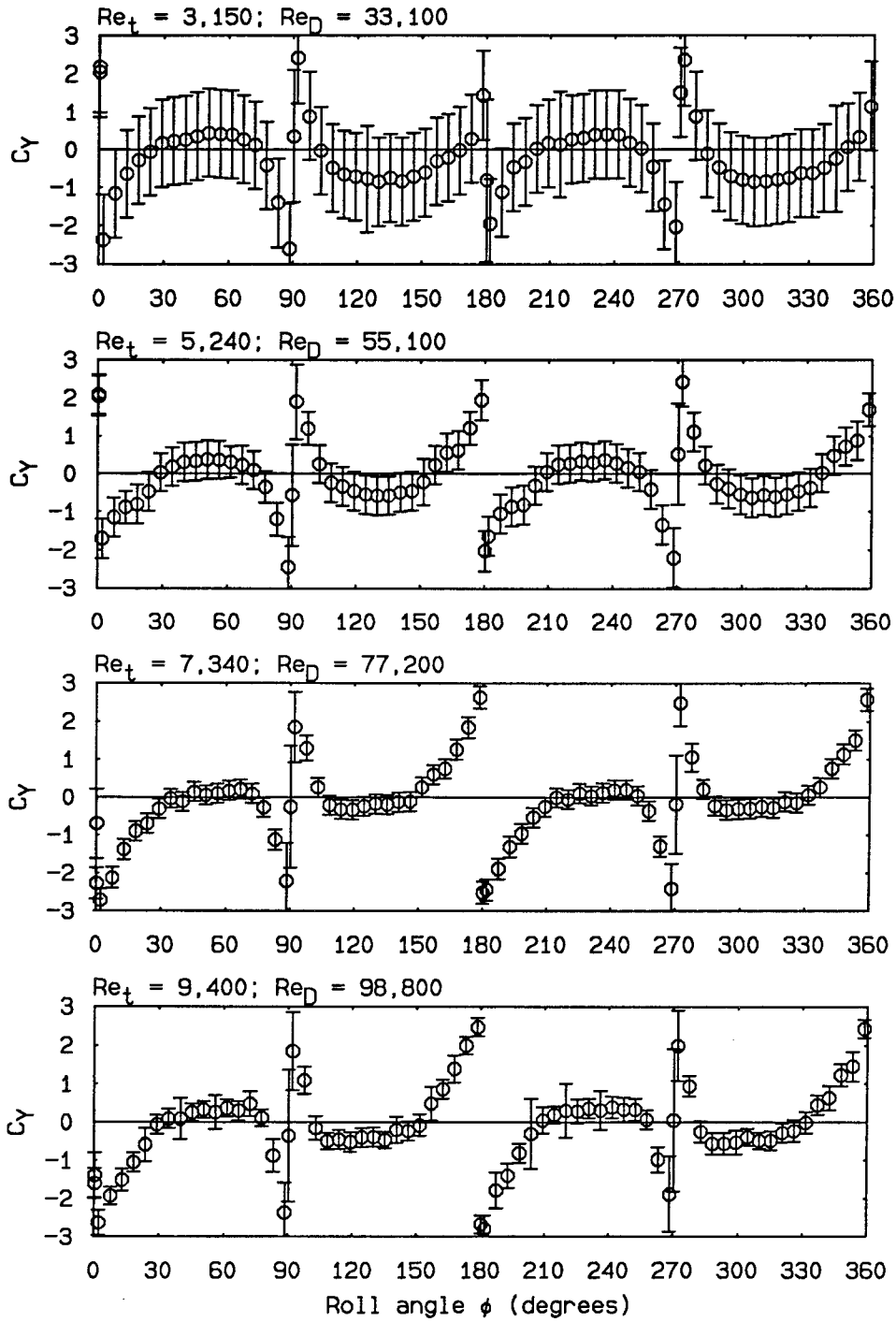

FIG. 5.11 Roll angle-side force characteristics: large elliptic cross section tip, $\alpha/\theta_c = 9.0$, $\phi_0 = 0.3^o$, $s/D = 0.46$, $d/D = 0.20$ (small access hole)

ilar to each other. When at a roll angle that is a multiple of 90°, the tip presented one of its two planes of symmetry to the oncoming flow. For $\phi \in \{90^o, 270^o\}$, the major-axes-plane of the tip was perpendicular to the incidence plane. This

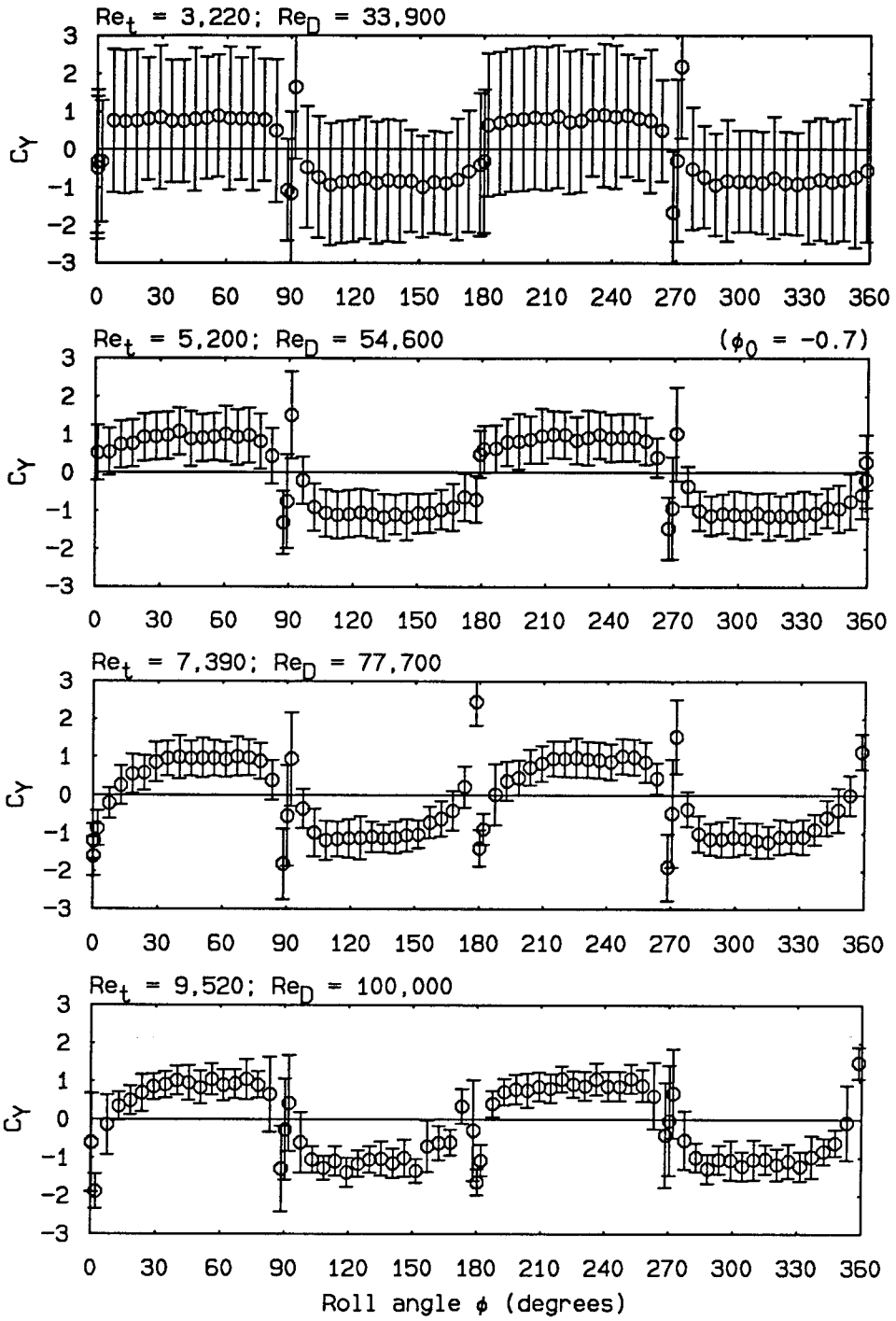

FIG. 5.12 Roll angle-side force characteristics: large elliptic cross section tip, $\alpha/\theta_c = 9.8$, $\phi_0 = 0.3^o$, $s/D = 0.41$, $d/D = 0.24$ (small access hole)

tip-flow symmetry condition will be referred to as the "perpendicular plane symmetry condition" for purposes of discussion (see Fig. 5.7). For $\phi \in \{0^o, 180^o\}$, the major-axes-plane was coincident with the incidence plane. This tip-flow symmetry

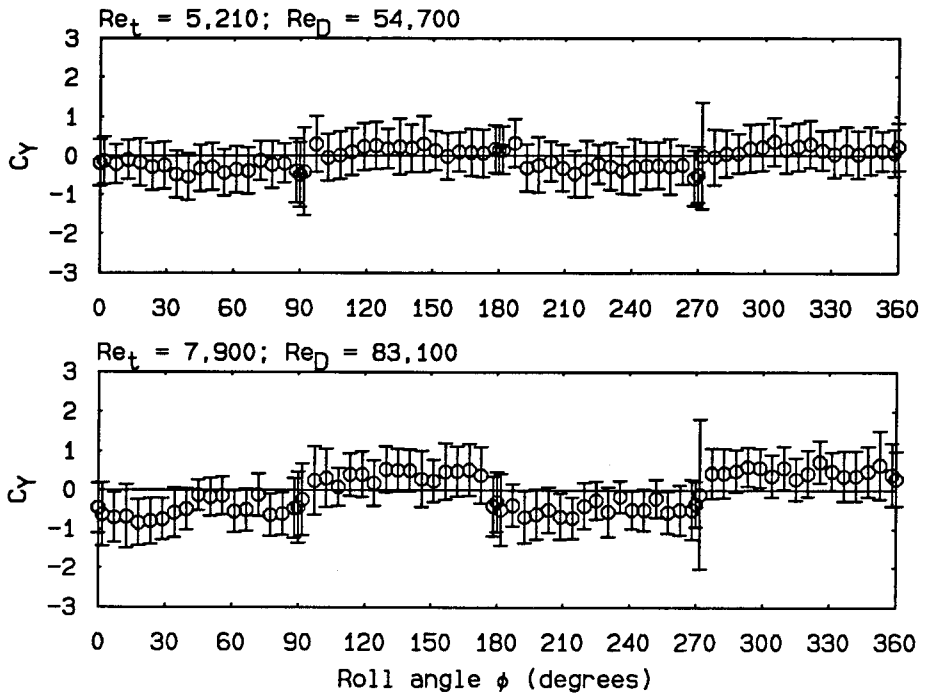

FIG. 5.13 Roll angle-side force characteristics: large elliptic cross section tip, $\alpha/\theta_c = 11.8$, $\phi_0 = 0.0^o$, $s/D = 0.57$, $d/D = 0.30$ (small access hole)

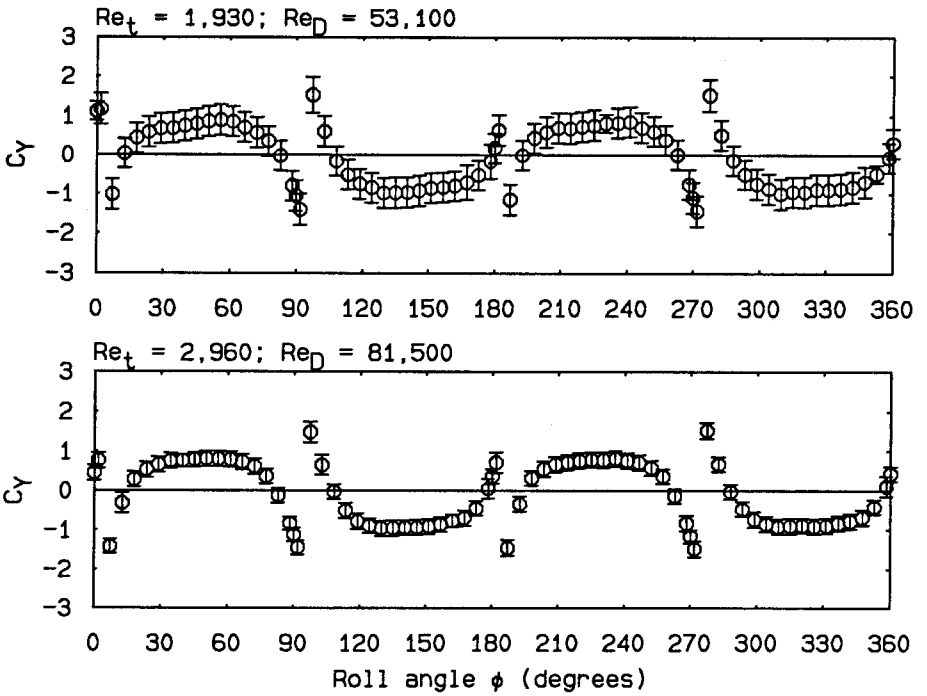

FIG. 5.14 Roll angle-side force characteristics: small elliptic cross section tip, $\alpha/\theta_c = 5.8$, $\phi_0 = 0.0^o \pm 3.6^o$, $s/D = 1.0$, $d/D = 0.20$ (small access hole without rear access hole insert)

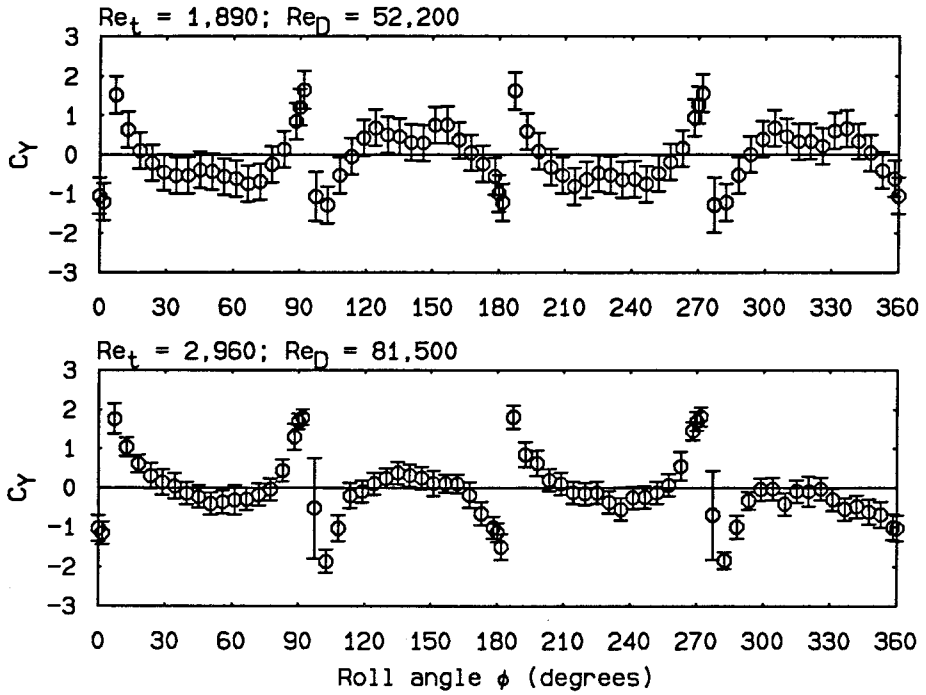

FIG. 5.15 Roll angle-side force characteristics: small elliptic cross section tip, $\alpha/\theta_c = 7.8$, $\phi_0 = 0.0^o \pm 3.6^o$, $s/D = 0.95$, $d/D = 0.36$ (small access hole)

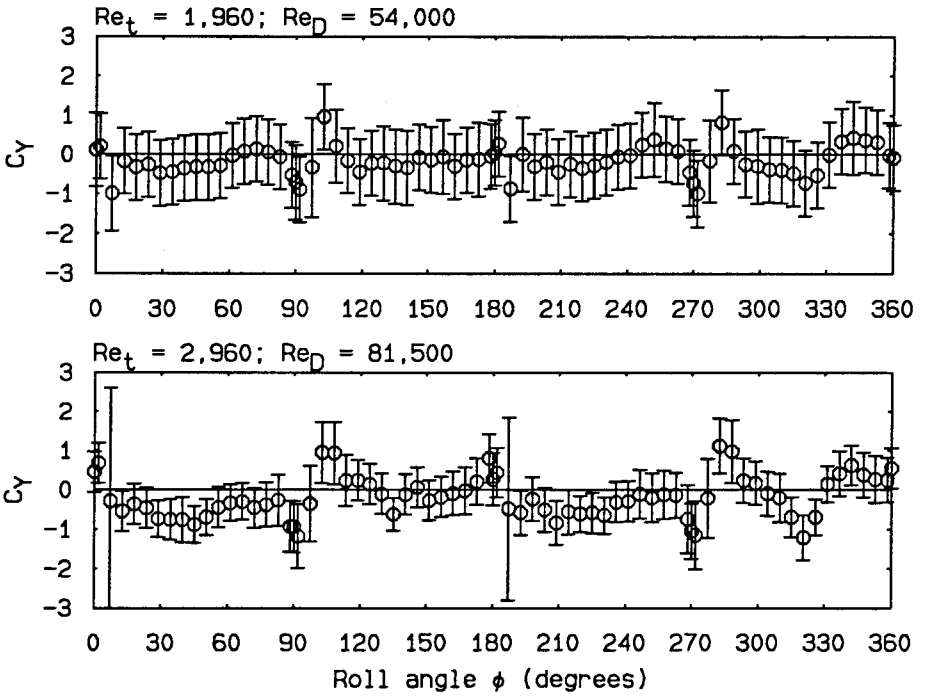

FIG. 5.16 Roll angle-side force characteristics: small elliptic cross section tip, $\alpha/\theta_c = 9.8$, $\phi_0 = 0.0^o \pm 3.6^o$, $s/D = 0.66$, $d/D = 0.27$ (small access hole)

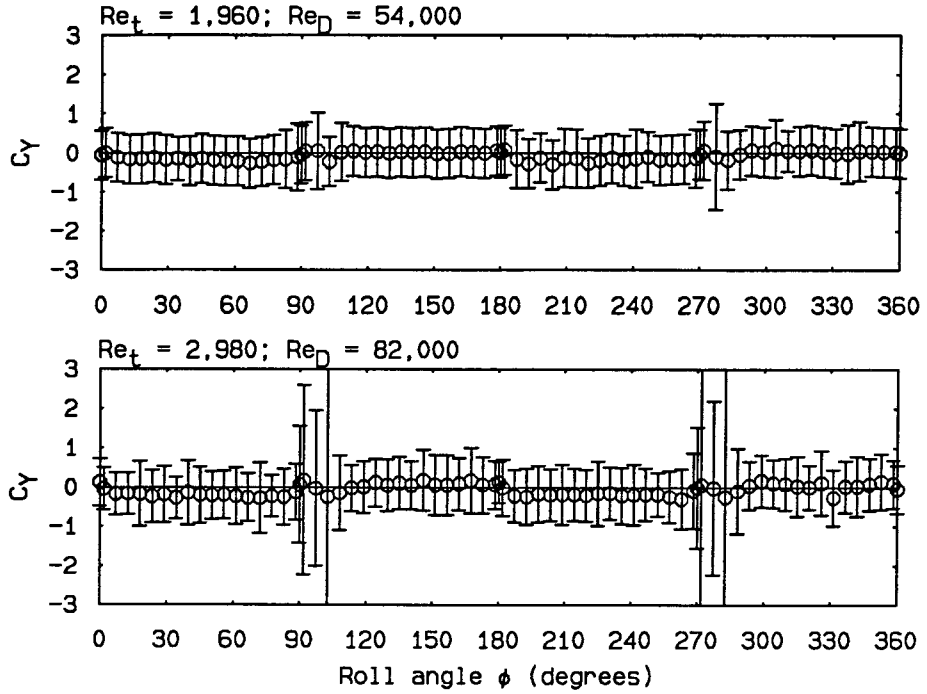

FIG. 5.17 Roll angle-side force characteristics: small elliptic cross section tip, $\alpha/\theta_c = 11.8$, $\phi_0 = 0.0^o \pm 3.6^o$, $s/D = -0.60$, $d/D = -0.096$ (large access hole)

condition will be referred to as the "coincident plane symmetry condition" for purposes of discussion. Figure 5.9 seems to indicate that the changes in the side force coefficient, and hence the vortex wake asymmetry, as the tip was rotated through the perpendicular plane symmetry condition were different in character from the changes in C_Y as the tip is rotated through the coincident plane symmetry condition. This difference can be attributed to the fact that for $\phi \in \{90^o, 270^o\}$, the major axes of the elliptic cross section are perpendicular to the incidence plane, so that the elliptic cross sections are "broad-side-on" to the flow, while for $\phi \in \{0^o, 180^o\}$, the major axes of the elliptic cross sections are parallel to the incidence plane, so that the cross sections are "narrow-side-on" to the flow. As the tip rotates into one of the two symmetry conditions, the rate of change with roll angle at which the tip and flow approach symmetry will be different for the two different symmetry conditions.

As the Reynolds number increased, the variation of the mean side force co-

efficients with roll angle became less smooth in some cases. This could have been caused by surface imperfections that became more effective in influencing the flow as the boundary layer thicknesses decreased with increasing Reynolds number. Such a mechanism was described by Hunt (1982), among others. Reynolds number effects will be discussed in greater detail in a later section.

Because the large elliptic cross section tip exhibited a larger range of side force behaviors than the small elliptic cross section tip, attention will be focused on the large tip for most of this chapter. As can be seen from the figures, the variation of the ϕ–C_Y curves with Re_t and Re_D was small. A nominal speed of 50 cm/sec yielded side forces large enough to avoid both the low force and resolution difficulties at a speed of 30 cm/sec, as discussed above, and possible errors caused by the model oscillations that sometimes occurred at speeds of 70 and 90 cm/sec, to be discussed in the context of flow unsteadiness in a later section. Because of these advantages, most of the rest of the force measurement experiments to be discussed were conducted at a nominal speed of 50 cm/sec.

The primary focus of the force measurement experiments was the side force on the body. The maximum side force coefficients obtained in the experiments were of the same size as those reported in the literature, in the range ± 1 to ± 3. No base pressures were measured in the experiments, so the lift and drag of the model could not be corrected for base forces. Rough values of the lift and drag coefficients without base pressure corrections indicated that the side force coefficients were of the same size as the lift and drag coefficients, as is often discussed in the literature. For these reasons, only results for side force coefficients are presented and discussed in this study.

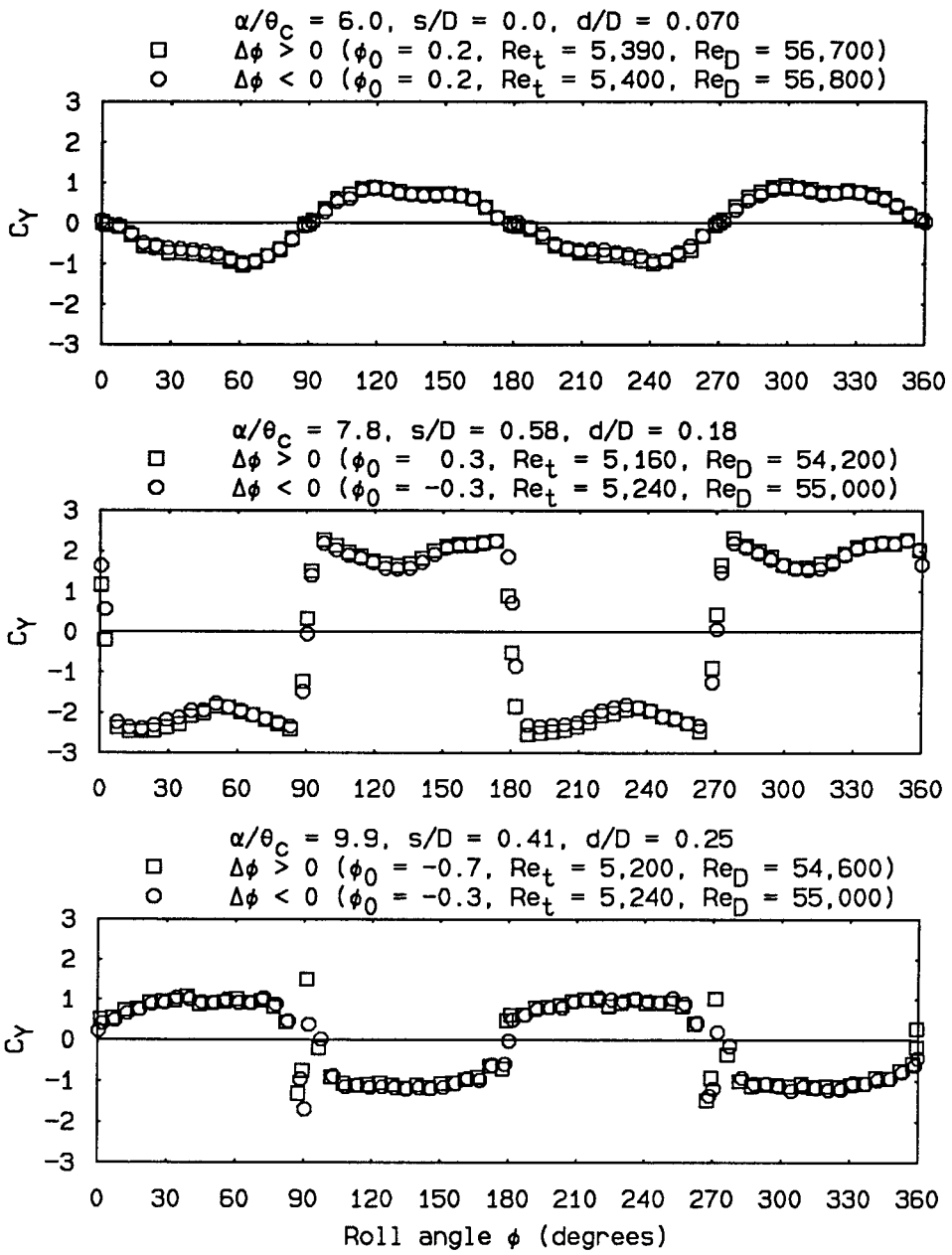

FIG. 5.18 Roll hysteresis checks: large elliptic cross section tip ($\alpha/\theta_c = 6.0$ – large access hole; $\alpha/\theta_c = 7.8, 9.9$ – small access hole)

5.7.2 Data reliability tests

Four sets of tests were conducted to determine the reliability of the roll angle-side force characteristic data. The first of these was a check for roll hysteresis effects. The roll angle sweep was performed in both directions. The tests were performed for three different angles of attack, at a nominal speed of 50 cm/sec. The results

of these tests are shown in Fig. 5.18. These results show that the ϕ–C_Y curves had essentially no dependence on the direction of the roll angle sweep. These tests also demonstrated the repeatability of the data and the uniqueness of the ϕ–C_Y curves. There were some variations between roll directions at $\phi = 90^o$ and 270^o for $\alpha/\theta_c = 9.9$. However, in these regions the change in C_Y with ϕ was very rapid. As can be seen in the figure label, ϕ_0 was slightly different for the two tests. The possible slight differences in ϕ in this region of rapid side force coefficient change are sufficient to explain the differences in values of C_Y shown in the figure.

The second reliability test was a check for speed hysteresis effects. Two roll angle sweeps were performed, one for a tunnel speed that was increased from 0 to 50 cm/sec and allowed to stabilize, the second for a tunnel speed that was decreased from 90 to 50 cm/sec, after the tunnel had been run at 90 cm/sec for several minutes. The results of these tests are shown in Fig. 5.19. These data show that there were essentially no speed hysteresis effects and again demonstrate the repeatability of the data and the uniqueness of the ϕ–C_Y curves.

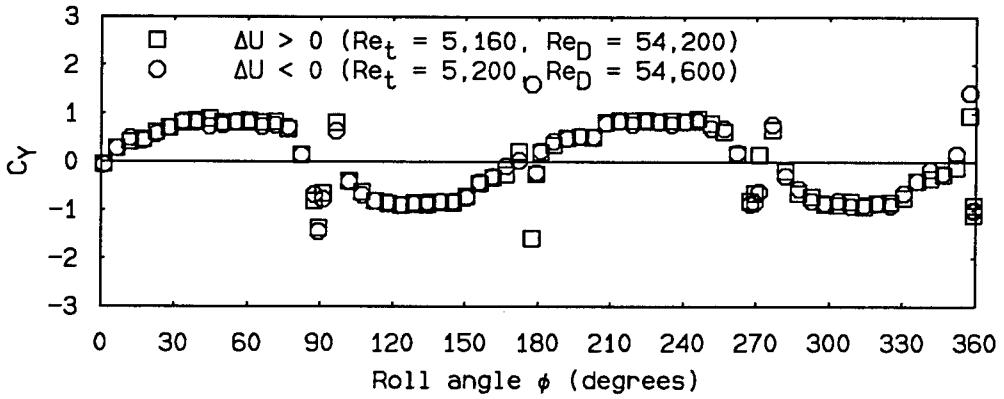

FIG. 5.19 Speed hysteresis check: large elliptic cross section tip, $\alpha/\theta_c = 9.9$, $\phi_0 = -0.7^o$, $s/D = 0.64$, $d/D = 0.51$ (small access hole)

The third reliability check was a set of tests to determine base or end effects. Three different end conditions were studied. These conditions are shown in Fig. 5.20. The first condition was obtained from the "fully-extended" configuration shown in

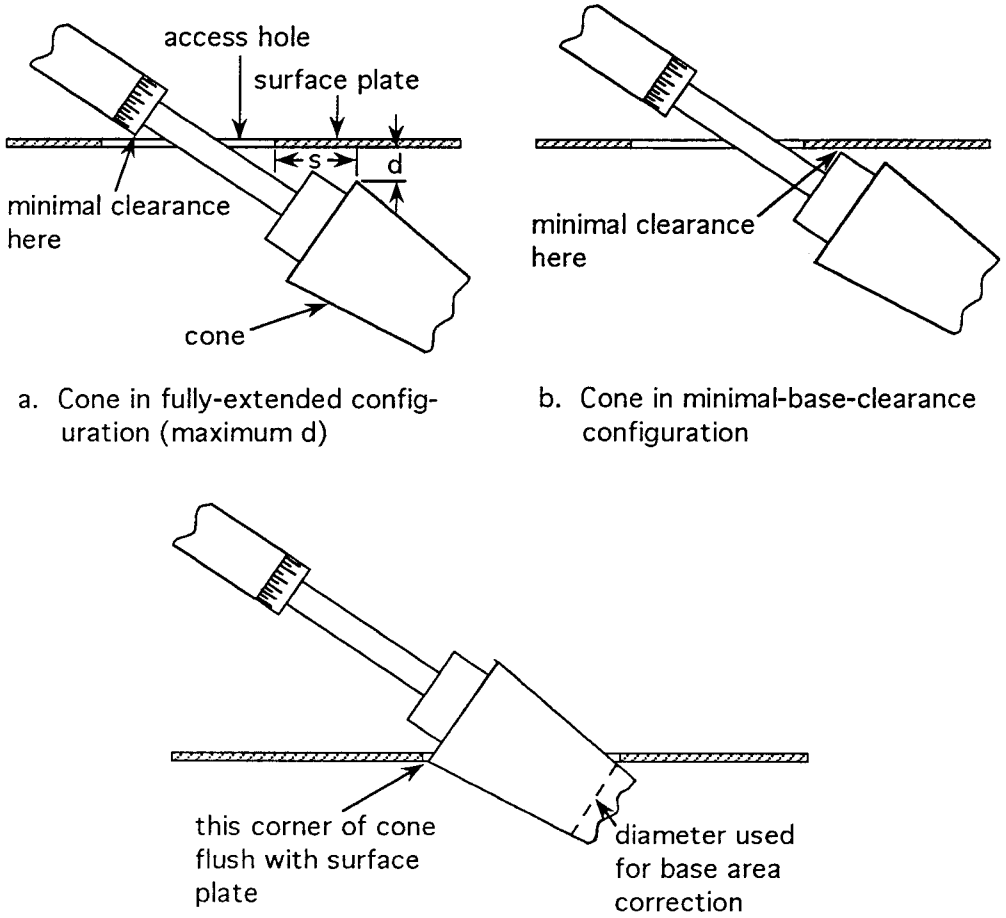

a. Cone in fully-extended configuration (maximum d)

b. Cone in minimal-base-clearance configuration

c. Cone in fully-retracted configuration

FIG. 5.20 End condition definitions

Fig. 5.20a. The cone was lowered until the roll angle indicator almost made contact with the upper surface of the surface plate. In this configuration, the cone was at the maximum depth in the water channel that could be achieved, and hence d attained its maximum value. The second condition was obtained from the "minimal base clearance" configuration shown in Fig. 5.20b. In this configuration, the cone was raised until the cone base or the cone attachment bolts just cleared the bottom surface of the surface plate. The third condition was obtained from the "fully-retracted" configuration shown in Fig. 5.20c. In this configuration, the cone was raised until none of the base of the cone was submerged in the channel. Each of

these three end conditions was tested with the large elliptic cross section tip at a nominal speed of 50 cm/sec and nominal angles of attack of 30°, 40°, and 50°.

The results of these tests are shown in Figs. 5.21 through 5.23. Two curves are shown in each figure for the fully-retracted configuration. The first curve is the side force coefficient computed with the actual cone base area. It was recognized that in the fully-retracted configuration, the area over which pressures could act to produce side force would be reduced. For this case, then, the side force was computed with the area based on the largest completely-submerged cone diameter, the diameter shown in Fig. 5.20c.

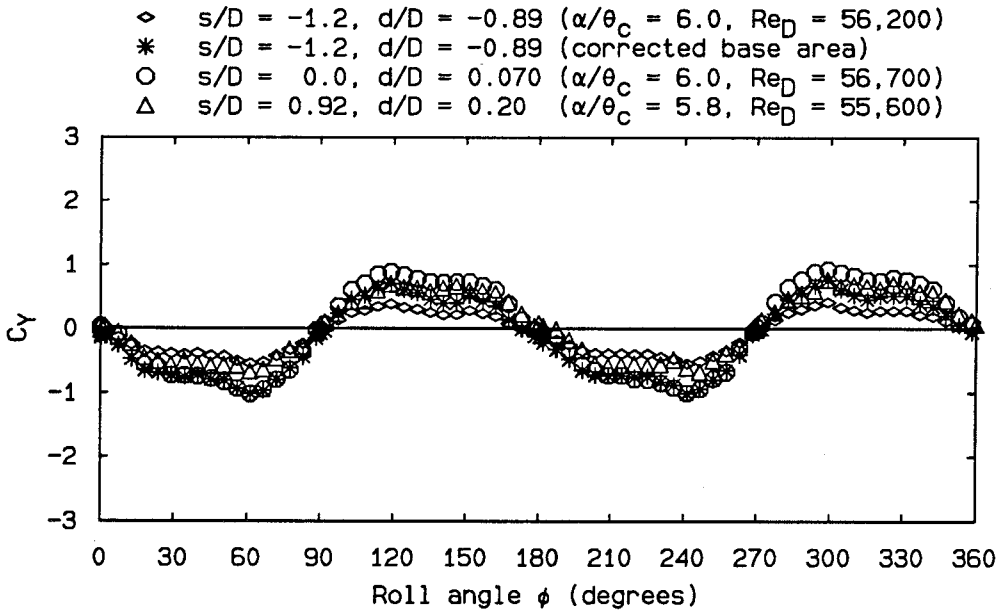

FIG. 5.21 End effects: large elliptic cross section tip, nominal $\alpha/\theta_c = 6$, nominal $Re_D = 56{,}000$; ◇ – fully-retracted configuration (large access hole); ∗ – fully-retracted configuration with base area correction (see text); o – minimal-base-clearance configuration (large access hole); △ – fully-extended configuration (small access hole)

These figures show that the end conditions had effects on the magnitude of the side force coefficients but not on the general shape of the ϕ–C_Y curves. It is also clear from these figures that the maximum uncorrected side force coefficients were obtained in the minimal-base-clearance configuration of Fig. 5.20b. For α/θ_c

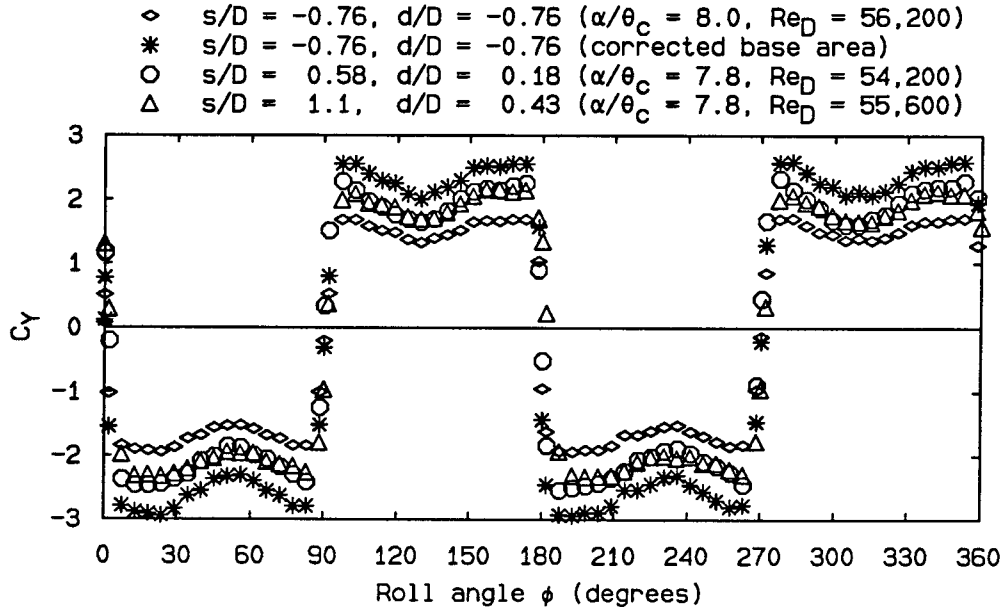

FIG. 5.22 End effects: large elliptic cross section tip, nominal $\alpha/\theta_c = 8$, nominal $Re_D = 55,000$ (see Fig. 5.21 for explanation of symbols)

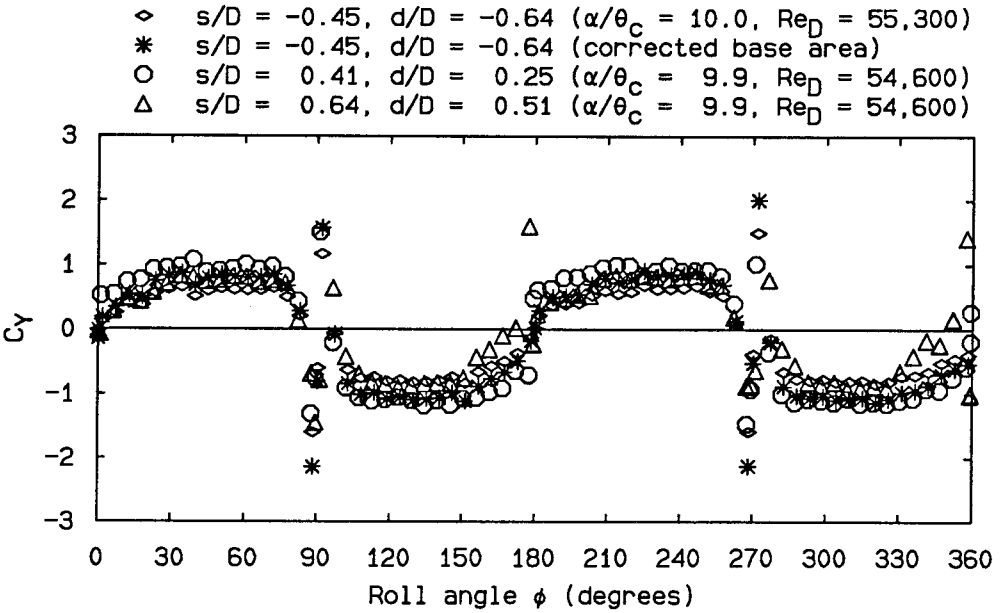

FIG. 5.23 End effects: large elliptic cross section tip, nominal $\alpha/\theta_c = 10$, nominal $Re_D = 55,000$ (see Fig. 5.21 for explanation of symbols)

nominally 6 and 10, the base area corrections brought the side force coefficients for the fully-retracted end condition essentially to the same magnitudes as for the the

minimal-base-clearance end condition. However, the base area correction caused the side force coefficients for the fully-retracted case to overshoot the coefficients for the minimial-base-clearance case for α/θ_c nominally 8. Why this happened is not clear. Since the minimal-base-clearance end condition gave the maximum uncorrected side force coefficients, it was used for the majority of the tests. The basic data shown in Figs. 5.8 through 5.17 were obtained in the minimal base clearance configuration.

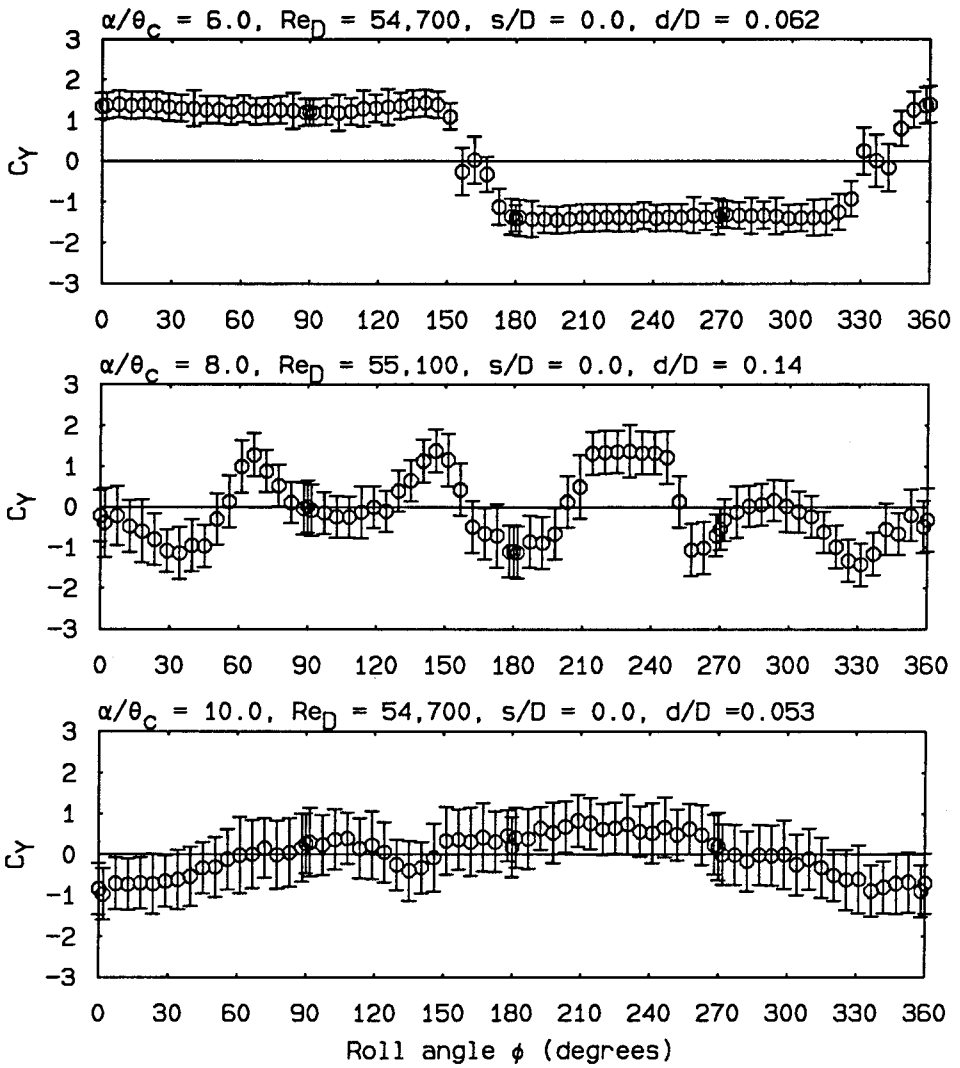

FIG. 5.24 Roll angle-side force characteristics: sharp conical tip, $\phi_0 = 0^o$ (nominally), large access hole

The fourth reliability check was a test using the cone with a sharp conical tip, in what could be considered the baseline configuration. These tests were conducted

to ensure that the behaviors discussed above were indeed caused by the elliptic cross section tips and not the cone model. The tests were conducted for nominal angles of attack of 30°, 40°, and 50°, and a nominal speed of 50 cm/sec. The results of these tests are shown in Fig. 5.24. This figure shows a wide range of behaviors as the angle of attack is increased. The results at $\alpha/\theta_c = 6.0$ seem to show a switch between two mirror image states, such as the switch discussed by Lamont and Hunt (1976). The results at $\alpha/\theta_c = 8.0$ show a greater variation of side force coefficient with roll angle, a variation that almost disappears at $\alpha/\theta_c = 10.0$. A comparison of this figure to Figs. 5.8 through 5.17 shows that the side force coefficient behavior caused by the elliptic cross section tips completely overrides the behavior caused by the cone and the sharp conical tip.

5.7.3 Reynolds number effects

As was stated previously, the basic data in Figs. 5.8 through 5.17 do not show large changes as the Reynolds number is varied. This weak dependence on Reynolds number is shown more directly in Figs. 5.25 through 5.29, which present Reynolds number effects for the large elliptic cross section tip. Note that both Re_t and Re_D values are given in each figure.

These figures do show a slight dependence of the magnitude of the side force coefficient on the Reynolds number. However, the overall trends do not seem to be very dependent on the Reynolds number. This could have been anticipated. The primary viscous effect in flows past bodies at high angle of attack is the circumferential location of the lines where the boundary layer separates from the surface of the body. This location is not a strong function of the Reynolds number for laminar separation. As is the case for the flow past a circular cylinder, the location of the separation line is primarily dependent upon the state of the boundary layer prior to separation. A laminar boundary layer will separate from the body at a smaller circumferential angle (measured from the most windward point on the body) than a turbulent boundary layer. Lamont (1980) shows the pressure distributions about an axisymmetric body (a tangent ogive nose on a cylindrical afterbody) for laminar

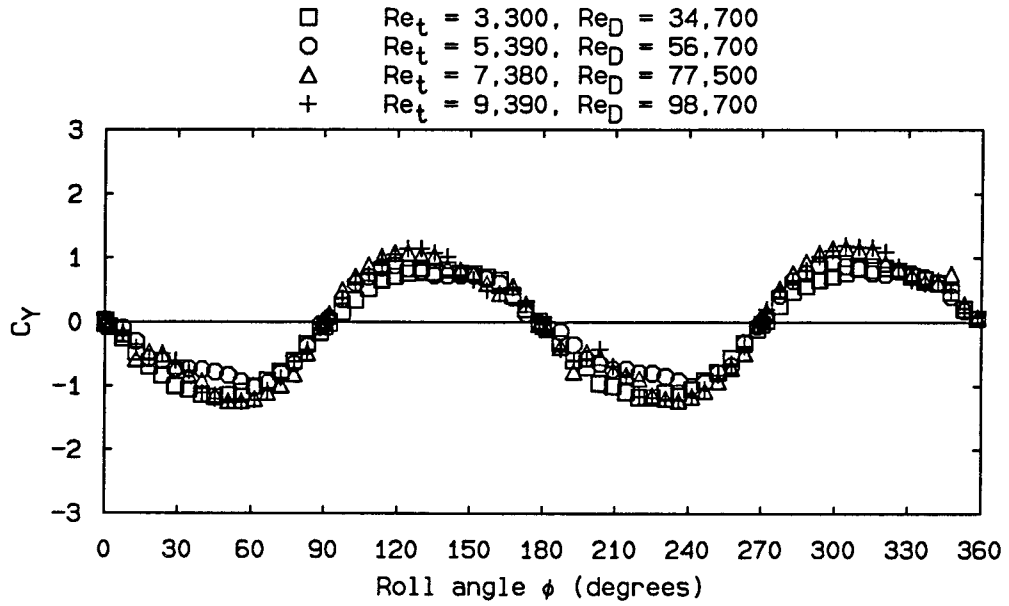

FIG. 5.25 Reynolds number effects: large elliptic cross section tip, $\alpha/\theta_c = 6.0$, $\phi_0 = 0.2^o$, $s/D = 0.0$, $d/D = 0.070$ (large access hole)

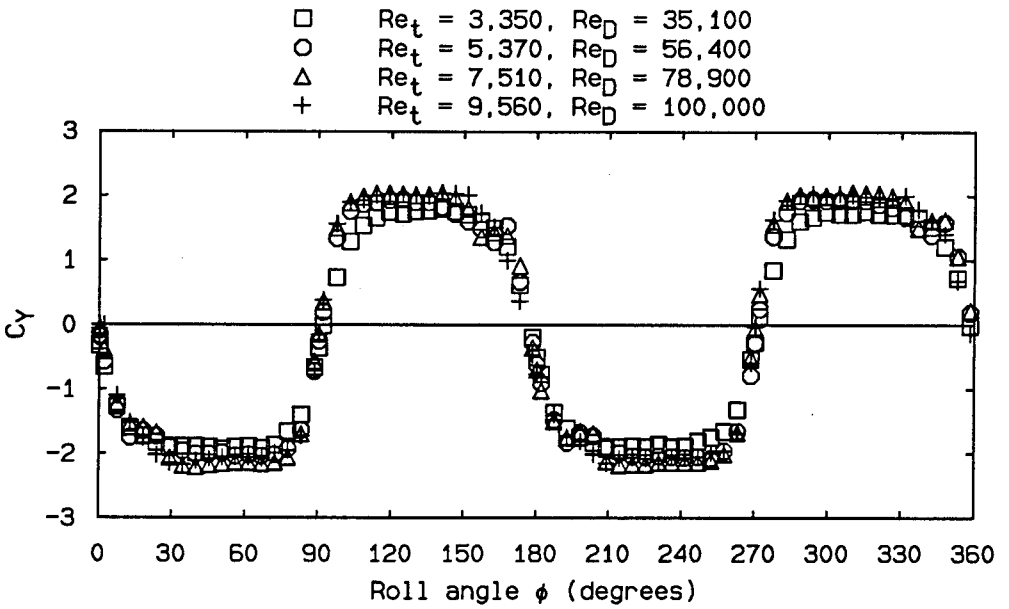

FIG. 5.26 Reynolds number effects: large elliptic cross section tip, $\alpha/\theta_c = 7.0$, $\phi_0 = 0.3^o$, $s/D = 0.66$, $d/D = 0.15$ (small access hole)

and turbulent separations. Each type of separation produces a distinctive circumferential pressure distribution that is very similar to the corresponding pressure

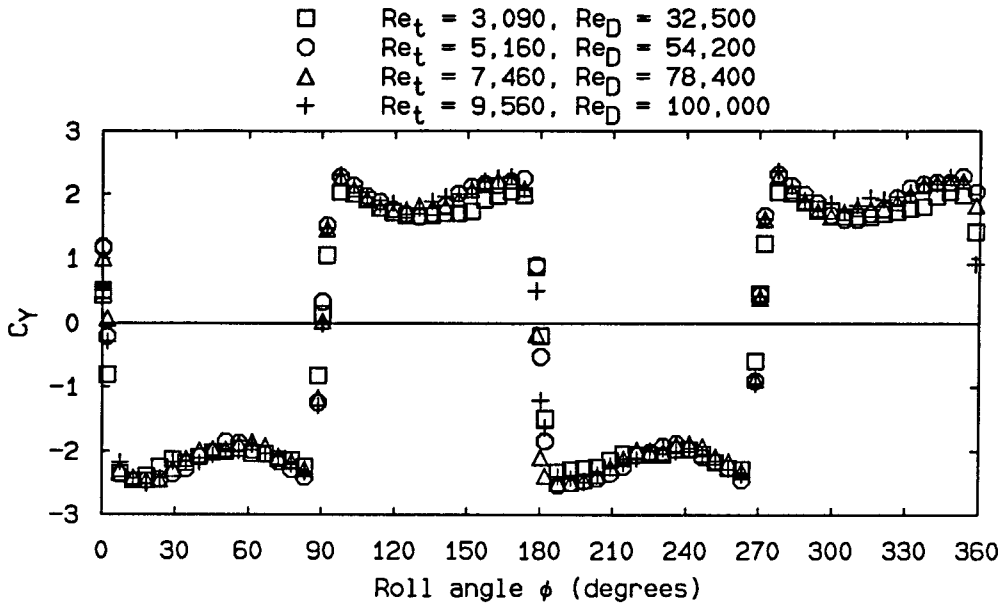

FIG. 5.27 Reynolds number effects: large elliptic cross section tip, $\alpha/\theta_c = 7.8$, $\phi_0 = 0.3^o$, $s/D = 0.58$, $d/D = 0.18$ (small access hole)

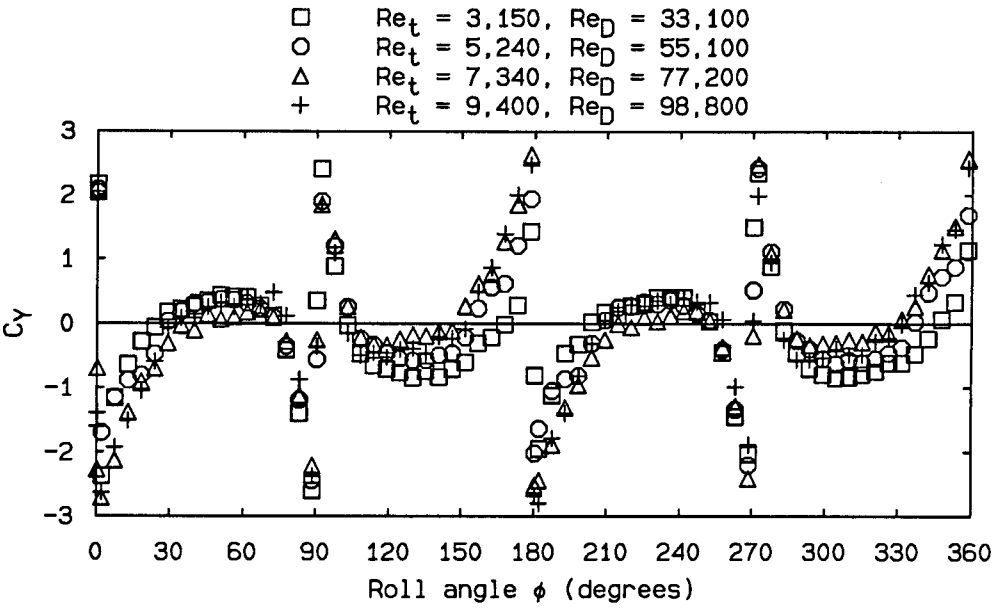

FIG. 5.28 Reynolds number effects: large elliptic cross section tip, $\alpha/\theta_c = 9.0$, $\phi_0 = 0.3^o$, $s/D = 0.46$, $d/D = 0.20$ (small access hole)

distribution on a circular cylinder in transverse flow. By using these pressure distributions, Lamont was able to establish the boundaries in Re_D–α/θ_c space where

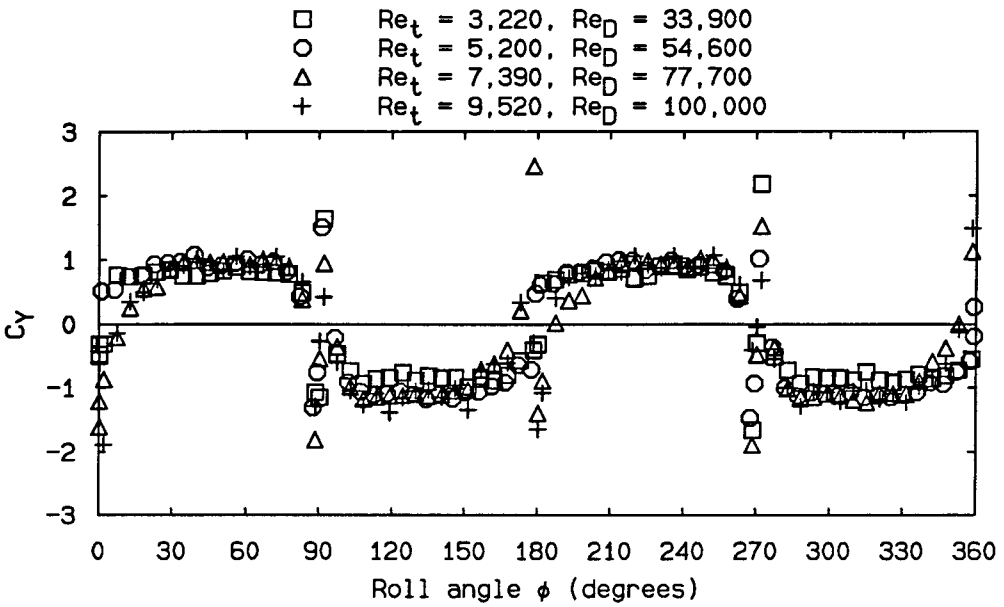

FIG. 5.29 Reynolds number effects: large elliptic cross section tip, $\alpha/\theta_c = 9.8$, $\phi_0 = 0.3^o$, $s/D = 0.41$, $d/D = 0.24$ (small access hole)

laminar, transitional, or turbulent separation would take place. Lamont concluded that the critical Re_D below which the separation would be laminar was on the order of 200,000 and essentially independent of angle of attack. The maximum value of Re_D studied in these experiments was 100,000. Since this is the Reynolds number based on the base diameter of the cone, the local Reynolds number along the cone was less than 100,000. Thus all of the conditions studied in these experiments should have resulted in laminar separations, according to the criterion established by Lamont. Since the separations were laminar, no major changes with Reynolds number should have been expected. The data indicate that this statement is correct.

The lack of Reynolds number dependence thus provides a cross-check on the data. The high-force-level results for the higher Reynolds numbers indicate that the low side forces and corresponding resolution difficulties did not seriously compromise the results for the mean side force coefficients at the lower Reynolds numbers. The similarities between the results also indicate that the unsteadiness and model oscillations that occurred at the higher Reynolds numbers also did not seriously

compromise the results.

One interesting Reynolds number effect was observed. As the Reynolds number increased, the differences between wake asymmetry as the tip rotated through the perpendicular plane symmetry condition ($\phi \in \{90^o, 270^o\}$) and through the coincident plane symmetry condition ($\phi \in \{0^o, 180^o\}$) became more pronounced. As the Reynolds number increased, the boundary layers would have become thinner, making the details of the tip shape at the end of the tip more effective in influencing the wake through viscous effects, and amplifying the changes in behavior between the two different tip rotations through the symmetry conditions. This trend isn't entirely consistent, as can be seen from a close examination of the figures. However, the thinning of the boundary layers and the resulting amplification of the differences in tip rotation through symmetry does help to explain why the Reynolds number data in Fig. 5.28, for example, collapses onto a single curve for $\phi = 90^o$ and 270^o more readily than at $\phi = 0^o$ or 180^o.

5.7.4 Angle of attack effects

Figure 5.30 shows the changes in the ϕ–C_Y curves for the large elliptic cross section tip as the angle of attack was increased, for a nominal speed of 50 cm/sec. For $\alpha/\theta_c = 6.0$, the side force coefficient varied more or less as a two-cycle sinusoid, the desired result. As the angle of attack increased, however, the side force coefficient behavior departed from the desired smooth variation with roll angle that was the aim of the elliptic cross section tip design. As α/θ_c increased from 6.0 to 7.0 to 7.8, the ϕ–C_Y curve approached a two-cycle square wave. Then, as α/θ_c increased further, to 9.0, C_Y began to exhibit reductions in magnitude between the magnitude peaks on either side of the zero crossings. Finally, at $\alpha/\theta_c = 9.8$, the side force was almost entirely the opposite sign from the side force at $\alpha/\theta_c = 6.0$, except near the zero crossings at the values of ϕ corresponding to the tip-flow symmetry conditions. In aircraft dynamics, this would be referred to as "control reversal." For higher angles of attack, the side force was essentially zero (see Fig. 5.13 for $\alpha/\theta_c = 11.8$), indicating that at this high angle of attack, the large elliptic cross

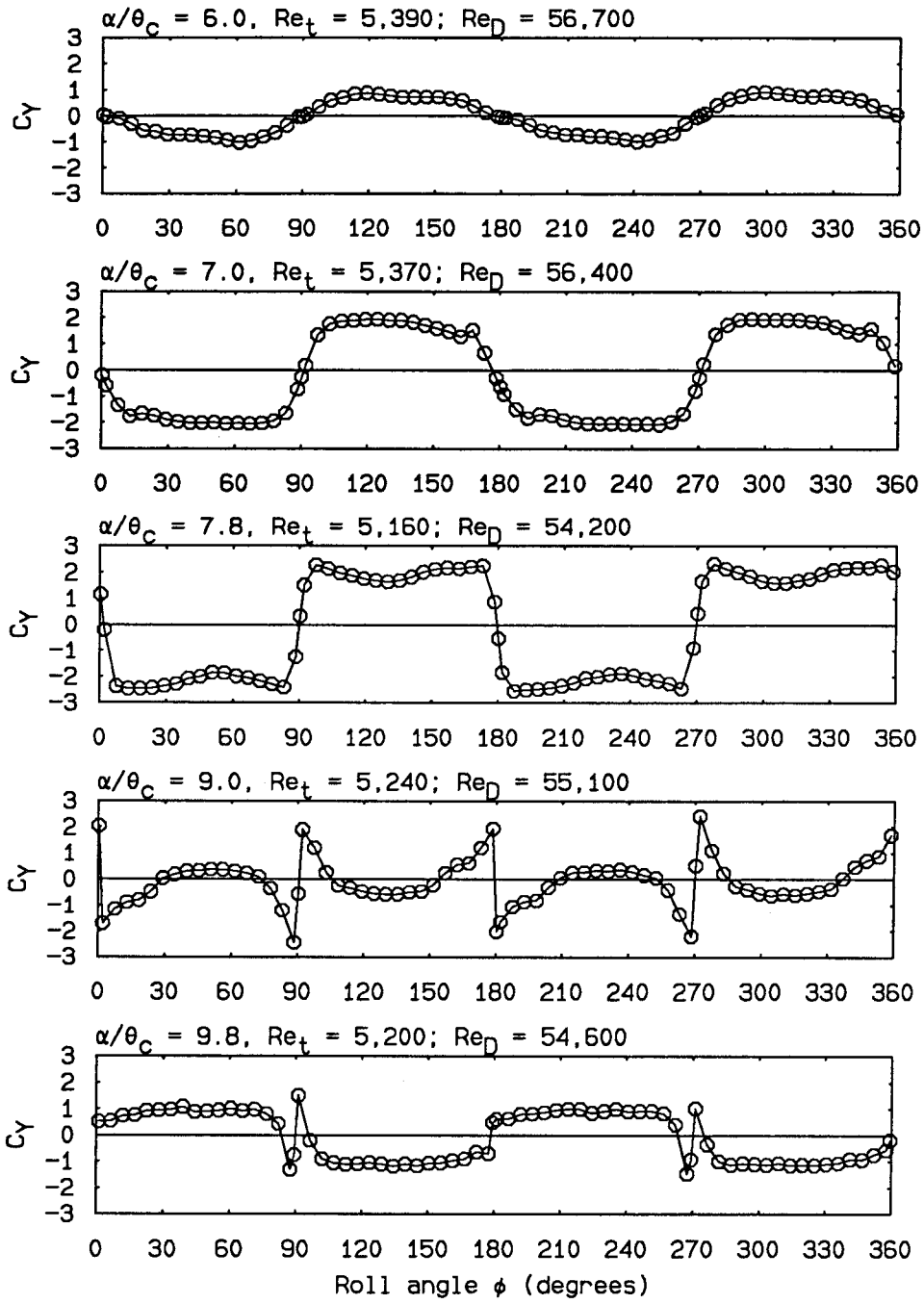

FIG. 5.30 Angle-of-attack effects: large elliptic cross section tip, nominal $U_\infty = 50$ cm/sec

section had lost its effectiveness. The reductions in magnitude of C_Y between the peaks on either side of the zero crossings were also noted by Zilliac *et al.* (1991) for their axisymmetric body at large angle of attack when they used a chisel tip. Such reductions can also be seen in the sectional side force coefficients of Moskovitz

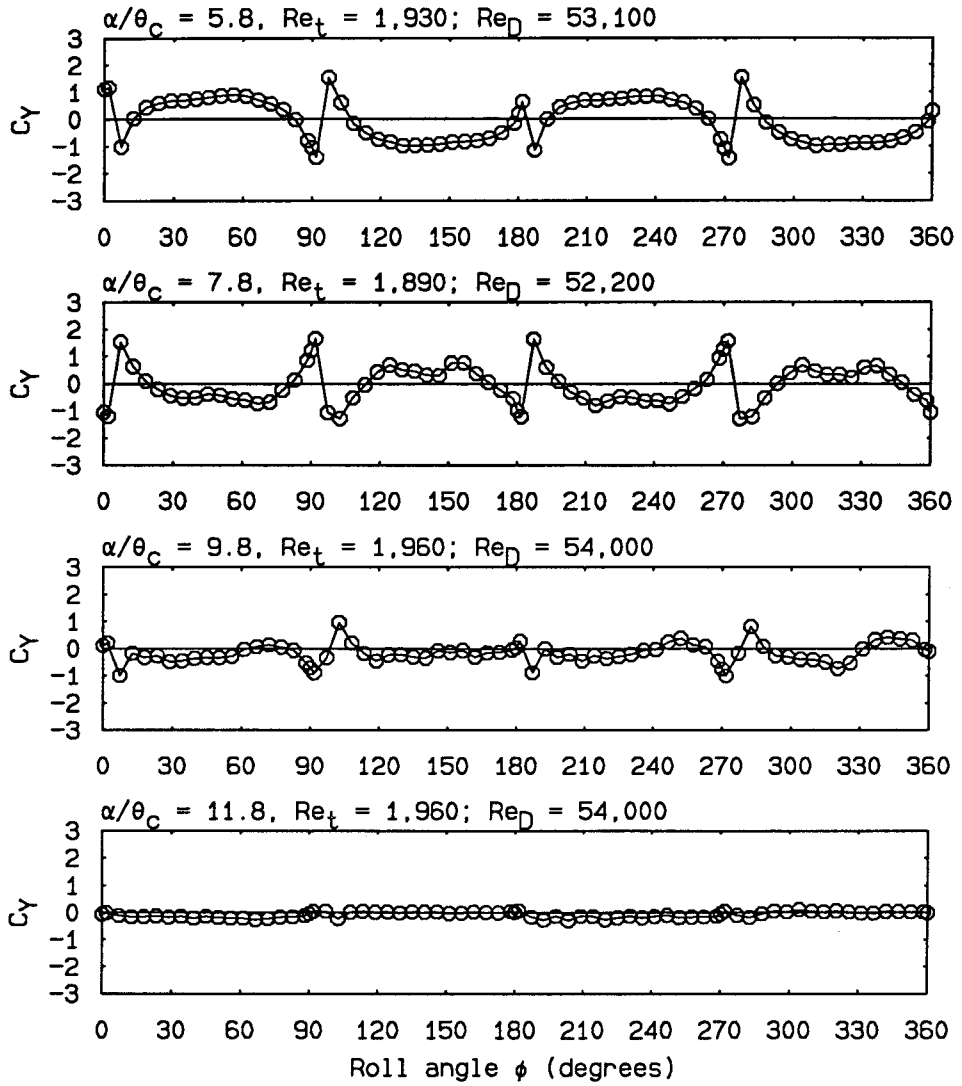

FIG. 5.31 Angle-of-attack effects: small elliptic cross section tip, nominal $U_\infty = 50$ cm/sec

(1989), in his tests with elliptic cross section tips.

Figure 5.31 shows the changes in the relation between roll angle and side force coefficient for the small elliptic cross section tip as the angle of attack was increased. For $\alpha/\theta_c = 6.0$, the lowest angle of attack studied with the small elliptic tip, the ϕ–C_Y curve demonstrates the control-reversal behavior demonstrated by the large elliptic tip for $\alpha/\theta_c = 9.0$ and 9.8. For $\alpha/\theta_c = 7.8$, the ϕ–C_Y curve is reversed from that at $\alpha/\theta_c = 5.8$. The reason for this reversal is unknown. At the two highest angles of attack, the side force has essentially disappeared. These results

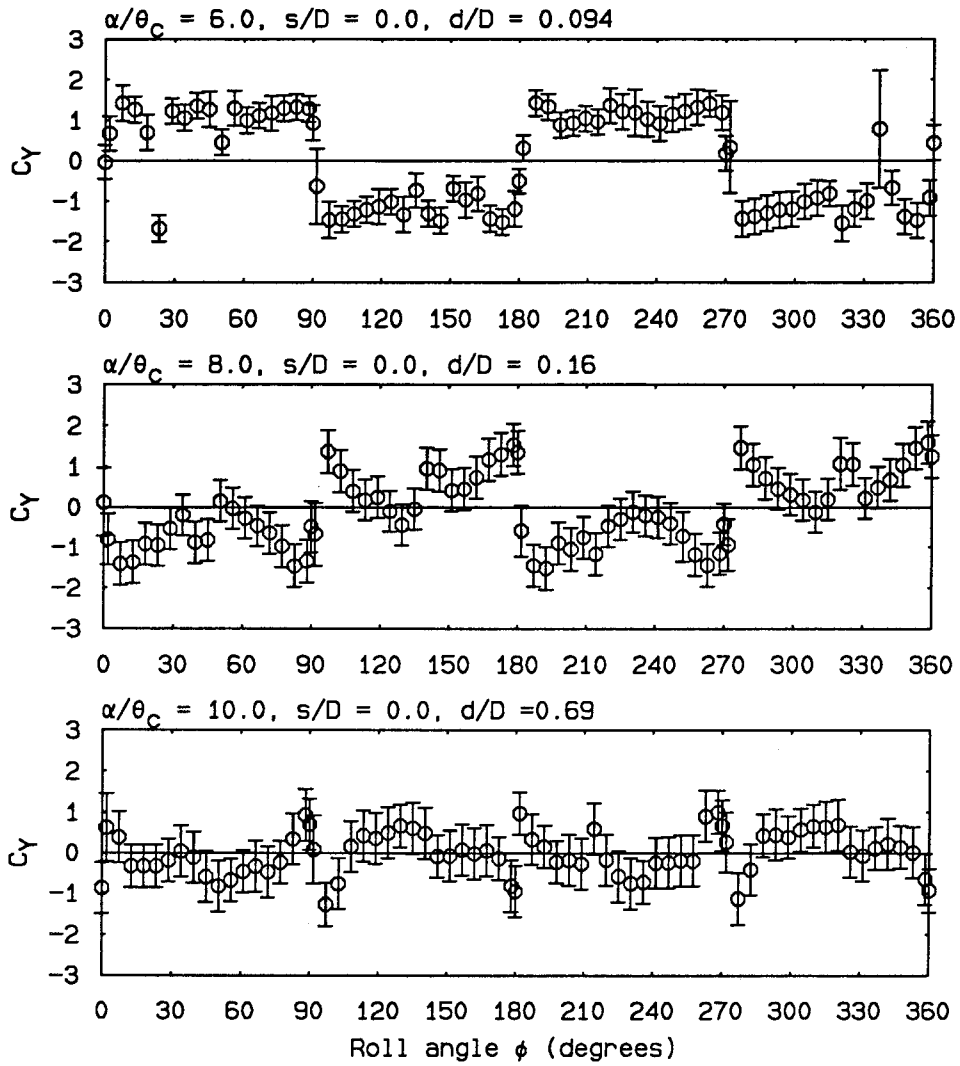

FIG. 5.32 Roll angle-side force characteristics: "chisel" tip, $\phi_0 = 0.0^o \pm 3.6^o$, $Re_D = 55,100$

are somewhat similar to the results obtained with the chisel tip, shown in Fig. 5.32. The similarities between these two figures indicate that the effectiveness of the small elliptic cross section tip in controlling the vortex wake asymmetry is not much greater than that of the chisel tip, probably as a result of the large flatness of the small elliptic tip.

5.8 Unsteady forces and the effects of disturbances

Lamont and Hunt (1976) observed variations in the sectional side force coefficients of a tangent ogive-cylindrical afterbody model with the body roll angle. The variations seemed to indicate that the vortex wake was "switching" between two mirror images. They postulated that free-stream turbulence and/or model vibrations were the source of these switches, and that if these effects were removed, the roll angle variations would disappear. The free-stream turbulence level in their facility was estimated to be 0.7%. Hunt and Dexter (1978) used the same model as Lamont and Hunt in a wind tunnel with a free-stream turbulence level of 0.01%. The model was very rigidly mounted to the tunnel. Hunt and Dexter observed a dramatic reduction in flow unsteadiness and the virtual elimination of vortex wake switching. The average pressure difference values used as a diagnostic matched the maximum sustained pressure difference values measured by Lamont and Hunt. Although much of the flow unsteadiness had been removed, some inherent unsteadiness remained, and the dependence on roll angle was still present. Hunt and Dexter concluded that high free-stream turbulence levels would contribute to high levels of flow unsteadiness and hence reduced values of the time-averaged pressures and forces on the body.

Howard *et al.* (1989) observed similar effects in tests on a missile configuration to determine the influence of varying levels of free-stream turbulence. Howard *et al.* added turbulence-generating to their wind tunnel to increase the turbulence levels, beginning at 0.23% for the tunnel without turbulence screens, and increasing to 0.53% and 2.14% as each of two screens were added to the tunnel. They observed a large reduction in mean side force coefficients when the turbulence level was increased from 0.23% to 0.53% and a smaller reduction when the turbulence level was increased from 0.53% to 2.14%. Their tests were conducted at $Re_D = 110,000$. Howard *et al.* attributed the first, larger reduction in side force coefficients to the movement of the boundary layers from laminar to transitional separation with the increase in free-stream turbulence. However, it seems that based on the results of

Hunt and Dexter (1978), the increase in free-stream turbulence might simply have increased the level of unsteadiness in the flow and hence decreased the magnitude of the time-averaged coefficients.

Ericsson (1990) discusses the effects of model oscillations on the results for the time-averaged side force coefficients on an axisymmetric body at large angle of attack. Ericsson suggests that the asymmetric flow separation is strongly coupled to the model motion through what are referred to as "moving wall" effects. These effects produce large lateral oscillations of the model which result in small values of the time-averaged side force coefficient, although instantaneous values of C_Y might be very large. Ericsson recommends that a rotary rig should be used in such experiments to allow the model to respond to the forces on it. The alternative approach recommended by Hunt and Dexter (1978) is the rigid mounting of the model in the tunnel. The model cannot be mounted too rigidly, however, if a force balance is being used, since the model must be allowed to deflect slightly for the balance to work. It would seem then that in this case, the best approach would be to monitor the instantaneous side forces in cases of high flow unsteadiness, to determine the maximum side forces acting on the model.

This discussion of flow unsteadiness and model oscillation effects has been included because under some test conditions, flow unsteadiness and model oscillations were observed. It was noted in Sec. 5.7.1 that the error bars in the figures were computed in part based on the RMS levels of the output voltages of the balance side force elements, so that large error bars for higher Reynolds numbers, where resolution was not a problem, indicate large flow unsteadiness. Examples of such error bars can be seen in Fig. 5.11 for $Re_t = 7,340$. For values of ϕ very close to 90^o and 270^o, the error bars are much larger than for other values of ϕ, indicating high flow unsteadiness at these ϕ. Also, this figure shows that the error bars drop rapidly in size for values of ϕ away from 90^o and 270^o. Large model oscillations were also observed at these ϕ for nominal speeds of 70 and 90 cm/sec for some angles of attack. In order to understand what was happening at these test conditions, time histories

of the side force coefficients for the large elliptic cross section tip were taken.

The output voltages of the balance-amplifier system were passed through a lowpass filter with the cutoff frequency set to 20 Hz. The computer was programmed to sample the output voltages at a rate of 40 Hz. The voltages were reduced to side force coefficients in the same manner as the time-averaged output voltages. Time histories of the side force coefficients were taken at nominal roll angles of 45^o and 90^o. Roll angles of 45^o corresponded to maximum values of the side force coefficient where the error bars were small. Roll angles of 90^o corresponded to zero crossings of the side force coefficient where the error bars were large. Time histories were taken at an angle of attack of 30^o ($\alpha/\theta_c = 6$), where the difference in size between the error bars at $\phi = 45^o$ and 90^o was in fact small, and at an angle of attack of 50^o ($\alpha/\theta_c = 10$), where the difference in size between the error bars at $\phi = 45^o$ and 90^o was large. The tests were conducted at a nominal speed of 50 cm/sec.

The results of these tests are shown in Figs. 5.33 and 5.34. Included in each figure is the corresponding roll angle-side force characteristic for each test condition, with an indication on each characteristic as to where the time histories were taken. The abscissa in each figure is actual time normalized by the axial flow period $L/U_\infty \cos\alpha$. The dashed line in each figure indicates the value of the side force coefficient averaged over the time shown in the figure. Figure 5.33 compares the time histories between the two ϕ of 44.5^o and 89.5^o for $\alpha/\theta_c = 6.0$. Just as the difference in the error bars at these two ϕ were small, so were the differences in the fluctuations of the side force coefficient at these two ϕ small. Figure 5.34 shows that the results were much different for $\alpha/\theta_c = 10.0$. For $\phi = 44.5^o$, the fluctuations were small, corresponding to the small error bars on the time-averaged value. However, at $\phi = 91.3^o$, this figure shows that C_Y experienced large fluctuations in time, and that the resulting time-averaged value was very small. These large fluctuations in side force coefficient between equal and opposite values are reminiscent of the switching between mirror-image states observed by Lamont and Hunt (1976). It is not believed that these fluctuations were the result of Kárman-like vortex shedding

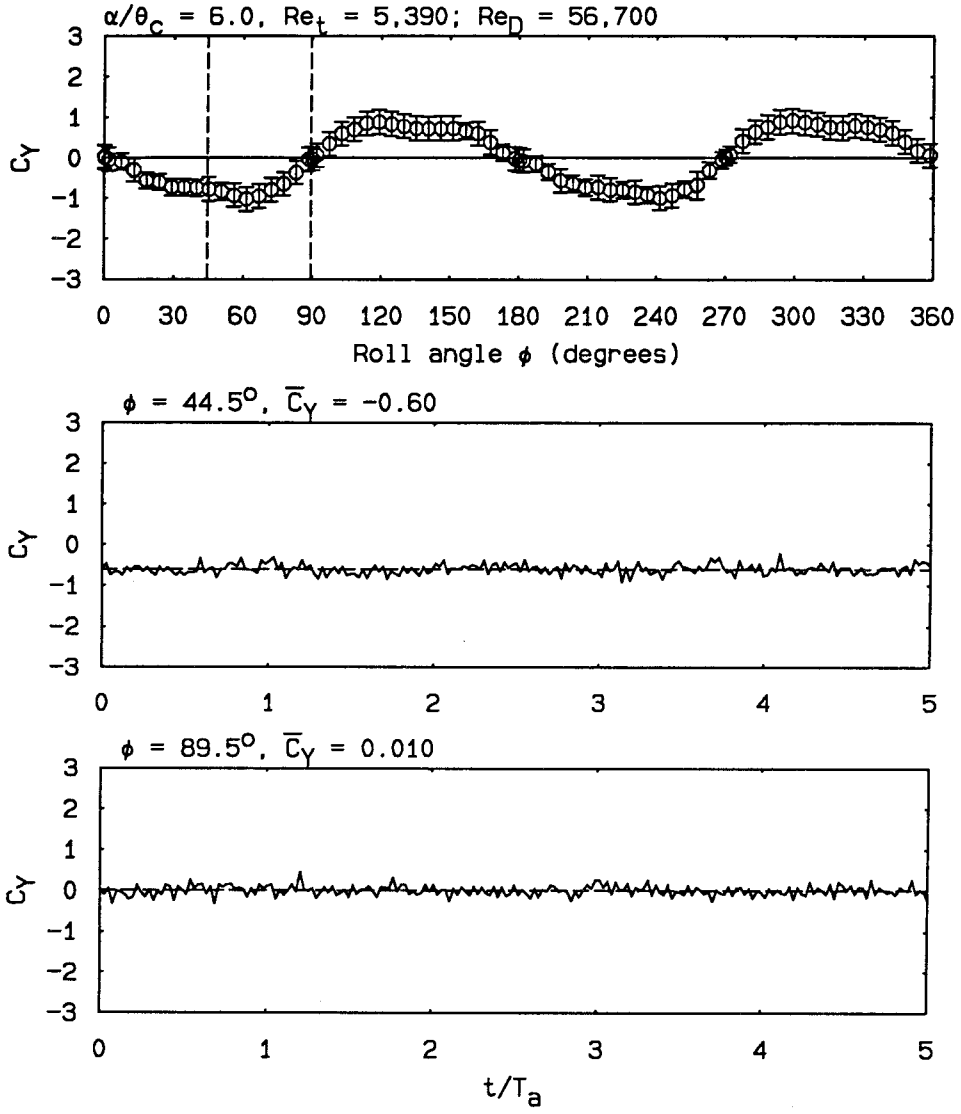

FIG. 5.33 Unsteady forces: large elliptic cross section tip, $\alpha/\theta_c = 6.0$, $Re_t = 5,450$, $Re_D = 57,200$, $T_a = 1.02$ sec, $s/D = 0.0$, $d/D = 0.069$ (large access hole)

(which would have had a higher frequency). Apparently the flow at this tip-flow symmetry condition (the perpendicular plane symmetry condition) and this angle of attack was very sensitive to disturbances. Time histories taken for a nominal speed of 70 cm/sec gave very similar results. The results described here are similar to those obtained by Lamont and Hunt (1976) and Yanta and Wardlaw (1981). These researchers found small fluctuations at conditions where the side force was large, and large fluctuations at conditions where the (mean) side force was small,

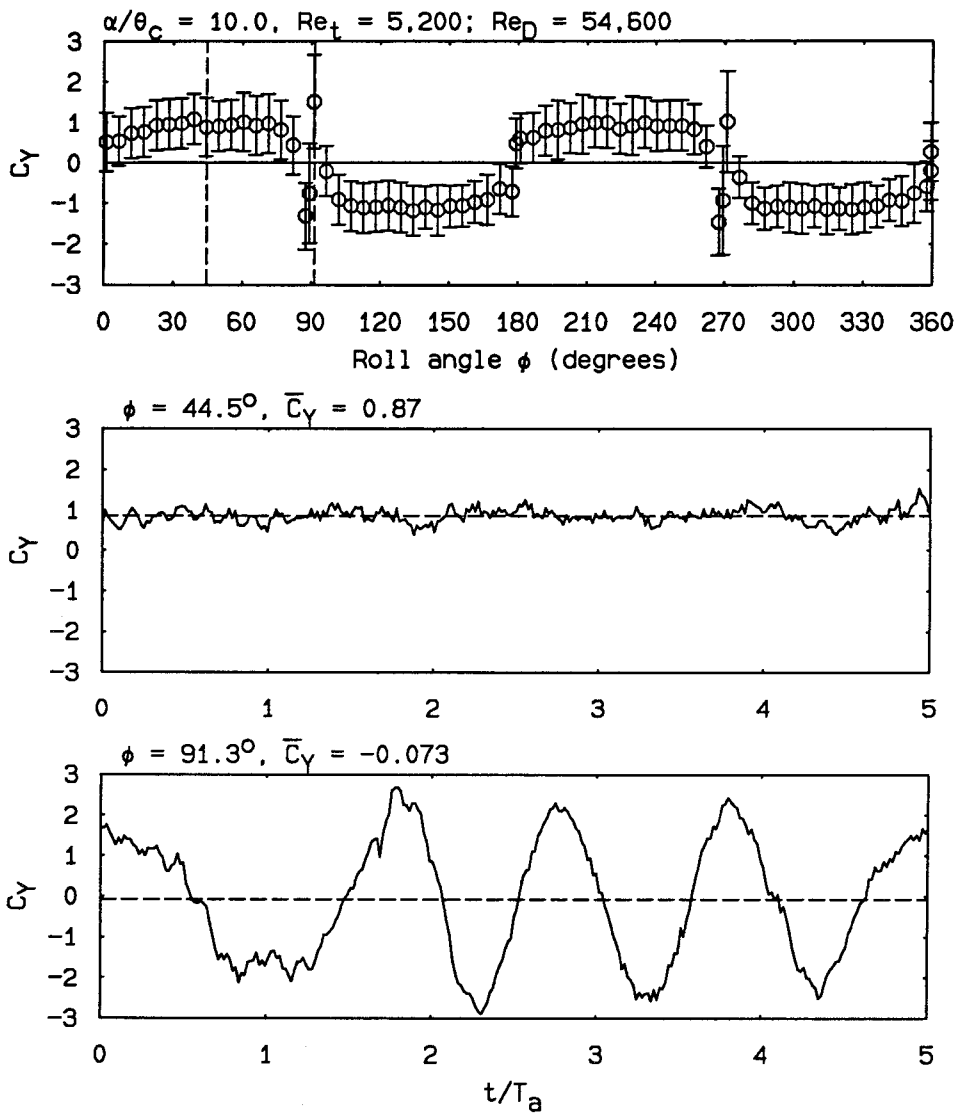

FIG. 5.34 Unsteady forces: large elliptic cross section tip, $\alpha/\theta_c = 10.0$, $Re_t = 5,300$, $Re_D = 55,700$, $T_a = 1.41$ sec, $s/D = 0.41$, $d/D = 0.24$ (small access hole)

for nominally axisymmetric bodies at large angle of attack.

No time histories were taken at the coincident plane symmetry condition ($\phi \in \{0^o, 180^o\}$). However, figures such as Fig. 5.11 show that the error bars near these ϕ were small, indicating that the flow at these ϕ were steadier. Figures 5.8 through 5.13 also indicate by the size of the error bars that the unstable flow at the perpendicular plane symmetry condition only occurred for $\alpha/\theta_c > 8.0$.

In order to make sure that these time histories were not reflecting model and sting oscillations at some natural frequency of the model-sting combination, a test of the natural frequency of the model-sting combination was conducted. The value of α/θ_c was set to 10.0, the speed was set to 50 cm/sec, and the roll angle was set to 44.2^o. Then, the model was displaced to one side by hand and released, and the resulting balance output voltages were measured as a function of time. These voltage fluctuations are not shown here because the sampling frequency of the computer data acquisition system had not been set to a high enough value to completely capture the model-sting oscillations. However, it was very obvious that the model-sting natural frequency was much higher than that of the fluctuations in the figures above, indicating that these fluctuations were the result of fluid-dynamical processes.

All of these results taken as a whole indicate that the only conditions for which flow unsteadiness and model oscillation might have had a compromising effect on the data were the ϕ corresponding to the perpendicular plane symmetry condition for $\alpha/\theta_c > 8.0$. The time histories show that at these conditions, the time-averaged side force coefficients do not represent the actual side forces acting on the cone. However, the large differences in magnitude and frequency between the small and large fluctuations in side force coefficient suggest that the small fluctuations were caused by the unsteadiness inherent in the flow, as documented by Hunt and Dexter (1978). This result indicates that the FSWT free-stream turbulence level, quoted by Ward (1976) to be 0.38% at a free-stream speed of 4.57 m/sec (and hence probably smaller at the speeds covered in these experiments, which were all less than 1 m/sec) was sufficiently low to measure accurately the time-averaged side forces on the cone, at least away from the very sensitive flows at the perpendicular plane symmetry conditions. Similarly, model oscillations also apparently were not a major factor in the measurement of the side force coefficients.

CHAPTER 6

Vortex wake geometry studies

6.1 Introduction

Contrary to the indications given by the results in Ch. 4, the side force coefficient did not vary smoothly with elliptic cross section tip roll angle, as shown by the results in Ch. 5. The reasons for this contradiction were unclear, so a more extensive flow visualization investigation of the vortex wake geometry was undertaken. These experiments are discussed in this chapter.

6.2 Model, apparatus, and procedure

The basic model used in these experiments was the 5^o right circular cone described in Sec. 2.2.2 and shown in Fig. 2.3. Since the large elliptic cross section tip exhibited a wider range of side force behavior as the angle of attack was varied, only this tip was used in the experiments. The cone was attached to the sting mechanism described in Sec. 5.2.3 and shown in Fig. 5.2 (without the force balance). The experiments were conducted using the same facility, apparatus, and procedure described in Ch. 4, with a slight modification to the video image recording apparatus. This modification, shown in Fig. 6.1, consisted of a mirror suspended vertically from a shaft and rotated at 45^o to the free-stream direction. The estimated accuracy of the mirror alignment was $\pm 1^o$. The mirror was approximately 1.8 cone base diameters high, 1.5 cone base diameters wide, and was always located at least 5 cone base diameters downstream of the cone base, to minimize interference with the vortex wake. The video camera was moved from underneath the test section to beside the test section, where it was aligned perpendicular to the test section wall

with an estimated accuracy of $\pm 1^o$. The maximum angle of attack that could be studied was still limited to 45^o because of the space limitations on the laser sheet optics underneath the channel test section (the laser sheet optics were omitted from Fig. 6.1 for clarity; see Fig. 4.1). A linear optical encoder mounted on the traverse was used to track the axial location of the laser sheet with respect to the cone with an accuracy of ± 0.01 mm.

Three angles of attack, corresponding to $\alpha/\theta_c = 6$, 8, and 9, were studied using the large elliptic cross section tip. During the initial flow visualization experiments discussed in Ch. 4, it was discovered that the optimal speed range for laser sheet visualization of the vortex wake was 10 cm/sec $\leq U_\infty \leq$ 20 cm/sec. At 10 cm/sec, the flow was steady and well-established, thus providing excellent flow visualization. At 20 cm/sec, the flow was beginning to become unsteady, particularly towards the rear of the cone. Also, rapid dye diffusion began to be a problem. Therefore, in these experiments the primary speed used was 15 cm/sec. A complete roll angle sweep ($0^o \leq \phi \leq 360^o$) was performed at this speed with the laser sheet located at a particular row of dye injection holes, with a 9^o change between each ϕ. Then, a partial roll angle sweep ($45^o \leq \phi \leq 135^o$) was performed at 10 cm/sec and at 20 cm/sec with the laser sheet located at this row and one other row, either forward or aft of the complete sweep row. The partial roll angle sweep corresponded to the transition from the first maximum-asymmetry flow condition through a symmetric flow condition to the second maximum-asymmetry flow condition.

The same data reduction procedure as described in Sec. 4.3 was used in these experiments. The reduction in alignment accuracy from $\pm 0.1^o$ in Ch. 4 to $\pm 1^o$ as mentioned above led to greater difficulties in reducing the data, particularly in fitting the ellipse equation to the apparent cone cross section in the figure. The estimated error in the resulting vortex locations was between 5% and 10%. However, since the goal of these experiments was primarily to investigate qualitative vortex wake variations with tip roll angle as speed and angle of attack were varied, the data were deemed sufficiently accurate for the purposes of the investigation. No error

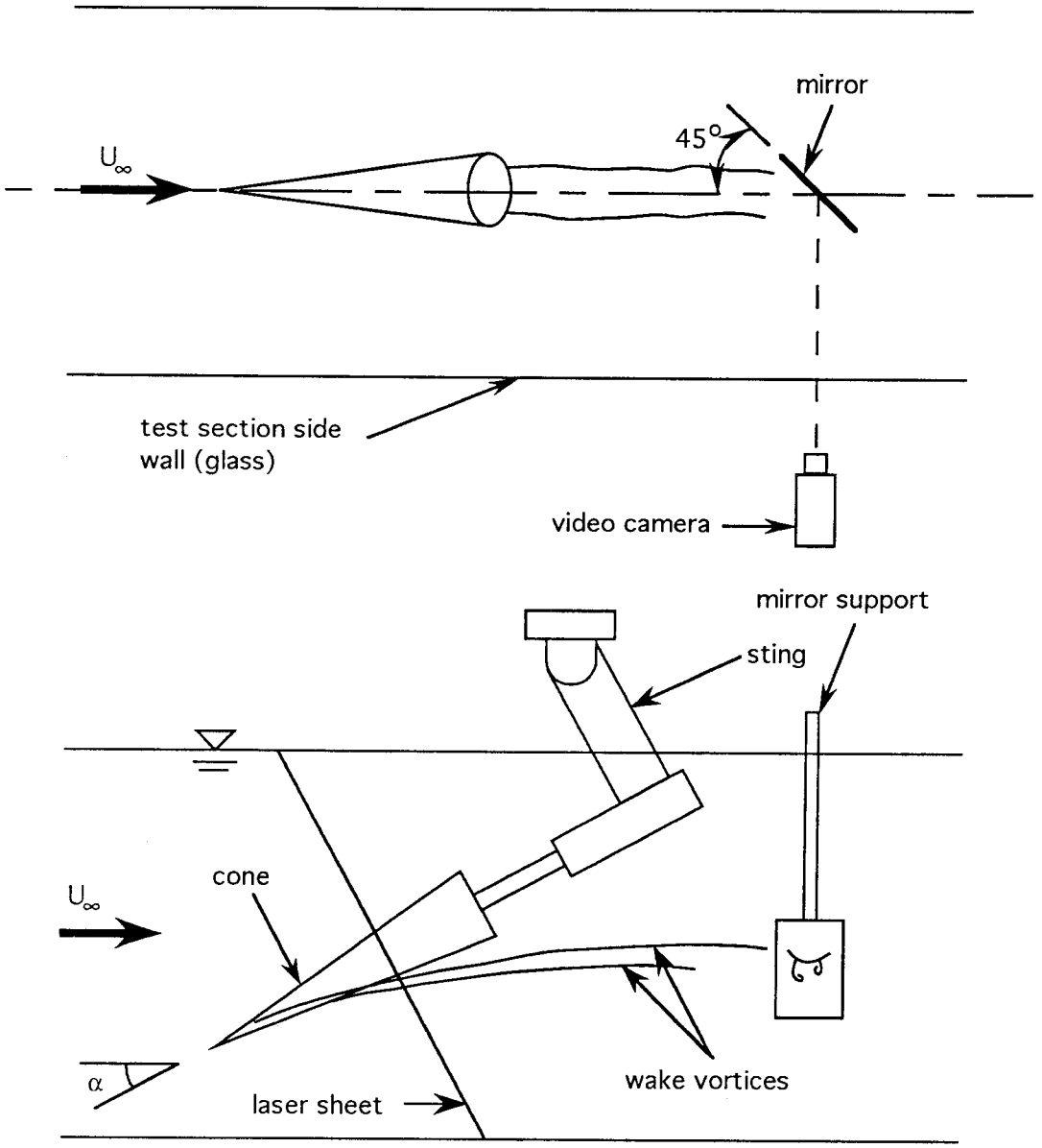

FIG. 6.1 Schematic of apparatus for vortex wake flow visualization experiments with modifications to mirror and camera locations (laser sheet optics omitted for clarity; see Fig. 4.1)

bars appear in the figures, for purposes of clarity. As will be seen from the results, the qualitative changes in the vortex wake as speed and angle of attack varied were quite large.

6.3 Estimated side force calculation

In order to obtain an idea of how changes in the vortex wake geometry might affect the side force on the cone, the side force on a circular cylinder in potential flow with two vortices placed at arbitrary locations behind the cylinder was calculated. The resulting sectional side force was then integrated over the cone to give the side force on the body. The vortex locations measured from the experiments and an estimate of the vortex strengths were used in the resulting formula for side force coefficient.

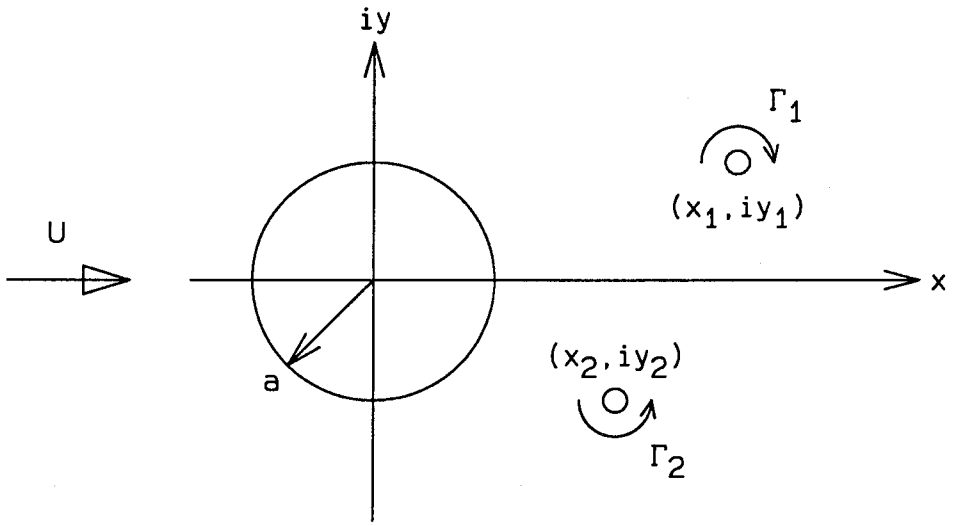

FIG. 6.2 Potential flow calculation definitions

The flow situation for the potential flow calculations is shown in Fig. 6.2. A circular cylinder of radius a is placed in a cross flow of velocity U in the positive x direction. Two vortices of strengths Γ_1 and Γ_2 are placed at (x_1, iy_1) and (x_2, iy_2) in the flow field. The complex potential for this flow is given by

$$W = U\left(z + \frac{a^2}{z}\right) + \frac{i\Gamma_1}{2\pi}\left[-\log(z - z_1) + \log\left(z - \frac{a^2}{z_1^*}\right) - \log z\right] + \frac{i\Gamma_2}{2\pi}\left[-\log(z - z_2) + \log\left(z - \frac{a^2}{z_2^*}\right) - \log z\right], \tag{6.3.1}$$

where $i = \sqrt{-1}$, $z = x + iy$, $z_j = x_j + iy_j$, $(j = 1, 2)$, and z_1^* and z_2^* are the complex conjugates of z_1 and z_2, respectively (Milne-Thomson 1968). The corresponding complex velocity is given by

$$\begin{aligned}\frac{\mathrm{d}W}{\mathrm{d}z} = u - iv = U\left(1 - \frac{a^2}{z^2}\right) + \frac{i\Gamma_1}{2\pi}\left(\frac{-1}{z - z_1} + \frac{1}{z - \frac{a^2}{z_1^*}} - \frac{1}{z}\right) \\ + \frac{i\Gamma_2}{2\pi}\left(\frac{-1}{z - z_2} + \frac{1}{z - \frac{a^2}{z_2^*}} - \frac{1}{z}\right),\end{aligned} \tag{6.3.2}$$

where u and v are the x and y components of the velocity, respectively. The Blasius formula for the forces on a body in a potential flow field is given by

$$X - iY = \frac{i\rho}{2}\oint_C \left(\frac{\mathrm{d}W}{\mathrm{d}z}\right)^2 dz, \tag{6.3.3}$$

where X and Y are the forces in the x and y directions, respectively, and C is any closed contour surrounding the body (Milne-Thomson 1968, p. 173). In this case, the contour chosen was the body contour given by $z = ae^{i\theta}$, $0 \le \theta < 2\pi$. Squaring the expression for the velocity given by Eq. 6.3.2 and then integrating using partial fraction expansions and the method of residues gives the result

$$\begin{aligned}\frac{1}{\rho}(X - iY) =& iU\Gamma_1\frac{a^2}{z_1^2} + iU\Gamma_2\frac{a^2}{z_2^2} + \frac{\Gamma_1^2}{2\pi a}\frac{1}{\frac{z_1}{a} - \frac{a}{z_1^*}} + \frac{\Gamma_2^2}{2\pi a}\frac{1}{\frac{z_2}{a} - \frac{a}{z_2^*}} \\ &- \left(\frac{\Gamma_1\Gamma_2 + \Gamma_1^2}{2\pi a}\right)\frac{a}{z_1} - \left(\frac{\Gamma_1\Gamma_2 + \Gamma_2^2}{2\pi a}\right)\frac{a}{z_2} \\ &- \frac{\Gamma_1\Gamma_2}{2\pi a}\left(\frac{1}{\frac{a}{z_1^*} - \frac{z_2}{a}} + \frac{1}{\frac{a}{z_2^*} - \frac{z_1}{a}}\right).\end{aligned} \tag{6.3.4}$$

If z, z_1, z_1^*, z_2, and z_2^* are nondimensionalized by a, Γ_1 and Γ_2 are nondimensionalized by $2\pi aU$, and the forces X and Y are nondimensionalized by $\frac{1}{2}\rho U^2 a$, then Eq. 6.3.4 yields for the nondimensional sectional force coefficients C_x and C_y

$$\begin{aligned}\frac{1}{4\pi}(C_x - iC_y) =& \frac{i\gamma_1}{z_1^2} + \frac{i\gamma_2}{z_2^2} + \gamma_1^2\frac{z_1^*}{z_1 z_1^* - 1} + \gamma_2^2\frac{z_2^*}{z_2 z_2^* - 1} \\ &- (\gamma_1\gamma_2 + \gamma_1^2)\frac{1}{z_1} - (\gamma_1\gamma_2 + \gamma_2^2)\frac{1}{z_2} \\ &- \gamma_1\gamma_2\left(\frac{z_1^*}{1 - z_2 z_1^*} + \frac{z_2^*}{1 - z_1 z_2^*}\right).\end{aligned} \tag{6.3.5}$$

Here, z, z_1, z_1^*, z_2, and z_2^* are now used to denote *nondimensional* values, and γ_1 and γ_2 are the nondimensional vortex strengths. The correctness of Eq. 6.3.5 was confirmed by numerically integrating around the cylinder the pressure distribution obtained from the velocities given by Eq. 6.3.2 for a few test cases.

Equation 6.3.5 gives the force coefficients per unit length (or the sectional force coefficients) on a circular cylinder in cross flow. In order to obtain the total force on the cone, the sectional force coefficients must be integrated over the cone. Before this is done, a modification of the coordinate system is in order. First, the body will be assumed to be completely conical; the details of the elliptic cross section tip shape will be ignored. Let the origin of the coordinate system be at the tip of the cone. Let the z axis be directed along the axis of the cone, with z increasing toward the base of the cone. Let x and y as in Fig. 6.2 be measured from the centerline of the cone. Note that the definitions of the variables x and y remain the same, while the variable z can now refer to either the complex number $x + iy$ or the cone axial coordinate. The appropriate definition of the variable z will be made clear by the context. Let the x and y axes be rotated 180°, so that y is positive to the right when viewed from the base of the cone (as in Sec. 4.3 and Fig. 4.2). This means that the sign of C_y in Eq. 6.3.5 must be reversed in order to match the results of Ch. 5. In these coordinates, x is positive down in Fig. 4.2. This somewhat odd choice of coordinates was made so that the side force would be positive to the right in the pilot's eye view of Fig. 4.2, z would be zero at the body tip and increasing toward the body base, and the entire coordinate system would be right-handed. One result of this choice of coordinates is that positive roll angle ϕ as defined throughout this study now corresponds to a negative rotation about the cone z axis, according to the right-hand rule.

In an inviscid flow, and in the absence of any body forces, the force on a solid body is given by

$$\mathbf{F} = -\oint_S p\,\mathbf{n}\,dS, \tag{6.3.6}$$

where $\mathbf{F}$ is the vector force on the body, p is the pressure distribution on the body, and $\mathbf{n}$ is the unit normal on the body surface, directed outwards from the body. For the coordinate system and body shape described above, this expression reduces to

$$Y = -\int_0^L \int_0^{2\pi} p \sin\theta \, a(z) \, d\theta dz \tag{6.3.7}$$

for the side force on the cone, where θ is the circumferential angle coordinate, z is the cone axial coordinate, L is the cone length, and $a(z)$ is the cone radius as a function of z (in this case, $a = z\tan\theta_c$). The base is ignored because it has no area facing the sides over which pressure could act to contribute to the side force. Note that the integral $\int_0^{2\pi} p \sin\theta \, a(z) \, d\theta$ is simply the sectional side force on the cone. This was obtained in Eq. 6.3.5 from the complex velocity field given by Eq. 6.3.2 and the Blasius formula (Eq. 6.3.3), so that Eq. 6.3.7 can be expressed as

$$Y = \int_0^L C_y \frac{1}{2}\rho U^2 \, a(z) \, dz. \tag{6.3.8}$$

Note that Eq. 6.3.2 can be expressed as

$$\begin{aligned} \frac{dW}{dz} = U\Bigg[1 - \left(\frac{a}{z}\right)^2 &+ \frac{i\Gamma_1}{2\pi U a}\left(\frac{-1}{\frac{z}{a} - \frac{z_1}{a}} + \frac{1}{\frac{z}{a} - \frac{a}{z_1^*}} - \frac{1}{\frac{z}{a}}\right) \\ &+ \frac{i\Gamma_2}{2\pi U a}\left(\frac{-1}{\frac{z}{a} - \frac{z_2}{a}} + \frac{1}{\frac{z}{a} - \frac{a}{z_2^*}} - \frac{1}{\frac{z}{a}}\right)\Bigg] \end{aligned} \tag{6.3.9}$$

or

$$\frac{dW}{dz} = U w'\left(\frac{z}{a}; \frac{z_1}{a}, \frac{z_2}{a}, \gamma_1, \gamma_2\right). \tag{6.3.10}$$

If conical flow is assumed, then z_1/a and z_2/a and their complex conjugates are independent of the cone axial coordinate z. In this equation, $z = re^{i\theta}$ is the variable of integration for Eq. 6.3.3 which yields the sectional side force that appears in Eq. 6.3.8. However, since the pressure distribution resulting from this complex velocity field is being integrated on the surface of the cone, $r = a$, so that $z = ae^{i\theta}$. Since z only appears in Eq. 6.3.9 as z/a, then the variable of integration in Eq. 6.3.9 is independent of a and is therefore independent of the axial coordinate z. If finally we assume that γ_1 and γ_2 are constants, where $\gamma_j = \Gamma_j/2\pi a(z)U$, $j = 1, 2$, then the

entire expression for the complex velocity in the cross-flow plane given by Eq. 6.3.9 is independent of the axial coordinate z. Note that the assumption of constant γ_j implies that the vortex strength Γ_j grows linearly with axial coordinate z, in the form $\Gamma_j = 2\pi U \gamma_j z \tan\theta_c$, $j = 1, 2$. The end result of these considerations is that the sectional side force coefficient that appears in Eq. 6.3.8 is independent of the axial coordinate z. Using the result for the sectional side force coefficient C_y of Eq. 6.3.5 (with a change of sign to obtain agreement with the sign convention of Ch. 5), Eq. 6.3.8 reduces to

$$Y = \int_0^L C_y \frac{1}{2}\rho U^2 \, a(z)\, dz = \frac{1}{2}\rho U^2 C_y \int_0^L a(z)\, dz = \frac{1}{2}\rho U^2 C_y \int_0^L \tan\theta_c \, z \, dz$$
$$= \frac{1}{2}\rho U^2 C_y \tan\theta_c \frac{L^2}{2}. \tag{6.3.11}$$

Using $\tan\theta_c = D/2L$, this equation becomes

$$Y = \frac{1}{2}\rho U^2 C_y \frac{D^2}{8\tan\theta_c}. \tag{6.3.12}$$

In this equation, the cross-flow velocity U is related to the actual free-stream speed U_∞ by $U = U_\infty \sin\alpha$. Thus the total side force coefficient C_Y as defined in Ch. 5 is related to the sectional side force coefficient C_y obtained from Eq. 6.3.5 by

$$C_Y = \frac{Y}{\frac{1}{2}\rho U_\infty^2 \frac{\pi D^2}{4}} = \frac{\sin^2\alpha}{2\pi \tan\theta_c} C_y. \tag{6.3.13}$$

Equation Eq. 6.3.5 requires the positions and strengths of the two wake vortices. The experiments gave the vortex positions but no information about their strengths. Thus some sort of estimate for the vortex strengths was required. Previous investigations of the vortex wakes of axisymmetric bodies at high angle of attack (Thomson and Morrison 1971; Mendenhall and Nielsen 1975; Wardlaw and Yanta 1980; Chin and Lan 1988) have shown that in general, the vortex closer to the body is stronger than the vortex farther away. This trend was incorporated into a model of the vortex strength as a function of radial distance r from the centerline of the cone. The vortex locations were measured using the procedure described in the

previous section for a particular α/θ_c and Re_t. A maximum nondimensional vortex strength magnitude γ_{max} was associated with the vortex location corresponding to the minimum nondimensional radial distance $(r/a)_{min}$ between vortex and cone centerline. Note that the cylinder radius a here corresponds to the local cone radius R_c as described in Sec. 4.3 and shown in Fig. 4.2. A minimum nondimensional vortex strength magnitude γ_{min} was associated with the vortex location corresponding to the maximum nondimensional radial distance $(r/a)_{max}$ between vortex and cone centerline. The magnitudes of the strengths of the vortices at all other radial distances from the cone centerline were computed by a linear interpolation in (r/a) between γ_{max} and γ_{min}. The signs of the vortex strengths were then assigned so that the vortex labeled "1" in Fig. 6.2 was negative and the vortex labeled "2" was positive. The values of γ_{max} and γ_{min} were then adjusted until the computed side force coefficients were in best agreement with the measured side force coefficients. The vortex locations measured at $\alpha/\theta_c = 6.0$ and $Re_t = 1,413$ were chosen to compute the side force coefficients, and the values of γ_{max} and γ_{min} were adjusted so that the computed C_Y matched the measured C_Y for $\alpha/\theta_c = 6.0, Re_t = 3,300$. This particular test was selected because the measured mean side force coefficients at this flow condition had the smoothest variation with cone roll angle.

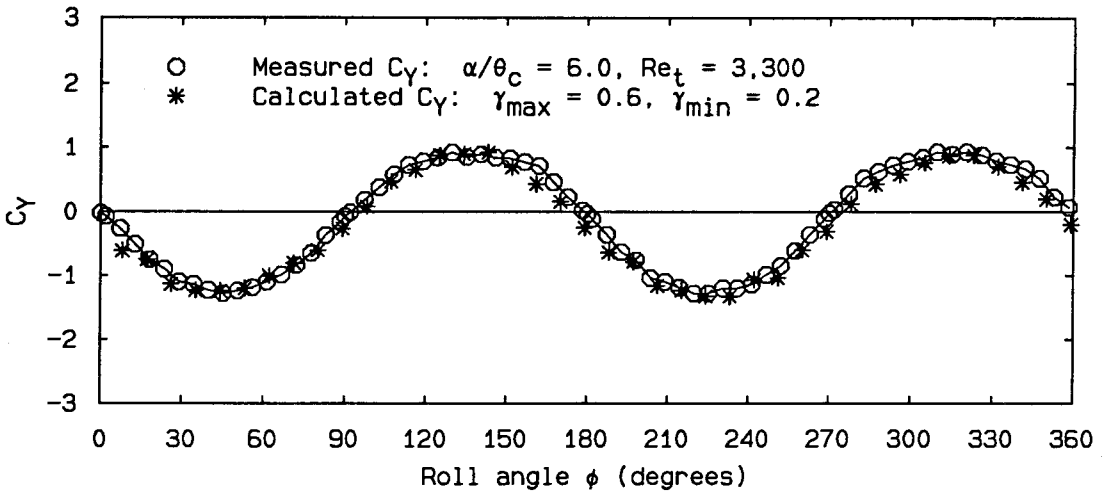

FIG. 6.3 Comparison of measured and calculated side force coefficients used to adjust γ_{min} and γ_{max} in vortex strength model (vortex locations for calculated C_Y obtained at $\alpha/\theta_c = 6.0, Re_t = 1,413$)

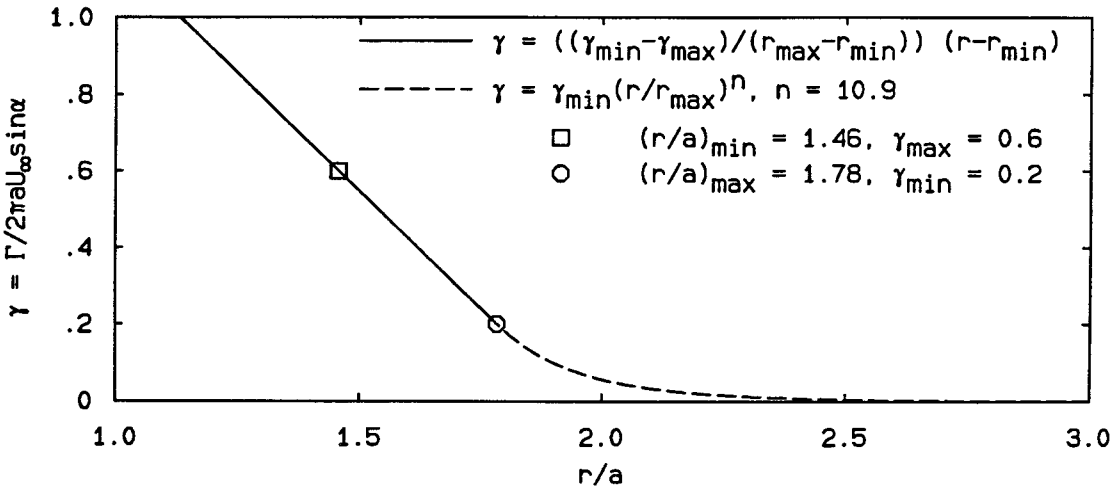

FIG. 6.4 Nondimensional vortex strength model

The results of these calculations are shown in Fig. 6.3. The resulting value for γ_{max} was 0.6 at $(r/a)_{min} = 1.46$, and the resulting value for γ_{min} was 0.2 at $(r/a)_{max} = 1.78$. The experimental results showed that r/a was less than 1.46 or greater than 1.78 for some flow conditions. For vortex locations with $r/a < 1.46$, the nondimensional vortex strengths were obtained by linear extrapolation. The linear portion of the vortex strength model was thus represented by

$$\gamma = (\gamma_{min} - \gamma_{max}) \left(\frac{r - r_{min}}{r_{max} - r_{min}} \right), \tag{6.3.14}$$

with the particular values listed above. The vortex strengths for r/a much larger than 1.78 could not be obtained from linear extrapolation, because the sign of the vortex strength would change. For $r/a > 1.78$, γ was obtained from

$$\gamma = \gamma_{min} \left(\frac{r}{r_{max}} \right)^n, \tag{6.3.15}$$

where n was chosen such that the slopes of the linear and exponential portions of the nondimensional vortex strength curve would match at $(r/a)_{max}$. For the values of $(r/a)_{min}$, $(r/a)_{max}$, γ_{max}, and γ_{min} listed above, n was 10.9. The entire resulting nondimensional vortex strength model is shown in Fig. 6.4. The values obtained from this model were in general agreement with those reported in the investigations listed above.

The side force coefficients calculated from Eq. 6.3.5 and Eq. 6.3.13 using the measured vortex locations and the strengths obtained from the model described above were the result of a number of *ad hoc* assumptions. The first was the arbitrary placement of vortices behind the cylinder in the potential flow model. The resulting calculation neglected the effects if any of the forces required to hold the vortices in place. The second was the assumption of an entirely conical body. This neglected the details of the elliptic cross section tip shape. However, since for a cone the body area increases toward the rear of the cone, flow conditions at the rear of the cone will have a larger effect on the total side force than conditions near the tip, so that neglecting the details of the tip shape should not be critical. The third assumption was that of conical flow. As the experimental results will show, the flow was not conical over the entire cone for a large portion of the test conditions. The assumption of conical flow was made to simplify the integration for the total side force. The main purpose of these calculations was to get an idea of how changes in the vortex wake *geometry* might affect the body side force. As the results of Fig. 6.3 show, even with all of these assumptions the model predicts fairly well both the actual magnitude of the side force coefficient and how the side force coefficient varies with roll angle, at least for this flow condition. However, for other cases, the model did a much better job of predicting the trend of the variation of side force coefficient with roll angle than it did of predicting the actual magnitude of the side force coefficient. Therefore, in the following figures the calculated side force coefficients were scaled so that the maximum magnitude of the calculated C_Y was the same as the maximum magnitude of the measured C_Y, for purposes of comparison.

6.4 Results

The basic results of the vortex wake geometry experiments are shown in Figs. 6.7 through 6.11. Each figure includes the vortex locations at a particular dye injection hole row for either a complete roll angle sweep at 15 cm/sec ($Re_t = 1,413$) and a partial sweep at either 10 cm/sec ($Re_t = 942$) or 20 cm/sec ($Re_t = 1,884$),

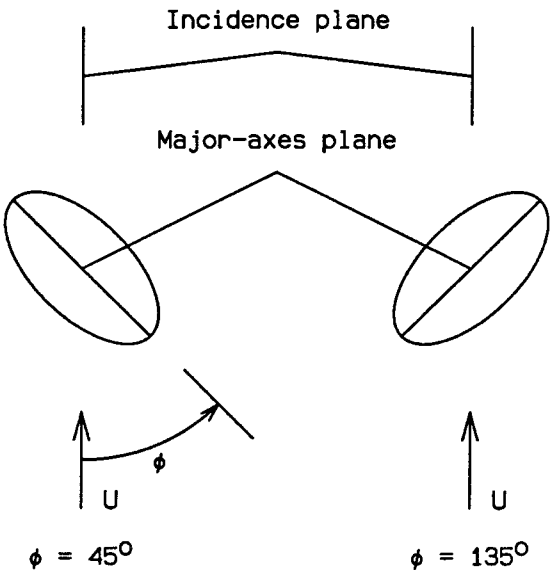

FIG. 6.5 Beginning and ending orientations for partial ϕ sweeps

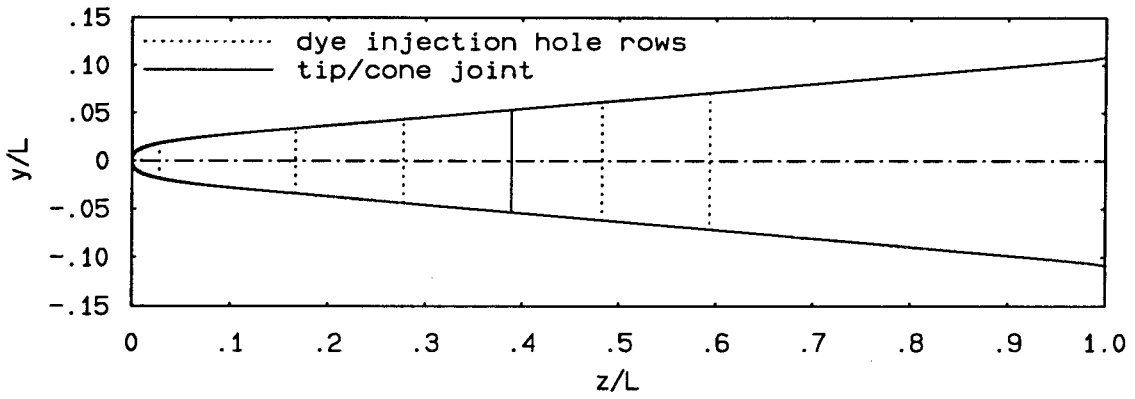

FIG. 6.6 Large elliptic cross section tip-cone geometry

or partial sweeps at 10 cm/sec ($Re_t = 942$) and 20 cm/sec ($Re_t = 1,884$). Figure 6.5 shows the beginning and ending elliptic cross section orientations for the partial sweeps. Figure 6.6 is included as a reminder of the large elliptic cross section tip-cone geometry and as an aid in visualizing the locations of the laser sheets described in the figures. Because of flow unsteadiness and the resulting difficulty in obtaining vortex locations from the video images, the vortex locations shown for all α/θ_c at $Re_t = 1,884$ are the average of 4 vortex locations obtained from the videotape

record, as are the vortex locations shown for $\alpha/\theta_c = 9$ at $Re_t = 1,143$. The flows for the other cases were steady enough so that 1 vortex location obtained from the videotape record at each roll angle was sufficient. The coordinates in the vortex location parts of the figures correspond to the system of body coordinates described in the previous section, with y positive to the right, z increasing toward the rear of the cone, and x chosen such that the entire coordinate system is right-handed. The x and y coordinates in the figure are normalized by the local cone radius R_c, which corresponds to the cylinder radius a of Sec. 6.3. Recall from Sec. 4.3 that the digitization and data reduction procedures resulted in the vortex coordinates automatically being normalized by the local cone radius. The signs of the x and y coordinates of the vortex locations shown in the figures were adjusted so that their use in Eq. 6.3.5 would give the correct results. The curve showing the possible stationary vortex positions behind a circular cylinder in potential flow as calculated by Föppl is again included for comparison in each figure. The axial location of the laser sheet $z_{\text{laser sheet}}$, where the vortex locations were obtained, is included in the caption for each figure, nondimensionalized by the overall model length $L = 45.72$ cm for the large elliptic cross section tip and the cone afterbody. Also included in each figure are the measured and calculated side force coefficients as a function of roll angle. For $\alpha/\theta_c = 6$, the measured side force coefficients shown were obtained at a nominal FSWT speed of 30 cm/sec (see Ch. 5). These are the coefficients that were used in obtaining the vortex strength model discussed in the previous section. The measured side force coefficients shown for $\alpha/\theta_c = 8$ and 9 were obtained for a nominal FSWT speed of 50 cm/sec.

The vortex locations for $\alpha/\theta_c = 6$ were measured at the rearmost dye injection row. Because these locations showed a small and essentially smooth variation with roll angle, the vortex locations were only measured at this row for this α/θ_c. The vortex locations for $\alpha/\theta_c = 8$ and $\alpha/\theta_c = 9$ did show a change in behavior between the two dye injection rows at which measurements were made. Figures 6.8 and 6.10 show a small and essentially smooth variation in the vortex positions for the

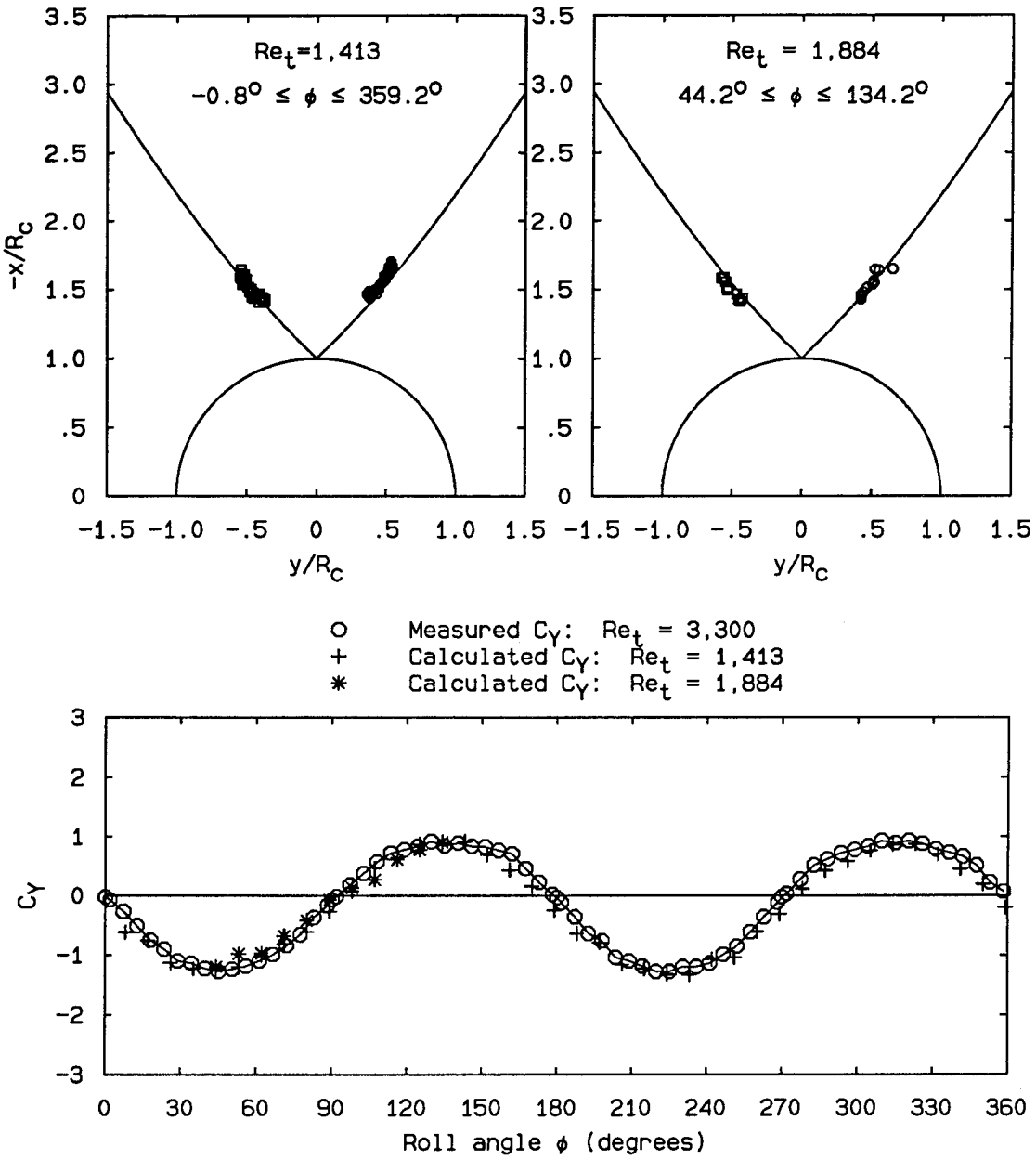

FIG. 6.7 Vortex wake geometry and computed side force coefficients: large elliptic cross section tip, $\alpha/\theta_c = 6$, $z_{\text{laser sheet}}/L = 0.59$

smaller value of $z_{\text{laser sheet}}/L$ at each α/θ_c. The calculated side force coefficients computed using these vortex locations show a much smoother variation with roll angle than the measured C_Y. For the larger value of $z_{\text{laser sheet}}/L$ at $\alpha/\theta_c = 8$ and $\alpha/\theta_c = 9$, however, the variation in vortex positions is much larger and not as

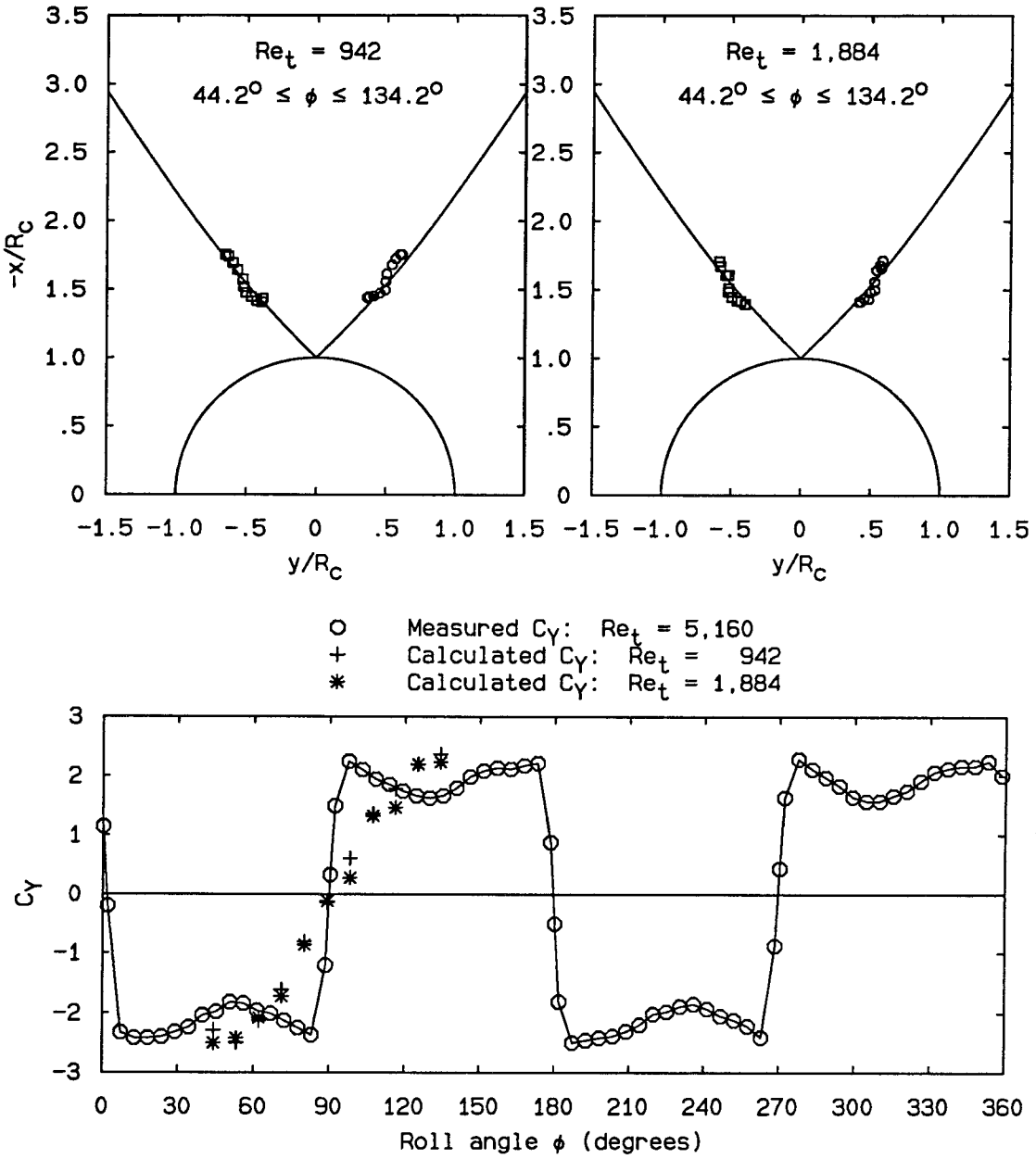

FIG. 6.8 Vortex wake geometry and computed side force coefficients: large elliptic cross section tip, $\alpha/\theta_c = 8$, $z_{\text{laser sheet}}/L = 0.28$

smooth. At $\alpha/\theta_c = 8$ and $z_{\text{laser sheet}}/L = 0.48$ (Fig. 6.9), the calculated side force coefficients begin to reflect the square-wave behavior of the measured C_Y. At $\alpha/\theta_c = 9$ and $z_{\text{laser sheet}}/L = 0.48$ (Fig. 6.11), the calculated C_Y begin to demonstrate the reduction in magnitude between zero crossings shown by the measured C_Y.

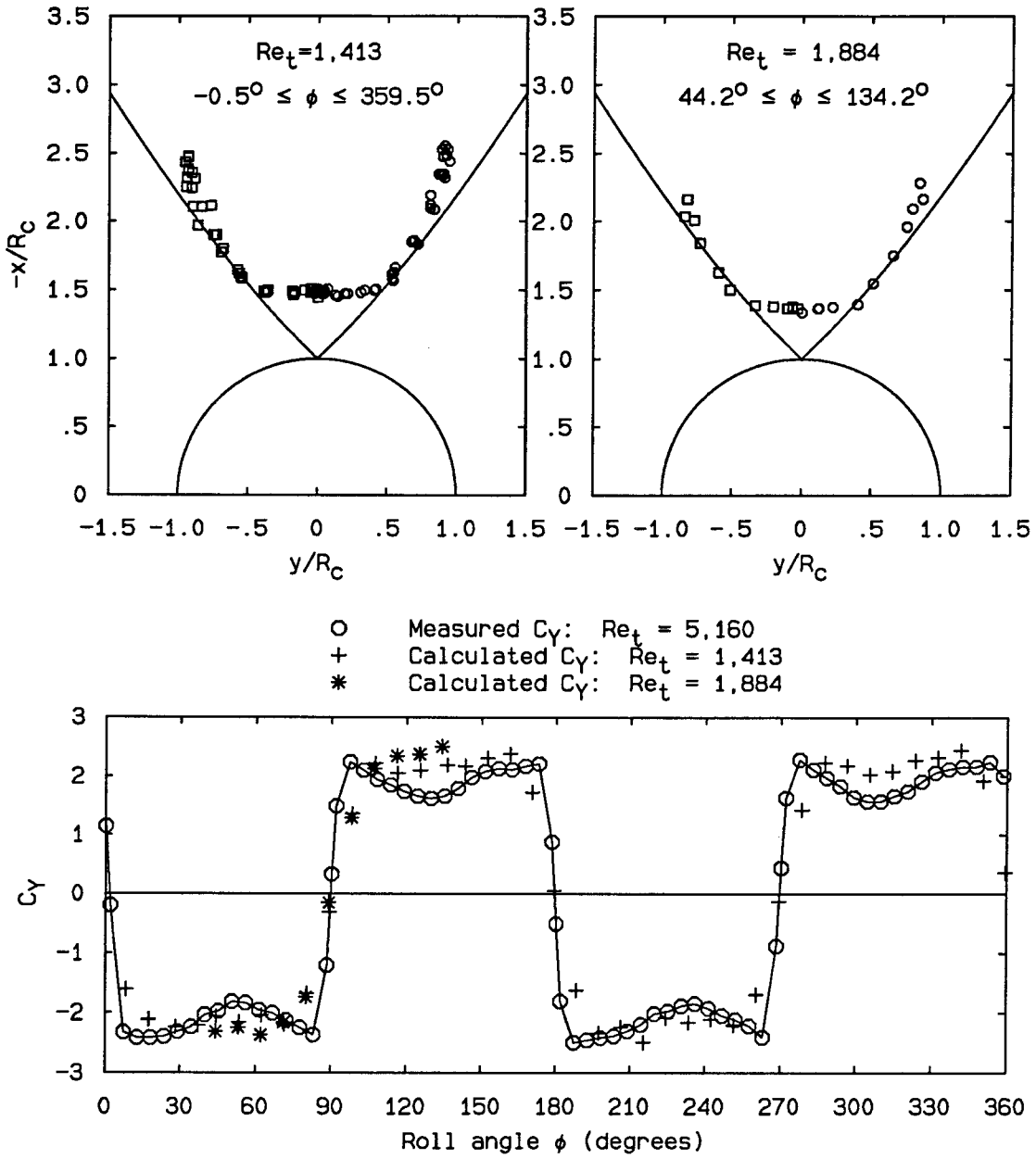

FIG. 6.9 Vortex wake geometry and computed side force coefficients: large elliptic cross section tip, $\alpha/\theta_c = 8$, $z_{\text{laser sheet}}/L = 0.48$

One difference that can be observed between the vortex wake geometries at the fore and aft laser sheet locations is the relation of the vortex loci to the Föppl curve. For the smaller $z_{\text{laser sheet}}/L$ at $\alpha/\theta_c = 8$ and $\alpha/\theta_c = 9$ (Figs. 6.8 and 6.10), the vortex loci show a smooth transition between portions of the loci that are transverse

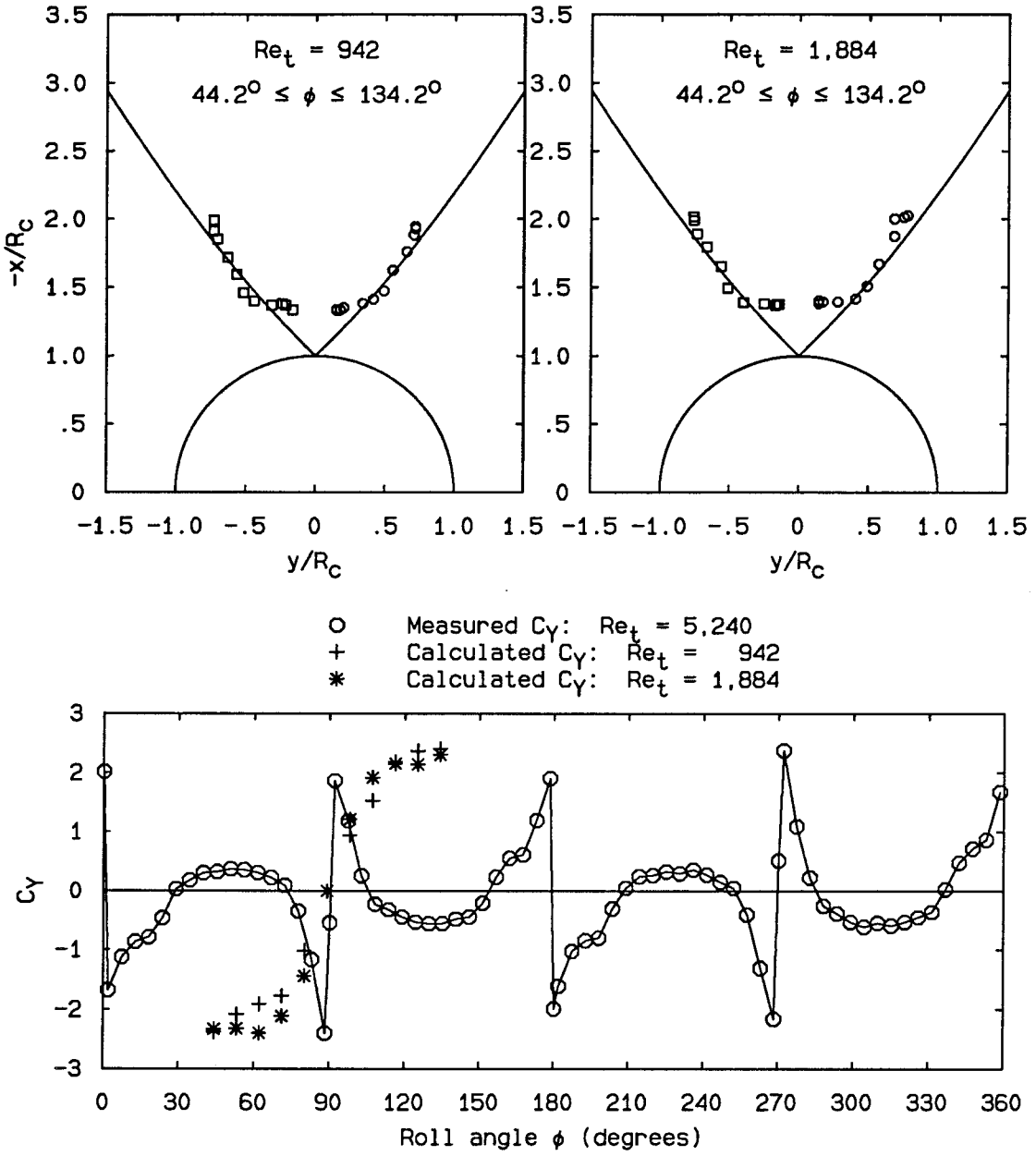

FIG. 6.10 Vortex wake geometry and computed side force coefficients: large elliptic cross section tip, $\alpha/\theta_c = 9$, $z_{\text{laser sheet}}/L = 0.28$

to the Föppl curve and portions that are tangent to the Föppl curve, as described in Sec. 4.4 and shown in Fig. 4.5. For the larger $z_{\text{laser sheet}}/L$ at $\alpha/\theta_c = 8$ (Fig. 6.9), this transition portion of the loci has apparently shrunk to a point and has disappeared altogether for the larger $z_{\text{laser sheet}}/L$ at $\alpha/\theta_c = 9$ (Fig. 6.11).

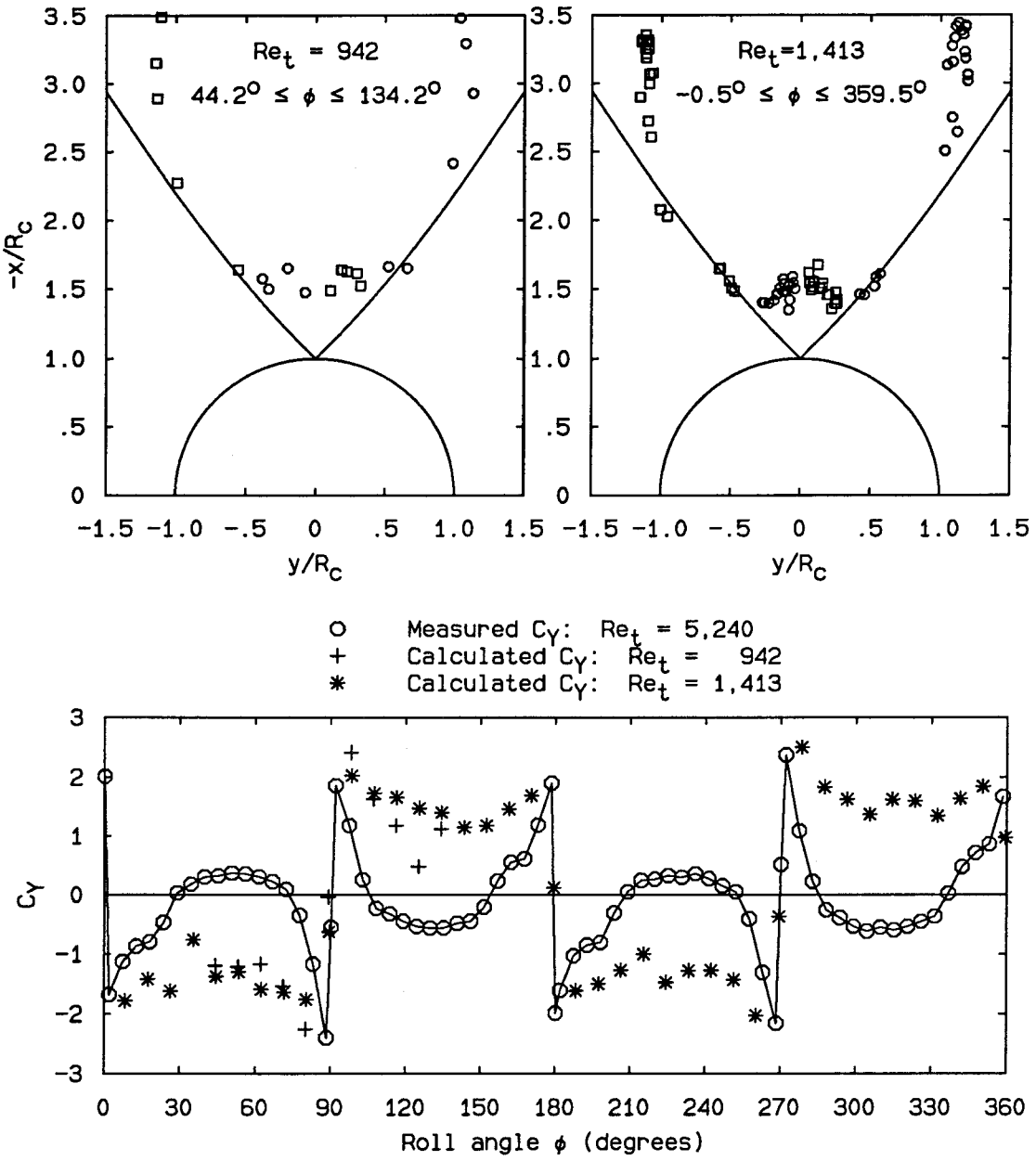

FIG. 6.11 Vortex wake geometry and computed side force coefficients: large elliptic cross section tip, $\alpha/\theta_c = 9$, $z_{\text{laser sheet}}/L = 0.48$

The main difference between the results for the fore and aft laser sheet locations is the location of the vortex of each vortex pair that is closer to the cone. For the smaller $z_{\text{laser sheet}}/L$, each vortex in each pair of vortices remains on one side of the cone centerline. However, for the larger $z_{\text{laser sheet}}/L$, after the vortex pair

passes through the symmetric wake configuration, the vortex that is closer to the cone sometimes actually crosses the cone centerline. This can be seen for a few vortex locations in Fig. 6.9, where $\alpha/\theta_c = 8$ and $z_{\text{laser sheet}}/L = 0.48$. The most dramatic evidence of "vortex crossover" is shown in Fig. 6.11, where $\alpha/\theta_c = 9$ and $z_{\text{laser sheet}}/L = 0.48$. The vortex locations for $\alpha/\theta_c = 9$ and $Re_t = 1,143$ have been plotted in a slightly different manner in Fig. 6.12. In this figure, the symbols were chosen to indicate both the left and right vortex locations of each pair of vortices and the sign of the associated vortex wake asymmetry angle β as defined in Sec. 4.3 and Fig. 4.2. As can be seen from this figure, the left vortex in all but two vortex pairs with $\beta > 0$ has crossed over from $y/R_c < 0$ to $y/R_c > 0$. Similarly, the right vortex in all but three vortex pairs with $\beta < 0$ has crossed over from $y/R_c > 0$ to $y/R_c < 0$.

The crossover is just beginning at $\alpha/\theta_c = 8$ for $z_{\text{laser sheet}}/L = 0.48$. At this α/θ_c and $z_{\text{laser sheet}}/L$, the variation of the computed side force coefficient with roll angle is just beginning to approach the square wave behavior of the measured C_Y (see Fig. 6.9). The large amount of crossover at $\alpha/\theta_c = 9$ for $z_{\text{laser sheet}}/L = 0.48$ occurs at the same time that the computed C_Y are beginning to show the reduction in magnitude after the magnitude peaks on either side of the zero crossings that the measured C_Y demonstrate.

How this vortex wake geometry behavior could be related to the side force coefficient behavior can be understood from an examination of Fig. 6.13. This figure shows the vortex locations corresponding to $44.2^o \leq \phi \leq 134.2^o$ at $z_{\text{laser sheet}}/L = 0.48$ for $\alpha/\theta_c = 9$ and $Re_t = 942$. The pair of connected vortex locations labeled "$\phi = 89.5^o$" correspond to an essentially symmetric vortex wake geometry, and the corresponding computed C_Y is almost 0. As ϕ moves away from this value to the next value on either side, $\phi = 80.5^o$ or $\phi = 98.5^o$, the vortices undergo a relatively large shift to an asymmetric configuration that results in the maximum computed side force. The vortex in the asymmetric pair that ends up closer to the cone was on the opposite side of the cone centerline when the vortex wake was symmetric. As

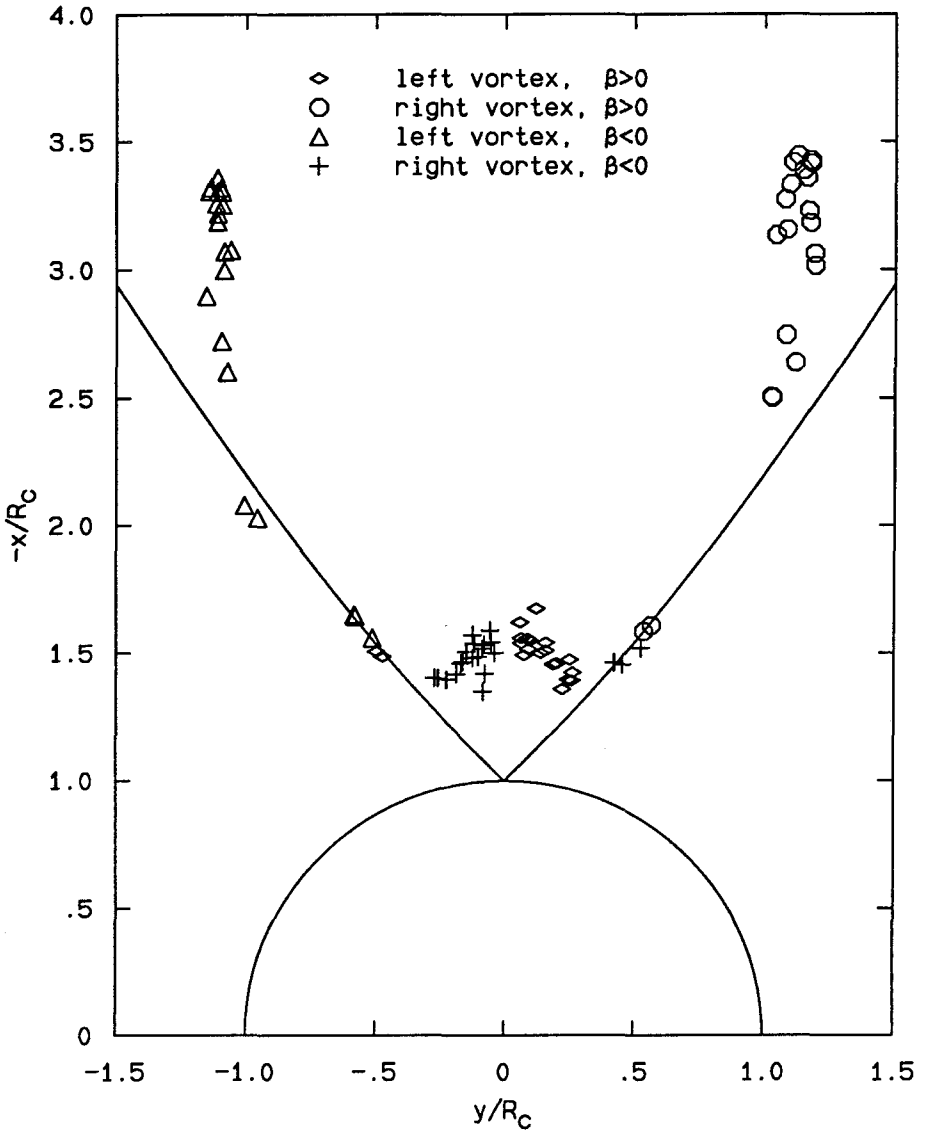

FIG. 6.12 Illustration of "vortex crossover:" $\alpha/\theta_c = 9$, $Re_t = 1,413$, $z_{\text{laser sheet}}/L = 0.48$

ϕ moves still further away from 89.5°, the vortices become even more asymmetric, but the magnitude of the computed side force is reduced. This could be caused by the fact that the vortex closer to the body has moved sufficiently far across the centerline of the body to reduce its influence on the side of the body on which that vortex was originally located. A more accurate model of the vortex wake might even show the change in sign of the side force coefficient after the magnitude peak demonstrated by the measured C_Y as ϕ moves away from 89.5°. This behavior

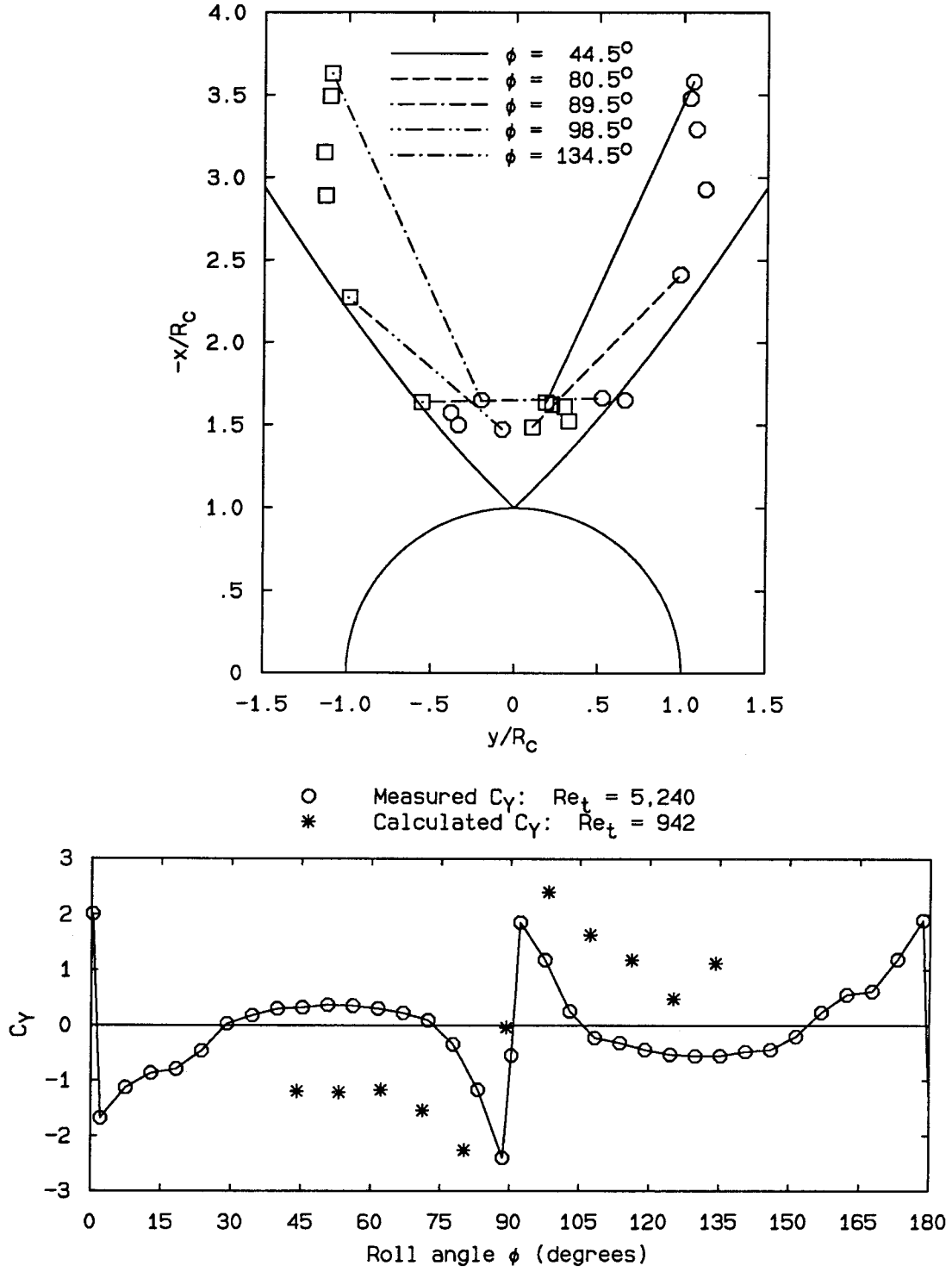

FIG. 6.13 Detail of vortex wake geometry variations with roll angle: large elliptic cross section tip, $\alpha/\theta_c = 9$, $z_{\text{laser sheet}}/L = 0.48$

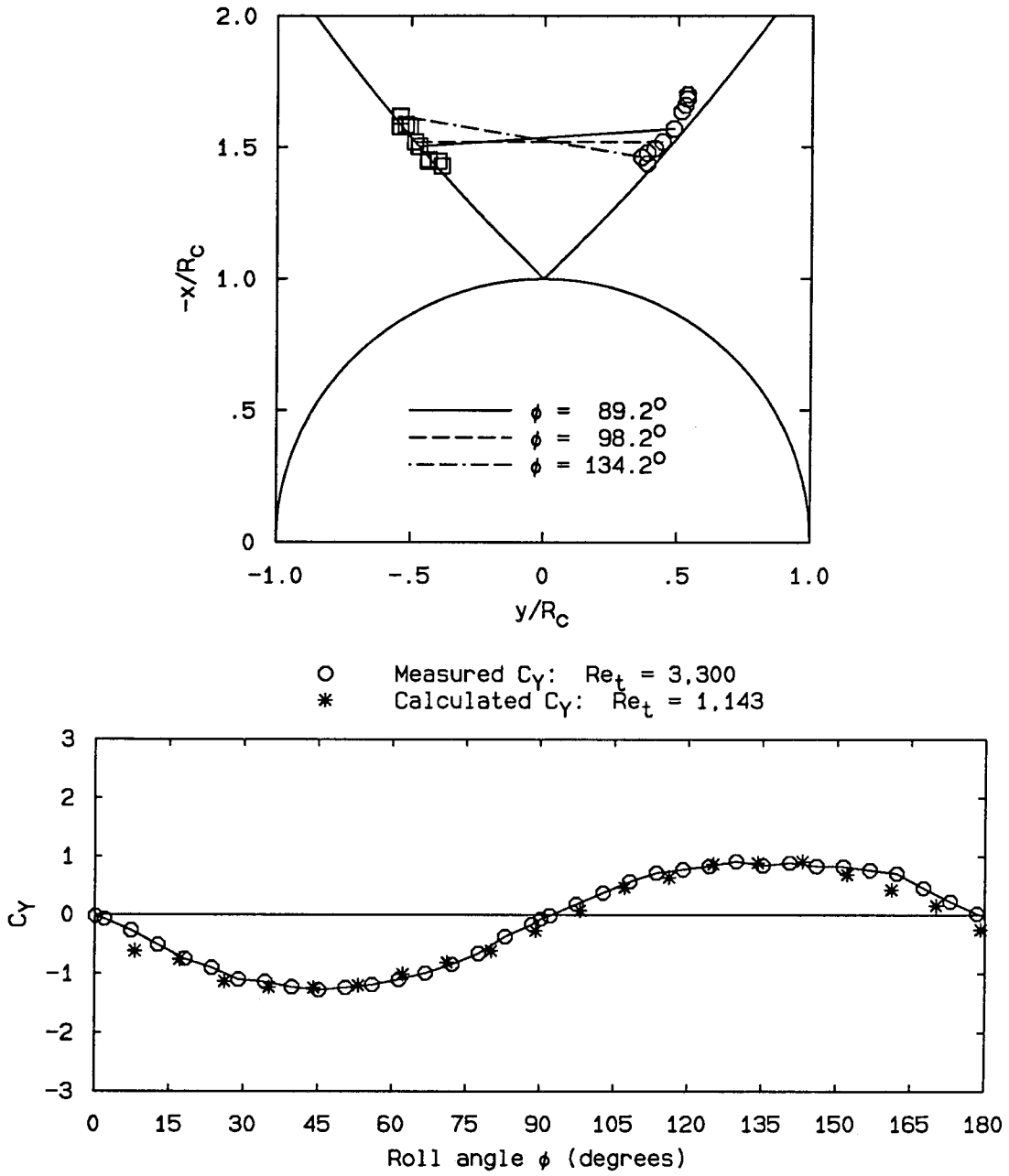

FIG. 6.14 Detail of vortex wake geometry variations with roll angle: large elliptic cross section tip, $\alpha/\theta_c = 6$, $z_{\text{laser sheet}}/L = 0.59$

is contrasted with that at $\alpha/\theta_c = 6$ and $z_{\text{laser sheet}}/L = 0.59$, shown in Fig. 6.14. In this case, the vortex locations vary smoothly with ϕ as they pass through the symmetric condition, there is no crossover, and both measured and computed C_Y

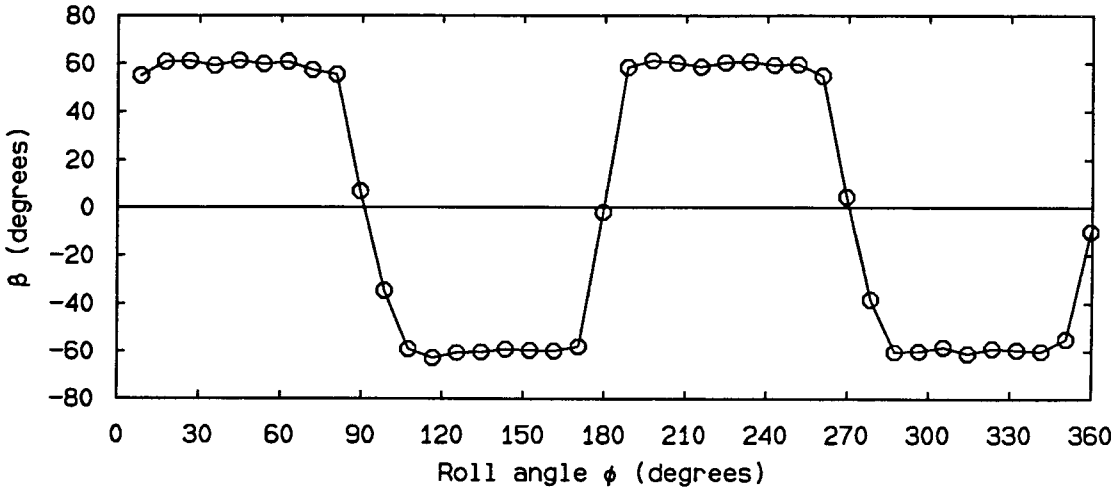

FIG. 6.15 Variation of wake asymmetry angle with cone roll angle: $\alpha/\theta_c = 9$, $Re_t = 1,413$

vary smoothly with ϕ.

How the use of the vortex wake asymmetry angle β might mislead concerning the true nature of the forces on the body is shown by Fig. 6.15. This figure shows that β varied with ϕ as a square wave for $\alpha/\theta_c = 9$ and $Re_t = 1,413$, when the variation of C_Y with ϕ was exhibiting peaks and reductions in magnitude between zero crossings, as in Fig. 6.13.

As discussed above, the vortex crossover and subsequent deviation of the computed side force coefficients from a smooth variation with roll angle occurred at the aft laser sheet locations. To determine the axial location at which such behavior might appear, two axial traverses of the vortex wake were conducted, one at $\alpha/\theta_c = 8$ and $Re_t = 1,884$, and one at $\alpha/\theta_c = 9$ and $Re_t = 942$, and both at $\phi = 44.2^o$, corresponding to a maximum asymmetry condition. The results of these traverses are shown in Figs. 6.16 and 6.17. Note that in these figures, the z axis begins at the origin of the elliptic cross section tip, as opposed to the apex of the cone as was assumed in the integration of the sectional side forces in Sec. 6.3. The semi-circles in the y/R_c–x/R_c planes of the figures correspond to the cone radii at the axial location of each vortex pair in the figure. The extent of the traverse

at $\alpha/\theta_c = 9$ was limited in z/L because the field of view of the video camera at larger z/L was not large enough to capture both vortices. The speed was reduced at $\alpha/\theta_c = 9$ to improve flow visualization quality. The axial measurement stations for $\alpha/\theta_c = 8$ that appear in Fig. 6.16 were at z/L of 0.28, 0.29, 0.35, 0.39, 0.43, 0.48, 0.54, and 0.59. The axial measurement stations for $\alpha/\theta_c = 9$ in Fig. 6.17 were at z/L of 0.28, 0.34, 0.39, 0.44, and 0.48.

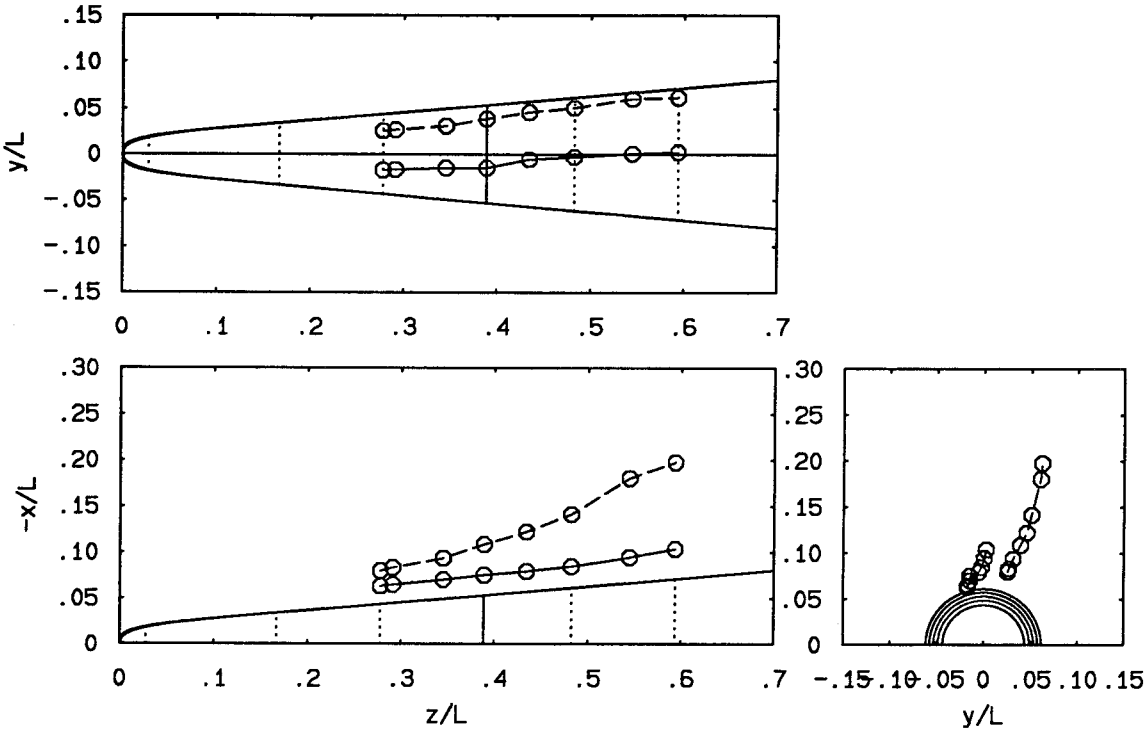

FIG. 6.16 Vortex trajectories: $\alpha/\theta_c = 8$, $Re_t = 1,884$, $\phi = 44.2^o$

Figure 6.16 shows that the vortex crossover seems to begin at $z/L \approx 0.48$ for $\alpha/\theta_c = 8$ and $\phi = 44.2^o$. The magnitude of the crossover at this α/θ_c is not large for any z/L. The results are a little different for $\alpha/\theta_c = 9$. Figure 6.17 shows that the crossover begins earlier, at $z/L \approx 0.34$, and that the crossover distance seems to be increasing slightly as z/L increases, for $\phi = 44.2^o$. In both of these cases, the crossover begins in the region where one vortex begins to break away from the cone. The motion of the one vortex away from the cone allows the other vortex to move underneath it, crossing over the centerline of the cone in the process. Recall the

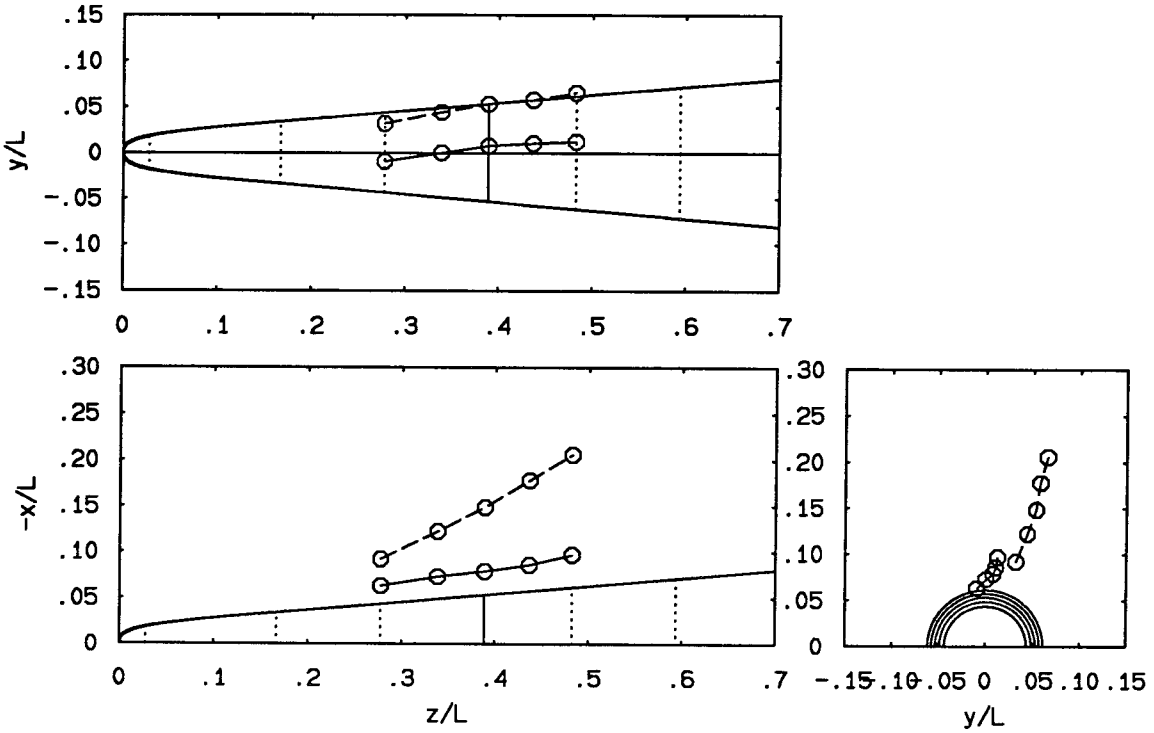

FIG. 6.17 Vortex trajectories: $\alpha/\theta_c = 9$, $Re_t = 942$, $\phi = 44.2^o$

discussion above that attributed the peak in magnitude of C_Y after the zero crossing to the large shift of the vortex pair away from the symmetric configuration, and then attributed the subsequent reduction in magnitude of C_Y to increasing vortex crossover which reduced the influence of the vortex closer to the body on the side of the body on which the vortex was originally located. If this analysis is correct, then it is the breakaway of one vortex which leads ultimately to the reduction in magnitude of C_Y between magnitude peaks. Since the breakaway and subsequent crossover occurs over the rearward part of the cone, the pressures induced by the vortex wake in this configuration make a greater contribution to the overall side force, because of the larger surface area over which the pressures can act.

Such behavior has been observed by previous investigators. Ward and Katz (1989) measured vortex trajectories behind an axisymmetric body with an ogive nose at high angle of attack. These trajectories show a connection between vortex breakaway and vortex crossover. Wardlaw and Yanta (1980), among others, noted

that the peak in the distribution of sectional side force over the length of an axisymmetric body at large angle of attack occurred when the first vortex was shed from the body. The side force was directed away from the side of the body from which the vortex had been shed. Other peaks occurred as subsequent vortices were shed from the body, the shedding alternating sides with increasing axial distance in the manner that had earlier given rise to the impulsive flow analogy (see Sec. 1.2). The relation between vortex breakaway and body side force was shown explicitly by the work of Kompenhans and Hartmann (1987). Kompenhans and Hartmann investigated the wake of an axisymmetric ogive nose of fineness ratio 3 mounted on a cylindrical afterbody at an angle of attack of 55^o and a Reynolds number $Re_D = 250,000$. The separation in this case was reported to be laminar. Kompenhans and Hartmann used a laser sheet method similar to the one used in the current experiments. They determined vortex positions at particular axial stations on the body and compared them to pressure distributions measured at the same axial locations. Kompenhans and Hartmann discovered that at the initial appearance of wake asymmetry, one vortex began to move away from the body, and the other vortex began to move underneath the first. The pressure distributions showed a suction peak on the side of the body where the vortex closer to the body was originally located. After the near vortex crossed the body centerline, near where the far vortex could be said to have been shed from the body, the suction peak changed body sides, which would lead to a change in sign of the sectional side force. Kompenhans and Hartmann attributed the change of side of the suction peak to a third vortex which appeared underneath and on the same side of the body as the vortex that had been shed. The locations of such secondary vortices were not documented in the current experiments. However, it was apparent from the results of Kompenhans and Hartmann that the close vortex could not have crossed over nor could the third vortex have been formed unless the far vortex had been shed.

Thus the unexpected (and undesired) changes in the roll angle-side force characteristics as angle of attack increased have been explained. For $\alpha/\theta_c = 6$, the

vortices show no crossover (and hence probably no breakaway), and the side force coefficient varies smoothly with roll angle. For $\alpha/\theta_c = 8$, the vortices begin to show breakaway and slight crossover, and the variation of side force coefficient with roll angle begins to approach a square wave. For $\alpha/\theta_c = 9$, the vortices show definite breakaway and relatively large crossover, and the side force coefficient first peaks on either side of the zero crossings and then reduces in magnitude as ϕ varies. The vortex trajectories indicate that the point of vortex breakaway moves closer to the tip as angle of attack increases, in agreement with the work of previous investigators. This would explain the increased reduction in magnitude of C_Y between peaks for $\alpha/\theta_c = 9.8$ (see Fig. 5.12).

The reason for a difference in the side force coefficient behavior between the large and small elliptic cross section tips can now be postulated. Figures 5.30 and 5.31 show how the variation of C_Y with ϕ changes with angle of attack for the large and small elliptic cross section tips, respectively. Figure 5.30 shows the gradual transition from no-vortex-breakaway, smooth-C_Y-variation behavior at $\alpha/\theta_c = 6$ to the vortex-breakaway, rough-C_Y-variation behavior at $\alpha/\theta_c = 9.8$ for the large elliptic cross section tip. In contrast to this, Fig. 5.31 shows the rough-C_Y-variation behavior at $\alpha/\theta_c = 6$ for the small elliptic cross section tip. This was the lowest angle of attack studied with the small tip. These two figures, and the analysis described above, suggest that the blunter large elliptic cross section tip postponed the vortex breakaway to larger angles of attack than those at which vortex breakaway occurred for the small elliptic cross section tip. Such behavior would be in agreement with the general reduction in vortex wake asymmetry caused by tip blunting as discussed in Sec. 1.3.1.

The basic model used in these experiments, the right circular cone, was supposed to represent the nose of an axisymmetric body. The elliptic cross section and chisel tips were designed to be modifications to the tip of this nose. However, based on the similarity in the results between these experiments and those of other investigators, the flow past the cone seemed to bear a greater resemblance to the flows

past nose-and-cylindrical-afterbody combinations than to the flow past a nose-alone configuration. The primary similarity was between the vortex breakaway that occurred on the cone in these experiments and on the cylindrical afterbody of other investigations. These results suggest that for the relative length scales involved, the cone stopped being an approximation to the nose of an aircraft or missile and began to be an approximation to the cylindrical afterbody of a missile configuration.

The effect of vortex breakaway on vortex wake geometry and side force might explain why Moskovitz (1989) obtained relatively smooth variations of sectional side force coefficient with roll angle for his elliptic cross section tip on an ogive-cylinder body and square-wave variations for his elliptic cross section tip on a cone-cylinder body. Flow visualization photographs in the thesis by Moskovitz show that in general, for a given angle of attack, the wake vortices remained attached to the body for a greater axial distance on the ogive-cylinder body than on the cone-cylinder body. Apparently the ogive shape of the nose helped to delay vortex breakaway, either because of the difference between the ogive and cone shapes, or because the ogive nose had a larger apex angle θ_A than the cone and thus the relative angle of attack α/θ_A was less for the ogive nose than the cone nose (see discussion of effects of apex angle in Sec. 1.2). This observation is a general observation because photographs of the flow past the cone-cylinder body and the ogive-cylinder body with elliptic cross section tips at a given angle of attack and tip roll angle are not provided in the thesis by Moskovitz, so a direct comparison cannot be made. However, photographs of the flow past a cone-cylinder body with a blunted tip and past an ogive-cylinder body with a sharp tip at given angles of attack and cylinder-diameter Reynolds numbers (Re_D) are provided. In these photographs, the wake vortices remain attached to the ogive-cylinder body for a greater axial distance than for the cone-cylinder body, even though the cone tip was blunted. The sectional side force coefficients in the elliptic cross section tip experiments of Moskovitz were obtained by integrating the pressure distributions obtained from rings of pressure taps at axial locations z/L of 0.25, 0.5, and 0.75, L being the

length of the nose and z the distance from the apex of the nose. The lengths of the cone and ogive noses were the same, and the pressure tap rings were located at the same axial locations on both noses. The cone semi-angle θ_c was 10^o. As was mentioned in Sec. 1.3, Moskovitz obtained sinusoidal variations of the sectional side force coefficient with tip roll angle for the cone-cylinder body for an angle of attack of 30^o ($\alpha/\theta_c = 3$), and square-wave variations for all higher angles of attack. These variations were the same for all three pressure tap stations. He obtained sinusoidal variations of the sectional side force coefficient with roll angle for the ogive-cylinder body for essentially all angles of attack tested, the maximum angle of attack being 60^o ($\alpha/\theta_c = 6$). However, this sinusoidal variation only occurred for the two foremost pressure tap rings for $\alpha = 60^o$. The rearmost tap ring showed a square-wave variation. Flow visualization photographs for this case are provided, and they indicate that vortex breakaway occurred ahead of this pressure tap ring.

The change in behavior between the large and small elliptic cross section tips in the current experiments, with the apparent vortex breakaway occurring at a smaller α/θ_c for the smaller tip, suggests that there is a scaling factor related to the tip radius R_t. For larger R_t, the tip can maintain the desired control over the vortex wake to a larger z/L before breakaway occurs and the desired control is lost. Recall that Figs. 6.8 through 6.11 showed that ahead of the breakaway point, the vortex locations and the computed C_Y varied smoothly with roll angle. This point is emphasized in Fig. 6.18, which is a repeat of part of Fig. 6.8. This figure shows the small and essentially smooth variation in the vortex locations with cone roll angle at $\alpha/\theta_c = 8$ and $z_{\text{laser sheet}}/L = 0.28$, and the corresponding smooth variations in computed C_Y and wake asymmetry angle β. The ability of the large elliptic cross section tip to provide smooth wake asymmetry variations with roll angle at large α/θ_c is shown even more graphically in Fig. 6.19. This figure shows the results of vortex wake measurements made at $\alpha/\theta_c = 9$ and $z_{\text{laser sheet}}/L = 0.17$, the forward-most dye injection row at which measurements could be made. The flow at this $z_{\text{laser sheet}}/L$ was steady enough so that the recording of only one vortex

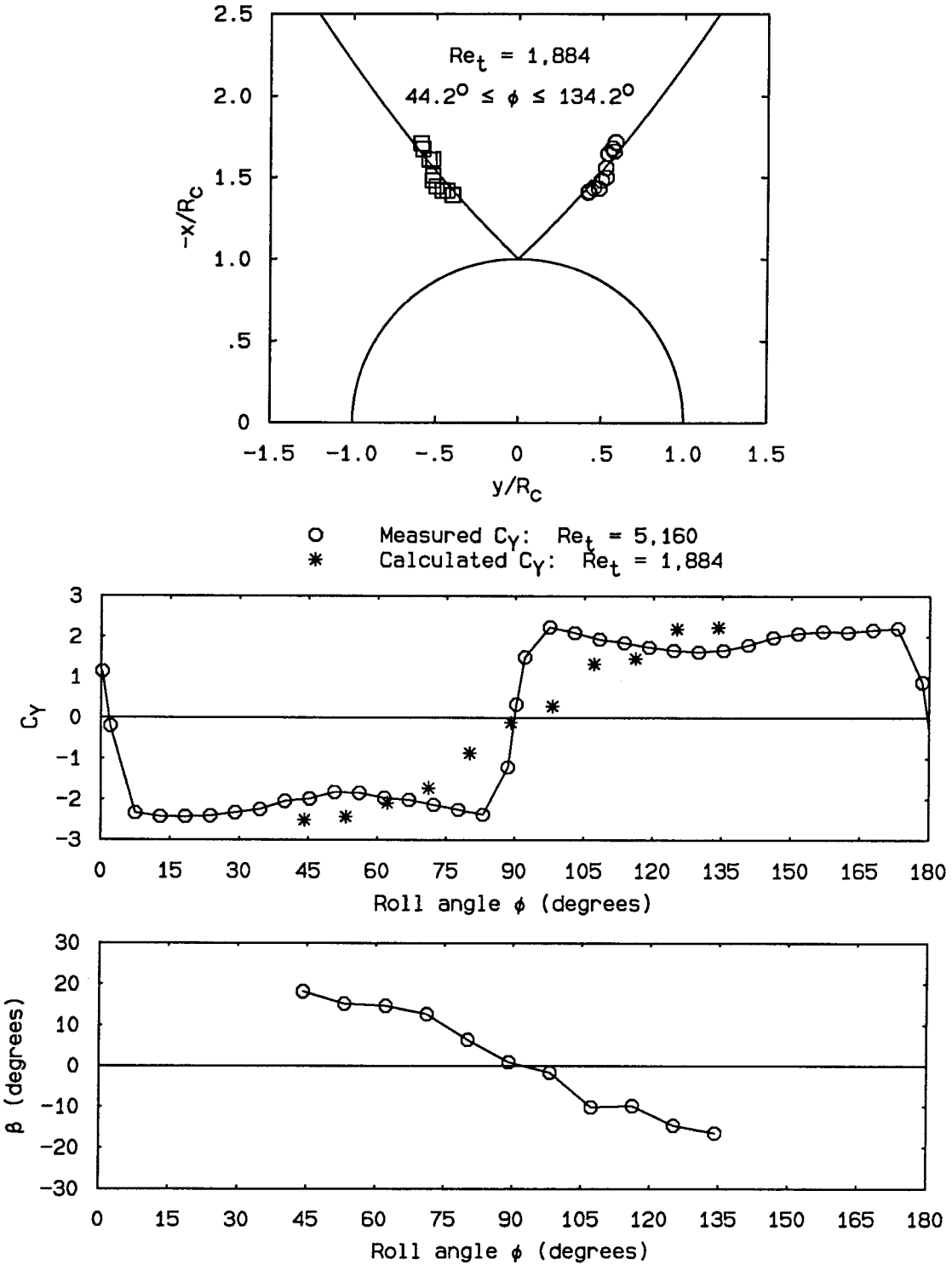

FIG. 6.18 Vortex wake geometry variations ahead of vortex breakaway: $\alpha/\theta_c = 8$, $z_{\text{laser sheet}}/L = 0.28$

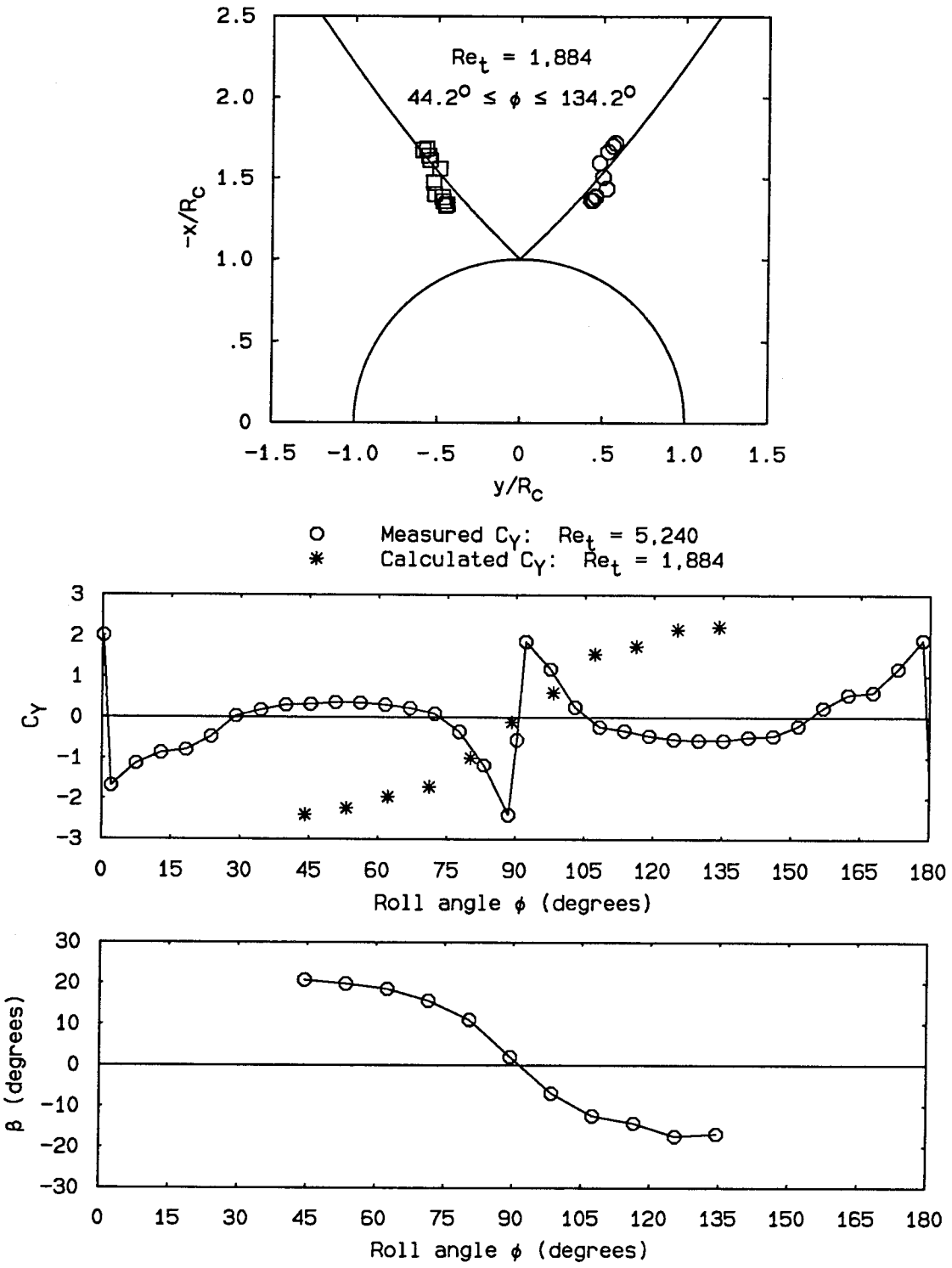

FIG. 6.19 Vortex wake geometry variations ahead of vortex breakaway: $\alpha/\theta_c = 9$, $z_{\text{laser sheet}}/L = 0.17$

location from the videotape record at each ϕ was sufficient. This figure demonstrates very smooth vortex position variation with roll angle, with corresponding smooth variations in computed C_Y and β. Note that these measurements were made at the highest angle of attack ($\alpha/\theta_c = 9$) and the highest tip Reynolds number ($Re_t = 1,884$; $Re_D = 19,800$) that could be obtained in these experiments.

There are a number of questions that remain unanswered. One of these is the effectiveness of the elliptic cross section tip when the boundary layer separations on the nose are transitional or turbulent. The numbers reported by Edwards (1978) for flight tests on the F-5F yield a typical tip Reynolds number of approximately 650,000, fully 2 orders of magnitude higher than the values obtained in the current experiments. At these values of Re_t, the separations on the nose would be turbulent. If the effectiveness of the tip is caused by its influence on the pressure distribution on the body nose, then perhaps Reynolds number effects would be minimized. However, this supposition needs to be verified experimentally. The effects of compressibility are also unknown. The Mach number is a less important parameter, however, because maneuvers at high angle of attack are typically executed at subsonic Mach number. Also, as discussed in Sec. 1.2, the influence of the asymmetric wake on the body side force is greatest at low Mach number. Another unknown is how a nose tip shape such as the one described in this thesis would affect the dynamic stability of an aircraft. The shape of the nose of the F-20, a descendant of the F-5, was set by dynamic stability considerations (Culick 1992). The impact of an elliptic cross section tip with a variable orientation on the dynamic stability characteristics of such an aircraft would need to be investigated.

The most important question related to these experiments which remains to be answered is what causes vortex breakaway. This problem seems to be related to the general problem of finding a description of the particular mechanism through which conditions at the tip of the body affect the wake farther downstream. The evidence seems to indicate a travelling-wave phenomenon in which vortex wake asymmetry and breakaway are the results of perturbations that are introduced at

the tip and grow as they move downstream. The sensitivity to the perturbation is set by the angle of attack through the relative angle of attack α/θ_A. Recall from Figures 6.7 through 6.11 that the variation in vortex position at a given laser sheet location increased as the angle of attack increased, indicating that the downstream growth of the "disturbance" introduced by the tip was greater for a higher angle of attack. Recall also the analysis of Keener and Chapman (1977), discussed in Sec. 1.2, which described the relation between asymmetry onset and the degree of vortex "crowding" at the apex of the nose. This analysis suggests that the more "crowded" the vortices are at the nose tip, the more sensitive they would be to disturbances at the tip. Recall further that the small elliptic cross section and chisel tips demonstrated ϕ–C_Y behaviors at all angles of attack that were similar to the ϕ–C_Y behavior of the large elliptic cross section tip at the higher angles of attack. The ϕ–C_Y behavior of the large elliptic cross section tip at the higher angles of attack was determined through the vortex wake geometry measurements to have been caused by vortex breakaway. These results taken together suggest that vortex breakaway occurred a short distance down the cone from the tip for the small elliptic cross section and chisel tips, even at the lowest angle of attack. The perturbations introduced at the tip by the small elliptic cross section and chisel tips could be considered much larger than that introduced by the large elliptic cross section tip. If vortex breakaway is considered to be a saturated end state resulting from a disturbance introduced at the tip, then the early vortex breakaways associated with the small elliptic cross section and chisel tips could be the result of the greater perturbation introduced at the nose of the body by these tips. The idea that the mechanism by which disturbances introduced at the tip of the body are transmitted to the vortex wake downstream is some sort of travelling wave phenomenon is also supported by the work of Degani and Tobak (1992). Degani and Tobak conducted experiments which seemed to indicate that the mean asymmetric force on a body at high angle of attack is the result of a convective instability of the vortex wake, so that the wake requires the continual introduction of disturbances at the tip in order to maintain asymmetry. All of these ideas and results suggest that

perhaps an analytical investigation of the receptivity to disturbances of two vortex filaments placed behind a cone at angle of attack would yield a greatly increased understanding of this part of the problem.

Despite the unanswered questions, all of the results of the vortex wake geometry measurements taken together suggest that the large elliptic cross section tip provides smooth control of the vortex wake asymmetry up to some point ahead of vortex breakaway. This means that the tip would probably not be effective in controlling the side force on a missile configuration, since it does not eliminate vortex shedding. However, these results suggest that the tip might be effective in controlling the side force on the nose of an aircraft, where vortex breakaway does not usually occur before the nose ends and the fuselage begins, as illustrated by the flow visualization photographs of Chambers *et al.* (1970) and Skow and Erickson (1982). The forces on the aircraft might be expected to be dominated by the flow past the wings and fuselage at the point of vortex breakaway, so that the influence of the shed vortices would be negligible. This statement is supported by Keener and Chapman (1974), who show that the angle of attack for asymmetry onset α_{AV} for a winged configuration is as high or higher than that for forebody-alone geometries. They conclude that the presence of a wing tends to reduce or eliminate the influence of the afterbody on asymmetric side forces. Since the noses of most high-performance aircraft are closer to ogives than cones, the delayed vortex breakaway for ogives, as suggested by the photographs by Moskovitz (1989), would probably enhance the ability of the elliptic cross section tip described in this thesis to provide a smooth variation with tip roll angle of the asymmetry of the vortex wake of the nose of an aircraft at high angle of attack. If the elliptic cross section tip could provide this smooth variation of vortex wake asymmetry over a substantial portion of the nose of the aircraft, then the resulting smooth variation of nose side force with tip roll angle would be translated into a smooth variation of aircraft yawing moment. The end result would be a feasible yaw control device for high-performance aircraft at high angle of attack.

CHAPTER 7

Conclusions

In addition to attached flow, four different basic flow separation patterns occur on a 5^o cone with a hemispherical tip over a tip Reynolds number range $889 \leq Re_t \leq 12,200$ and a relative angle of attack range $0 \leq \alpha/\theta_c \leq 12$: boundary-layer thickening, separation bubble, a combination of separation bubble and local separations, and "U"-shaped global separation. The separation bubbles occur at relatively low values of Re_t and α/θ_c. Global separations form when local separations move forward as the cross-flow Reynolds number increases until they merge with the separation bubble at the model tip. The behavior of the edge of the separation bubble at small α/θ_c is very similar to the behavior of free shear layers, the principal similarity being the rollup of the bubble trailing edge into vortical structures.

The smooth elliptic cross section tips designed so that the radius, slope, and curvature of the tips match those of the cone to which the tips are attached are effective in varying the vortex wake asymmetry and hence side force coefficient on a cone. The differences between the tip-flow symmetry condition when the major axes of the elliptic cross sections are perpendicular to the incidence plane and when the major axes are coincident with the incidence plane cause a change between the two symmetry conditions in the rate of change of the side force coefficient with roll angle as the tip rotates through each of the two symmetry conditions. The relation between tip roll angle and side force coefficient exhibits no roll angle or velocity hysteresis. Only the magnitude and not the shape of the ϕ–C_Y curves are dependent upon end effects. The ϕ–C_Y curves are almost completely independent of Reynolds number for a tip Reynolds number range $3,100 \leq Re_t \leq 9,600$ and a corresponding base-diameter Reynolds number range $32,000 \leq Re_D \leq 100,000$.

The relation between tip roll angle and side force coefficient for the cone is a strong function of the relative angle-of-attack α/θ_c. At small α/θ_c, the side force coefficient for the cone varies smoothly with cone roll angle. As α/θ_c increases, the variation of side force coefficient with roll angle first approaches a square-wave behavior, and then shows reductions of magnitude and changes of sign between peaks in magnitude that occur on either side of zero crossings.

At large α/θ_c, the vortex wake at the tip-flow symmetry condition in which the major axes of the large elliptic cross section tip are perpendicular to the incidence plane is very unstable. The side force coefficient of the cone undergoes large fluctuations with time that suggest a switching behavior in the vortex wake.

The behavior of the roll angle-side force characteristics for the cone can be understood from the vortex wake geometry variations. For small α/θ_c, the vortex locations vary smoothly with cone roll angle, indicating a smooth variation of side force coefficient with roll angle. For larger α/θ_c, the vortex locations on the aft portion of the cone undergo a large shift away from a symmetric configuration as the tip moves away from a symmetry condition. This causes a large change in the side force coefficient. As the tip rotates further away from the symmetry condition, the vortex closer to the cone moves across the cone centerline, causing a reduction and eventual change of sign of the side force coefficient.

The vortex crossover that results in a change of sign of the side force coefficient occurs downstream of the point where the vortex at the greater distance from the cone breaks away from the cone. Ahead of the vortex breakaway location, the vortex locations vary smoothly with cone roll angle, indicating a smooth variation of side force coefficient with roll angle ahead of the breakaway point. Smooth variations with vortex location ahead of vortex breakaway occur for $\alpha/\theta_c = 9$ and $Re_t = 1,884$. Increasing the tip radius of the elliptic cross section tip causes the vortex breakaway to occur farther back on the cone, increasing the effectiveness of the tip in controlling the vortex wake. The large elliptic cross section tip would probably be a viable yaw

control device for a high-performance aircraft at high angle of attack.

Future work

Two areas of interest regarding the tip geometry merit further study: the delay of vortex breakaway caused by increasing tip radius, and the effect of cone semi-angle (or apex semi-angle, in the case of the ogive nose) on the effectiveness of the elliptic cross section tip in controlling vortex wake asymmetry. A correlation between tip Reynolds number and axial location of vortex breakaway for cones with blunted tips should be established, if indeed such a correlation exists. If α/θ_A is indeed the correct governing parameter for the flow past the cone or ogive with an elliptic cross section tip, then the smoothly-varying side force behavior found at lower values of α/θ_A would be carried to higher actual angles of attack if the cone semi-angle θ_c or the ogive apex angle θ_A were increased. The effectiveness of the elliptic cross section tip in controlling vortex wake asymmetry ahead of vortex breakaway indicates that tests with the tip on an aircraft configuration at high angle of attack are certainly warranted. Another topic that warrants further consideration is the effectiveness of the elliptic cross section tip at tip Reynolds numbers high enough for transitional or turbulent boundary layer separation. Finally, the need for an analytical description of the mechanism by which disturbances at the tip are propagated downstream into the vortex wake remains paramount.

References

ABRAMOWITZ, M. and STEGUN, I. A., eds. [1964] *Handbook of Mathematical Functions With Formulas, Graphs, and Mathematical Tables (National Bureau of Standards Applied Mathematics Series* **55**, National Bureau of Standards, Washington, D. C.; tenth printing 1970).

AHN, S. and SIMPSON, R. L. [1992] "Cross-flow separation on a prolate spheroid at angles of attack," *AIAA 30th Aerospace Sciences Meeting, 6–9 January 1992 (Reno, Nevada), AIAA Paper No. 92–0428.*

ALLEN, H. J. and PERKINS, E. W. [1951a] "Characteristics of flow over inclined bodies of revolution," *NACA RM A50L07.*

ALLEN, H. J. and PERKINS, E. W. [1951b] "A study of the effects of viscosity on flow over slender inclined bodies of revolution," *NACA Report No. 1048.*

ALLEN, J. M., HERNANDEZ, G., and LAMB, M. [1983] "Body-surface pressure data on two monoplane-wing missile configurations with elliptical cross sections at Mach 2.50," *NASA TM 85645.*

ALLEN, J. M. and PITTMAN, J. L. [1984] "Analysis of surface pressure distributions on two elliptic missile bodies," *J. Spacecraft and Rockets* **21**(6), 528–533.

BERNHARDT, J. E. and Williams, D. R. [1992] "The effect of Reynolds number on vortex asymmetry about slender bodies," *private communication of article submitted to Phys. Fluids.*

BIPPES, H. and TURK, M. [1984] "Oil flow patterns of separated flow on a hemisphere cylinder at incidence," *DFVLR FB 84-20.*

BROWN, C. E. and MICHAEL, W. H., JR. [1955] "On slender delta wings with leading edge separation," *NACA TN 3430.*

BRYSON, A. E. [1959] "Symmetric vortex separation on circular cylinders and cones," *Transactions A. S. M. E., J. Applied Mechanics*, **26**(4), 643–648.

CHAMBERS, J. R., ANGLIN, E. L., and BOWMAN, J. S., JR. [1970] "Effects of a pointed nose on spin characteristics of a fighter airplane model including correlation with theoretical calculations," *NASA TN D–5921.*

CHAMPIGNY, P. [1984]"Reynolds number effect on the aerodynamic characteristics of an ogive-cylinder at high angles of attack," *AIAA 2^{nd} Applied Aerodynamics Conference, 21–23 August 1984 (Seattle, Washington), AIAA Paper No. 84–2176.*

CHIN, S. and LAN, C. E. [1988] "Calculation of symmetric and asymmetric vortex separation on cones and tangent ogives based on discrete vortex models," *NASA CR–4122.*

CHONG, M. S., PERRY, A. E., and CANTWELL, B. J. [1990] "A general classification of three-dimensional flow fields," *Phys. Fluids A* **2**(5), 765–777.

CHU, J., HALL, R. M., and KJELGAARD, S. O. [1988] "Low-speed vortical flow over a 5-degree cone with tip geometry variations," *SAE Aerospace Technology Conference and Exposition, 3–6 October 1988 (Anaheim, California), SAE Paper No. 881422.*

COE, P. L., CHAMBERS, J. R., and LETKO, WILLIAM [1972] "Asymmetric lateral-directional characteristics of pointed bodies of revolution at high angles of attack," *NASA TN D–7095.*

CULICK, F. E. C. [1992] *Private communication.*

DEGANI, D. [1991] "Effect of geometrical disturbance on vortex asymmetry," *AIAA J.* **29**(4), 560–566.

DEGANI, D. and SCHIFF, L. B. [1989a] "Numerical simulation of vortex unsteadiness on slender bodies of revolution at large incidence," *AIAA 27th Aerospace Sciences Meeting, 9–12 January 1989 (Reno, Nevada), AIAA Paper No. 89–0195.*

DEGANI, D. and SCHIFF, L. B. [1989b] "Numerical simulation of the effect of spatial disturbances on vortex asymmetry," *AIAA 27th Aerospace Sciences Meeting, 9–12 January 1989 (Reno, Nevada), AIAA Paper No. 89–0340.*

DEGANI, D. and TOBAK, M. [1992] "Experimental study of controlled tip disturbance effect on flow asymmetry," *Phys. Fluids A* **4**(12), 2825–2832.

DEXTER, P. C. and HUNT, B. L. [1981] "The effects of roll angle on the flow over a slender body of revolution at high angles of attack," *AIAA 19th Aerospace Sciences Meeting, 12–15 January 1981 (St. Louis, Missouri), AIAA Paper No. 81–0358.*

DYER, D. E., FIDDES, S. P. and SMITH, J. H. B. [1982] "Asymmetric vortex formation from cones at incidence – a simple inviscid model," *The Aeronautical Quarterly* **33**(4), 293–312.

EDWARDS, O. R. [1978] " Northrop F-5F shark nose development," *NASA CR–158936.*

ERICSSON, L. [1990] "The fickle effect of nose microasymmetry on the high-alpha aerodynamics," *AIAA 28th Aerospace Sciences Meeting, 8–11 January 1990 (Reno, Nevada), AIAA Paper No. 90–0067.*

ERICSSON, L. [1990] "Lateral oscillations of sting-mounted models at high alpha," *J. Spacecraft and Rockets* **27**(5), 508–513.

ERICSSON, L. E. and READING, J. P. [1979] "Alleviation of vortex-induced asymmetric loads," *J. Spacecraft and Rockets* **17**(6), 546–553.

ERICSSON, L. E. and READING, J. P. [1980] "Vortex-induced asymmetric loads in 2-D and 3-D flows," *AIAA 18th Aerospace Sciences Meeting, 14–16 January 1980 (Pasadena, California), AIAA Paper No. 80–0181.*

ERICSSON, L. E. and READING, J. P. [1981a] "Review of vortex-induced asymmetric loads – Part I," *Z. Flugwiss. Weltraumforsch* **5**(3), 162–174.

ERICSSON, L. E. and READING, J. P. [1981b] "Review of vortex-induced asymmetric loads – Part II," *Z. Flugwiss. Weltraumforsch* **5**(6), 349–366.

ERICSSON, L. E. and READING, J. P. [1986] "Asymmetric vortex shedding from bodies of revolution," in M. J. Hemsch and J. N. Nielsen, eds.,*Tactical Missile Aerodynamics* (M. Summerfield, series editor-in-chief, *Progress in Astronautics and Aeronautics* **104**, American Institute of Aeronautics and Astronautics, New York, 1986), 243–296.

FIDDES, S. P. [1980] "A theory of the separated flow past a slender elliptic cone at incidence," *AGARD CP–291 Computation of Viscous-Inviscid Interaction*, Paper No. 30.

FIDLER, J. E. [1980] "Active control of asymmetric vortex effects," *AIAA 18th Aerospace Sciences Meeting, 14–16 January 1980 (Pasadena, California), AIAA Paper No. 80–0182.*

FOX, R. W. and MACDONALD, A. T. [1978] *Introduction to Fluid Mechanics, 2nd ed.* (John Wiley and Sons, New York).

GHARIB, M. [1985] "Effect of flow oscillations on cavity drag and a technique for their control," *JPL Publication 85-72.*

GOWEN, F. E. and PERKINS, E. W. [1958] "A study of the effect of body shape on the vortex wakes of inclined bodies at a Mach number of 2," *NACA RM A53I17.*

GRAVES, E. B. [1977] "Aerodynamic characteristics of a monoplanar missile concept with bodies of circular and elliptical cross sections," *NASA TM 74079.*

GREGORIOU, G. [1982] "Modern missile design for high angle of attack," *AGARD LS–121 High Angle of Attack Aerodynamics*, Paper No. 5.

GUYTON, R. W. and MAERKI, G. [1992] "X-29 forebody jet blowing," *AIAA 30th Aerospace Sciences Meeting, 7–10 January 1992 (Reno, Nevada), AIAA Paper No. 92–0017.*

GUYTON, R. W., OSBORN, R. F. and LEMAY, S. P. [1991] "Forebody vortex control aeromechanics," *AGARD CP–497 Manoeuvring Aerodynamics*, Paper No. 16.

HALL, R. M. [1987] "Forebody and missile side forces and the time analogy," *AIAA 25th Aerospace Sciences Meeting, 12–15 January 1987 (Reno, Nevada), AIAA Paper No. 87–0327.*

HALL, I. M., ROGERS, E. W. E. and DAVIES, B. M. [1957] "Experiments with inclined blunt-nosed bodies at M = 2.45," *ARC R&M No. 3128.*

HARTWICH, P., HALL, R. and HEMSCH, M. [1990] "Navier-Stokes computations of vortex asymmetries controlled by small surface imperfections," *AIAA 28th Aerospace Sciences Meeting, 8–11 January 1990 (Reno, Nevada), AIAA Paper No. 90–0385.*

HO, C.-H. and HUERRE, P. [1984] "Perturbed free shear layers," *Ann. Rev. Fluid Mech.* **16**, 365–424.

HORNUNG, H. G. and PERRY, A. E. [1984] "Some aspects of three-dimensional separation, part I: streamsurface bifurcations," *Z. Flugwiss. Weltraumforsch.* **8**(2), 77–87.

HOWARD, R. M., RABANG, M. P. and ROANE, D. P., JR. [1989] "Aerodynamics effects of a turbulent flowfield on a vertically-launched missile," *J. Spacecraft and Rockets* **26**(6), 445–451.

HSIEH, T. [1977] "An investigation of separated flows about a hemisphere-cylinder at incidence in the Mach number range from 0.6 to 1.5," *AIAA 15th Aerospace Sciences Meeting, 24–26 January 1977 (Los Angeles, California), AIAA Paper No. 77-179.*

HSIEH, T. and WANG, K. C. [1976] "Concentrated vortex on the nose of an inclined body of revolution," *AIAA J.* **14**(5), 698–700.

HUNT, B. L. [1982] "Asymmetric vortex forces and wakes on slender bodies (invited paper)," *AIAA 9th Atmospheric Flight Mechanics Conference, 9–11 August 1982 (San Diego, California), AIAA Paper No. 82–1336.*

HUNT, B. L. and DEXTER, P. C. [1978] "Pressures on a slender body at high angle of attack in a very low turbulence air stream," *AGARD CP–247 High Angle of Attack Aerodynamics*, Paper No. 17.

JORGENSEN, L. H. [1977] "Prediction of static aerodynamic characteristics for slender bodies alone and with lifting surfaces to very high angles of attack," *NASA TR R-474.*

JORGENSEN, L. H. and NELSON, E. R. [1974] "Experimental aerodynamic characteristics for a cylindrical body of revolution with various noses at angles of attack from 0^o to 58^o and Mach numbers from 0.6 to 2.0," *NASA TM X–3128.*

JORGENSEN, L. H. and NELSON, E. R. [1975] "Experimental aerodynamic characteristics for a cylindrical body of revolution with side strakes and various noses at angles of attack from 0^o to 58^o and Mach numbers from 0.6 to 2.0," *NASA TM X-3130.*

KEENER, E. R. [1986] "Flow-separation patterns on symmetric forebodies," *NASA TM 86016.*

KEENER, E. R. and CHAPMAN, G. T. [1974] "Onset of aerodynamic side forces at zero sideslip on symmetric forebodies at high angles of attack," *AIAA Mechanics and Control of Flight Conference, 5–9 August 1974 (Anaheim, California), AIAA Paper No. 74–770.*

KEENER, E. R. and CHAPMAN, G. T. [1977] "Similarity in vortex asymmetries over slender bodies and wings," *AIAA J.* **15**(9), 1370–1372.

KEENER, E. R., CHAPMAN, G. T., COHEN, L. and TALEGHANI, J. [1976] "Side forces on a tangent ogive forebody with fineness ratio of 3.5 at high angles of attack and Mach numbers from 0.1 to 0.7." *NASA TM X-3437.*

KEENER, E. R., CHAPMAN, G. T., COHEN, L. and TALEGHANI, J. [1977] "Side forces on forebodies at high angles of attack and Mach numbers from 0.1 to 0.7: two tangent ogives, paraboloid and cone," *NASA TM X-3438.*

KEENER, E. R., CHAPMAN, G. T. and KRUSE, R. L. [1976] "Effects of Mach number and afterbody length on onset of asymmetric forces on bodies at zero sideslip and high angles of attack," *AIAA 14th Aerospace Sciences Meeting, 26–28 January 1976 (Washington, D.C.), AIAA Paper No. 76–66.*

KOMPENHANS, J. and HARTMANN, K. [1987] "Flow visualization on an ogive-nosed circular cylinder body at high incidence by means of the laser light sheet method," *European Space Agency Technical Translation 1066 (translation of "Stroemungs-sichtbarmachung an einem hochangestellten Ogigkreiszylinderrumpf mit Hilfe der Laser-Lichtschnittmethode," DFVLR-FB-86-45).*

KOREN, S., ARIELI, R. and ROM, J. [1992] "Measurement of lateral aerodynamic characteristics of forebodies at high angles of attack in subsonic and transonic flows," *AIAA 30th Aerospace Sciences Meeting, 6–9 January 1992 (Reno, Nevada), AIAA Paper No. 92–0174.*

KRUSE, R. L., KEENER, E. R., CHAPMAN, G. T. and CLASER, G. [1979] "Investigation of the asymmetric aerodynamic characteristics of cylindrical bodies of revolution with variations in nose geometry and rotational orientation at angles of attack to 58^o and Mach numbers to 2," *NASA TM 78533.*

LAMONT, P. J. [1980] "Pressures around an inclined ogive cylinder with laminar, transitional, or turbulent separation," *AIAA J.* **20**(11), 1492–1499.

LAMONT, P. J. and HUNT, B. L. [1976] "Pressure and force distributions on a sharp-nosed circular cylinder at large angles of inclination to a uniform subsonic stream," *J. Fluid Mech.* **76**, 519–559.

LEGENDRE, R. [1956] "Separation de l'écoulement laminaire tridimensionnel," *La Recherche Aéronautique* **54**, 3–8.

LETKO, W. [1953] "A low-speed experimental study of the directional characteristics of a sharp-nosed fuselage through a large angle of attack range at zero sideslip," *NACA TN 2911.*

LIEPMANN, H. W. and ROSHKO, A. [1957] *Elements of Gasdynamics* (John Wiley and Sons, New York).

LIGHTHILL, M. J. [1963] "Attachment and separation in three-dimensional flows," in Rosenhead, L., ed., *Laminar Boundary Layers* (Clarendon Press, Oxford; reprinted 1988 Dover, New York).

LOWSON, M. V. [1989] "The three-dimensional vortex sheet structure on delta wings," *AGARD CP–438 Fluid Dynamics of Three-Dimensional Turbulent Shear Flows and Transition*, Paper No. 11.

MALCOLM, G. N. and NG, T. T. [1991] "Aerodynamic control of fighter aircraft by manipulation of forebody vortices," *AGARD CP–497 Manoeuvring Aerodynamics*, Paper No. 15.

MASKELL, E. C. [1955] "Flow separation in three dimensions," *RAE Report No. Aero 2565.*

MENDENHALL, M. R. and NIELSEN, J. C. [1975] "Effects of symmetrical vortex shedding on the longitudinal aerodynamic characteristics of wing-body-tail combinations," *NASA CR–2473.*

MILNE-THOMSON, L. M. [1968] *Theoretical Hydrodynamics, 5th ed.* (MacMillan, New York).

MODI, V. J. and STEWART, A. C. [1992] "Approach to side force alleviation through modification of the pointed forebody geometry," *J. Aircraft* **29**(1), 123–130.

MOSKOVITZ, C. A. [1989] *An experimental investigation of the physical mechanisms controlling the asymmetric flow past slender bodies at large angles of attack*, Ph. D. thesis, North Carolina State University.

MOSKOVITZ, C. A., HALL, R. M. and DEJARNETTE, F. R. [1989] "Effects of nose bluntness, roughness, and surface perturbations on the asymmetric flow past slender bodies at large angles of attack," *AIAA 7^{th} Applied Aerodynamics Conference, 31 July – 2 August 1989 (Seattle, Washington), AIAA Paper No. 89-2236-CP.*

MOSKOVITZ, C. A., HALL, R. M. and DEJARNETTE, F. R. [1991] "New device for controlling asymmetric flowfields on forebodies at large alpha," *J. Aircraft* **28**(7), 456–462.

OSWATITSCH, K. [1958] In Goertler, H., ed., *Die Ablönsungsbedingung von Grenzschichten, Grenzschicht Forschung* (Springer-Verlag, Berlin and New York).

PEAKE, D. J. and TOBAK, M. [1980] "Three-dimensional interactions and vortical flows with emphasis on high speeds," *AGARDograph No. 252.*

PEAKE, D. J. and TOBAK, M. [1982] "Three-dimensional separation and attachment," *AGARD LS–121 High Angle of Attack Aerodynamics*, Paper No. 1.

PEAKE, D. J. and TOBAK, M. [1982] "Three-dimensional flows about simple components at angle of attack," *AGARD LS–121 High Angle of Attack Aerodynamics*, Paper No. 2.

PERRY, A. E. and CHONG, M. S. [1986] "A series expansion study of the Navier-Stokes equations with applications to three-dimensional separation patterns, *J. Fluid Mech.* **173**, 207–223.

PERRY, A. E. and CHONG, M. S. [1987] " A description of eddying motions and flow patterns using critical-point concepts," *Ann. Rev. Fluid Mech.* **19**, 125–155.

PERRY, A. E. and FAIRLIE, B. D. [1974] "Critical points in flow patterns," in F. N. Frenkiel and R. E. Munn, eds., *Turbulent Diffusion in Environmental Pollution* (H. E. Landsberg and J. Van Mieghem, eds., *Advances in Geophysics* **18B**, Academic Press, New York, 1974).

PERRY, A. E. and LIM, T. T. [1978] "Coherent structures in coflowing jets and wakes," *J. Fluid Mech.* **88**, 451–463.

PERRY, A. E., LIM, T. T. and CHONG, M. S. [1980] "The instantaneous velocity fields of coherent structures in coflowing wakes and jets," *J. Fluid Mech.* **101**, 243–256.

PICK, G. S. [1975] "Investigation of side forces on ogive-cylinder bodies at high angles of attack in the M = 0.5 to 1.1 range," *NSRDC Report No. 4533, reprint of AIAA Paper No. 71-570.*

PIDD, M. and SMITH, J. H. B. [1990] "Asymmetric vortex flow over circular cones," *AGARD CP–494 Vortex Flow Aerodynamics*, Paper No. 18

POLHAMUS, E. C. [1984] "A review of some Reynolds number effects related to bodies at high angles of attack," *NASA CR 3809.*

RAINBIRD, W. J., CRABBE, R. S. and JUREWICZ, L. S. [1963] "A water tunnel investigation of the flow separation about circular cones at incidence," *National Research Council of Canada Report No. LR-385.*

ROM, JOSEF [1992] *High Angle of Attack Aerodynamics* (Springer-Verlag, New York).

SARPKAYA, T. [1966] "Separated flow about lifting bodies and impulsive flow about cylinders," *AIAA J.* 4(3), 414–420.

SKOW, A. M. and ERICKSON, G. E. [1982] "Modern fighter aircraft design for high-angle-of-attack maneuvering," *AGARD LS–121 High Angle of Attack Aerodynamics*, Paper No. 4.

SMITH, J. H. B. [1968] "Improved calculations of leading-edge separation from slender, thin, delta wings," *Proc. Roy. Soc. London, Series A* **306**, 67–90.

THOMSON, K. D. and MORRISON, D. F. [1971] "The spacing, position, and strength of vortices in the wake of slender cylindrical bodies at incidence," *J. Fluid Mech.* **50**, 751–783.

TOBAK, M. and PEAKE, D. J. [1982] "Topology of three-dimensional separated flows," *Ann. Rev. Fluid Mech.* **14**, 61–85.

VAN DYKE, M. [1982] *An Album of Fluid Motion* (Parabolic Press, Stanford, California).

WARD, T. [1976] "The Hydrodynamics Laboratory at the California Institute of Technology–1976," *Trans. A. S. M. E., J. Fluids Eng.* **98**(6), 740–748.

WARD, K. C. and KATZ, J. [1989] "Development of flow structures in the lee of an inclined body of revolution," *J. Aircraft* **26**(3), 198–206.

WARDLAW, A. B., JR. [1979] "High-angle-of-attack missile aerodynamics," *AGARD LS–98 Missile Aerodynamics*, Paper No. 5.

WARDLAW, A. B., JR. and YANTA, W. J. [1980] "The flow field about, and forces on slender bodies at high angles of attack," *AIAA 18th Aerospace Sciences Meeting, 14–16 January 1980 (Pasadena, California), AIAA Paper No. 80–0184.*

WERLÉ, H. [1962] "Le décollement sur les corps de révolution a basse vitesse (observations au tunnel hydrodynamique a visualisation," *La Recherche Aéronautique* **90**, 3–14.

WERLÉ, H. [1982] "Flow visualization techniques for the study of high incidence aerodynamics," *AGARD LS–121 High Angle of Attack Aerodynamics*, Paper No. 3.

YANTA, W. and WARDLAW, A. [1981] "Multi-stable vortex patterns on slender, circular bodies at high incidence," *AIAA 19th Aerospace Sciences Meeting, 12–15 January 1981 (St. Louis, Missouri), AIAA Paper No. 81–0006.*

ZILLIAC, G. G., DEGANI, D. and TOBAK, M. [1991] "Asymmetric vortices on a slender body of revolution," *AIAA J.* **29** (5), 667–675.